Initiation of Gaseous Detonation by Conical Projectiles

Jimmy Verreault

Doctor of Philosophy

Department of Mechanical Engineering

McGill University

Montreal,Quebec

December 2011

A thesis submitted to the
Faculty of Graduate Studies and Research
In partial fulfillment of the requirements of the degree
Doctor of Philosophy

Abstract

Initiation and stabilization of a detonation by hypersonic conical projectiles launched into combustible gas mixtures is investigated. This phenomenon must be understood for the design and optimization of specific hypersonic propulsion devices, such as the oblique detonation wave engine and the ram accelerator. The criteria for detonation initiation by a projectile is also related to fundamental aspects of detonation research, such as the requirement for direct initiation of a detonation by a blast wave. Experimental results of this problem also offer useful references for validation of numerical and theoretical modeling.

Projectiles with cone half angles varying from 15° to 60° were launched into stoichiometric mixtures of hydrogen/oxygen with 70% argon dilution at initial pressures between 10 and 200 kPa. The projectiles were launched from a combustion-driven gas gun at velocities up to 2.2 km/s (corresponding to 133% of the Chapman Jouguet velocity). Pictures of the flowfields generated by the projectiles were taken via Schlieren photography.

Five combustion regimes were observed about the projectile ranging from prompt and delayed oblique detonation wave formation, combustion instabilities, wave splitting, and an inert shock wave. Two types of transition from the prompt oblique detonation wave regime to the inert shock regime were observed. The first (the delayed oblique detonation wave regime) showed an inert shock attached to the tip of the projectile followed by a sharp kink at the onset of an oblique detonation wave; this regime occurred by decreasing the cone angle at high mixture pressures. The second (the combustion instabilities regime) exhibited large density gradients due to combustion ignition and quenching phenomena; this regime occurred by decreasing the mixture pressure at large cone angles.

A number of theoretical models were considered to predict critical conditions for the initiation of oblique detonations. The Lee-Vasiljev model agreed qualitatively well with the experimental results for relatively blunt projectiles (cone half-angle larger than 35°) and low mixture pressures (lower than 100 kPa). The trend of the critical Damköhler number calculated along the projectile cone surface was similar to that of the experimental results for slender cones (cone half-angles lower 35°) and high mixture pressures (higher than 100 kPa). Steady 2D simulations of reacting flows over finite wedges using the method of characteristics with a one-step Arrhenius chemical reaction model reproduced the three regimes observed for direct initiation of a detonation: the subcritical, critical and supercritical regimes. It is shown that in order for a 2D wedge to be equivalent to the problem of blast initiation of a detonation (which is the essence of the Lee-Vasiljev model), the Mach number normal to the oblique shock needs to be greater than 50 and the wedge angle has to be smaller than 30°.

The formation and structure of the oblique detonation waves stabilized on semi-infinite wedges and cones were investigated with method of characteristics calculations and also validated with CFD simulations. Excellent agreement was reached between the angle of overdriven oblique detonations obtained from the simulations and those from a polar analysis. For wedge or cone angles equal or lower than the minimum angle for which an oblique detonation is attached (according to the polar analysis), a Chapman-Jouguet oblique detonation was initiated. In the conical configuration, the curvature around the cone axis allowed an oblique detonation to be self-sustained at an angle less than without the curvature effect. At larger activation energies, the initiation process of an oblique detonation wave at the tip of a semi-infinite wedge or cone was identified. The process begins with shock-initiated reaction occurring on the wedge or cone surface, and the resulting compression waves increase the shock angle until a transition to oblique detonation occurs. Depending on the activation energy of the reaction model, the transition can be gradual or discontinuous, resulting in an overshoot of the wave angle that then decays to the final oblique detonation angle.

Unsteady 2D computational simulations were also conducted and showed the cellular structure of an oblique detonation wave. Instabilities in the form of transverse shock waves along the oblique detonation front arise for large activation energies. By tracking the trajectory of the transverse waves in time, a cellular pattern is recognized, similar to that observed for normal detonation waves. For increasing wedge angles, the degree of overdrive of the oblique detonation increases, and the cell size of the oblique detonation structure decreases.

Résumé

Cette étude a pour objet l'initiation et la stabilisation d'une onde de détonation par un projectile conique hypersonique projeté dans un milieux combustible gazeux. On retrouve ce phénomène dans certains propulseurs hypersoniques, comme le moteur à onde de détonation oblique et le ram accelerator (ou ramac). Le critère pour l'initiation d'une détonation par un projectile est relié à des aspects fondamentaux de la recherche en détonique, tel que les conditions nécessaires pour l'initation directe d'une détonation par une forte onde de choc. Les résultats expérimentaux de ce problème offrent aussi d'utiles références pour la validation d'études numériques et théoriques.

Des projectiles conique dont le demi-angle varie de 15° à 60° ont été lancés dans des mélanges stoechiométriques d'hydrogène et d'oxygène avec une dilution d'argon à 70% à des pressions initiales de 10 à 200 kPa. Les projectiles ont été accélérés par un canon qui produit la propulsion à partir de la combustion gazeuse de mélanges stoechiométriques composées d'hydrogène et d'oxygène à des pressions initiales élevées. Des vitesses de l'ordre de 2.2 km/s ont été atteintes, correspondant à 133% de la vitesse Chapman Jouguet. Des photographies de l'écoulement autour des projectiles ont été prises avec un système Schlieren.

Cinq régimes de combustion ont été observés autour des projectiles: formation d'une onde de détonation oblique prompte et retardée, instabilités de combustion, séparation d'ondes, et onde de choc inerte. Deux types de transition entre les régimes de détonation oblique prompte et de choc inerte on été observés. La première (qui concerne le régime onde de détonation retardée) a produit une onde de choc inerte attachée au nez du projectile suivie d'une augmentation abrupte de l'angle de choc au passage à la détonation oblique. Cette transition a eu lieu en diminuant l'angle de cône à de hautes pression de mélange. La deuxième (qui concerne le régime instabilités de combustion) a révélé la présence de forts gradients de densité causés par des phénomènes d'allumage et d'extinction du mélange combustible. Cette transition a été observée en diminuant la pression de mélange à des angles de cône élevés.

Quelques modèles théoriques ont été considérés afin de prédire les conditions critiques pour l'initiation de détonations obliques. Le modèle de Lee-Vasiljev s'est avéré en accord qualitatif avec les résultats expérimentaux pour des projectiles relativement émoussés (des demi-angles de cône plus grand que 35°) et de basses pressions de mélanges (plus petit que 100 kPa). La tendance du nombre de Damköhler critique calculé sur la surface du cône s'est avéré similaire à celle des résultats expérimentaux pour des projectiles élancés (des demi-anges de cône plus petit que 35°) et des pressions de mélanges élevées (plus grand que 100 kPa). Des simulations 2D en mode permanent d'écoulements réactifs autour de dièdres finis en utilisant la méthode des caractéristiques comprenant un modèle chimique à une équation de forme Arrhenius ont reproduis les trois régimes observés dans les études d'initiation directe de détonations: les régimes sous-critique, critique et sur-critique. Il est démontré qu'un dièdre est équivalent au problème d'initiation directe d'une détonation si le nombre de Mach normal au choc oblique est supérieur à 50 et si l'angle du dièdre est inférieur à 30°.

La formation et la structure des ondes de détonation obliques stabilisées sur des dièdres et des cônes semi-infinis ont été étudiées avec la méthode des caractéristiques et validées avec des simulations numériques. Un excellent accord a été observé entre l'angle d'une détonation oblique forte obtenu des simulations et celui dérivé d'une analyse des polaires. Pour un angle de dièdre ou de cône égal ou inférieur à l'angle minimal pour lequel une détonation oblique est attachée (selon les polaires), une détonation oblique Chapman-Jouguet a été initiée. Pour une configuration conique, la courbure autour de l'axe du cône a permis une détonation oblique d'être non supportée à un angle inférieur à celui sans l'effet de courbure. Pour des énergies d'activation élevées, le procédé d'initiation d'une onde de détonation oblique par un dièdre ou un cône a été identifié. Le procédé débute par l'initiation de réactions chimiques par onde de choc oblique sur la surface du dièdre ou du cône. Des ondes de compression sont produites et augmentent l'angle du choc jusqu'à la transition à la détonation oblique. Selon l'énergie d'activation du modèle chimique, la transition peut être graduelle ou abrupte, auquel cas l'angle du choc atteint un maximum et ensuite diminue à l'angle de détonation oblique.

Des simulations numériques 2D en mode non permanent ont révélé la structure cellulaire d'une onde de détonation oblique. Des instabilités sous forme d'ondes de choc transversales au front de la détonation oblique surviennent pour des énergies d'activation élevés. En suivant la trajectoire de ces ondes transversales dans le temps, un modèle cellulaire est identifié, similaire au modèle d'une détonation droite. En augmentant l'angle du dièdre, le degré de force de la détonation oblique augmente, et la taille cellulaire de sa structure diminue.

Acknowledgements

My graduate school experience at McGill University has been extremely rewarding on both professional and personal levels. My advisor, Prof. Andrew J. Higgins, guided me to undertake and bring to success scientific challenges with a rigorous methodology. His thorough knowledge on the subject, keen and original ideas, and wide experience on experimental research always inspired me to push further the boundaries of possibilities.

I am grateful to my friend and fellow graduate student, Patrick L. Batchelor, for teaching me to run ballistic range experiments, a vital part of the project. I wish to thank the professors at McGill University who kindly provided me with timely advice and suggestions. Prof. John H.S. Lee gave me extremely valuable knowledge on detonation and gasdynamics, Prof. Jeff Bergthorson helped me with chemical kinetics modeling, and Prof. Evgeny V. Timofeev shared his knowledge on computational modeling. The help of Prof. Matei I. Radulescu, from University of Ottawa, on detonation modeling was an essential element of the numerical investigation. James Quirk is acknowledged for making his Amrita environment available for use in this study. The general interests on the topic and the personal encouragements from Robert Stowe and Paul Harris from Defense Research and Development Canada — Valcartier were greatly appreciated.

New ideas and insights originated from discussions with the members of the Shock Wave Physics Group, especially with Oren Petel, François-David Tang, Daniel

Szirti, Jean-Sébastien Grondin, Anne Jesuthasan and Vsevolods Kamenskihs. Special thanks go to Jason Loiseau and François-Xavier Jetté for carefully revising this dissertation.

The completion of the experimental campaign would not have been possible without the help of the technical staff, especially Gary Savard, John Boisvert, Ray Lemay, Tony Micozzi and Andreas Hofmann. Their dedication to assist me with machining different parts of the launcher is deeply appreciated.

The company of my family and the support of Meenakshi Venkat all along the course of my doctoral studies has contributed to overcome challenges encountered with moral support, encouragements and love.

This research project was supported in part by Defense Research and Development Canada — Valcartier, the Natural Sciences and Engineering Research Council of Canada and McGill University.

Table of Contents

List of Tables

Table page

List of Figures

CHAPTER 1
Introduction

1.1 Overview

Fill a chamber with a combustible gaseous mixture, fire a projectile at 2 – 3 km/s into it and assuming you are able to monitor the flow conditions (such as the temperature, pressure or density) near the projectile as it travels through the mixture, you are able to observe very interesting flow patterns induced by the passage of the projectile. In such an experiment, strong shock waves are produced by the hypersonic projectile and ignition of the reactive mixture may occur behind these shocks. Complex interactions between these two phenomena (gasdynamics and chemistry) can produce very different types of flowfields. This technique offers several advantages for the study of detonation initiation. The independent parameters (such as the mixture composition and pressure, or the projectile velocity and diameter) can be easily modified to determine the required conditions to initiate a detonation wave from a hypersonic projectile.

In the present work, flowfields around hypersonic projectiles launched into combustible mixtures were recorded with a high-speed camera in order to distinguish whether the bodies successfully initiated a detonation wave, induced combustion behind the leading shock but failed to trigger a detonation, or only produced a non-reacting shock wave. The requirements for detonation initiation were therefore established from the experiments. The originality of this work, compared to previous studies on detonation initiation from projectiles, lies in the fact that the role of the projectile nose shape is determined by using conical-nosed bodies. The cone angle and the initial pressure of the mixture are the two parameters that were varied over a wide range to determine their effect on the requirements for detonation initiation.

In the following sections, the research motivation, relevant background concepts and the structure of this dissertation are presented.

1.2 Motivation

A detonation is a process that liberates a very large amount of energy in very short time and length scales. From a theoretical viewpoint, the detonation process offers a great deal of unresolved scientific challenges concerning its initiation, propagation and failure mechanisms, as well as its multi-scale structure. Applications of a gaseous detonation can be divided into two main categories: detonation hazards where the phenomenon is desired to be avoided and hypersonic propulsion devices where the phenomenon needs to be controlled. Also, experimental data on projectiles traveling into a reactive mixture are useful to the computational fluid dynamics (CFD) community for validation purposes.

Detonation research. A detonation wave can be characterized by *hydrodynamic* parameters that link the upstream to the downstream states through conservation laws. In the Chapman-Jouguet (CJ) theory, a single solution for a steady, self-sustained detonation is obtained when the conservation laws are solved together with the CJ postulate, which states that the fluid velocity is sonic with respect to the shock front at the downstream state. The propagation velocity of such a detonation is referred to as the CJ velocity and represents a hydrodynamic parameter. These parameters determined from the CJ theory (presented in Section 1.3.1) were shown to be very accurate when compared with experimental results.

In order to predict the conditions required for a detonation wave to be initiated, propagate or fail, the *dynamic* parameters need to be determined. These parameters are related to the structure of the detonation; they include the detonation thickness, detonation cell size, critical tube diameter, minimum tube diameter and critical energy for direct initiation. The determination of these parameters is an active field in experimental detonation research, since a complete theoretical understanding of the three-dimensional structure of a detonation wave is not available. The present investigation does not directly aim at determining detonation dynamic parameters. However, a theoretical model based on the blast wave analogy is compared against experimental results in Section 5.1.3. This model employs the critical energy required to directly initiate a cylindrical detonation, which has a dependence on the cell size of the mixture. Therefore, this study helps validate the use of certain dynamic parameters, determined in previous works, in the prediction of detonation initiation.

Hypersonic propulsion. Despite the fact that the feasibility of a practical detonation-powered propulsion device has yet to be demonstrated, numerous investigations have been performed to resolve different issues related to the general problem. The two propulsion devices driven by a detonation that have received the most attention are the oblique detonation wave engine (ODWE) and the ram accelerator.

Figure 1–1 illustrates the concept of the ODWE, also called the shock-induced combustion ramjet. The ODWE decouples the fuel injection and mixing processes from the combustion process by injecting the fuel ahead of the combustor from the

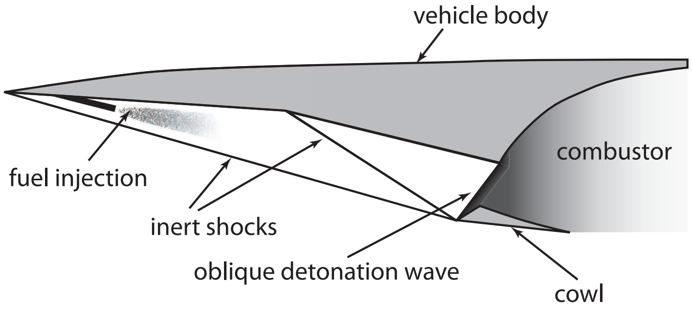

Figure 1–1: Schematic of the ODWE

forebody of the flight vehicle so that the fuel is well mixed with the air before it reaches the combustor. The first shock wave is produced at the tip of the vehicle, upstream of where the fuel is injected. The second shock wave greatly enhances the mixing rate and is designed such that it increases the flow temperature below the autoignition temperature of the mixture. Upon reaching the combustor, the mixture encounters the wedge-like engine cowl which causes the formation of an oblique detonation wave. The mixture is burnt within a very short distance (the thickness of the detonation), thus significantly reducing combustor length and related mass, volume and drag. Even though this concept shows great promise, several issues must be addressed. First, the incoming air momentum is relatively high, which makes the mixing process more difficult and thus the hydrogen tends to remain near the forebody wall. Second, premature ignition of the mixture can occur from the boundary layer or from the undesirable shock waves generated by the injector geometry or the fuel jet. Finally, the initiation and stabilization of the oblique detonation is required over the entire duration of the flight.

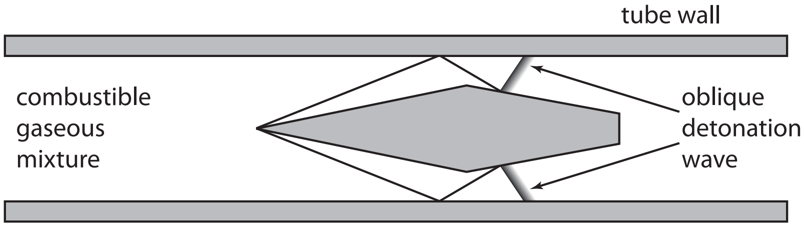

Figure 1–2: Schematic of the ram accelerator

The results presented in this investigation are of relevance to the ODWE since they identify the flow conditions for which an oblique detonation wave is initiated and stabilized. This concept was originally proposed in the 1950's [27] and was extensively investigated numerically by the research group at the UTIAS (University of Toronto Institute for Aerospace Studies) [91, 104, 26, 107].

The ram accelerator, shown in Fig. 1–2, is a hypervelocity launcher in which a projectile travels through a tube pre-filled with a combustible mixture of gases. The projectile, which resembles the centerbody of a conventional ramjet, compresses the gas mixture between itself and the tube wall as it travels supersonically through the gas. One mode of operation of the ram accelerator consists of the initiation of an oblique detonation wave on the rear part of the projectile, resulting in a zone of high pressure acting on the base of the projectile, causing its acceleration. In this mode of operation, the initiation and stabilization of the oblique detonation wave on the rear part of the body is also critical.

The ram accelerator concept was proposed by Hertzberg [44]. A series of experimental investigations were conducted at the University of Washington [45] and at the Institute of Saint-Louis [106]. The current state of the art in ram accelerator research can be found in the proceedings of the most recent international workshop on ram accelerators [5] and the current challenges are outlined by Higgins [47].

CFD validation. An adequate computational code can be a very useful tool to simulate the flowfield in the propulsion devices mentioned above. Investigations of different geometries and flow conditions can be carried out at purely computational costs. However, the size of the devices exceeds the smallest length scale of the detonation structure by many orders of magnitude. The size of a sufficiently refined computational domain to fully resolve the detonation structure is often the main obstacle to faithfully simulate the flowfields in ODWEs or ram accelerators.

The flow over a hypersonic spherical- or conical-nosed projectile can be more easily simulated numerically due to the simple geometry and smaller physical length scale. Simulations of the spherical case were extensively conducted in the 1990's to model detonation initiation and to reproduce the combustion instabilities observed experimentally (see Sec. 2.1.2). Numerical investigations of a reactive flow over a wedge and a cone were performed in the last 20 years (see Sec. 2.2.3), but there is a limited number of experimental results they can be validated against.

In order to provide experimental results for the validation of computational simulations, the present investigation utilizes Schlieren photographs of the flowfield around hypersonic conical projectiles. The variation of the independent parameters over a wide range produces very different flowfields (described in Section 4.1) with a range of chemical time scales and different types of fluid dynamics / chemistry interactions. The experimental results included in this work thus represent a unique reference for validation of CFD simulations of a reactive flow over a cone.

1.3 Background Concepts

A detonation wave is one of the two possible mechanisms of reactive wave propagation in a combustible gas mixture; the other one is a deflagration wave. A gaseous detonation wave propagates at a supersonic velocity, generally between Mach 4 and 7. A strong shock front leads the detonation wave and significantly increases the pressure and temperature of the mixture to trigger the chemical reactions. Therefore, in a detonation wave, the chemical reactions are triggered by adiabatic compression. A deflagration wave travels at much slower speed, generally at centimeters or meters per second. In this case, heat and mass transfer from the reacted gas to the fresh gas is responsible for the propagation of the deflagration.

In the following subsections, a brief overview of the relevant aspects related to a detonation wave is given. A more thorough description of the phenomenon can be found in Ficket and Davis [33], Strehlow [111] and Lee [69].

1.3.1 Chapman-Jouguet Theory

The flow conditions across a shock wave can be obtained by applying the conservation laws to a control volume that includes the shock. The flow properties are assumed in thermodynamic equilibrium on both sides of the control volume. The resulting equations are the so-called Rankine-Hugoniot relations. The same procedure can be followed for a detonation wave by including a heat release term in the energy equation to account for the chemical energy release. This analysis, referred to as the hydrodynamic theory or the Chapman-Jouguet theory, relates the thermodynamic state of the system at the equilibrium downstream and upstream states of the detonation. In the detonation reference frame, the conservation of mass, momentum, and energy in one dimension are given by:

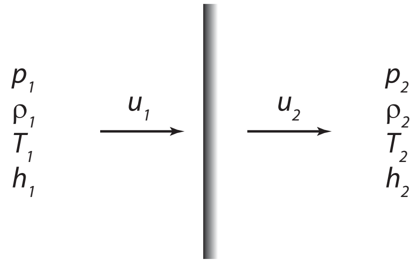

$$\begin{aligned}\rho_1 u_1 &= \rho_2 u_2 \\ p_1 + \rho_1 u_1^2 &= p_2 + \rho_2 u_2^2 \\ h_1 + q + \frac{u_1^2}{2} &= h_2 + \frac{u_2^2}{2}\end{aligned}$$

For a calorically perfect gas, the enthalpy is defined as $h = c_p T$ and the equation of state is $p = \rho R T$. Since the thermodynamic state upstream of the detonation is known, this system of five equations includes a total of six unknowns (u_1, u_2, p_2, ρ_2, T_2, h_2). In order to close the system, the velocity of the incoming gas u_1 needs to be set. It can be shown that a physical solution is obtained for a value of u_1 larger than a certain value, the CJ velocity U_{CJ}. At this CJ detonation velocity, a unique solution for the downstream state is obtained, with u_2 equal to the sonic velocity of the products. For $u_1 > U_{CJ}$, two possible solutions exist at the downstream state where u_2 is either subsonic or supersonic. The case where u_2 is subsonic refers to a *strong* detonation, whereas a *weak* detonation corresponds to a supersonic downstream velocity. Generally, it is recognized that the velocity of a self-propagating planar detonation wave is U_{CJ}. Several reasons are typically advanced as to why this should be the preferred solution. First, this value is the minimum velocity that obeys the conservation laws. Second, the entropy increase across a detonation is also minimum at the CJ velocity. Third, a self-propagating strong detonation can be discarded based on the fact that with a subsonic downstream velocity, expansion waves can enter the detonation structure and attenuate the leading shock. Finally, there is an abundance of experimental evidence that a freely propagating detonation travels at the CJ velocity.

1.3.2 ZND Detonation Structure

A simple model of a detonation structure was proposed by Zeldovich, von Neumann and Doering (ZND). In this one-dimensional model, the detonation is treated as a leading inert shock that adiabatically compresses the gaseous mixture, followed by a reaction zone where the energy is released. Figure 1–3 shows a schematic of the ZND detonation structure with the profile of the flow properties. The reaction zone is composed of a thermally neutral region, the induction zone, and a region of chemical energy release. The solution of this structure is typically obtained by calculating the flow properties behind the leading shock using the Rankine-Hugoniot relations (without the heat release term in the energy equation) and by solving the conservation laws cast in a set of one-dimensional ordinary differential equations (this model will be derived in detail in Section 7.1). Referring to the Mach number profile,

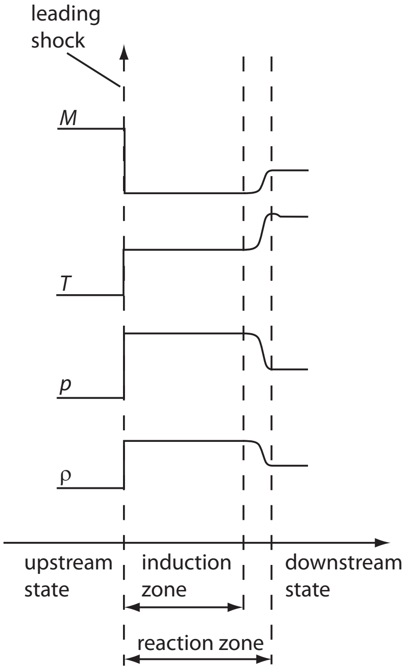

Figure 1–3: Schematic of the ZND detonation structure

the flow is subsonic in the reaction zone, is accelerated due to the chemical energy release and reaches sonic velocity at the equilibrium downstream state.

1.3.3 Cellular Detonation Structure

The one-dimensional ZND detonation structure is a theoretical representation that describes the propagation mechanism based on the coupling between the leading shock and the chemical energy release. However, the actual detonation structure is by nature three-dimensional and unsteady. This structure was identified experimentally by placing a film coated with soot on the wall of a detonation tube. After the experiment, a cellular pattern could be observed on the film. It is now recognized that this cellular pattern is related to the propagation of transverse shock waves (triple points) within the detonation structure. Figure 1–4 illustrates a schematic

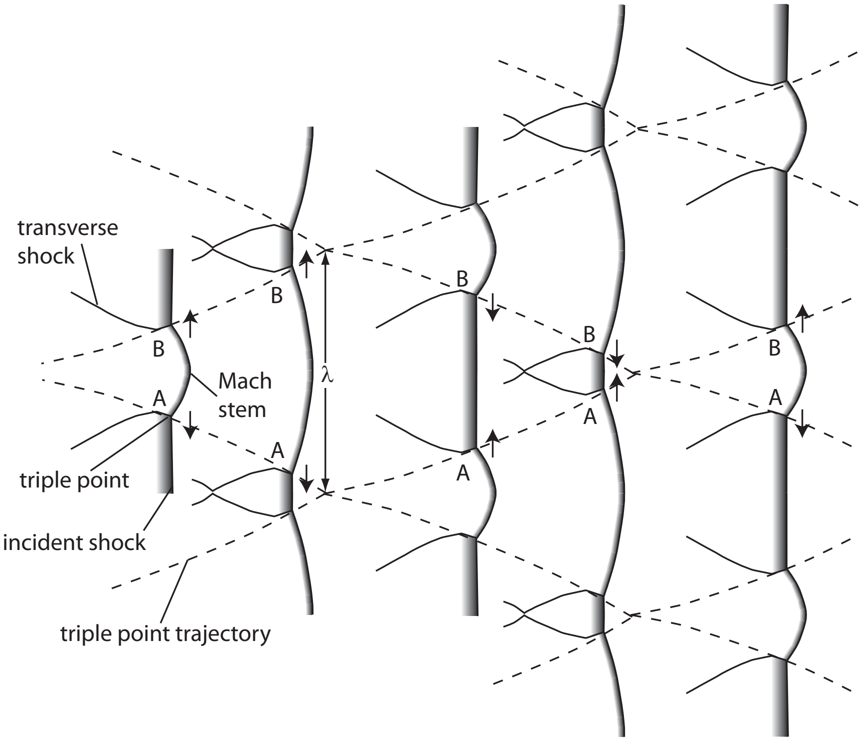

Figure 1–4: Schematic of the cellular detonation structure showing the detonation at different times and the cellular pattern traced by triple points

of the cellular detonation structure at different instants in time (the detonation propagates to the right). The triple points are located at the intersection of a Mach stem, an incident shock and a transverse shock. The trajectory of the triple points is given by the dashed lines, forming cells of width λ. The motion of two triple points A and B along the detonation is shown by arrows. The reaction zone behind the Mach stem is shorter than behind the incident shock. In the schematic, the size of the different cells is the same. In actual mixtures, the size of the different cells can be relatively regular or highly irregular, depending on the mixture composition and initial pressure and temperature.

1.3.4 Detonation Initiation by a Projectile

The requirement to initiate a detonation wave is an important consideration for detonation hazards and hypersonic propulsion (where the phenomenon has to be avoided and controlled, respectively). The most common means to initiate a detonation are a strong blast wave triggered by a source of energy release and a deflagration that accelerates to transition to a detonation (deflagration to detonation transition, or DDT). A detonation can also be initiated by a projectile traveling at a hypersonic velocity into a combustible gas mixture. The requirement for detonation initiation by a projectile depends most importantly on the mixture composition and pressure, and on the projectile size and velocity. Figure 1–5 presents four flowfield configurations around a spherical projectile observed in previous studies. A bow shock is produced in front of the sphere in the inert case (Fig. 1–5a). The flow is subsonic at the nose of the projectile and becomes supersonic as it turns around the body. For highly reactive experimental conditions, a normal detonation segment is initiated in front of the projectile nose (Fig. 1–5b). Expansion waves produced by the flow acceleration around the sphere attenuate the detonation, which becomes a self-supported, oblique, CJ detonation in the farfield. For critical conditions between detonation initiation and failure, two possible flowfields can be observed. Generally, for projectile velocities slightly less than the CJ speed, unsteady ignition and quenching of the mixture behind the bow shock take place, producing combustion instabilities (Fig. 1–5c). For projectile velocities greater than the CJ speed, the reaction front is coupled with the shock in front of the sphere and the expansion waves cause the splitting between the reaction front and the shock wave (Fig. 1–5d). The types of

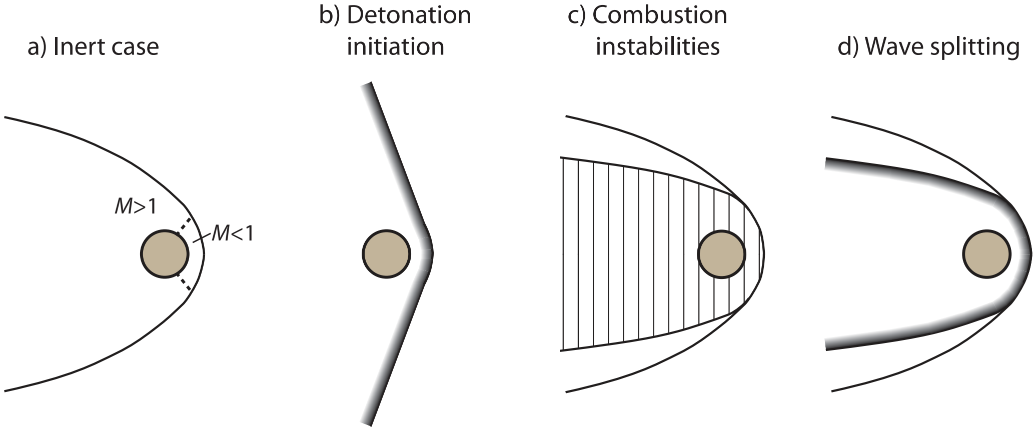

Figure 1–5: Flowfields around spherical projectiles traveling into a combustible mixture observed in previous studies

flowfields induced by conical projectiles as a function of their cone angle has yet to be determined. The observation, classification and prediction of these flowfields represent one of the objectives of the present study.

1.4 Scope

The present investigation aims primarily at experimentally establishing the necessary conditions to initiate and stabilize an oblique detonation wave from hypersonic conical projectiles. Ultimately, determining the influence of the cone angle and the mixture pressure on the ability to initiate an ODW is the main objective. Simple theoretical models based on energy and chemical kinetics considerations provide a means to predict the initiation or failure of a detonation wave and to classify the different types of flowfields observed. More complex analyses using a method of characteristics program can be used to solve steady 2D flowfields of reacting flows over finite and semi-infinite wedges. From these simulations, the critical conditions for detonation initiation are determined and the mechanism of initiation of oblique detonation is revealed.

A review of the previous studies on detonation initiation by projectiles and shock-induced combustion behind oblique shock waves is given in Chapter 2. A thorough review of the experimental work is provided, whereas an overview of the computational and theoretical studies is included. The experimental apparatus is described in Chapter 3, along with the experimental conditions tested. The experimental results are presented in Chapter 4. A description of the typical flowfields observed is given, along with plots summarizing all of the experimental results. Observation of these results guided the theoretical investigation on specific aspects of the observed flowfields. Chapter 5 presents the blast wave model applied to detonation initiation from hypersonic projectiles. A critical Damköhler number is then proposed based on a modified ZND model. Chapter 6 aims at identifying the conditions for which the Lee-Vasiljev model is valid. Numerical simulations of planar blast and planar piston initiation of a detonation are presented and compared with simulations of reacting flows over 2D wedges obtained with the method of characteristics. In Chapter 7, simulations at supercritical conditions are provided, showing different features of overdriven oblique detonations. Finally, the stability of oblique detonation waves is investigated in Chapter 8 by exploring their cellular structure through numerical simulations.

CHAPTER 2
Literature Review

In this chapter, the different experimental methods to initiate combustion behind a shock wave produced by projectiles and wedges are described. Previous investigations related to this subject are presented and divided into two categories: bow-shock-induced combustion and oblique-shock-induced combustion. An overview of the theoretical and computational work related to these phenomena is also given.

2.1 Bow-Shock-Induced Combustion

2.1.1 Experimental

Overview. Ballistic range facilities that launch supersonic and hypersonic blunt projectiles into combustible mixtures have been used for seven decades to study high-speed combustion phenomena. Some of the early experimental work was similarly motivated by the same interests that stimulate research into this topic currently (apply the detonation phenomena to hypersonic propulsion devices). However, fundamental chemistry- and gasdynamics-related phenomena were discovered and analyzed as part of these investigations. As the present study focuses primarily on oblique-shock-induced combustion, some of these phenomena are of secondary importance. The purpose of this section is thus to provide a general view of the possible types of flowfields that can be initiated by a projectile. Only brief physical explanations provided by the different authors are reported herein. Table 2–1 presents a

Table 2–1: Summary of the bow-shock-induced combustion experiments (CI: Combustion Instabilities, DI: Detonation Initiation)

Authors	Year	Institution	Main contributions	
Zeldovich and Leipunskii [130]	1943		Demonstrate shock-induced combustion	
Zeldovich and Shliapintoch [131]	1949			
Ruegg and Dorsey [103]	1961	Nat. Bur. of Standard	Show the existence of comb. inst., ignition delay vs comb. pulsation period, acoustic model	CI
Behrens, Struth and Wecken [7]	1965	Inst. of St-Louis		
Lehr [71]	1972			
McVey and Toong [84]	1971	Mass. Inst. of Tech.	Wave-interaction model to explain combustion inst.	
Alpert and Toong [2]	1972			
Chernyavskii, Baulin and Mkrtumov [14]	1973	Moscow State Un.	Stabilization of a detonation on a projectile	DI
Chernyi and Chernyavskii [15]	1974			
Chernyi, Chernyavskii and Baulin [16]	1986			
Vasiljev [120]	1994	Russian Academy of Science, Novosibirsk	Presentation and validation of the hypersonic blast wave analogy	
Higgins [46]	1996	Un. of Washington		
Kaneshige and Shepherd [57]	1996	California Inst. of Tech.	Comparison of the shock-curvature model with experiments	
Kaneshige [56]	1999			
Kasahara, Horii, Endo and Fujiwara [60]	1996	Nagoya Un.	Map of the combustion instabilities regimes	CI
Kasahara, Arai, Chiba, Takazawa, Tanahashi and Matsuo [58]	2002	Muroran Inst. of Tech.	Shock-curvature model with krypton-diluted mixtures	DI

summary of the research and contributions to the problem of shock-induced combustion and detonation initiation from hypersonic spherical-nosed bodies. The first shock-induced combustion experiments using a ballistic range facility were conducted by Zeldovich and Leipunskii [130] and Zeldovich and Shliapintoch [131] in the 1940's. They demonstrated shock-induced combustion and also oscillatory combustion occurring in front of the body from streak photographs. In the early 1960's, Ruegg and Dorsey [103] were the first to publish flow visualization of shock-induced combustion phenomena initiated by hypersonic spheres. They used the ballistic range method to study combustion in hypersonic flows while avoiding the problem of supersonic mixing and premature ignition encountered in high-enthalpy flows provided by wind tunnels. The development of high-speed photography methods constituted a secondary objective. The group from the Institute of Saint-Louis (Behrens et al. [7]) performed similar experiments with comparable objectives. In the early 1970's, T.Y. Toong made significant contributions to the field by proposing one-dimensional theoretical mechanisms responsible for the so-called regular instabilities regime (McVey and Toong [84]) and the large-disturbance regime (Alpert and Toong [2]). At the same period, Lehr [71] published one of the most famous photographs of the regular combustion instabilities. His research also contributed to the determination of the conditions required to initiate a detonation wave (not necessarily stabilized) by a hypersonic blunt projectile. Shortly after, the group from Moscow State University made a major contribution by being the first to show a detonation wave stabilized on a projectile. In order to predict the conditions required to initiate a detonation by the passage of a high-speed body, Vasiljev [120] presented a model based on the critical strength of a cylindrical blast wave generated by the projectile to initiate a cylindrical detonation. He conducted ballistic experiments using spherical and flat nosed projectiles to validate his model. Investigations on detonation initiation by hypersonic spheres were also conducted by Higgins [46] and Kaneshige and Shepherd [57] for projectile velocities larger than the Chapman-Jouguet (CJ) velocity of the mixture. Kaneshige [56] presented a model that predicted the conditions for which the chemical reactions are quenched due to curvature of the bow shock. The most recent contributions come from Japanese groups. At Nagoya University, Kasahara et al. [60] explored different regimes of combustion instabilities. At the Muroran Institute of Technology, Kasahara et al. [58] investigated the detonation initiation criteria of krypton-diluted mixtures for projectile velocities reaching $1.8U_{\mathrm{CJ}}$ (the CJ velocity). They used a bow shock curvature model in their analysis.

Research on Combustion Instabilities. The first reported experiment of a projectile inducing combustion as it traveled through a combustible gaseous mixture was the pioneering work of Zeldovich and Leipunskii [130]. Their motivation was to demonstrate ignition of the mixture through adiabatic shock compression. In this early work, they assumed that if ignition occurred on the stagnation streamline, a detonation would result in the farfield. They also pointed out that in order to ignite the mixture, the residence time of a fluid particle along the stagnation streamline behind the shock must at least be equal to the induction time of the mixture. In a later work by Zeldovich and Shliapintoch [131], streak photographs were recorded and combustion pulsations could be observed, which became a largely studied phenomenon in subsequent decades. The purpose of the following studies (from 1960 to 1975) consisting of launching hypersonic spheres into a combustible mixture was mainly to identify the origin of the combustion instabilities observed around the projectiles. Ruegg and Dorsey [103] were the first to show photographs of such flowfields. They showed the difference between launching spheres into air (an inert mixture), where a bow shock was formed around the body, and into a mixture of hydrogen and air, where pulsations were observed around and behind the projectile. These pulsations represented strong density gradients caused by combustion initiation and quenching phenomena. Such a flowfield was observed for projectile Mach numbers between 5 and 6. For faster projectiles, a smooth reaction front decoupling from the bow shock was observed without pulsations. The combustion instabilities were correctly assumed to originate at the front of the sphere. However, the authors treated the combustion oscillations between the body and the bow shock as acoustic oscillations, with very little conclusive evidence.

Behrens et al. [7] and Struth [113] continued the investigation of the combustion instabilities observed by Ruegg and Dorsey. They also found that for spheres traveling faster than the mixture CJ velocity, a smooth reaction front decoupled from the bow shock, and different combustion pulsation regimes occurred for slower projectile velocities. They identified three different types of combustion oscillations (note that some of these flowfields would now be classified differently): transition from a lower to a higher pulsation frequency, transition from smooth to oscillatory combustion and periodic ignition. A comparison between the self-ignition time of the mixture, between the sphere and the bow shock, and the period of the pulsations showed good agreement for cases of long ignition times (i.e., for relatively low projectile velocities).

These cases corresponded to the periodic ignition regime. However, the agreement did not hold for faster bodies. For these cases, an acoustic oscillation model was suggested, which was similar to that of Ruegg and Dorsey's study. There was no validation of this model. The last series of experiments coming from the Institute of Saint-Louis was conducted by Lehr [71]. He presented three shock-induced combustion regimes: a smooth reaction front decoupling from the bow shock for projectile velocities larger than the mixture CJ velocity, high frequency pulsations for projectile velocities slightly under the detonation velocity and low frequency oscillations for even slower bodies. His explanation for the combustion pulsations was also related to the induction time of the flow behind the bow shock. The resolution of his photographs was considerably better than the previous studies, and more accurate measurements of the shock stand-off distance and the pulsation frequency could be made. His comparison between the calculated ignition time and the measured pulsation period agreed well for the experimental cases reported.

The major outcome of the above-mentioned studies was to show the existence of (low and high frequency) combustion pulsations in the flowfield around spheres traveling slightly slower than the mixture detonation velocity. Despite good agreement between the induction time and the pulsation period, this comparison did not explain the origin of the pulsation mechanism, which is itself an unsteady phenomenon with respect to the body. A clear and complete theoretical model was therefore lacking until the wave-interaction model proposed by T.Y. Toong. Most of the experiments conducted at the Massachusetts Institute of Technology aimed at identifying the mechanism responsible for the combustion oscillations. Following their terminology, the regular, periodic instability regime referred to the case where high frequency pulsations were observed around the spherical body with a constant period of oscillation. For other flow conditions, the oscillations occurred at a lower frequency and the intensity of the pulsations appeared to be greater. This regime was referred to as the large-disturbance regime. The proposed theoretical model to explain this behavior is based on one-dimensional wave-interaction processes that take place between the nose of the sphere and the normal segment of the bow shock. A detailed description of this model is given in McVey and Toong [84] and the following is a brief description.

A schematic of this model is displayed in Fig. 2–1. The starting point of the wave-interaction model assumes a normal shock wave standing in front of the nose of the sphere. The shock compresses the gas, increasing its pressure and temperature, and chemical reactions are triggered. A certain distance is required for the exothermic reactions to occur, where the chemical energy is released. This distance determines the induction zone, which highly depends on the temperature behind the shock. The reaction front therefore lies somewhere between the normal shock and the sphere. In an ideal situation without any disturbance in the flow, this system would be in steady state and no pulsations would be observed around the sphere. However, whenever a disturbance arises in the form of a compression wave, this wave interacts with the normal shock and strengthens it (time t_1 in Fig. 2–1). The new, stronger shock compresses the gas to a higher temperature, as compared to the gas temperature before the interaction between the compression wave and the normal shock. Immediately after the interaction, the gas weakly compressed is adjacent to

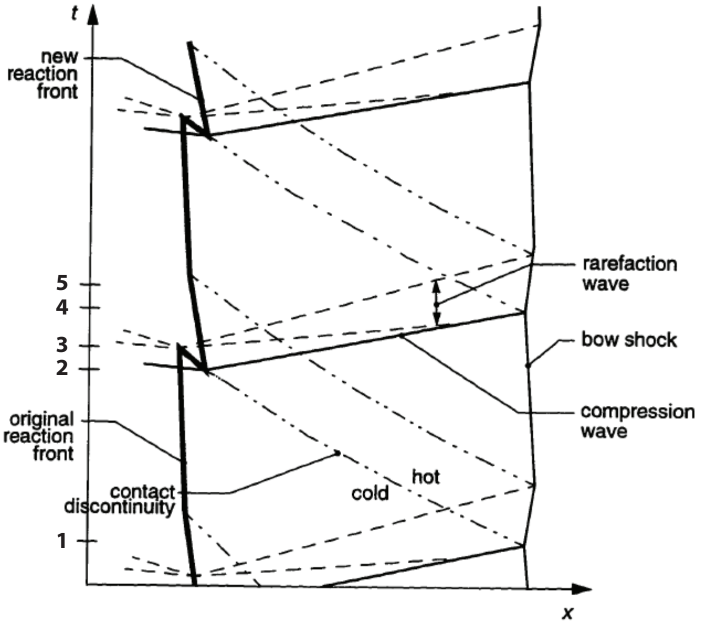

Figure 2–1: Wave-interaction model of McVey and Toong [84]

the gas strongly compressed, and both regions are separated by a contact discontinuity. The gas temperature in the strongly compressed region being higher than that of the weakly compressed region, the induction length is reduced. During the period between t_2 and t_3, two reaction fronts exist, the one in the strongly compressed region being ahead of the other. The appearance of the second reaction front (at t_2) results in the generation of compression waves, strengthening the bow shock at t_4. At t_3, the two reaction fronts merge and a rarefaction wave propagates towards the normal shock. When this rarefaction reaches the shock, the latter is weakened (at t_5). The gas is then less compressed and the original, longer induction length is re-established, which terminates the cycle. The new cycle begins with the compression waves interacting with the bow shock at t_4. According to this model, the body does not play any role in the pulsation mechanism once the cycles have been initiated. This can be valid if the induction length is much shorter than the bow shock standoff distance. McVey and Toong graphically presented this one-dimensional model on an $x - t$ diagram and when applied to a two-dimensional flow, it qualitatively agreed with the frequency of the observed regular instabilities. They also worked out the induction time of the mixture, knowing the induction length from the photographs and calculating the gas conditions behind the normal shock using the shock relations. There was a satisfactory agreement between the values derived from their experiments and values acquired from shock tube experiments.

A similar wave-based interaction mechanism for the large-disturbance regime was subsequently presented by Alpert and Toong [2]. They qualitatively and quantitatively differentiated the features of the regular from the large-disturbance regimes by considering the diameter of the pulsation striations and the distance between the striations (which is equivalent to the pulsation frequency). Both characteristics were measured from Schlieren photographs. They also introduced a Damköhler parameter ($\bar{Q}$, which was equivalent to a non-dimensional heat release parameter) to classify the two types of oscillations. If $\bar{Q} << 1$, the ratio of the induction length across the contact discontinuity (in the strongly and weakly compressed regions) was close to unity and the regular regime was identified in the flowfield. When $\bar{Q}$ approached unity, they showed that the compression waves that interacted with the normal shock were stronger, resulting in a higher gas temperature in the strongly compressed regions. The induction length in the strongly compressed regions thus became significantly shorter than that in the weakly compressed regions. Consequently, the distance between the ignition of the new reaction front and the extinguishment of the old one was increased. The effect of this large induction length difference was the large variation in the normal shock strength and the increase in the time required to complete one cycle. The one-dimensional wave-interaction model therefore provides a good qualitative explanation for the observed combustion pulsations for the regular and the large-disturbance regimes.

The most recent investigation of the combustion instabilities produced by hypersonic projectiles was conducted by Kasahara et al. [60]. They reported additional flowfield photographs of regular and large-disturbance regimes and of some cases where the pulsation envelope (determined by the diameter of the striations) was itself oscillating. They briefly showed combustion instabilities from conical-nosed projectiles, but for only one value of cone angle.

Research on Detonation Initiation and Stabilization. The ability to initiate a detonation wave by the passage of a hypersonic body in a gaseous detonable mixture and to keep the detonation attached to the projectile drew considerable attention given that both phenomena are necessary for the use of a detonation wave in hypersonic propulsion devices. Chernyavskii et al. [14], Chernyi and Chernyavskii [15] and Chernyi et al. [16] conducted ballistic experiments using hemispherical projectiles where the body velocity was varied from 93% to 120% the mixture CJ velocity. For velocities less than the CJ velocity, they observed combustion oscillations around the projectile followed by a transition to a detonation wave near the rear of the projectile. The transition location seemed to be constant with respect to the moving body, suggesting that the general flowfield was developed to its steady configuration. For projectile velocities slightly larger than the detonation velocity, it was observed that an oblique detonation wave was initiated near the projectile shoulder and self-sustained in the farfield. By further increasing the body velocity, a normal overdriven detonation wave ahead of the projectile underwent a transition to an oblique detonation in the farfield. Despite the absence of a thorough parametric investigation of the conditions required to initiate and stabilized a detonation wave, the main contribution of the work accomplished at Moscow State University was to show the existence of such phenomena.

In an attempt to predict the experimental conditions to initiate a detonation from a blunt body, Lee [68] and Vasiljev [120] invoked the so-called hypersonic blast wave analogy. A detailed derivation of this model is given in Section 5.1.2 and what follows is a brief description. A hypervelocity body traveling in an inert gas produces a strong shock wave around it for which the shape of the shock is nearly independent of the body Mach number [10]. When such a projectile is launched into a combustible mixture, if the shock wave is sufficiently strong, chemical reactions couple to the shock to initiate a detonation wave. This situation can also be thought of as being equivalent to a line source of energy lying along the projectile flight axis that when released instantaneously drives a cylindrical blast outwards. The key idea of this model is that the energy deposited by the projectile into the mixture must at least equal the critical energy to directly initiate a cylindrical detonation wave in this mixture. Therefore, one must approximate both the cylindrical blast wave energy requirement and the amount of energy deposited by the projectile for given experimental conditions. The energy the projectile transfers to the mixture can be simply calculated from its aerodynamic drag per unit length. Lee approximated the minimum energy for a direct initiation of a cylindrical detonation by stipulating that when the blast velocity (neglecting the effect of combustion) has decayed to the CJ velocity of the mixture, the blast radius must be at least equal to some critical radius. This critical radius can be related to other dynamic detonation parameters of the gaseous mixture, such as the cell size, as presented by Lee [67]. By equating the energy provided by the projectile and the critical energy for detonation initiation, the following relation is obtained:

$$\frac{M_{proj}}{M_{CJ}} = 5\left(\frac{\lambda}{d_{proj}}\right) \tag{2.1}$$

where M_{proj} and M_{CJ} are the projectile and CJ Mach numbers, respectively, λ is the detonation cell size and d_{proj} is the projectile diameter. A more detailed derivation of Equation 2.1 is provided in Section 5.1.2, and a quantitative comparison with experimental values is presented in Section 5.1.3. Even though Vasiljev [120] conducted ballistic range experiments using hemispherical or flat-nosed projectiles in an attempt to validate a relation equivalent to Equation 2.1, the prediction of a critical energy to initiate a cylindrical detonation in the mixture was not determined. In fact, Vasiljev used his experimental results to obtain this critical energy.

Experimental validation of the hypersonic blast wave analogy was achieved by Higgins [46]. He launched spherical bodies into combustible mixtures and varied the projectile Mach number and diameter for different mixture pressures to verify the validity of Equation 2.1. He concluded that the Lee-Vasiljev model defines well the boundary between detonation initiation and failure for projectile velocities equal to the mixture CJ velocity, which is in accordance with the model assumption that the flow is in the hypersonic regime. By varying the sphere diameter and keeping the body velocity near the mixture CJ velocity, Higgins confirmed that the body diameter should be at least 5 times the cell size of the mixture for the entire range of pressures investigated (0.1 – 2 atm).

Kaneshige and Shepherd [57] conducted similar experiments at about the same time period. However, instead of using the global approach of the Lee-Vasiljev model using energy consideration, they preferred to consider local effects that a fluid particle is subjected to along a streamline curved around a hypersonic sphere. According to this shock-curvature model, the criterion for initiating a detonation is determined from the competing effects between the energy release from chemical reactions and the quenching effect due to the expansion of the flow around the body. A detailed derivation of the model was presented by Kaneshige [56], and was based on earlier work of Hornung [50] and Gilinskii and Chernyi [37]. With such a model, it can be shown that the chemical reactions are quenched when the bow shock curvature, κ, exceeds some critical value, κ_c. Kaneshige and Shepherd stated that failure to initiate a detonation occurs for $\kappa_{wave} > \kappa_c$, critical flowfield regimes (such as the combustion instability regimes) are observed for $\kappa_{wave} \approx \kappa_c$ and an oblique detonation wave is always initiated for $\kappa_{wave} < \kappa_c$. The comparison between this model and their experimental results was not conclusive enough for rigorous validation. The discrepancy was mainly attributed to neglecting the effect of combustion on the shock (or detonation) shape around the sphere by using the approximation of a hyperbolic shock shape. To overcome this difficulty, the efforts made at the California Institute of Technology following this study were directed towards numerically simulating the experiment (see Hung [52]).

The shock-curvature model was also used by Kasahara et al. [58] with a slightly different approach. They measured the shock (or detonation) wave angle above and below the sphere (where the bow shock diameter is four times the sphere diameter) and defined the attenuation rate as the ratio of the velocity normal to the detonation at that location and the CJ velocity. This attenuation rate simply determines whether the downstream combustion regime is an oblique shock (null attenuation rate), an oblique detonation (attenuation rate of 1) or shock-induced combustion (attenuation rate between 0 and 1). They related the attenuation rates to different values of U_{proj}/U_{CJ} by using different mixture compositions to vary U_{CJ}. They showed that for a projectile velocity near the CJ value, the downstream combustion regime sharply underwent a transition from an oblique shock to an ODW by increasing the mixture pressure. For the cases where $U_{proj} = 1.62 U_{CJ}$, this transition was gradual for high pressures and the shock-induced combustion regime took place for intermediate pressures. In their study, they also related the attenuation rate with the shock curvature measured from the photographs. It was shown that a minimum shock radius was required to initiate an ODW.

2.1.2 Computational

Extensive computational modeling of shock-induced combustion by spherical-nosed bodies was conducted in the 1990's. Most of the efforts were directed to reproduce the different regimes of combustion instabilities observed in experiments and to develop a parameter that predicts and classifies these regimes. Fewer studies focused on the determination of the conditions required to initiate and stabilize a detonation wave. A brief overview of these computational studies is given below.

Large contributions to the computational modeling of this problem were made by Matsuo and Fujiwara. The goal of their initial work [80, 81] was to qualitatively reproduce the combustion oscillations observed in experiments, and more precisely the regular regime of Lehr's experiments [71]. In their simulations, a total variation diminishing (TVD) formulation with explicit time integration was used and the chemistry was modeled with a two-step chemical reaction. They successfully reproduced the oscillation mechanism and their numerical shadowgraph resembled the experimental one. They also considered the wave-interaction model of McVey and Toong [84], pointing out that the body surface plays a role in the physical system and should be taken into account in the model. They therefore proposed an improved model accounting for the waves reflected from the projectile nose, which agreed with their numerical simulations.

The next goal was to quantitatively reproduce the combustion oscillations of the regular regime, based on the pulsation frequency, using a detailed reaction mechanism. The reference cases for all the simulations were Lehr's experiments, where the projectiles were launched into stoichiometric H_2/air mixtures. A comparison between the experimental frequencies and the frequencies obtained from different numerical studies is shown in Table 2–2. The studies of Hosangadi et al. [51] and Wilson and Sussman [127] were the first to aim at reproducing the correct pulsation frequency. For a projectile velocity of 1 931 m/s, their simulations showed a frequency of 450 to

500 kHz and 530 kHz, respectively. The following studies of Sussman [115], Matsuo et al. [79], Yungster and Radhakrishnan [129] and Choi et al. [18] all reproduced frequencies in very good agreement with the experimental values, for both projectile velocities.

Table 2–2: Pulsation frequency from numerical studies of Lehr's experiments

	Proj vel of 1 685 m/s	Proj vel of 1 931 m/s
	Frequency (kHz)	
Experimental	148	712
Hosangadi et al. [51]	—	450 - 500
Wilson and Sussman [127]	—	530
Sussman [115]	135	711
Matsuo et al. [79]	160	725
Yungster and Radhakrishnan [129]	163	701 - 716
Choi et al. [18]	155	707

Ahuja et al. [1] also conducted numerical experiments to simulate the combustion oscillations using a finite-difference, shock-fitting method. They reproduced both the regular and large-disturbance regimes. Matsuo and Fuji [76] also succeeded in modeling the large-disturbance regime and compared their results with the wave-interaction mechanism of Alpert and Toong [2].

In order to classify the different flowfield regimes and to predict the flow conditions that produce them, Matsuo and Fuji [78] suggested a non-dimensional parameter equivalent to the first Damköhler number. This parameter is defined as the ratio of the fluid characteristic time scale and the chemical characteristic time scale. The former is given by $\tau_f = d_{proj}/a$, where d_{proj} is the projectile diameter and a is the sound speed behind the bow shock. The latter is defined as $\tau_c = T_2/\left(\frac{dT}{dt}\right)_{max}$, where T_2 is the temperature behind the bow shock and $\left(\frac{dT}{dt}\right)_{max}$ is the maximum temperature gradient calculated from a temporal self-ignition temperature profile. The results indicated that an increasing value of the Damköhler number implied a transition from the steady regime to the high frequency mode (the regular regime) followed by the low frequency mode (the large-disturbance regime). The transition from the high to the low frequency modes occurred at a Damköhler number of 80. A dimensional analysis was also conducted by Choi et al. [17] in which an additional parameter was introduced: a heat release parameter that represents the normalized amount of total chemical energy released behind the bow shock. This parameter was proposed to account for the situations where the completion of combustion along the stagnation streamline was not reached. They suggested the use of both non-dimensional parameters to correctly predict the combustion regime.

The goal of the most recent numerical studies related to combustion instabilities produced by blunt bodies was to show that the observed pulsations were equivalent to one-dimensional detonation pulsations. Accurate simulation of the propagation of a one-dimensional detonation is itself an extensively studied problem and still represents a computational challenge. Matsuo and Fuji [77] and Daimon and Matsuo [23, 24] conducted such simulations and compared the pulsating motion of a well-established detonation with the combustion instabilities around blunt bodies and related similar features.

A numerical and theoretical analysis on detonation initiation by spherical bodies was conducted by Ju et al. [53]. They proposed two criteria necessary to initiate a detonation, referred to as the energetic and kinetic criteria. The models were compared with the experimental results of Higgins and Bruckner [48] where spherical projectiles ranging from 5 to 25 mm in diameter were launched in $2H_2+O_2+7Ar$ at the CJ detonation speed. The comparison showed that both criteria needed to be fulfilled to initiate a detonation wave.

2.2 Oblique-Shock-Induced Combustion

2.2.1 Experimental

The terminology of oblique-shock-induced combustion implies that the chemical reactions are triggered after the mixture crosses an oblique (or conical) shock wave attached at the tip of a wedge (or conical) body. Downstream of the shock, the flow is generally supersonic in the body-fixed frame of reference, which is the main difference compared to the flow behind a bow shock, which is always subsonic behind the normal segment. Combustion in a supersonic flow typically decreases its velocity and in principle, there is a possibility that the flow chokes (or becomes sonic) downstream of the oblique shock. The key features of oblique-shock-induced combustion flowfields are an attached oblique (and apparently inert) shock wave, an induction zone that can be observed along the wedge surface downstream of the shock, and a reaction front that may couple with the oblique shock to form an oblique detonation wave (ODW). The formation, steadiness and stability of ODWs are of great relevance to hypersonic propulsion and investigations of these phenomena have been conducted since 1960 using different types of experimental facilities. The four most relevant ones are the use of supersonic wind tunnels or expansion tubes to produce a supersonic flow, the two-layer detonation experiment, ballistic range facilities that launch hypersonic conical projectiles into quiescent combustible mixtures and the detonating cord experiment. The previous studies using these four methods are presented in this section, and Table 2–3 summarizes the most important contributions to the problem of oblique-shock-induced combustion.

Supersonic Wind Tunnels and Expansion Tubes. The period between 1958 and 1970 marked a major advancement in the attempt to stabilize a standing (normal) detonation wave in a mixture accelerated to supersonic velocities using a wind tunnel. The goal was to produce a normal detonation wave that is standing at a fixed location in the laboratory reference frame. Nicholls et al. [89], Gross and Chinitz [40], Nicholls [88], McKenna [83], Richmond and Shreeve [99] and Bellet and Deshayes [8] all conducted experiments of this type, and a review of the above studies was made by Rubins and Bauer [100]. Of greater interest for the present work is the case where an attempt to stabilize an oblique detonation wave (with respect to the freestream flow direction) was made. Rubins and Rhodes [102] were the first to use an oblique shock wave to trigger chemical reactions in a supersonic flow. They injected hydrogen into a Mach 3 stream, and the oblique shock was produced by a 28° wedge. The post shock Mach number was roughly 1.6. They clearly delineated the difference between the shock-induced combustion regime, where the chemical reactions are decoupled from the shock, and the ODW regime, where coupling occurs. The goal of their work was to study chemical reaction kinetics in the shock-induced combustion regime, in a similar manner as in a shock tube experiment. A probe captured the flow gas species concentrations in the reaction zone to validate their computational model. The gas sampling along with Schlieren photographs confirmed combustion of the mixture behind the oblique shock wave. Rubins and Cunningham [101] then

Table 2–3: Summary of the oblique-shock-induced combustion experiments

Authors	Year	Institution	Type of experiment
Nicholls et al. [89]	1958	University of Michigan	Produce a standing detonation wave using a supersonic wind
Nicholls [88]	1963		
Gross and Chinitz [40]	1960	Fairchild Engine and Aircraft Corporation	
McKenna [83]	1967	Wright-Patterson Air Force Base	
Richmond and Shreeve [99]	1967	Boeing Scientific Research Laboratories	
Bellet and Deshayes [8]	1970	E.N.S.M.A., France	
Rubins and Rhodes [102]	1963	Arnold Air Force Station, Tennessee	Supersonic wind tunnel
Rubins and Cunningham [101]	1965		
Kamel et al. [55]	1996	Stanford University	Expansion tube
Morris et al. [86]	1998		
Liu et al. [75]	1988	University of Michigan	Two-layer detonation
Fan et al. [32]	1988		
Dabora et al. [21]	1989		
Tonello et al. [118]	1995		
Viguier et al. [124]	1994	University of Poitiers	
Desbordes et al. [25]	1995		
Viguier et al. [122]	1996		
Viguier et al. [123]	1998		
Behrens et al. [6]	1967	Institute of Saint-Louis	Hypersonic conical projectile
Endo et al. [31]	1997	Nagoya University	
Kasahara et al. [59]	2001	Muroran Institute of Technology	
Sturtzer et al. [114]	2007	Tohoku University	
Higgins et al. [49]	1998	McGill University	Detonating cord experiment
Radulescu et al. [97]	2000		
Radulescu et al. [98]	2003		

installed a model at the exit of the supersonic nozzle to produce a flowfield that would be encountered in air-breathing hypersonic propulsion engines. Two model configurations were studied: two wedges (in a rectangular symmetry) that produced a system of two subsequent oblique shock waves, and a converging conical shock (in an axysimmetric configuration). The purpose was to demonstrate the feasibility of shock-induced combustion applied to hypersonic propulsion. They observed ignition of the mixture downstream of the shock system in both configurations, even though boundary-layer separation in the rectangular symmetry prevented the expected ignition of the mixture in a few cases. In brief, ignition of a mixture compressed by an oblique shock wave was shown by the early work of P.M. Rubins. In all his reported studies, the combustion front was decoupled from the shock and no detonation phenomena were investigated.

Between 1970 and 1990, very few experiments were reported on oblique-shock-induced combustion. Oblique detonation phenomena resulting from the two-layer detonation experiment (described in Section 2.2.1) motivated a few groups to study the initiation of an ODW from a wedge. At Stanford University, Kamel et al. [55] and Morris et al. [86] published studies on ODW initiation by wedges and presented unique flowfield visualization using PLIF imaging [41]. They employed an expansion tube facility (thoroughly described in Kamel et al. [54] and Morris et al. [85]) as a means to accelerate flows to supersonic and hypersonic velocities. A detailed theoretical analysis of this apparatus can be found in Trimpi [119]. An expansion tube consists of three sections: a high-pressure driver filled with a light gas, a lower-pressure driven section filled with the mixture to be studied, and a very low-pressure expansion section filled with a light gas. When the flow from the driver expands into the driven section by rupturing a diaphragm a shock wave is created. The shock accelerates as it transits into the expansion section, and entrains the shocked gas with it at hypersonic velocities. Behind the shock a contact surface separates the light gas originally in the expansion section from the test gas originally in the driven section. The experiment starts when the contact surface reaches the wedge (located in the expansion section) and terminates at the arrival of a rarefaction wave (produced when the shock entered the expansion section). The test time of this experiment is roughly 150 μs. The relatively short test time of this facility, compared to wind tunnels, constitutes a disadvantage. However, by using an expansion tube, one can premix the gases prior to the experiment without having to deal with supersonic mixing and risks of prematurely igniting the mixture. The reported flow velocity in Kamel et al. [55] varied from Mach 4.2 to 6.7. They showed overlaid Schlieren and OH PLIF images of a shock-induced combustion case, where the combustion clearly did not affect the oblique shock, and of an overdriven ODW case, where coupling could be observed. Even though they claimed that the observed ODW reached its steady-state angle, this was questionable, since the wedge angle (40°) was larger than the maximum wedge angle for which an ODW can be steadily attached for their experimental conditions. A theoretical analysis predicts detachment of the detonation for these conditions. Given the short test time of their facility, they could not draw conclusions on the steadiness of their observed flowfields. Morris et al. [86] continued the investigation by varying the studied mixture composition with different levels of nitrogen dilution at two different exit flow conditions. Without rigorously investigating the conditions that produced different flowfield regimes, the key features of the oblique-shock-induced combustion phenomenon were identified, such as the existence of an induction zone, the coupling between the combustion front with the shock, and the detachment of a detonation at the nose of steep wedges.

Two-Layer Detonation. The concept of the two-layer detonation experiment was proposed in the 1960's by Sommers [109], Sommers and Morrison [110] and Dabora et al. [22] at the University of Michigan. This concept consists of a long rectangular channel in which a thin film suspended longitudinally allows for the channel to be filled with two different mixtures and to prevent them from mixing prior to the experiment. One of the two mixtures is generally very reactive and characterized by a large CJ velocity (this is the primary mixture). A detonation is initiated and allowed to propagate down the primary section. Behind the detonation, the lateral expansion of the burnt gas pushes the thin film into the secondary mixture, thus creating an aerodynamic wedge traveling at the CJ velocity of the primary mixture. In the secondary section, different mixtures can be used depending on the type of investigation. Dabora et al. [22] used only inert gases in the secondary section. In their experiment, they evaluated the detonation velocity and the minimum width of the primary section for which the detonation can propagate (i.e., the quenching distance). They compared these results to the case where the primary section is bounded by four solid walls and found a velocity deficit that depended on the channel width, the primary mixture reactivity and the density ratio between the two mixtures. This early work therefore studied the effect of a non-rigid boundary on the propagation of a normal detonation wave.

Twenty years later, this experiment was revisited at the University of Michigan, this time using a secondary section filled with an explosive gaseous mixture. The work of Liu et al. [75] and Fan et al. [32] aimed at investigating the effect of varying the equivalence ratio of the secondary H_2-O_2 mixture and analyzing the resulting global features of the flowfield. They differentiated the cases where an oblique shock was transmitted in the secondary mixture without causing reactions, an ODW was initiated by the aerodynamic wedge and an ODW was initiated upon the reflection of an oblique shock off the solid wall. A similar study was conducted by Dabora et al. [21] using hydrocarbon mixtures in the secondary section. The CJ velocity of the secondary mixture was always lower than that of the primary one. They controlled the angle of the aerodynamic wedge by varying the initial pressure ratio between the two mixtures. They identified three flowfield regimes in the secondary section: an inert oblique shock wave, a CJ oblique detonation wave and an overdriven oblique detonation wave. The minimum wedge angle for which an ODW was initiated corresponded to a detonation polar analysis of the experiment. The motivation of their work was the determination of the conditions required for ODW initiation with the pressure as the independent parameter, and to validate the prediction of the theoretical polar analysis. The last published work coming from the University of Michigan was done by Tonello et al. [118]. Their study consisted of varying the equivalence ratio in both sections and observing the flowfield in the secondary mixture. In some cases, the CJ velocity of the secondary mixture was larger than that of the primary mixture and in these cases, the secondary detonation outran the primary detonation. Inversely, for the cases where the CJ velocity of the secondary mixture was lower, a steady oblique detonation wave was observed. Furthermore, they experimentally showed the existence of an induction zone at the tip of the wedge. They identified a triple point at the location where the inert oblique shock sharply underwent a transition to an ODW. They briefly related this system with the predicted oblique shock angle and ODW angle from polar analysis, which agreed well.

Research on the formation of oblique detonation waves and their structure using a two-layer detonation facility was continued at the University of Poitiers between 1994 and 1998. Most of the work focused on analyzing the features of the induction zone that preceded the onset of the oblique detonation wave. Viguier et al. [124] showed Schlieren photographs where the transition from an oblique shock to an ODW was observed. They used two different combustible mixtures (H_2-air and CH_4-air) and varied systematically the pressure in the secondary section. The interesting phenomenon that occurred in most of the studied cases was the presence of an oblique deflagration that originated from the tip of the aerodynamic wedge and extended downstream at an angle slightly larger than the wedge angle. They confirmed that the observed flame was a deflagration by deducing its normal propagation velocity from the photograph to be on the order of 100 m/s. Desbordes et al. [25] speculated that this deflagration was either caused by the hot detonation products of the primary mixture or by viscous dissipation in the growing boundary layer behind the oblique shock. They related their results with Lehr's experiment [71], where a hypersonic conical projectile was launched into a stationary mixture. In Lehr's study, a smooth reaction front was seen to decouple from the shock attached to the tip of the cone.

A more rigorous investigation is required to determine whether the two flowfield structures are equivalent, since the symmetry of the two cases and the nature of the boundary (solid cone vs detonation products) are different. Numerical simulations of this problem were presented by Viguier et al. [122] in an effort to further identify the ignition mechanism of the oblique deflagration behind the oblique shock and of the ODW. The simulations clearly showed that the induction length of the mixture subjected to the post-oblique shock conditions dictated the location of the reaction front that eventually coupled with the shock to initiate the ODW. The origin of the oblique deflagration was still undetermined. Viguier et al. [123] presented the last results of the two-layer detonation experiment related to the study of the ODW formation. In this work, they improved the diagnostics with the use of a PLIF system to identify the regions of active chemistry, and the use of the smoke foil technique to record the trajectory of the transverse waves of the detonation structure. In the case they considered, an inert oblique shock was attached to the wedge tip. Behind this shock, they observed a quasi-normal detonation wave that was slightly overdriven, which was confirmed by PLIF images. A triple point was defined at the intersection of this quasi-normal detonation and the oblique shock. An ODW was initiated from this triple point downstream. The authors also claimed that the quasi-normal detonation wave supported and stabilized the ODW. The smoke foil records revealed that at the critical conditions for ODW initiation, the location of the triple point oscillated and periodic point explosions along the oblique deflagration (between the tip of the wedge and the quasi-normal detonation) were necessary to prevent quenching of the ODW.

The overall results published using the two-layer detonation technique showed unique features of the initiation of an oblique detonation wave that are of great relevance to the present study. The induction zone, the triple point and the oblique deflagration are phenomena that were encountered in the present study and they will be presented in Section 4.1.

Hypersonic Conical Projectiles. Some difficulties are encountered with the use of the facilities described earlier in this section. The risk of premature ignition of combustible mixtures in high-enthalpy facilities (supersonic wind tunnels) is encountered and supersonic mixing represents a major challenge. In expansion tubes, the short duration of the experiment (150 μs) does not typically permit a steady flowfield, and the test section is generally limited to relatively low pressures. In the two-layer detonation experiment, the exact role the detonation products of the primary mixture plays on the ignition mechanism of the secondary mixture is still undetermined. All these difficulties can be overcome by launching conical projectiles at hypersonic velocities into quiescent combustible mixtures. In such experiments, the challenge is the ability of accelerating multi-gram projectiles to sufficiently high speeds (generally above 2 km/s) while ensuring their integrity during the acceleration and to maintain them at zero angle of attack as they pass through the test section. Due to these complications, very few reported results of this experiment can be found. Behrens et al. [6] were the first to investigate the flowfields that occur around hypersonic conical projectiles. Three combustion regimes were identified in their study: a smooth reaction front decoupling from the oblique (or conical) shock wave, combustion instabilities similar to the large-disturbance regime of Alpert and

Toong [2] and an inert shock wave without combustion activity. The initiation of a detonation wave was never observed, and a classification of the observed regimes was not attempted. In some cases, a smooth reaction front extending horizontally downstream of the projectile shoulder was observed and the authors attributed these cases to boundary layer combustion on the surface of the projectiles. They based their hypothesis on the fact that the angle of the conical shock corresponded to the shock angle without heat addition behind the shock. However, as shown by the two-layer detonation experiment, combustion can occur downstream of an inert oblique shock without changing its angle as long as the reaction front does not couple with the shock. The hypothesis of Behrens et al. on boundary layer combustion thus has to be investigated further.

The next ballistic range experiments using conical projectiles were conducted in the late 1990's by Endo et al. [31] who systematically varied the projectile cone half angle (from 30° to 90°) and the mixture initial pressure (from 0.1 to 0.5 atm). They observed three different combustion regimes. For high pressures and large cone angles, an oblique detonation wave was initiated and self-sustained in the farfield. In these cases, a detached normal detonation was observed in front of the body. At lower mixture pressures, a quasi-normal detonation was observed behind the projectile. An ODW was initiated at the intersection of this normal detonation and the bow shock. The third regime consisted of combustion instabilities observed in the wake of the projectile. Therefore, Endo et al. were the first to show an ODW initiated by a conical projectile. However, the initiation mechanism was very similar to that of blunt bodies (or spherical projectiles), since a normal detonation wave was detached in front of the cone. In the cases where an ODW was initiated and self-sustained, they deduced the normal velocity component of the wave which agreed well with the CJ velocity of the mixture.

Kasahara et al. [59] conducted the most systematic investigation of this problem by varying the projectile velocity (from 2.9 to 4.1 km/s), the cone half-angle (from 30° to 90°) and the mixture pressure (from 0.1 to 0.5 atm). In this work, they analyzed the flow features in depth for the case where a normal, overdriven, detached detonation in front of the cone decayed to a self-sustained CJ oblique detonation due to the rarefaction waves emanating from the projectile shoulder. By varying the three independent parameters mentioned above, they determined the conditions for which an ODW was initiated. However, even at the largest mixture pressure studied (0.5 atm), a cone half-angle steeper than 45° was necessary to initiate an ODW. At these conditions, the cone was still relatively blunt and the initiation mechanism again resembled that of spherical projectiles. Therefore, an induction zone at the tip of the cone, as identified from the two-layer detonation experiment, was not observed.

The most recent work on this problem was reported by Sturtzer et al. [114]. They showed very good quality Schlieren photographs of combustion activity initiated by hypersonic conical projectiles, but with limited variation of experimental parameters. This work consisted of preliminary results for a more extended investigation, which has not been published at the moment of writing.

While a number of studies using conical projectiles have shown oblique detonation initiation, most of the cases were in fact initiation by a detached bow shock in front of an effectively blunt projectile. Initiation of oblique detonation via a highly inclined, attached oblique shock, such as would be encountered in hypersonic propulsion applications, has not been observed. To study this regime of oblique detonation initiation is the central motivation for the present investigation.

Detonating Cord Experiment. In Section 2.1.1, the hypersonic blast wave analogy was introduced. The essence of this model lies in the fact that detonation initiation from the energy deposited by a projectile (via its drag) is governed by the same mechanism as for the case of direct initiation of detonation by an instantaneous energy release. The validity of this analogy was addressed in a number of ballistic range investigations (Vasiljev [120], Higgins [46], Kaneshige [56], Kasahara et al. [58]). However, the projectile velocity in ballistic range experiments (2 – 3 km/s) is generally comparable to the detonation velocity of the mixture (e.g., the detonation velocity of hydrogen-air mixtures are about 2 km/s). In order to provide a faster energy deposition, a detonating cord placed along the axis of a cylindrical chamber containing a detonable gas mixture was used in the work of Higgins et al. [49] and Radulescu et al. [97, 98]. A detonation in the high explosive cord propagated at about 6 – 8 km/s (17 – 23 times the sound speed of the mixture), providing a rate of energy deposition closer to the ideal case of instantaneous deposition.

Higgins et al. [49] used a cylindrical chamber 77.5 cm long and 48.5 cm in diameter. They instrumented the apparatus with contact gauges, ionization probes and pressure transducers. Radulescu et al. [98] performed field trials where the chamber consisted of a plastic bag 8 m long and 2 m in diameter. In addition to using contact gauges, ionization probes and pressure transducers, visualization of the flowfield was recorded with self-luminous high-speed photography. In both studies, pentaerythritoltetranitrate (PETN) explosive was used for the detonating cord, depositing 31 – 537 kJ/m. Since the observed flowfields were steady in the reference frame of the detonation in the cord, they used the analogy between 2D steady and 1D unsteady flowfields in order to describe the evolution of the phenomenon in the radial direction in time, rather than in the radial and axial directions. Three regimes were identified in both investigations: supercritical, critical and subcritical regimes.

In the supercritical regime, the energy deposited by the cord was larger than the critical energy. At the center of the chamber (near the detonating cord), the blast wave was mostly driven by the source energy. At this location (at a small radius from the cord), the blast velocity was much larger than the detonation velocity of the mixture. For increasing radius away from the cord, the blast decayed monotonically to the CJ velocity of the mixture and remained constant in the farfield. Away from the cord, the blast was supported by the exothermic chemical reactions to form a self-supported detonation wave. When the energy deposited by the cord was only slightly larger than the critical value, the decaying blast wave reached a sub-CJ velocity and remained roughly constant momentarily; this was the quasi-steady regime. At the end of this quasi-steady state, an explosion occurred between the blast and the reaction front. The new reaction front produced by this explosion accelerated towards the blast in a DDT-like event. The blast velocity was quickly restored to the CJ value and remained constant in the farfield. The radius at which the blast velocity was restored to the CJ value was referred to as the explosion length. As the energy deposited was further reduced, a different critical regime occurred. Initiation behind the blast wave was observed to be governed by localized explosion centers which originated at a relatively small radius (about 20 cm). The coalescence of the explosion bubbles further away from the cord (at about $60 - 80$ cm) marked the onset of a CJ detonation. The subcritical regime was observed when the energy deposited by the cord was insufficient to trigger any detonation centers. In this case, the blast velocity decayed below the CJ velocity and was never accelerated above this value.

The concept of explosion length is expressed theoretically as follows for different geometries [66]:

$$R_o = \left(\frac{E_j}{p_o}\right)^{1/j}$$

where $j = 1, 2, 3$ for planar, cylindrical and spherical geometries, respectively. Radulescu et al. [97] measured experimentally the explosion length at critical conditions for detonation initiation in a cylindrical geometry. By comparing this result with the critical explosion length in a spherical configuration, they confirmed the invariance of the explosion length with geometry. This parameter appeared to be a representative length scale of the critical detonation initiation by a strong blast. Since the cell size λ represents the characteristic length scale of a mixture detonability limit, Radulescu et al. showed the existence of a linear proportionality between the two length scales of the form $R_o^* = 32\lambda$.

The results from the detonating cord experiments illustrate well the different features of the flowfield when a cylindrical detonation is directly initiated by a strong blast wave, especially near the critical conditions for initiation. In the present work, the blast wave model will be used to predict the conditions required to initiate a detonation from hypersonic conical projectiles. Therefore, the results will be analyzed and discussed in relation with these flow features. The blast wave model will be described in detail in Section 5.1.2 and its applicability to hypersonic projectiles will be discussed in Section 6.3.

2.2.2 Theoretical

Several theoretical studies on ODWs have been conducted that are of great relevance to the present investigation, especially to the modeling section (Chapter 7). These investigations can be divided into two categories: established ODWs and the formation of ODWs. Most of the analytical studies were concerned with the former, whereas most of the computational work (presented in Section 2.2.3) dealt with the latter.

Gross [39] conducted the first theoretical analysis on ODWs by solving the conservation equations across an established ODW attached to a wedge. The formation and structure of the ODW were not taken into account. The chemical heat released was expressed in the energy equation by the parameter Q. Gross obtained ODW polars, which are a graphical representation relating the wedge angle to the calculated ODW angle. He compared the ODW polars with inert oblique shock polars. The existence of overdriven, CJ and underdriven ODWs was theoretically demonstrated. Gross used the terms strong and weak to refer to the terms overdriven and underdriven, respectively, which could lead to confusion with strong and weak inert oblique shocks. Buckmaster and Lee [12] proposed a model where the shock front and the reaction front are attached to a wedge at two different angles. The motivation was to consider the case where the reaction front decouples from the shock front, similar to a flowfield shown in the numerical study of Fujiwara et al. [34]. They also solved the conservation equations across the ODW with a heat release parameter Q. In their results, they presented polars where the angle difference between the two fronts was varied. Compared with the case of parallel fronts, the effect of increasing the angle difference was to increase the range of wedge angles for which an ODW is attached. However, an ODW attached to a negative wedge angle was an admissible solution, which seemed unlikely to have physical significance. A polar analysis of ODWs was also performed by Pratt et al. [94]. They described the terminology of the different types of ODWs, which is shown in Fig. 2–2 by relating the ODW angle β and the wedge angle θ. The upper branch of the polar corresponds to a strong (S) ODW and the lower branch to a weak (W) ODW, which is equivalent to a strong and weak oblique shock. The weak ODWs are divided into three cases: weak overdriven (OD), CJ and weak underdriven (UD), where the downstream Mach number is less, equal and greater than one, respectively. In their work, they recognized that the weak underdriven ODW was a non-physical solution. For this portion of the polar lower branch, Ashford and Emanuel [3] suggested that a CJ ODW followed by an expansion wave (a Taylor wave) would occur. Therefore, they substituted a physical solution for a non-physical one, but no experimental results were available for validation. Realistic chemistry was incorporated in a polar analysis of ODWs by Emanuel and Tuckness [30]. They also produced a report [29] that includes 340 solutions to provide comprehensive tables for quick reference.

The structure of an attached ODW was solved theoretically in the work of Powers and Stewart [93]. They used the steady two-dimensional Euler equations in

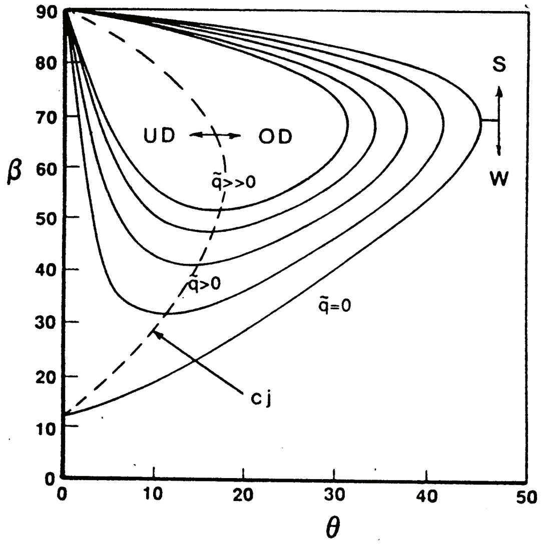

Figure 2–2: ODW polars from Pratt et al. [94]

their model, with a one-step Arrhenius equation to simulate the chemistry. They also used the hypersonic approximation, implying that the kinetic energy of the flow was much larger than the thermal and chemical energy. They solved the flowfield between the shock front and the wedge for two cases: an irrotational flow for which the wedge is curved and the shock front is straight and a rotational flow for which the wedge is straight and the shock front is curved. Powers and Gonthier [92] showed that by using a two-step chemistry model (with the first step exothermic and the second step endothermic), pathological ODWs could be obtained with a relatively large value of endothermicity that influenced the minimum ODW angle, which corresponds to the angle of a CJ ODW. The stability of an ODW subjected to imposed perturbations was addressed by Buckmaster [11]. He based his model on the conservation laws across the ODW. He found that for an infinitely large activation energy, the disturbances along the ODW grew further downstream. A stability analysis was also carried out by Lasseigne and Hussaini [64]. They considered two cases where the perturbations were imposed by freestream velocity disturbances or by an oscillatory wedge rotating about a fixed pivot. They showed that by increasing the degree of overdrive the amplitude of the oscillatory ODW response increased as well.

The formation mechanism of an ODW at the tip of a wedge was theoretically considered by Ghorbanian and Sterling [36]. They assumed an inert oblique shock attached at the tip of the wedge inclined at an angle of θ_w. Behind this shock, there was a thermally neutral region called the induction zone. Downstream of this region, the chemical energy was released. At the location of energy release, the wedge angle was set to a different value, referred to as the base angle θ_b. Therefore, their model consisted of a double wedge configuration with the tip of the base corresponding to the location of energy release. By varying the base angle, they showed the possible flow configurations behind the induction zone: a deflagration with or without an expansion wave behind it, a CJ ODW with or without an expansion wave behind it and an overdriven ODW. For the configurations where an ODW was produced by the base, the intersection between the detonation and the inert oblique shock created a triple point and triggered a new ODW that propagated in the farfield. The flow conditions in the different regions were solved with shock and detonation polars.

2.2.3 Computational

The early computational studies on ODW initiation from a wedge aimed at demonstrating the use of an ODW in a hypersonic propulsion device. Detailed and reduced chemical reaction mechanisms were considered to simulate realistic flowfields. The most recent investigations used a one-step chemical reaction to reduce the computational cost and to obtain highly-resolved simulations.

The initiation of an ODW was first simulated numerically using detailed chemistry by Cambier et al. [13]. With under-resolved simulations (the width of their grid cells was 4 mm), they presented the flowfield of an attached ODW. More resolved simulations were conducted by Li et al. [72]. Their work was the first to show the formation process of an ODW attached to a wedge characterized by an induction zone, an energy-release front and the coupling point where the ODW is formed. They investigated different mixtures and wedge angles. The stability of the simulated ODW structure was verified by imposing a temperature perturbation in the freestream. In an attempt to reduce the computational effort, Thaker and Chelliah [117] modeled the initiation of an ODW using a four-step reaction mechanism. The general features of the flowfield were similar to the results obtained using a detailed reaction mechanism. Fusina et al. [35] also performed computational simulations of the formation process of an ODW. They considered incoming flow conditions that are representative of a shcramjet's combustor inlet. They confirmed the stability of their results by imposing air pockets into the incoming reactive flow. Walter and Figueira da Silva [125] simulated the initiation of an ODW over finite-length wedges. The weak overdriven ODW was attenuated by expansion waves originating from the wedge corner. Cases where the ODW angle decreased to the CJ angle and where the reaction front decoupled from the leading shock were both observed. Choi et al. [20] simulated the experimental results of Morris et al. [86], where a $2H_2+O_2+17N_2$ mixture flowing at Mach 5.85 encountered a wedge with a turning angle greater than the maximum attachment angle. By varying the length of the wedge, they observed three different regimes: decoupled shock-induced combustion, oscillatory combustion and detached overdriven detonation wave. They classified each regime using two Damköhler numbers based on the flow conditions behind a normal and an oblique shock.

Computational simulations of ODW initiation using a one-step chemical reaction were conducted by Grismer and Powers [38]. They considered the straight-shock, curved-wall configuration. The wall shape corresponded to the path of a streamline determined *a priori*. Their goal was to determine the conditions for which the ODW remained stably attached to the wedge tip. In their results, stability was ensured for a degree of overdrive less than $f_n = (U_\infty/U_{CJ})^2 = 1.77$. They validated their results against exact solutions given in Powers and Stewart [93]. Papalexandris [90] also carried out simulations using a one-step chemical reaction. He explored the effect of changing the activation energy and the wedge angle on the features of the induction zone. He observed cases where the reaction front smoothly coupled with the inert oblique shock to form the ODW, and where a triple point was formed at the intersection of the reaction front and the oblique shock. He also considered finite length wedges and concluded that if the triple point was not influenced by the expansion waves emanating from the wedge corner, an ODW was established in the farfield and was attenuated to a CJ ODW by the expansion waves. Highly-resolved numerical simulations of the ODW structure were performed by Choi et al. [19]. For large activation energies, instabilities along the ODW front were observed and believed to be similar to the cellular structure of normal detonation waves. The transverse waves in the detonation structure were observed to propagate in only one direction, away from the wedge tip.

The initiation of an ODW from sharp cones was simulated by Sislian and Zhang [108] using a detailed reaction mechanism. They reproduced the features of the overall ODW structure (the induction zone and the reaction front coupling with the oblique shock at the triple point) for different cone angles. Harris et al. [42] also conducted similar simulations. The goal of their study was to determine the effect of different grid refinement levels and different Riemann solver schemes on the general structure of the ODW.

In conclusion, the problem of bow-shock-induced combustion using blunt projectiles has been extensively studied from both experimental and computational investigations. In these studies, an ODW in the farfield is usually preceded by an overdriven, normal detonation located in front of the projectile. On the other hand, ODWs have also been initiated using other types of facilities: supersonic wind tunnels, expansion tubes and the two-layer detonation experiment. In these studies, sharp wedges were used and in some cases, an ODW was preceded by an induction zone at the tip of the wedge. Since a ballistic range facility offers several advantages (the test gases are well mixed *a priori*, the test time is on the order of 500 μs, the shock/detonation is initiated from a solid body), it is of interest to investigate the initiation of ODWs from conical projectiles with a wide range of cone angles.

CHAPTER 3
Experimental Apparatus

The most common technique to accelerate multi-gram projectiles is a two-stage light gas gun. An alternative method has been developed in the past five years at McGill University with the construction of a 1.27 cm-bore detonation-driven gas launcher. A detailed description of this facility is given by Verreault et al. [121] and a complete performance analysis was carried out by Batchelor [4]. A general description of this apparatus is given in Section 3.1. This section is divided to present the operation of the launcher driver, the test section, the mixture investigated, the visualization system and the projectile fabrication. Finally, Section 3.2 describes the experimental conditions investigated.

3.1 Description of the Ballistic Range Facility

3.1.1 Detonation-Driven Gas Launcher

A photograph of the launcher is presented in Appendix A (Fig. A–1) and its operation is schematically shown in Fig. 3–1. Prior to an experiment, the launch tube is evacuated and the driver section of the launcher is filled with a very high pressure H_2/O_2 mixture. The gases are filled independently using the partial pressure method and left to mix for 15 minutes. This amount of time may appear very short considering that the mixing relies only on molecular diffusion once the driver is filled. However, the jet of the gases during filling greatly enhances the mixing process. Also, since failed ignition in the driver never occurred during the experimental campaign,

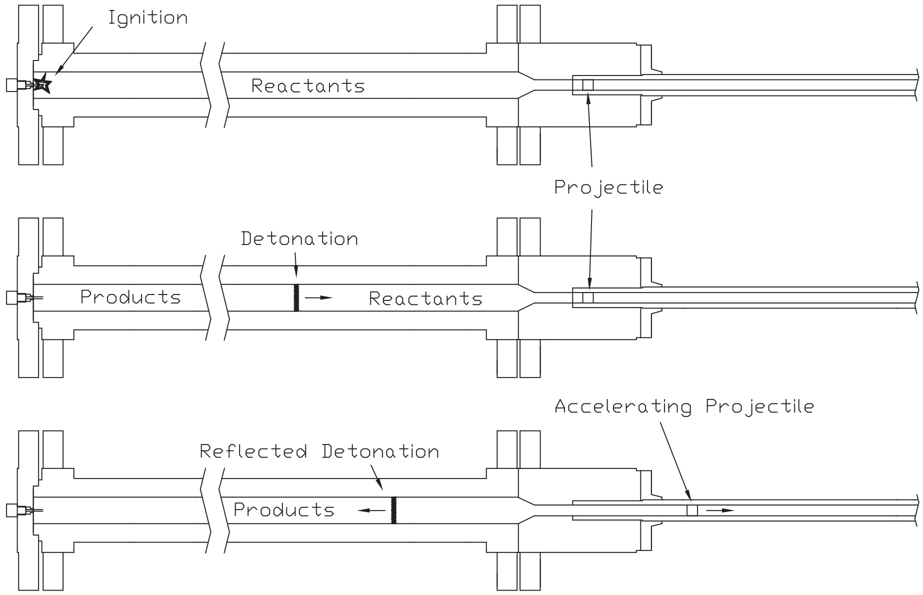

Figure 3–1: Schematic of the launcher operation

it can be concluded that the gases were sufficiently mixed. The mixture is then ignited using a weak pyrotechnic device commercially available for igniting Estes model rocket motors. It is presumed that the mixture transitions from deflagration to detonation (DDT) rapidly. Across a normal detonation wave, the pressure increase factor is on the order of 20. After the detonation reflects off the back of the projectile, the pressure behind the reflected detonation is now approximately 40 times greater than the initial pressure. The maximum initial driver pressure during the campaign was 10 MPa, providing a 400 MPa pressurized gaseous propellant, with a temperature above 4 000 K.

The performance of this detonation-driven launcher is in the range of 1 800 – 2 200 m/s for projectile masses of 2.5 – 4 g and initial driver pressures of 6 – 10 MPa. The maximum velocity recorded during the campaign was 2 700 m/s.

The concept of using a gaseous detonation as the propellant for a gas gun was suggested by Presles and Bauer [95], although no experiments were performed and the propellant selected (ethylene/oxygen/nitrogen) was limited in predicted performance to velocities of about 2.5 km/s. A unique facility was developed by Kryukov [63], in which a 0.5-m-diameter, 110-m-long tube was pressurized at up to 15 atm with hydrogen/oxygen ($4H_2 + O_2$). Detonation in this mixture impacted on a 9.1-kg, gyro-stabilized disk (0.5-m in diameter and 6-mm thick), which was then accelerated down a 50-m-long evacuated section of tube. Velocities of 3.5 km/s were demonstrated, and the facility was used to successfully shock-synthesize diamond upon impact against carbon-rich iron targets.

3.1.2 Test Section

A photograph of the test section is shown in Appendix A (Fig. A–2) and a schematic is depicted in Fig. 3–2. Prior to an experiment, the test section is evacuated and filled with the gaseous mixture to investigate, which is prepared in a separate reservoir (see Section 3.1.3). A thin Mylar diaphragm (13 μm thick) resting against the muzzle end of the launch tube separates the evacuated launch tube from the combustible mixture of the test section. As the projectile reaches the muzzle of the launch tube, the high-pressure propellant behind it is vented through slots into a larger evacuated chamber. The projectile then enters the test section (16.5 cm in diameter, 92 cm long) equipped with windows to permit flow visualization. The 10-cm wide windows allow monitoring the flowfield from 34 cm to 44 cm downstream of the muzzle. The projectile carries an onboard NdFeB magnet that triggers the

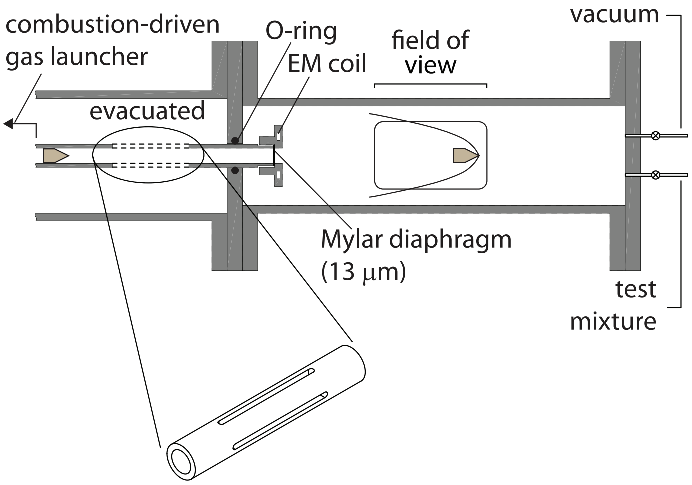

Figure 3–2: Schematic of the test section

camera and data acquisition system via a current induced in an electromagnetic coil (EM coil) positioned near the muzzle of the launcher.

3.1.3 Mixture Investigated

The mixture investigated in this work was stoichiometric hydrogen / oxygen with 70% argon dilution ($2H_2+O_2+7Ar$). This choice was motivated by two considerations. First, hydrogen is a well-studied fuel and its combustion kinetic rates are well known for numerical simulations. Second, in order to initiate an oblique detonation wave from a projectile, the CJ speed of the mixture has to be less than the projectile velocity. Based on the launcher performance, the nominal projectile velocity for all experiments was set to 2 000 m/s. The chosen mixture composition is characterized by a CJ velocity of 1 710 m/s (at an initial pressure and temperature of 200 kPa and 298 K, respectively).

An additional important parameter to consider for the characterization of the mixture is the detonation cell size. For the purpose of this investigation, the experimental measurements of the cell size as a function of initial pressure of Strehlow et al. [112] were used. From their results, a power law fit was employed to relate the two parameters as follows:

$$\lambda = 946.09p^{-1.375} \tag{3.1}$$

where p is the initial pressure in kPa and λ is the cell size in mm.

The test mixtures were prepared in an external mixing reservoir using the following procedure. The mixing reservoir was evacuated and then flushed with argon and re-evacuated. The three component gases were then filled in sequence, with their partial pressures determined by the desired mixture, using an OMEGA PX 212 gage with 0.25% accuracy. The mixture in the reservoir (typically at 2 to 3 atm) was allowed to mix for a minimum of 2 days prior to use in an experiment. A given batch of mixture could be used for 10 to 15 experiments. Once the mixing reservoir was significantly below atmosphere pressure, it was discarded and new mixture was prepared, so that any leaks in the reservoir would not contaminate the mixture with air.

3.1.4 Visualization

Photographs of the Schlieren assembly are shown in Appendix A (Fig. A–3 for the light source side and Fig. A–4 for the camera side). A continuous light is provided by a tungsten filament (OSRAM DYS, 600 W – 120 V). The field lenses of the system are large achromatic lenses with a diameter of 10.23 cm and a focal length of

152.5 cm. Photographs were taken using a high-speed framing camera (HSFC-PRO image-intensified camera) to monitor the flowfield around the projectile. This camera allows a minimum inter-frame time of 500 ns and a minimum exposure time of 3 ns. The total number of frames is limited to 8. For the purpose of the experiments, the inter-framing time is set to 20 – 30 μs with an exposure time of 0.5 μs. The projectile velocity is obtained by direct measurement from two photographs of the same experiment, taken at a known time interval apart.

3.1.5 Projectile Fabrication

In order to keep the driver performance near a nominal projectile velocity of 2 000 m/s, the mass of the projectile was restricted to less than 4 g. Mechanical stability of the projectile during its acceleration in the launch tube was essential to provide zero angle of attack as it traveled in the test section. Figure 3–3 illustrates four designs that were investigated; single body, front shell, rear shell and rear shell with aluminum tip designs. The effect of the different designs and materials on the projectile stability will be presented in Section 4.5. An aluminum tip was used for very acute cone angles in order to provide a fine tip. A shallow cavity on the back of the projectile ensured sealing against the launch tube via internal pressurization, preventing blow-by of the propellant gas.

The in-bore diameter of the launch tube is 1.27 cm, which corresponds to the projectile diameter for the complete set of experiments. This bore size is sufficiently large to observe detonation initiation from the projectiles, while keeping the physical size of the launcher to within the available space in the laboratory. The length of the launch tube is 2.44 m, or 192 projectile diameters.

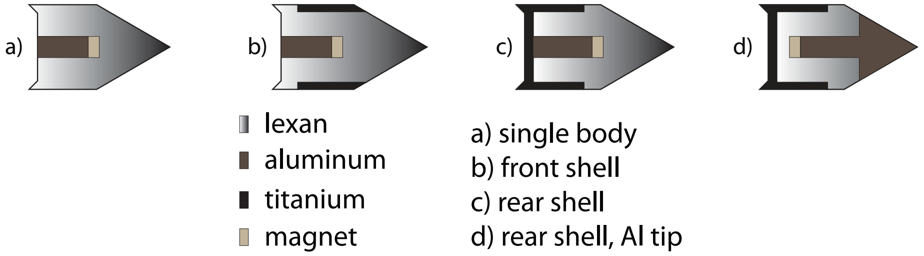

Figure 3–3: Projectile designs

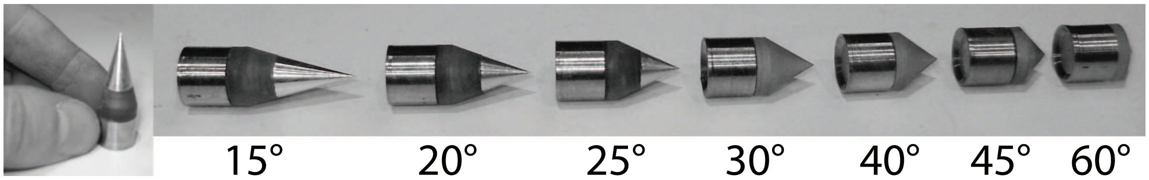

Figure 3–4: Projectiles with a cone half angle from 15° to 60°

All projectile designs used in this investigation were aerodynamically unstable and would eventually tumble in flight (due to lack of gyroscopic stabilization from the unrifled, smooth bore launch tube). The test section windows are located within 50 cm downstream of the muzzle; given this short distance of travel, canting of the projectile over this distance due to aerodynamic instability is negligible provided that the projectile exits the muzzle initially flying straight.

3.2 Experimental Conditions

To properly assess the role of the projectile nose on the detonation initiation criterion, it is important to study the effect of the cone angle over a wide range; cone half angles between 15° and 60° were investigated. For small cone angles, the chemical length scale behind the oblique shock increases due to the weaker shock and hence lower temperature. To keep the chemical length scale comparable to the characteristic length scale of the projectile, the pressure range was extended to relatively large values; initial pressures from 10 to 200 kPa were studied. The available range of cone angles and fill pressures greatly extends the parameter region compared to the work of Kasahara et al. [59] since they were limited to cone half angles greater than 30° and fill pressures less than 50 kPa. Table 3–1 summarizes the experimental conditions.

Table 3–1: Target experimental conditions

Mixture	$2H_2+O_2+7Ar$
Cone half angle (°)	15 – 60
Projectile velocity (m/s)	≈ 2 000
Mixture pressure (kPa)	10 – 200

CHAPTER 4
Experimental Results

The objective of the experimental campaign was to determine the conditions for which an ODW can be stabilized on a conical projectile. The cone angle and the mixture initial pressure were the two independent parameters. The projectile velocity was kept close to the nominal value of 2 000 m/s, but a variation in the projectile mass, driver pressure and launcher performance slightly affected the resulting projectile velocity. Table 3–1 summarizes the experimental conditions.

During the experimental campaign, a total of 192 individual trials were performed. Unfortunately, not all of them generated useful results due to experimental issues (unstable projectiles, contamination of the test mixture by propellant blowing by the projectile during launch and failures in the data acquisition). Twenty-nine experiments provided results that can be used for analysis. They are described in detail in Appendix B with a summary table for the experimental conditions, the Schlieren photographs and their description. By varying the above parameters, different combustion regimes were observed. Figure 4–1 shows the five different types of flowfields that are representative of the five combustion regimes observed throughout the experimental campaign. All of the experiments reported in this work (in Appendix B) could be related to one of these combustion regimes, which are described individually in Section 4.1. Section 4.2 presents a graphical representation of all the experimental results. The last three sections of this chapter concern the effect of

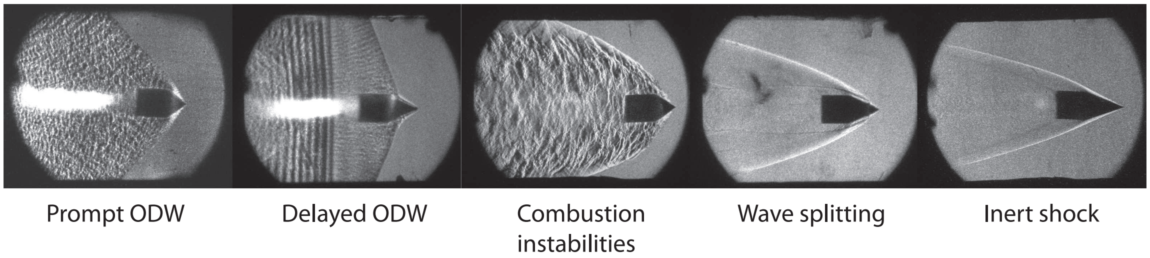

Figure 4–1: Flowfields observed

the projectile velocity on the results, the angle of the ODWs and the stability of the projectiles according to their fabrication design.

4.1 Description of the Combustion Regimes

Figure 4–2 shows the flowfield induced by a 40° half angle cone traveling at 2 180 m/s into a mixture initially at 101 kPa. According to the figure, an ODW is attached at the tip of the cone and is self-sustained in the farfield. One can observe that the ODW has a steeper angle in front of the cone than in the farfield. A cellular structure, characteristic of a self-sustained detonation, is visible on the entire front.

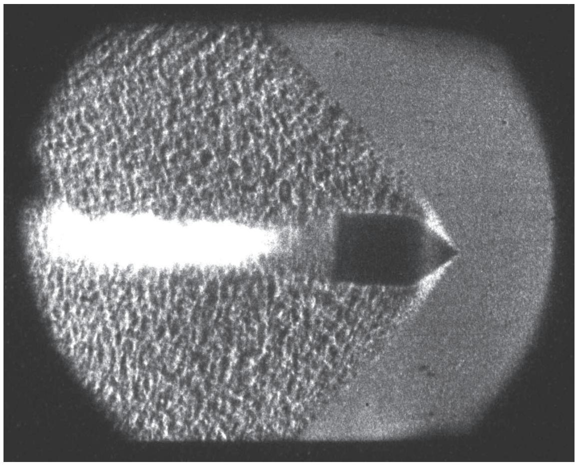

Figure 4–2: Prompt ODW, Shot 146

Table 4–1: Experimental conditions for Shot 146

Shot	Proj. vel.	Cone half angle	Pressure	Comb. regime
146	2 180 m/s	40°	101 kPa	prompt ODW

For such a flowfield, an ODW is initiated at the tip of the cone and seems to be stabilized in the farfield. Therefore this case is referred to as the prompt ODW regime. Table 4–1 summarizes the experimental conditions for this experiment.

Figure 4–3 illustrates the case where the cone half angle is relatively small (25°) and the mixture pressure is relatively high (120 kPa). The projectile velocity in this case is 1 740 m/s. According to this figure, an inert oblique shock is attached at the tip of the cone. At approximately half of the cone length, the oblique shock angle is sharply increased, which shows the onset of an ODW. In the farfield, the ODW is self sustained, similar to the prompt ODW regime. Note that the vertical stripes are an interference pattern resulting from the interaction between the shock wave and the protective acrylic plates acting as windows. Due to the fact that the onset of

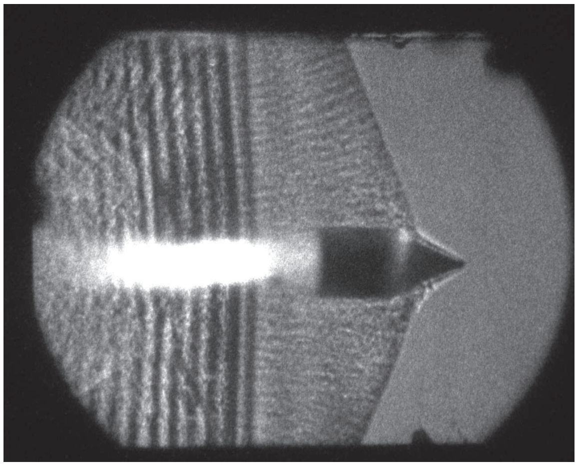

Figure 4–3: Delayed ODW, Shot 154

Table 4–2: Experimental conditions for Shot 154

Shot	Proj. vel.	Cone half angle	Pressure	Comb. regime
154	1 740 m/s	25°	120 kPa	delayed ODW

the ODW occurs at a significant distance downstream of the tip, this case is called the delayed ODW regime. Table 4–2 summarizes the experimental conditions under which this particular delayed ODW was observed.

A flowfield characterized by large density gradients is shown in Fig. 4–4. In this case, the projectile velocity, cone half angle and mixture pressure are respectively 1 800 m/s, 35° and 81 kPa. These fluctuations are very similar to the large-disturbance regime of Alpert and Toong [2]. The pulsations are attributed to unsteady combustion initiation and failure on the nose of the projectile. The angle of the oblique shock at the nose is steeper than an inert oblique shock. However, the reaction front fails to couple with the shock above and below the projectile and the angle of the oblique shock eventually decreases in the farfield. This flowfield

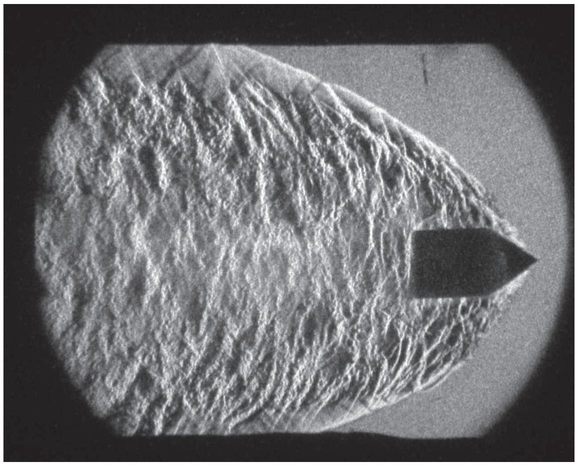

Figure 4–4: Combustion instabilities, Shot 171

Table 4–3: Experimental conditions for Shot 171

Shot	Proj. vel.	Cone half angle	Pressure	Comb. regime
171	1 800 m/s	35°	81 kPa	comb. inst.

is the combustion instabilities regime and Table 4–3 summarizes the experimental conditions for this experiment.

Figure 4–5 shows the flowfield produced by projectile traveling at 1 900 m/s with a cone half angle of 25° into a mixture initially at 80 kPa. In this flowfield, a smooth reaction front decouples from the shock around the cone and extends horizontally behind the projectile, thereby separating the reacted and the non-reacted gases. No combustion disturbances were observed for this regime and it is referred to as the

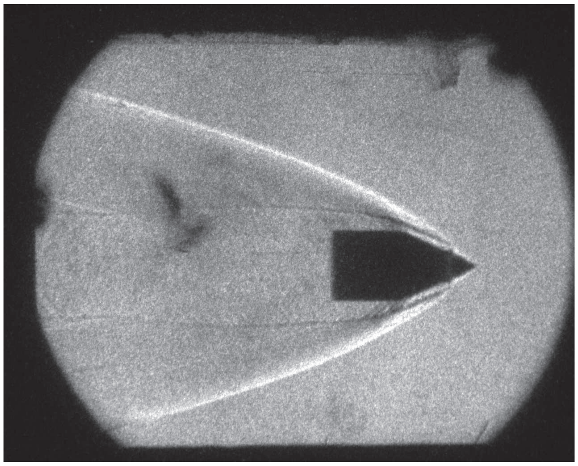

Figure 4–5: Wave splitting, Shot 156

Table 4–4: Experimental conditions for Shot 156

Shot	Proj. vel.	Cone half angle	Pressure	Comb. regime
156	1 900 m/s	25°	80 kPa	wave splitting

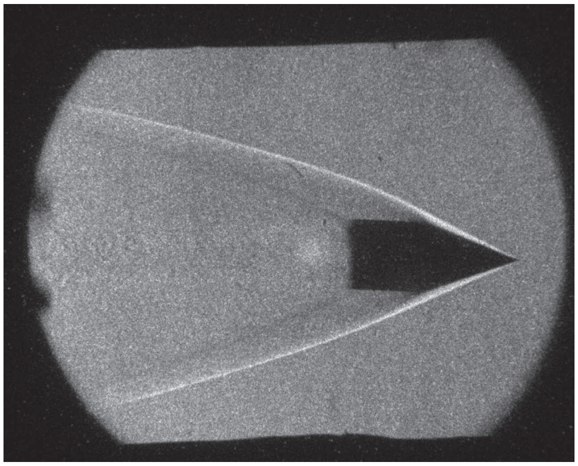

Figure 4–6: Inert shock, Shot 163

Table 4–5: Experimental conditions for Shot 163

Shot	Proj. vel.	Cone half angle	Pressure	Comb. regime
163	2 060 m/s	20°	63 kPa	inert regime

wave splitting regime. Table 4–4 summarizes the experimental conditions for this experiment.

Figure 4–6 presents the case where an inert oblique shock is produced by the passage of the projectile and there is an absence of any combustion activity. The projectile velocity, the cone half angle and the mixture pressure are 2 060 m/s, 20° and 63 kPa, respectively (summarized in Table 4–5). This flowfield is called the inert regime.

4.2 Map of Combustion Regimes

All of the experimental results are presented in Fig. 4–7, where the combustion regime is shown as a function of the cone angle and the initial mixture pressure for

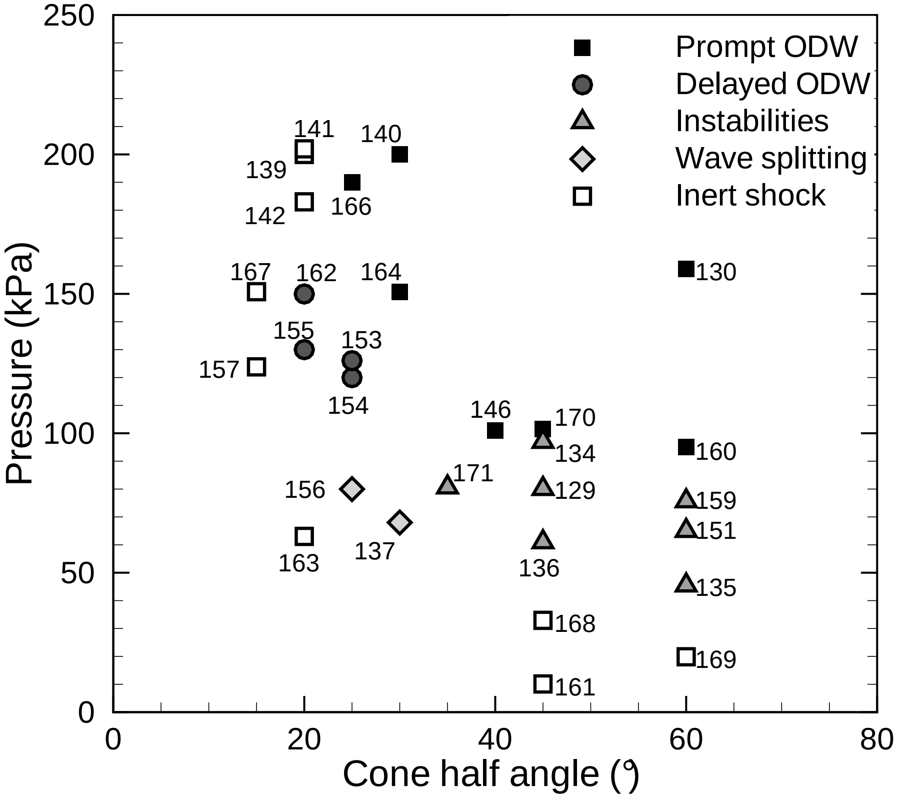

Figure 4–7: Map of the combustion regimes. Numbers refer to the shot #

each experiment. The projectile velocity was kept as near as possible to the nominal velocity of 2 000 m/s, even though a variation from 1 700 – 2 200 m/s was recorded.

According to this figure, a prompt ODW was initiated under conditions that favored fast chemical reactions: larger cone angles (resulting in stronger shocks) and higher pressures. Considering the shots with a cone half angle of 35° and larger, a pressure of 95 kPa was required to initiate a prompt ODW. Above this value, a prompt ODW was observed, except for Shot 134, independently of the cone half angle (larger than 35°). In the pressure range between 45 and 81 kPa, the combustion instabilities regime was observed for all experiments. Below a pressure of 45 kPa, three experimental results showed the inert shock regime. One can see that for relatively blunt cones ($> 35°$), the combustion regime was more predominantly affected by the mixture initial pressure than the cone angle.

For high mixture pressures, between 120 and 151 kPa, seven successful experiments were conducted for slender cones ($\leq 30°$). A prompt ODW was observed for the largest cone angle (Shot 164). For slightly smaller cone half angles (20° and 25°) the delayed ODW regime was observed, independently of the mixture pressure. The inert shock regime occurred for the smallest cone half angle of 15°. In the pressure range between 183 and 202 kPa, the transition from a prompt ODW to an inert shock occurred for a slight change in the cone half angle (from 25° to 20°). The delayed ODW regime was not observed for pressures higher than 150 kPa. Therefore, for a mixture pressure above 100 kPa, the combustion regime seems to be determined predominantly by the cone angle. The wave splitting regime was observed in two experiments where the conditions are such that the cone angle was smaller than that of the combustion instabilities regime, and the pressure is lower than that of the delayed ODW regime. For small cone angle and low pressure (Shot 163), no evidence of combustion in the flowfield was seen (i.e., the inert regime).

4.3 Effect of Projectile Velocity

In the description of the experimental results based on Fig. 4–7, it was mentioned that the projectile velocity ranged from 1 700 to 2 200 m/s. One could therefore argue that the map of combustion regimes is also affected by this parameter, which is not explicitly shown in Fig. 4–7.

To remedy this, the effect of the velocity on the delayed ODW regime is shown in Fig. 4–8. In this figure, the cone angle and the projectile velocity are the independent parameters, and the results are again classified into the five regimes previously described. For the results shown, the mixture pressure ranges from 120 to 150 kPa. Over the range of projectile velocities used, no dependence of the flowfield regime on projectile velocity was observed. Therefore, the cone angle appears to be the dominant parameter that affects the flowfield at high mixture pressures.

Similarly, Fig. 4–9 presents the effect of the projectile velocity on the combustion instabilities regime. In this figure, the mixture pressure and the projectile velocity are the independent parameters, and the cone half angle is constant at 45°. Shots 134 and 129 represent a velocity increase of 430 m/s but a pressure reduction of only 17 kPa with no observed effect on the combustion regime. However, the difference between Shots 134 and 170 is a velocity increase of 110 m/s combined with a pressure increase of 5 kPa, and here a regime transition from combustion instabilities to prompt ODW is observed. Therefore, in this case, the velocity increase probably influenced the initiation of a prompt ODW. Nevertheless, by taking into account the 6 results shown, one can observe that the mixture pressure more significantly affects the combustion regime than the projectile velocity does.

In brief, both the cone angle and the mixture pressure play a more important role than the projectile velocity in the determination of the different combustion regimes, hence in the initiation of an ODW. This motivates the use of these two parameters in the map of combustion regimes, as in Fig. 4–7.

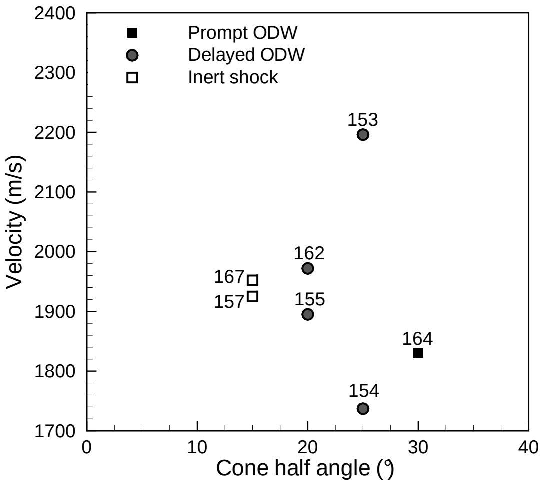

Figure 4–8: Effect of the velocity on the delayed ODW

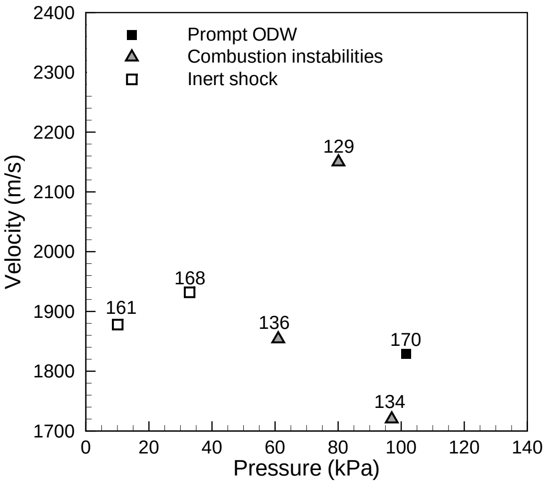

Figure 4–9: Effect of the velocity on the combustion instabilities

4.4 Detonation Angles

For all experiments where a prompt or delayed ODW was monitored, the ODW was self-supported in the farfield above and below the projectile. The experimental value of the ODW angle can thus be compared with a theoretical value by assuming that the normal velocity component of the ODW is equal to the CJ velocity of the mixture. With this assumption, the detonation angle can be predicted by the following relation:

$$\theta_{det} = \arcsin\left(\frac{U_{CJ}}{U_{proj}}\right) \tag{4.1}$$

which is the detonation analog to the Mach angle, with the detonation wave velocity replacing the acoustic speed in the Mach angle relation. The projectile velocity was measured from the experimental photographs. Figure 4–10 presents the comparison between the measured angles and the values predicted by the above relation. The

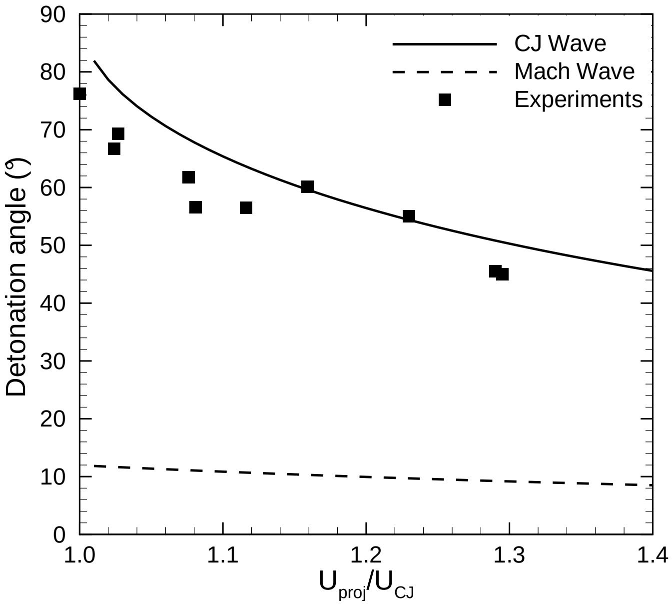

Figure 4–10: Detonation angle as a function of the ratio of the projectile velocity and the CJ velocity

trend of the experimental detonation angles follow that of the CJ wave, even though results where the measured wave angle is offset by as much as 10° lower than the predicted values are shown. This discrepancy is most likely caused by two phenomena. First, recalling that the camera field of view is located from 34 to 44 cm downstream of the launch tube muzzle, it cannot be ruled out that the flow has not fully developed to its steady configuration. Second, the curvature effect of the detonation front around the flight axis can cause a detonation velocity deficit (that produces a detonation angle deficit). The effect of the curvature on the detonation angle will be presented in Section 7.3.2. There is no doubt, however, that the observed waves are ODWs, since a nonreacting shock would have decayed to the Mach angle in the farfield, which is also shown as a dashed line in Fig. 4–10 and is seen to be much smaller than the observed wave angles.

4.5 Projectile Stability

As discussed in Section 3.1.5, fabrication methods for the projectiles (see Fig. 3–3) evolved throughout this study in an attempt to improve their in-bore mechanical stability. Even though a rigorous study has not been conducted to determine the optimal configuration and material, it was observed that the use of a single-body projectile made of lexan, aluminum or magnesium often produced a projectile flying at an angle of attack, as shown in Fig. 4–11. Angular motion of the projectiles as they traveled in the camera field of view was measured to be minimal. Therefore, the single-body projectiles were unstable in the launch tube likely due to material erosion; evidence of this erosion is clearly seen in Figs. 4–11c-d, where the originally cylindrical rear of the projectile has become a tapered "boattail" after traveling down the launch tube. When using a rear shell made of a stronger material (steel or titanium), the projectile stability was significantly improved.

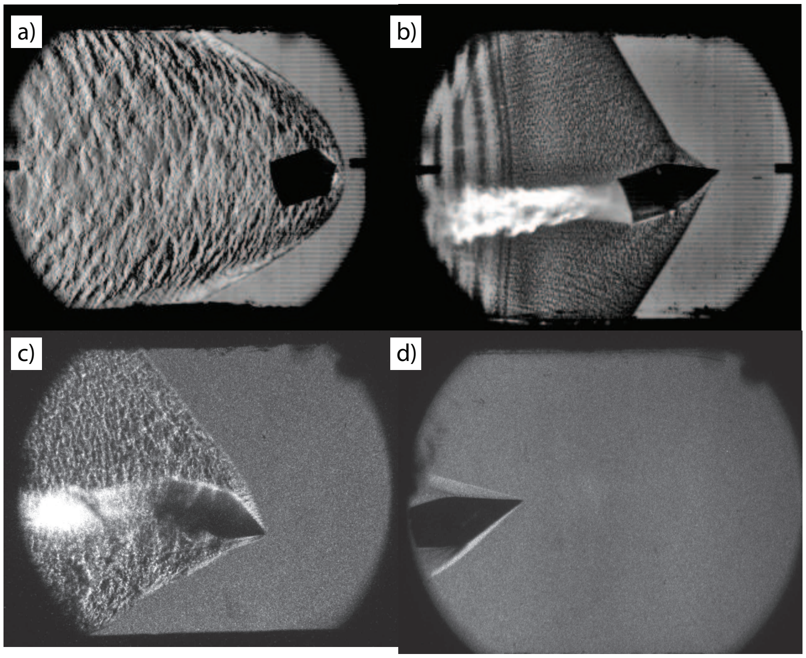

Figure 4–11: Examples of canted projectiles

CHAPTER 5
Simple Theoretical Models

The experimental results presented in Chapter 4 demonstrated that hypervelocity conical projectiles fired into a combustible mixture can produce very different flowfields involving complex interactions between gasdynamics and chemistry. This is especially the case for critical regimes at the boundary between successful initiation of an ODW (complete coupling of the combustion front with the oblique shock) and the absence of any apparent combustion activity. A thorough understanding of the interactions taking place in such critical flowfields is a challenging task. Extensive theoretical and computational investigations have been previously conducted in an attempt to reproduce the flowfields that have been experimentally observed in front of hypersonic spherical-nosed projectiles. The main difficulty in analyzing blunt flows of reacting gas lies in the fact that an assumption of the shock shape produced by the body is required in order to determine the chemical kinetics behind the shock. Since the flow is subsonic between the shock and the sphere, the chemical energy release influences the shock shape, altering the first assumption. However, in the case of an ODW initiated by a wedge or a cone, the flow is supersonic behind the inert shock at the tip and can remain supersonic even downstream of the chemical energy release zone. In this case, the solution of the flowfield can be carried out more easily, since the information is communicated throughout the flowfield only along characteristics.

In this chapter, simple theoretical models are presented in order to predict the experimental conditions required to initiate an ODW. Sections 5.1 and 5.2 consider the blast wave model and a chemical kinetics analysis, respectively. For each section, the prediction for detonation initiation is compared with experimental results. In Section 5.3, the results are interpreted in terms of an energy and power requirement. In Section 5.4, a general discussion is given on the results of this investigation. More involved theoretical calculations to predict the critical conditions for detonation initiation are presented in Chapter 6 by solving flowfields with the method of characteristics.

5.1 Blast Wave Model

5.1.1 Energy of Initiation

Blast initiation of a detonation (or direct initiation of a detonation) refers to the generation of a strong blast wave from a source of energy that is capable of triggering chemical reactions in the wake through adiabatic compression, with the reaction front coupling with the blast to form a detonation wave in the farfield. The source of energy can be released from a point, a line or a plane to generate a spherical, cylindrical or planar blast wave, respectively.

In the theory of blast initiation of a detonation, a given amount of energy is released instantaneously in a combustible gas. This energy release drives a strong blast that decays as it propagates away from the source. There are two possible outcomes when a strong blast propagates in a combustible mixture. If the source energy is insufficient, the blast decay is too fast for the chemical reactions to be triggered. In this case, the shock continuously decays and becomes an acoustic wave in the farfield; this is the subcritical regime. For a sufficient amount of energy release, the blast is able to initiate chemical reactions behind it. The exothermic reactions subsequently couple to the leading shock to initiate a self-propagating Chapman-Jouguet (CJ) detonation; this is the supercritical regime. Therefore, the only parameter that determines a successful initiation or failure to initiate a detonation in the farfield is the magnitude of the energy released by the source. Different theoretical models were developed to predict the critical energy for detonation initiation. The critical curvature model by He and Clavin [43] treated the problem as quasi-steady. In this model, the curvature of the blast wave was responsible for quenching the chemical reactions in the case of failure to initiate a detonation. Eckett et al. [28] showed that the blast initiation problem cannot be assumed to be quasi-steady, since the magnitude of the unsteady terms were significantly larger than that of the curvature term. In their model, the critical decay rate of the blast determined the minimum amount of energy that initiated a detonation in the farfield.

Experimentally, blast initiation can be realized by using very small and powerful initiators. Benedick et al. [9], for example, measured the critical mass of explosives to directly initiate spherical detonations in unconfined hydrocarbon-air mixtures.

In order to directly initiate a cylindrical detonation, a strong cylindrical blast needs to be generated from a line source of energy. In this case, the energy is expressed per unit length. The phenomenon of detonation initiation by hypersonic projectiles can be related to the concept of direct initiation of a cylindrical detonation, assuming that the passage of the projectile plays the role of the line source of energy that generates a cylindrical blast. In other words, by using the blast wave analogy (or the hypersonic equivalence principle), the shock generated by the projectile can be viewed as a cylindrical shock in a plane perpendicular to the direction of propagation. The blast wave analogy is mathematically based on the fact that the governing equations for an unsteady two-dimensional flow are identical to that of a steady three-dimensional flow with the hypersonic small-disturbance assumption. Therefore, in order for the blast wave analogy to be valid, the maximum deflection angle of the body needs to be very small ($\tau << 1$) and the Mach number has to be very large ($M >> 1$) such that $M\tau \geq 1$ or $M\tau >> 1$.

Once the condition of blast wave analogy is verified, the event can be analyzed in the plane perpendicular to the direction of propagation in cylindrical coordinates. The purpose is then to determine the critical conditions to initiate a cylindrical detonation. To use the theory of blast initiation of a detonation, the source has to deposit the energy instantaneously along a line of inifinitely small radius. However, since the size of the projectile is finite, it has to be much smaller than the characteristic length scale for blast initiation: the critical explosion length. This condition is expressed as:

$$r_p << R_o^* = \left(\frac{E_s^*}{p_o}\right)^{\frac{1}{j}} \tag{5.1}$$

where r_p is the projectile radius and $j = 2$ in cylindrical coordinates.

5.1.2 Lee-Vasiljev Model

The blast wave model applied to hypersonic projectiles was developed independently by Vasiljev [120] and Lee [68]. This theory states that the energy deposited by the projectile must be at least equal to the critical energy to directly initiate a detonation ($E_{proj} \geq E_c$). In a gas, one can assume that the hypersonic projectile produces a cylindrical blast wave propagating outwards from the flight axis. In a combustible mixture, this blast wave must be of sufficient strength to trigger a cylindrical detonation wave. Lee used the following equation to relate the velocity of the blast wave to its radius:

$$U_s^2 = \left(\frac{E_0}{2\pi I \rho_\infty} \frac{1}{r_s^2} \right) \tag{5.2}$$

where U_s is the blast wave velocity, E_0 is the blast energy, I is an integral that takes a value of 0.626 for $\gamma = 1.4$ and of 0.440 for $\gamma = 1.556$ (characteristic of the $2H_2+O_2+7Ar$ mixture), ρ_∞ is the initial density and r_s is the blast radius. Lee stipulated that in order to initiate a cylindrical detonation, the blast radius at which it has decayed to the CJ velocity of the mixture must be at least some critical radius of the form $\kappa\lambda$, where κ is a constant and λ is the characteristic detonation cell size of the mixture. Lee used $\kappa = 3.2$ in his theory. Equation 5.2 can thus be expressed as:

$$E^* = 10\gamma p_0 M_{CJ}^2 \lambda^2 \tag{5.3}$$

where the relation $M_{CJ} = U_{CJ}\sqrt{\rho_0/(\gamma p_0)}$ was used. This minimum energy can be equated to the energy per unit length deposited by the projectile, which is simply its drag:

$$E_{proj} = D = \frac{1}{2}\rho U_{proj}^2 A C_D = \frac{\pi d_{proj}^2}{8}\gamma p M_{proj}^2 C_D \tag{5.4}$$

where d_{proj} is the projectile diameter. Equations 5.3 and 5.4 can be combined to give:

$$\frac{d_{proj}}{\lambda} = \left(\frac{80}{\pi C_D}\right)^{1/2} \left(\frac{M_{CJ}}{M_{proj}}\right) \tag{5.5}$$

The value of the drag coefficient for cones can be approximated by a simple correlation from Linell and Bailey [74]:

$$\frac{C_D}{\sin^2 \phi_c} = \frac{10 + 32\xi \sin \phi_c}{1 + 16\xi \sin \phi_c}$$

where ϕ_c is the cone half angle and $\xi = \sqrt{M_{proj}^2 - 1}$. The detonation cell size λ for the $2H_2+O_2+7Ar$ mixture is approximated by a power law fit of the data from Strehlow et al. [112]:

$$\lambda = 946.09 p^{-1.375} \tag{5.6}$$

where p is the mixture pressure in kPa and λ is the cell size in mm.

Equation 5.5 dictates the critical conditions for detonation initiation based on the Lee-Vasiljev model. By combining eqs. 5.1 and 5.3, the condition for this model to be valid is expressed as:

$$r_p << R_o^* = \left(\frac{10\gamma p_o M_{CJ}^2 \lambda^2}{p_o}\right)^{\frac{1}{2}} = \sqrt{10\gamma} M_{CJ} \lambda \tag{5.7}$$

Since the mixture composition investigated is constant, the critical explosion length in the above equation only depends on the initial pressure (which determines the CJ Mach number and the detonation cell size). The ratio of the projectile radius

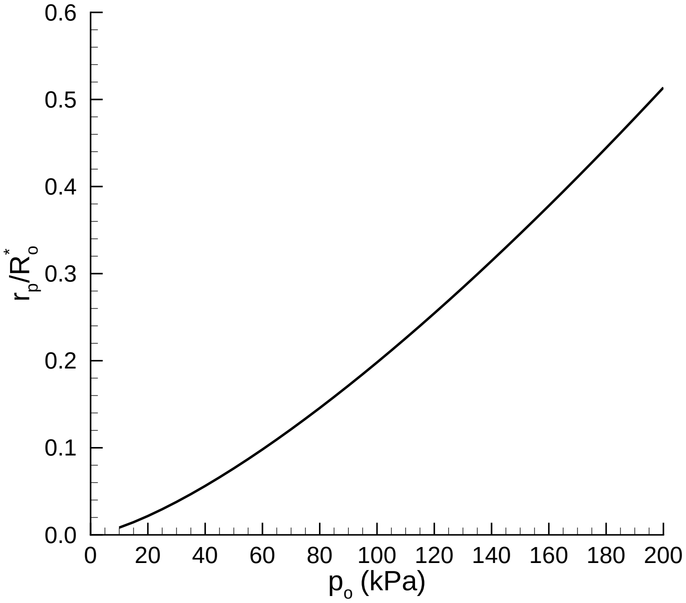

Figure 5–1: Ratio of the projectile radius and the critical explosion length as a function of initial pressure

and the critical explosion length as a function of initial pressure is illustrated in Fig. 5–1. It can be observed that for an initial pressure of about 60 kPa, $r_p/R_o^* = 0.1$, which can be considered as the limiting value to define the source as much smaller than the critical explosion length. For $p_o > 60$ kPa, the size of the source becomes comparable to the critical explosion length. Nevertheless, it is of interest to compare the Lee-Vasiljev model with the experimental results while keeping in mind that in some cases the assumptions of the model are violated.

5.1.3 Comparison with Experiments

The prediction of the experimental conditions to initiate a detonation wave based on the blast wave model (the energetic limit) is shown in Fig. 5–2, along with the complete set of experimental results. In the calculation of the energetic limit,

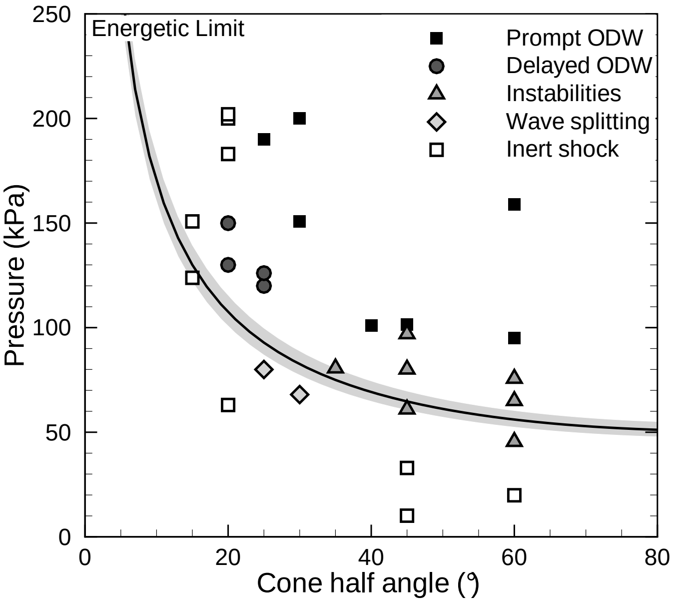

Figure 5–2: Comparison between the blast wave model and the experimental results

a projectile velocity of 2 000 m/s is assumed. Above the curve, the projectile drag is larger than the critical energy per unit length to directly initiate a cylindrical detonation. The shaded area on both sides of the curve illustrates the effect that a ±200 m/s projectile velocity range has on the limit. Based on the discussion given in Section 4.2, the mixture pressure is the parameter that most importantly affects the combustion regime for blunt cones ($> 35°$). This dependency is also observed by the energetic limit. According to this criterion, a pressure of 55 – 80 kPa is required to initiate an ODW for a cone half angle ranging from 35° to 60°. The theory curve becomes sensitive to pressure for blunt cones due to the dependence of critical energy on cell size, which in turn depends on pressure. Energy input from the projectile also depends on pressure through gas density. Experimentally, a similar sensitivity to pressure is seen for cone angles $> 35°$.

The experimental and theoretical qualitative trends, however, deviate for slender projectiles and high initial pressures. As discussed in Section 4.2, the flowfield is determined predominantly by the cone angle for cone half angles less than 30° and mixture pressures above 100 kPa. The energetic limit is also primarily influenced by the cone angle for mixture pressures above 100 kPa. However, for increasing pressure, the critical cone angles for detonation initiation based on the energetic limit deviate from the experimental critical cone angles. For instance, a cone half angle between 20° and 25° seems to be the critical value from the experimental results above 100 kPa, whereas the critical value of cone angle from the energetic limit is 7° at 200 kPa. Therefore, it appears that the blast wave model follows qualitatively the trend of the experimental results only for relatively blunt projectiles (cone half angle larger than 35°) and mixture pressures lower than 100 kPa.

A possible explanation for the deviation of the experimental and theoretical trends for slender projectiles and high pressures can be related to the violation of the model assumptions. First, as mentioned previously, the blast wave model assumes an infinite rate of energy release by the source. For a realistic case of finite-rate energy release, the blast model is valid for fast rates of energy release (or large power). As the power is decreased, the assumption of instantaneous energy release becomes less valid. In fact, below some critical power, it becomes impossible to directly initiate a detonation, no matter the total amount of energy release [61]. It can be shown that the rate of energy release (power) is equivalent to the initial strength of the blast generated by the source. It is therefore possible that the rate at which hypersonic projectiles deposit the energy plays a role in detonation initiation, which is determined from the strength of the conical shock attached to the projectiles. The shock strength depends on the projectile velocity and also on the cone angle. For blunt projectiles, the shock is relatively strong, corresponding to the case of a fast rate of energy deposition. However, for slender projectiles, the rate of energy deposition is reduced, due to a weaker conical shock. Therefore, the assumption of an infinite rate of energy deposition becomes less valid for low cone angles. The relation between the energy deposited and the power of the projectiles will be presented in Section 5.3. Also, in Section 6.3, the validity of the two blast wave model assumptions for different wedge angles will be addressed rigorously by solving both the near and far fields of reacting flows over finite wedges.

Second, the blast wave analogy assumes that the characteristic length scale for critical blast initiation of a detonation (the explosion length) is much greater than the length scale of the energy source (the projectile radius). As shown in Fig. 5–1, this assumption becomes less valid for $p_o > 60$ kPa. This probably contributes to the deviation between the Lee-Vasiljev model and the experimental results at high pressures. In the next section, chemical kinetics are considered in the near field to suggest a requirement for kinetic rates.

5.2 Critical Damköhler Number

5.2.1 Definition of the Damköhler Number

As discussed in Section 5.1.3, there is a qualitative agreement between the energetic requirement and the experimental results for cone half angles larger than 35° and pressures lower than 100 kPa. For lower cone angles, the energetic limit deviates from the experimental one, suggesting that a different failure mechanism becomes

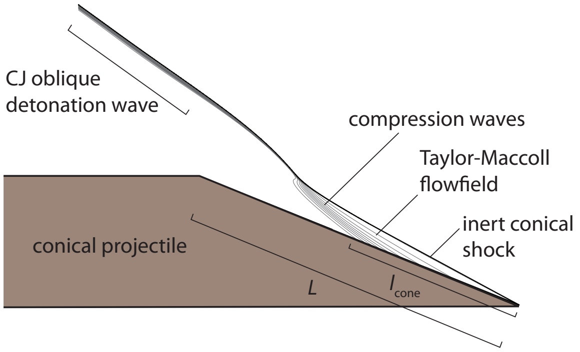

Figure 5–3: Schematic of a detonation initiation from a conical projectile

important at such conditions. The second requirement suggested in this work is that a minimum strength of shock is required to initiate chemical reaction.

Figure 5–3 presents a schematic of a detonation initiation from a conical projectile. An inert shock wave is attached to the cone tip. Downstream of the shock, a fluid particle is compressed from the shock to the cone surface (described by a Taylor-Maccoll flowfield). The highest temperature is along the cone surface. The autoignition location of the mixture along the cone surface occurs a certain distance downstream of the cone tip, which determines the induction length l_{cone}. The combustion front may eventually couple with the shock to initiate a CJ ODW which will be at a greater angle than the inert shock. Given a conical projectile velocity, the kinetic limit is obtained by using a Taylor-Maccoll algorithm to calculate the inert conical shock angle, which determines the flow temperature and velocity behind the shock and at the cone surface. Sections 7.1.2 and 7.1.3 describe the procedure to calculate reactive flow conditions behind oblique and conical shocks. A Damköhler number can be defined as $Da = \tau_f/\tau_c$, where τ_f is the fluid particle time scale on the cone surface ($\tau_f = L/U_{surf}$) and τ_c is the chemical time scale or induction time ($\tau_c = l_{cone}/U_{surf}$) with U_{surf} being the flow velocity along the cone surface. The conditions that result in a critical Damköhler number ($Da = 1$) determine the critical conditions based on the chemical kinetics along the cone surface.

5.2.2 Comparison with Experiments

The conditions resulting in a critical Damköhler number are graphically presented in Fig. 5–4 with the energetic limit and the experimental results. In the calculation of the critical Da, a projectile velocity of 2 000 m/s is assumed. On the right side of the curve, the induction length on the cone surface is less than the cone length. The shaded area on both sides of the limit represents a ±200 m/s variation in projectile velocity. By comparing the critical Da with the experimental results for pressures above 100 kPa, even though the theoretical critical cone half angle is 5 – 10° larger than the experimental critical value, the trend of the critical Da follows more closely the experimental trend, compared with the energetic limit. The conditions resulting in $Da = 1$ are much more influenced by the cone angle than by the mixture pressure. Experimentally, the criterion for detonation initiation is also largely influenced by the cone angle.

It can be concluded that for sufficiently strong shocks (i.e., for sufficiently large cone angles), the blast model qualitatively reproduces the experimental trend for detonation initiation. For weaker shocks (i.e., for slender projectiles) and high initial pressures, the blast model is not valid and the criterion for detonation initiation is rather influenced by near field considerations, such as the projectile size and the chemical kinetics behind the conical shock.

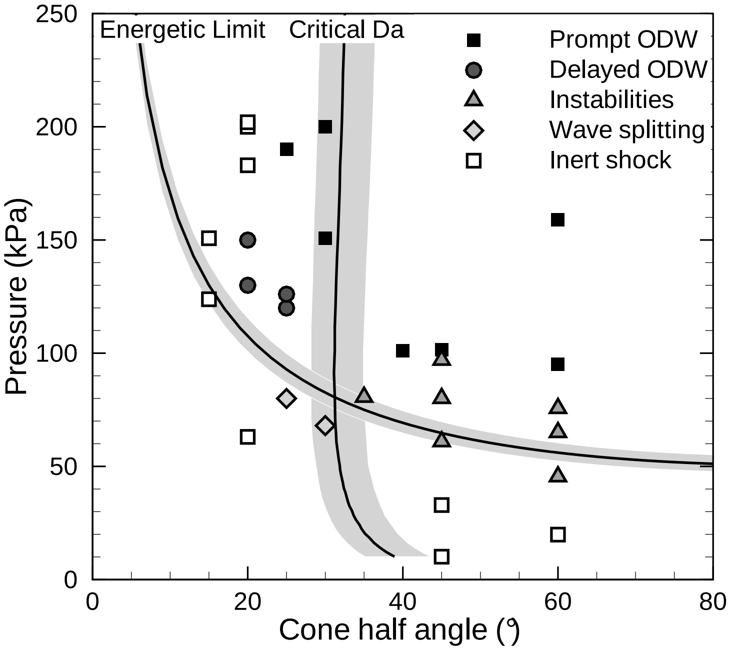

Figure 5–4: Comparison between the theoretical limits and the experimental results

5.3 Energy/Power Interpretation

This conclusion can be supported by relating the energetic limit and the critical Damköhler number discussed here with the energy and power requirements for direct initiation of a detonation, as investigated by Knystautas and Lee [61]. In experiments studying the initiation of a detonation in acetylene-oxygen mixtures by means of an electrical spark discharge, they found that for a sufficiently short duration spark (sub-microsecond), the critical conditions for direct initiation were only a function of the total energy deposited. As the time of the discharge was made longer by varying the characteristics of the spark generating circuit, however, they found that a critical rate of the energy release (i.e., power) was required for direct initiation, regardless of how much total energy was released. This critical power requirement was shown to be the power required to generate a shock wave of sufficient strength to initiate reaction in the gas. Thus, successful initiation of a detonation by a finite-rate energy release requires both a critical energy and power. In the present investigation, the cone angle of the projectile determines the shock strength for a given projectile velocity and thereby controls the energy deposition rate (power). Just as a very slow discharge of energy will not initiate detonation (regardless of the total energy deposited), a very sharp cone angle will also not result in the initiation of a detonation since in both cases a shock of sufficient strength to activate chemical reactions is not generated. The energy deposited by the projectile at a given velocity is determined by its drag coefficient and size (diameter).

To illustrate the energy and power requirements for direct initiation of a detonation in relation with the experimental results presented in this work, Fig. 5–5 relates the non-dimensional energy per unit length deposited by the projectiles (normalized by the critical energy — from the Lee-Vasiljev model — calculated for each firing) and the power of the projectiles. The power is expressed as $P = \left(E_{proj}U_{proj}\right)/L$, where L is the cone length. For sufficiently large values of power ($P > 3 \cdot 10^7$ W/m) a prompt ODW is initiated above a critical energy of $E_{proj}/E_c = 3$. Below this critical value, the combustion instabilities regime is observed. However, when the power of the projectile is lower than $3 \cdot 10^7$ W/m, a prompt ODW fails to be initiated, even for a non-dimensional energy of $E_{proj}/E_c = 4.8$. For a power between 10^7 and $3 \cdot 10^7$ W/m, the wave splitting, delayed ODW and inert shock regimes are observed. For a power less than 10^7 W/m, only the inert shock regime is obtained.

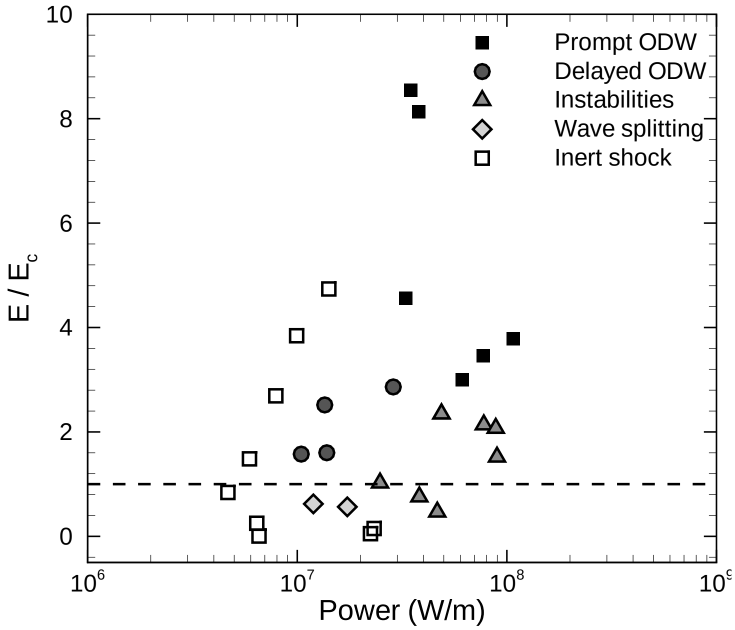

Figure 5–5: Map of combustion regimes in the energy-power parameter space

Fig. 5–5 clearly illustrates a requirement for both energy and power for detonation initiation from conical projectiles, similar to the energy and power requirement for blast initiation of a detonation [61]. For a sufficiently large power, the energy deposited is the only parameter that controls the resulting flowfield and the Lee-Vasiljev model agrees reasonably well with the experimental results. However, for lower values of power, the flowfield is influenced by the details of the initiation process and chemical kinetics in the projectile near field need to be considered.

5.4 Discussion on the Transitions

Earlier in this chapter, simple models (the kinetic and energetic limits) were presented to predict the conditions required to initiate an ODW from conical projectiles. These models were compared with the experimental results presented in

Chapter 4. A general discussion is given in this section based on the results from these models and the experimental results.

As discussed in Sections 5.1.3 and 5.2.2, the qualitative agreement between the experimental results and the two theoretical initiation criteria (the kinetic and energetic limits) suggest two failure mechanisms for detonation initiation: one due to slow chemical reaction rates and the other due to a lack of energy deposition by the projectile. A schematic of the two transitions from prompt ODW to inert shock regimes is shown in Fig. 5–6. By decreasing the cone angle at high mixture pressures, the oblique shock strength at the cone tip (and thus the temperature behind the shock) decreases. Since the chemical reaction rates have an exponential dependence on the gas temperature, the exothermic reactions are triggered farther from the cone tip, increasing the induction zone. If the gas particles traveling along the cone surface are ignited before they reach the projectile shoulder, compression waves are sent towards the oblique shock, thereby coupling the reaction with the shock and initiating an ODW. At high mixture pressures, the characteristic length scale of the detonation (the cell size or the detonation thickness) is relatively small. Therefore, the inert oblique shock attached at the cone tip abruptly kinks to an ODW where the compression waves interact with the oblique shock. By decreasing the cone angle even further, the shock strength becomes insufficient to initiate combustion before the gas particles reach the projectile shoulder. In this case, only an inert bow shock occurs.

The other type of transition from prompt ODW to inert shock regime is depicted at the bottom of Fig. 5–6. Blunt cones produce a strong shock behind which the

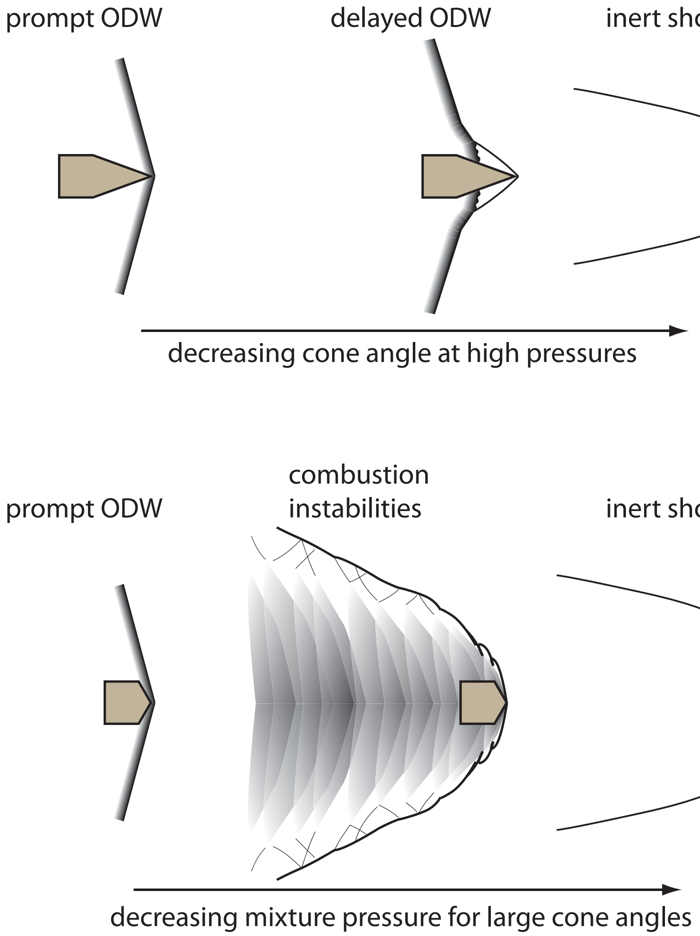

Figure 5–6: Schematic of the two transitions from prompt ODW to inert shock regimes

kinetic rates are very fast. The induction zone at the cone tip is therefore very small compared with the projectile diameter. By decreasing the mixture pressure, the projectile drag decreases as well (see Eq. 5.4), lowering the amount of energy deposited into the mixture. At the critical pressure, the combustion front fails to couple with the oblique shock to initiate an ODW. A complex interaction takes place between ignition of the mixture due to fast kinetics that produces compression waves (and strengthens the shock) and failure of the combustion front to fully couple with the shock. This critical regime qualitatively resembles the large-disturbance regime described by Alpert and Toong [2] and Matsuo and Fuji [76] with a wave interaction model, since it exhibits irregular low-frequency pulsations.

The one-dimensional wave interaction model that describes the large-disturbance regime is shown as an $x-t$ diagram in Fig. 5–7. This figure describes the propagation of the different waves along the stagnation streamlines between the bow shock created by a spherical-nosed projectile and the body surface. At time t_1, an explosion occurs at the reaction front, sending shock waves towards the body surface and the bow shock. The right-propagating shock interacts with the bow shock at t_2, forming a rarefaction wave and a contact discontinuity. The reaction front is closely coupled with the shock between t_1 and t_3. At t_3, the bow shock weakens and the reaction front decouples from it. The shock reflected from the body surface strengthens the bow shock at t_4, creating a contact discontinuity that separates a cold gas region (on the left of the discontinuity) from a hot gas region (on the right of the discontinuity). An explosion occurs at t_5 and a new cycle begins.

Despite the qualitative similarity between the combustion instabilities induced by conical projectiles observed in the present study and the large-disturbance regime previously observed around spherical-nosed projectiles, the one-dimensional wave interaction model cannot be applied to conical projectiles. Figure 5–8 shows a schematic of the combustion instabilities around spherical and conical bodies where the shock front and the reaction front are displayed. For the spherical case, the wave interaction model is applied along the stagnation streamline. In the conical case,

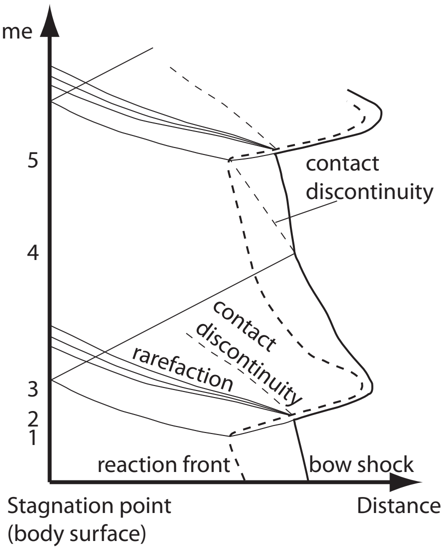

Figure 5–7: $x - t$ diagram of the wave interaction model proposed by Matsuo and Fuji [76]

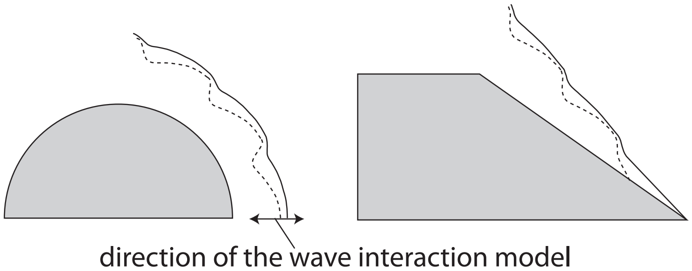

Figure 5–8: Schematic of the combustion instabilities around spherical and conical bodies

the model can no longer be applied at the axis of symmetry and a two-dimensional axisymmetric model is required. Furthermore, the combustion pulsations occur in a region where the curvature of the shock front may be significant. Such curvature can potentially enhance the ignition and failure mechanisms and thus alter the combustion instabilities. Section 7.3.3 presents the formation and structure of a conical detonation. In that analysis, the role of curvature around the flight axis on the detonation structure and stability is addressed.

CHAPTER 6
Theoretical and Numerical Simulations — Critical Oblique Detonation Initiation

In Section 5.1, the blast wave model (or the Lee-Vasiljev model) was derived and compared with experimental results. Based on energy considerations, this model predicts the critical conditions to initiate a detonation wave from a hypersonic projectile. As mentioned in the previous chapter, there are two key assumptions in the Lee-Vasiljev model: the hypersonic equivalence principle must be valid and the energy deposition from the source must be effectively instantaneous. It is the goal of this chapter to investigate rigorously the domain of validity of the Lee-Vasiljev model. In other words the conditions for which the two assumptions of the model are valid will be determined. To achieve this objective, three different situations will be considered as illustrated in Fig. 6–1. Numerical simulations of planar blast initiation of a detonation will be first investigated in one dimension. In this case, the energy is released instantaneously on a plane, which triggers a planar blast wave. When such a blast propagates in a combustible gas, the only parameter that determines the critical conditions for detonation initiation is the amount of energy per unit area that was released. Planar blast initiation can be equivalent to a planar piston initiation if the energy is deposited from the piston very rapidly (or effectively instantaneously). In this case, the critical energy for detonation is equal to that of

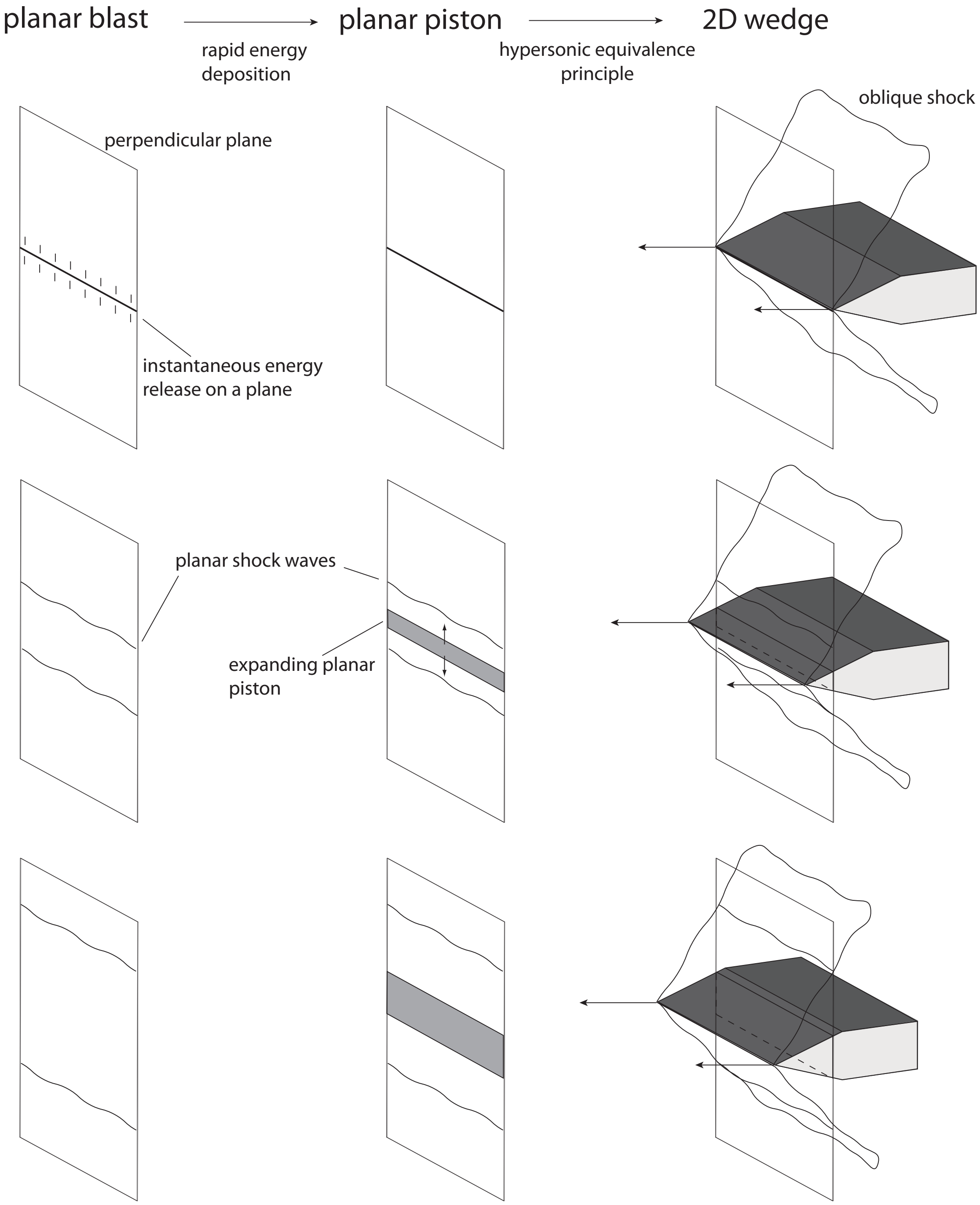

Figure 6–1: Schematic illustrating planar shock waves triggered by a planar blast, a planar piston and a 2D wedge

the planar blast configuration. The planar piston initiation can in turn be equivalent to a hypersonic two-dimensional wedge if the hypersonic equivalence principle applies (as outlined in Section 5.1.1). Therefore, if the two assumptions are valid, the Lee-Vasiljev model states that the critical energy to initiate a detonation from a hypersonic two-dimensional wedge is equal to that of a planar blast. The verification of this statement is the main objective of the simulations presented in this chapter. By doing so, the domain of validity of the Lee-Vasiljev model will be rigorously determined.

In Section 6.1, the numerical and theoretical methods used to model the flowfields are derived. Section 6.2 presents one-dimensional unsteady numerical simulations of the planar blast and planar piston initiation problems. Both non-reactive and reactive flows are considered. In Section 6.3, two-dimensional steady reactive flows encountering a wedge are solved with the Method of Characteristics (MoC).

6.1 Numerical and Theoretical Methods

6.1.1 Description of the Numerical Simulations

In the planar blast and planar piston initiation problems, the unsteady reactive Euler equations are used in one dimension. They are expressed as:

$$\frac{\partial}{\partial t}\begin{bmatrix}\rho\\ \rho u\\ \rho e\\ \rho Z\end{bmatrix}+\frac{\partial}{\partial x}\begin{bmatrix}\rho u\\ \rho u^2+p\\ (\rho e+p)\,u\\ \rho Z u\end{bmatrix}=\begin{bmatrix}0\\ 0\\ 0\\ \sigma\end{bmatrix} \tag{6.1}$$

where u is the velocity, p is the pressure, ρ is the density, e is the specific energy and Z is the reaction progress variable from the reactant ($Z = 1$) to the product ($Z = 0$). The chemistry is modeled with a single irreversible reaction of Arrhenius form. The source function is defined as:

$$\sigma = -\rho k Z \exp\left(-E_a \rho / p\right) \tag{6.2}$$

The equation of state can be expressed as:

$$p = (\gamma - 1)\,\rho\left[e - \frac{u^2 + v^2}{2} + ZQ\right] \tag{6.3}$$

where γ is the ratio of specific heats. The chemistry parameters are the heat release Q, the activation energy E_a and the pre-exponential factor k, which is a spatial scaling factor. These parameters are set to:

$$\gamma = 1.2 \qquad Q = 50 \qquad E_a = 20 \tag{6.4}$$

These parameters correspond to a stable behavior for a planar 1D unsteady detonation. The parameter k is adjusted to ensure that the one half-reaction length (the distance from a detonation leading shock to the location where $Z = 0.5$) is unity.

The governing equations are solved numerically using the Adaptive Mesh Refinement Interactive Teaching Aid (Amrita) environment developed by Quirk [96]. Amrita employs a hierarchical system of mesh patches according to a mesh refinement scheme defined by the user. The coarsest mesh, which covers the entire numerical domain, is set such that there is 16 grid points per half-reaction length of a CJ detonation wave. Mesh refinement is automatically applied at the locations of steep gradients in the flow properties to correctly resolve the flowfield. The most refined grid level corresponds to 256 grid points per half-reaction length. The Lax-Fridrichs scheme was used to evaluate the fluxes in the Euler equations. This scheme is of first order and was chosen for its robustness to simulate very strong shocks while avoiding negative pressures. This was especially encountered in piston-initiated shock waves where the piston was stopped instantaneously and created a very low pressure region in front of the piston face.

6.1.2 Description of the Theoretical Simulations (Method of Characteristics)

The flow behind an attached oblique shock is supersonic, as opposed to subsonic behind a bow shock formed by blunt projectiles. It is possible to take advantage of this feature to use a common technique to solve supersonic flows: the Method of Characteristics (MoC). In supersonic flows, information (or disturbances) propagates along specific path curves throughout the field. The orientation of these paths depends on the local conditions of the domain (flow conditions, walls, shock waves or ambient pressure boundary). These paths of propagation are called characteristic curves, or simply characteristics. By tracking the information carried along the characteristics, one can solve the flow conditions at the intersection points of the characteristics. From a mathematical point of view, by suitably transforming the coordinate system into the characteristic form, the governing partial differential equations become total differential equations, referred to as compatibility equations. These compatibility equations are solved *along* the characteristics. In steady supersonic flows, it can be demonstrated that the trajectories of the characteristics are simply the Mach lines. Therefore, the flow variables are solved by the compatibility equations and the trajectories of the characteristics are given by the Mach lines, allowing one to map out the entire domain of interest. The MoC is an *exact* method, as long as the number of characteristics is sufficient. This represents an advantage over numerical simulations where numerical dissipation and dispersion cannot be avoided. However, the MoC breaks down when the flow is decelerated to sonic or subsonic velocities, which can occur in this problem due to the chemical energy release or a very steep oblique shock wave.

The derivation of the procedure used in the MoC program closely follows the method outlined in Zucrow and Hoffman [132]. The MoC is applied to steady, two-dimensional rotational isentropic flow, which implies that the entropy is constant along any streamline, but can vary from one streamline to another. The governing equations are given by:

$$\frac{\partial}{\partial x}\begin{bmatrix} \rho u \\ \rho u^2 + p \\ \rho u v \\ (\rho e + p)\, u \\ \rho Z u \end{bmatrix} + \frac{\partial}{\partial y}\begin{bmatrix} \rho v \\ \rho u v \\ \rho v^2 + p \\ (\rho e + p)\, v \\ \rho Z v \end{bmatrix} = \begin{bmatrix} 0 \\ 0 \\ 0 \\ 0 \\ \sigma \end{bmatrix} \tag{6.5}$$

This set of partial differential equations are manipulated with the equation of state (Eq. 6.3) to obtain their characteristic form. The compatibility equations (or total differential equations) to be solved along the streamlines are:

$$dp + \rho U dU = 0 \tag{6.6}$$

$$dp - a^2 d\rho = \frac{\psi}{u} dx \tag{6.7}$$

$$\rho u dZ = \sigma dx \tag{6.8}$$

where a is the speed of sound, U is the magnitude of the velocity and $\psi = -Q\,(\gamma - 1)\,\sigma$. The compatibility equation to solve along the right-running characteristic C$^-$ and the left-running characteristic C$^+$ (or equivalently along the Mach lines) is:

$$\frac{\sqrt{M^2-1}}{\rho U^2} dp_\pm \pm d\theta_\pm + \left[\frac{\mu \sin\theta}{yM} - \frac{\psi}{\rho U^2 a}\right] \frac{dx_\pm}{\cos\left(\theta \pm \alpha\right)} = 0 \tag{6.9}$$

In this equation, the ± sign is positive along C$^+$ and negative along C$^-$. M represents the Mach number, θ the flow angle with respect to the x axis, μ the problem symmetry ($\mu = 0, 1$ for the rectangular and axisymmetric configuration, respectively) and $\alpha = \sin^{-1}\left(1/M\right)$ the Mach angle. Note that the velocity components u and v from the set of equations 6.5 were transformed into the velocity magnitude U and the flow angle θ. In addition to the total differential equations to be solved for along the streamlines and the C$^+$ and C$^-$ characteristics, their trajectory needs to be solved to construct the characteristic network. The slope of the streamlines is:

$$\Lambda = \frac{u}{v} = \tan\theta \tag{6.10}$$

and the slope of the characteristics is:

$$\Lambda = \tan\left(\theta \pm \alpha\right) \tag{6.11}$$

As explained in Zucrow and Hoffman, there are different methods to build the characteristic network in the domain of interest. A common method is to solve the flow conditions at the intersection of the C^- and C^+ characteristics. The streamline characteristic is extended backward from the solution point and the flow conditions are determined by interpolation between previously calculated characteristics. However, when the chemistry is included in the system, Eq. 6.8 can be very stiff and even a small error in the interpolation of the species concentration can lead to a significant deviation of the solution from the true one. To avoid such problems, the flow conditions are solved at the intersection of the C^+ characteristics with the streamlines and the C^- characteristics are extended backward. By doing so, interpolation on the reaction progress variable Z is avoided, which stabilizes the integration procedure. The total differential equations are integrated using a modified Euler predictor-corrector method.

As shown in the schematic of an ODW initiation (Fig 5–3), the chemical length scale on the wedge can be orders of magnitude larger than that in the ODW structure. It is therefore necessary to increase the number of characteristics (i.e., the spatial resolution) in the regions of short induction distance. The MoC program is capable of automatically doubling the number of characteristics in a recursive method based on a specified number of points per half-reaction length. The user can set this criterion along any streamline behind the oblique shock and at the tip of the wedge along its surface. Also, for the simulations with finite wedges, the characteristic network coarsens at increasing distance from the wedge corner. The refinement method also doubles the number of characteristics anywhere in the flowfield if the distance between two characteristics exceeds a value specified by the user. For the simulations presented in this chapter, the specified value is $10\eta_{tip}$, where η_{tip} is the distance between two characteristics at the tip of the wedge (where the simulation is initialized). This distance is defined as $\eta_{tip} = \Delta_{hrl}/n$, where Δ_{hrl} is the half-reaction length of a CJ detonation and n is the number of characteristics per half-reaction length. The parameter n was used to evaluate the sensitivity of the characteristic density on the results. This parameter was set to 20 unless a higher value was required. A typical simulation size varies between 1 and 5 million calculation points.

6.2 Planar Blast and Planar Piston Initiation

6.2.1 Non-Reactive Simulations

In this section, the decay of a non-reactive blast wave triggered by an instantaneous energy release or a piston is investigated. A schematic of the two problems is given in Fig. 6–2 for the planar geometry. For the case of a planar blast initiation, the energy is released instantaneously on a plane. Strong planar shock waves then decay as they propagate away from the plane of symmetry. For the case of planar piston initiation, the strong shocks are triggered by a piston expanding at a constant velocity until the final position R_p is reached. Rarefaction waves then propagate from the piston face to the planar blast, which starts to decay. The decay of the blast wave in the two configurations will be compared with numerical simulations.

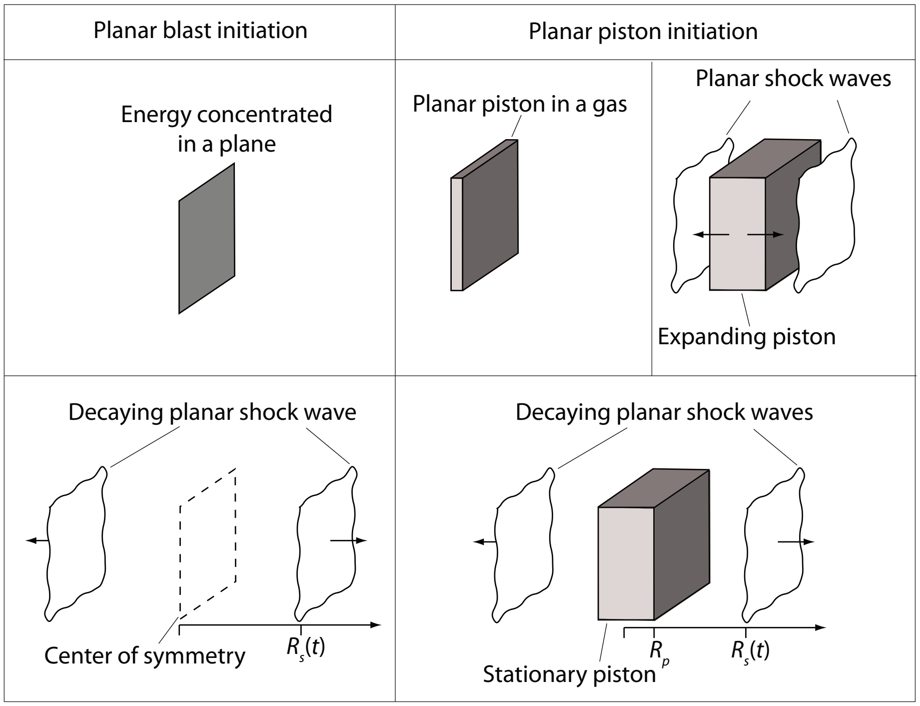

Figure 6–2: Schematic illustrating planar shock waves triggered by a planar blast and a planar piston

The non-reactive simulations were performed as follows. The same parameters as the reactive cases were used (Eqs. 6.4) with the exception of the reaction progress variable. The non-reactive simulations were initialized with $Z = 0$ everywhere in the numerical domain. Therefore, the scaling factor k is the same in both non-reactive and reactive simulations, using Δ_{hrl} (the half-reaction length) as the reference length scale for normalization.

The decay of a non-reactive blast wave triggered by an instantaneous energy release from a source can be solved analytically using a similarity solution. The complete derivation can be found in the original work of Taylor [116] and Sedov [105] and only the key results are given here. The flow conditions behind the blast wave are expressed as:

$$u_s = \frac{2}{\gamma+1}M_s, \qquad p_s = \frac{2}{\gamma+1}M_s^2, \qquad \rho_s = \frac{\gamma+1}{\gamma-1} \tag{6.12}$$

$$\frac{u}{u_s} = f\left(\frac{r}{R_s}\right), \qquad \frac{\rho}{\rho_s} = g\left(\frac{r}{R_s}\right), \qquad \frac{p}{p_s} = f\left(\frac{r}{R_s}\right) \tag{6.13}$$

where subscript s refers to the post-shock condition. M_s and R_s are the shock Mach number and distance from the initiation location, respectively. The velocity, density and pressure profiles behind the blast are a function of the non-dimensional distance from the shock (r/R_s) only. These profiles can be found in the book by Korobeinikov [62]. The evolution of the shock strength as it decays can be expressed as a function of the source energy as follows:

$$M_s^2 = \left(\frac{2}{j+3}\right)^2 \frac{E_s}{\alpha_j \gamma R_s^{j+1}} \tag{6.14}$$

where j accounts for the geometry ($j = 0, 1$ and 2 for the planar, cylindrical and spherical geometries, respectively) and the source energy is normalized as $E_s = \tilde{E}_s / \left(\tilde{p}_o \tilde{\Delta}_{hrl}^{j+1}\right)$. Relations for the energy integral α_j are given in Korobeinikov [62]. For the planar geometry, this parameter is $\alpha_0 = 2.257$.

The relation 6.14 is plotted in Fig. 6–3 for the planar geometry and for a non-dimensional source energy per unit area of $E_s = 1625$. Also shown in this figure is a numerical simulation of the same value of source energy. The simulation was initialized with the similarity solution behind the shock (Eqs. 6.13), a shock location

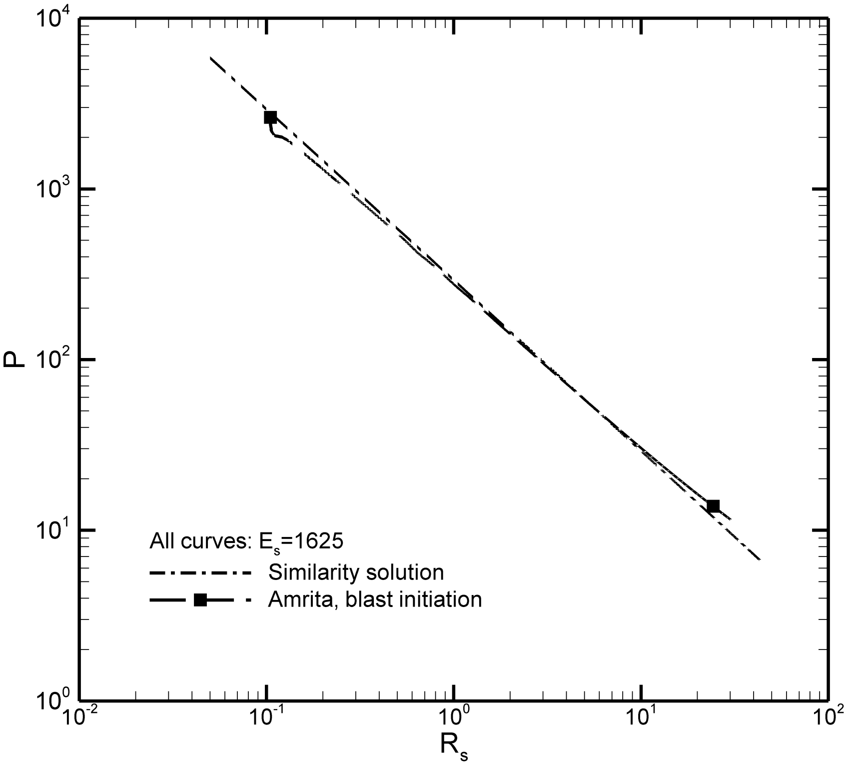

Figure 6–3: Similarity solution and numerical simulation of a shock decay triggered by a planar blast

of $R_s = 0.107$ and a shock strength of $M_s = 50$. The numerical simulation follows closely the analytical result until the blast has decayed to a shock pressure of about 20, which corresponds to a shock Mach number of about 4. The numerical result starts to deviate from the analytical one because the strong shock relations (Eq. 6.12) are no longer valid.

While the decay of the shock depends only on the source energy in the blast initiation problem, it also depends on the piston strength and final position in the piston-driven problem. The energy liberated from the piston is the total work done to the gas, or $E_s = p_s R_p$, where p_s is the post shock pressure and R_p is the final position of the piston. In the simulations presented next, the strength of the piston is varied (thus varying p_s) and the final position R_p is adjusted to keep the energy constant at $E_s = 1625$. Figure 6–4 shows three different profiles associated with various piston Mach numbers. For the weakest piston ($M_{s,o} = 7.3$), the final position is $R_p = 30.7$ half-reaction lengths away from the plane of symmetry. The shock pressure during its decay is significantly greater than that of the blast initiation (about twice greater). As the strength of the piston increases, the final position is moved closer to the plane of symmetry. For a piston Mach number of $M_{s,o} = 50.2$, the final position is only

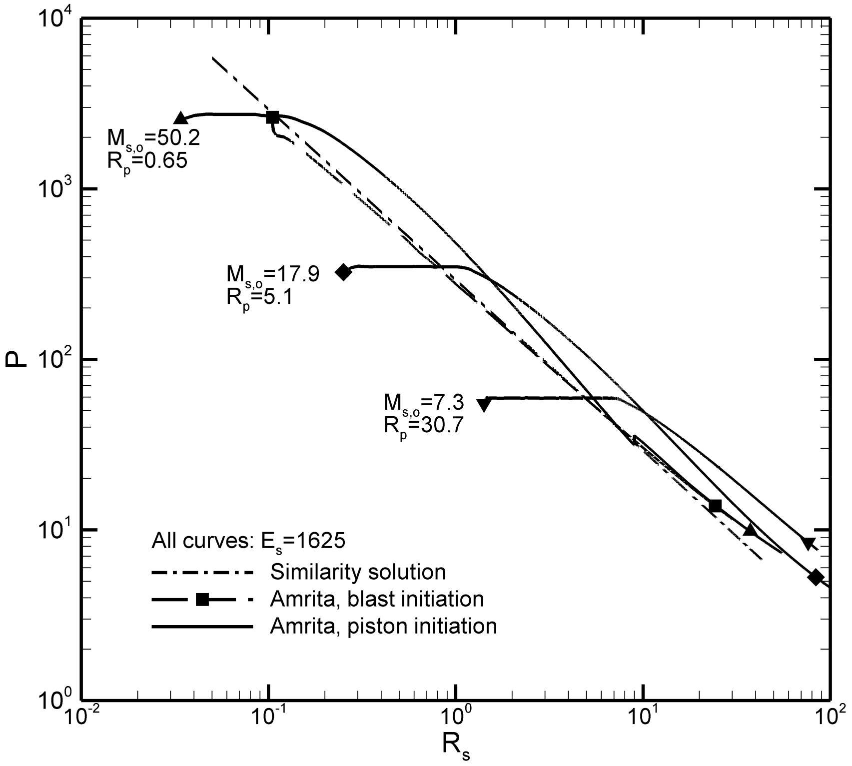

Figure 6–4: Numerical simulations of a shock decay triggered by a planar piston

$R_p = 0.65$ half-reaction length. The shock pressure profile associated with this case follows relatively well that of the planar blast initiation. The slope of the profile is similar in both cases and the two curves merge at a pressure of about 50. At the limit of an infinitely strong piston, its final position would tend to zero and the shock decay would follow exactly that of a planar blast. Therefore, the profiles shown in Fig. 6–4 provide a quantitative evaluation of the difference between a finite piston strength and an ideal blast initiation. It can be concluded that an initial shock Mach number of at least $M_{s,o} = 50$ is required to treat the two problems as equivalent.

6.2.2 Reactive Simulations

As introduced in Section 5.1.1, there are two possible outcomes when a strong blast propagates in a reactive medium: the subcritical and supercritical regimes. The pressure profiles associated with these two regimes are presented in Fig. 6–5. The dashed line refers to the shock pressure of a CJ detonation. Also shown in this figure is a critical shock pressure profile. In this case, the shock pressure decreases to sub-CJ values, remains relatively constant in the quasi-steady state, increases suddenly at the onset of a detonation and relaxes to the CJ value in the farfield. From such a critical profile, the initiation distance parameter δ is defined as the location where the pressure crosses the CJ value during the reacceleration process ($\delta = 215$ in Fig. 6–5). The relation between the initiation distance and different values of source energies is displayed in Fig. 6–6. For a source energy larger than 1 800, the onset of detonation occurs at roughly the same location ($\delta \approx 80$). As the source energy decreases below a value of 1 800, the initiation distance starts to increase exponentially. From such a trend, it is possible to determine a critical energy

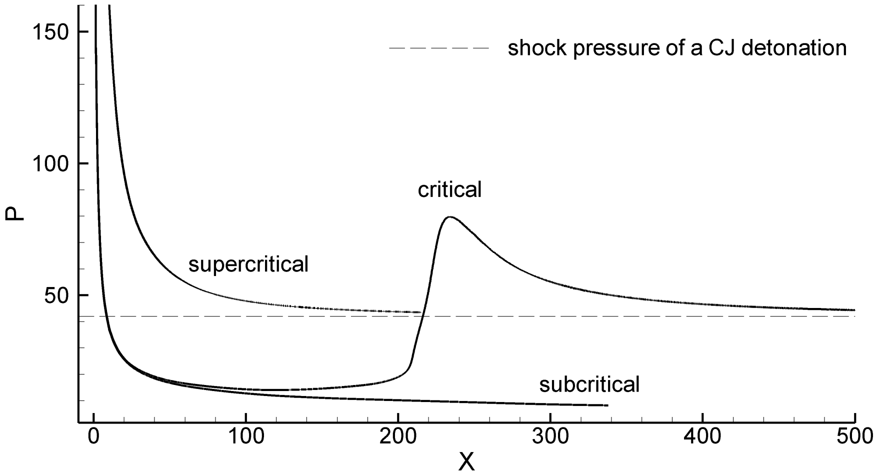

Figure 6–5: Evolution of the shock pressure showing the three regimes of detonation initation when a shock propagating in a reactive gas

for detonation initiation. It is important to note that since the chemistry is modeled by a single-step irreversible reaction, this reaction always proceeds to completion even for very low gas temperatures. Therefore, even for $E_s < 1\,400$, the gas will react if one considers a sufficiently long domain. It can thus be argued that a critical energy cannot be unambiguously defined for this system. However, for the purpose of this investigation, it is sufficient to seek the range of energy values that induces an exponentially increasing initiation distance, as it is shown in Fig. 6–6.

Similar trends between the initiation distance and the source energy were observed for the planar piston problem. However, in this case the critical energy depends on the strength of the piston M_p, or equivalently on the initial shock strength $M_{s,o}$. Figure 6–7 presents the critical energy as a function of the initial shock strength for the planar blast and planar piston problems. For a weak initial shock ($M_{s,o} = 6.6$), $E_{critical}$ for the planar piston is much smaller than the value of the planar blast. As

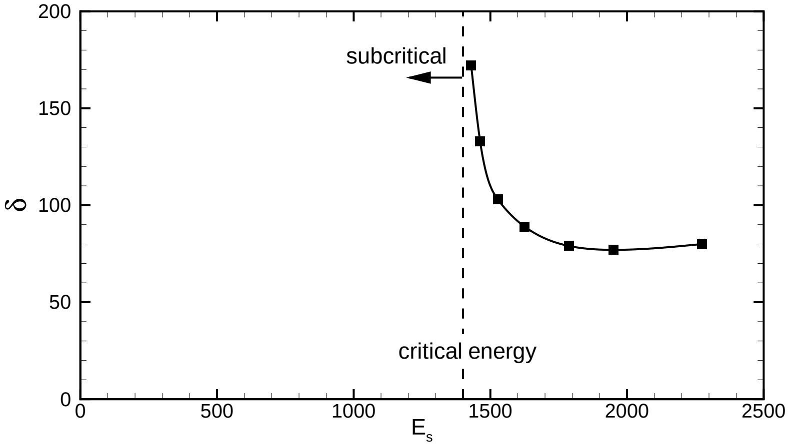

Figure 6–6: Relation between the initiation distance and the source energy for the case of blast initiation of a detonation

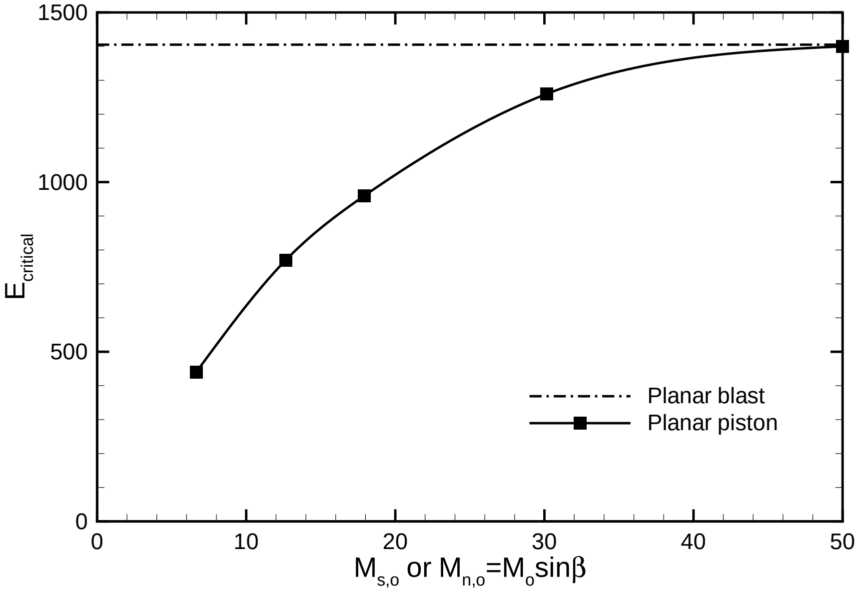

Figure 6–7: Critical energy for detonation initiation by a planar blast and a planar piston for different values of initial Mach number

the strength of the piston increases, $E_{critical}$ approaches the planar blast critical energy. For an initial shock Mach number of $M_{s,o} = 50$, the two problems give the same critical energy for detonation initiation. It can thus be concluded that in order for the two initiation methods to be equivalent, the strength of the piston needs to be such that the initial shock Mach number is larger than 50. This is in agreement with the observations related to the non-reactive simulations (with respect to Fig. 6–4).

6.3 Initiation by a Two-Dimensional Wedge

A Method of Characteristics (MoC) program was used to simulate hypersonic reactive flows over wedges. This program was validated against different test problems. For a well-established overdriven ODW, the detonation angle given by the MoC program agreed very well with the detonation angle calculated with the conservation laws (or detonation polars). Furthermore, the formation of an ODW was validated against Computational Fluid Dynamics (CFD) by comparing the shock trajectory. Chapter 7 presents these validations in detail, in addition to simulations of reacting flows over semi-infinite wedges and cones.

For the simulations presented in this section, finite wedges are considered. Simulations of reacting flows over finite wedges provide a means to determine critical conditions for oblique detonation initiation. The expansion waves emanating from the corner of the wedge constitute a quenching mechanism that competes with the chemical exothermic reactions. The expansion (or rarefaction) waves tend to weaken the shock to a Mach wave in the farfield and the chemical energy release tends to steepen the oblique shock to a CJ ODW angle. In a subcritical case (where the expansion waves dominate the chemical energy release), the chemical reactions are turned off and the oblique shock decays to a Mach wave in the farfield. In a supercritical case (where the chemical energy release dominates the expansion waves), an overdriven ODW generated by the wedge weakens to a CJ ODW in the farfield. In this case, the expansion waves are unable to quench the chemical reactions behind the shock. A more interesting and complex case occurs when both terms are equally important; this is a critical case. Therefore, the goal of the next MoC simulations is to determine the critical conditions for detonation initiation from finite wedges. These results will also be compared to the case of critical detonation initiation from a planar piston and a planar blast. This comparison will allow the determination of the conditions for which the Lee-Vasiljev model is valid.

Figure 6–8 shows a schematic of the problem setup. The parameters U_o, ϕ and h are the freestream velocity, wedge angle and wedge height, respectively. The flow conditions are normalized with the freestream pressure $\tilde{p_o}$ and density $\tilde{\rho_o}$. The tilde sign (˜) refers to a dimensional quantity. The non-dimensional variables are defined as:

$$p = \frac{\tilde{p}}{\tilde{p_o}}, \qquad \rho = \frac{\tilde{\rho}}{\tilde{\rho_o}}, \qquad U = \tilde{U}\sqrt{\frac{\tilde{\rho_o}}{\gamma \tilde{p_o}}} = \frac{\tilde{U}}{\tilde{a_o}}, \qquad a = \sqrt{\frac{\gamma p}{\rho}},$$

$$u = U\cos\theta, \qquad v = U\sin\theta, \qquad M = \frac{U}{a}$$

The freestream conditions are set as:

$$p_o = 1, \quad \rho_o = 1, \quad u_o = 22.8, \quad v_o = 0, \quad Z_o = 1 \tag{6.15}$$

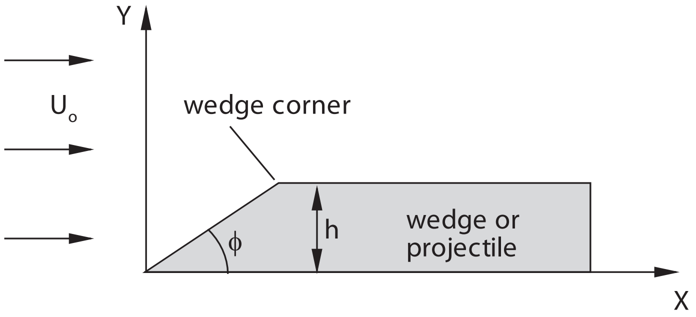

Figure 6–8: Problem schematic for the MoC simulations with finite wedges

The freestream velocity u_o corresponds to the freestream Mach number, which is considerably larger than what is generally encountered in real experiments. The motivation for choosing such a high freestream velocity will become clear at the end of this chapter.

Figure 6–9 presents the flowfield for a subcritical case (where the expansion waves quench reaction and cause failure to initiate an ODW). The wedge is shown at the bottom left of the graph at $X < 110$ and $Y < 3.5$. The contours of the reaction progress variable are shown with the reactant in white and the product in black. Decoupling between the reaction front and the shock front is clearly shown. The calculation domain is bounded by the shock front and the last C^+ characteristic. For all simulations, the domain of interest is limited to $X \leq 1000$. A supercritical case is illustrated in Fig. 6–10. In this case, coupling between the reaction front and the oblique shock (hence the onset of an ODW) occurs at approximately $X = 150$. A self-supported ODW extends in the farfield. A critical case is presented in Fig. 6–11. The reaction front decouples from the oblique shock and reaccelerates at approximately $X = 350$ to trigger the initiation of an ODW far from the wedge.

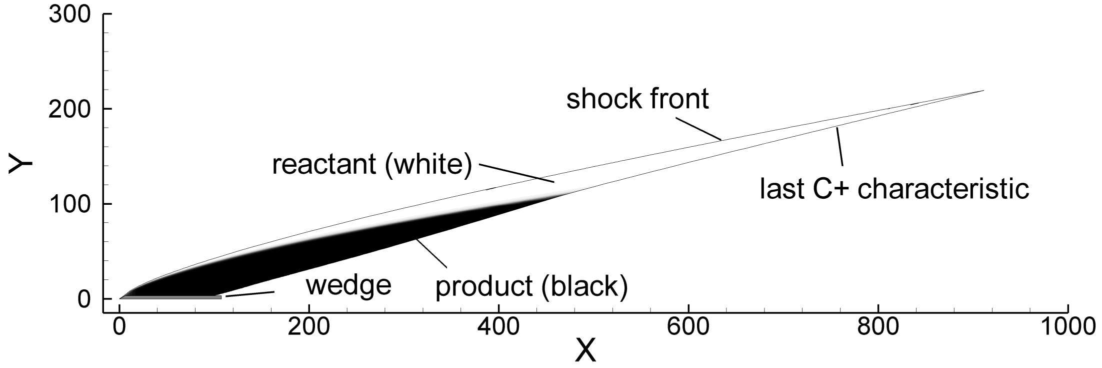

Figure 6–9: Contours of the reaction progress variable for a subcritical case

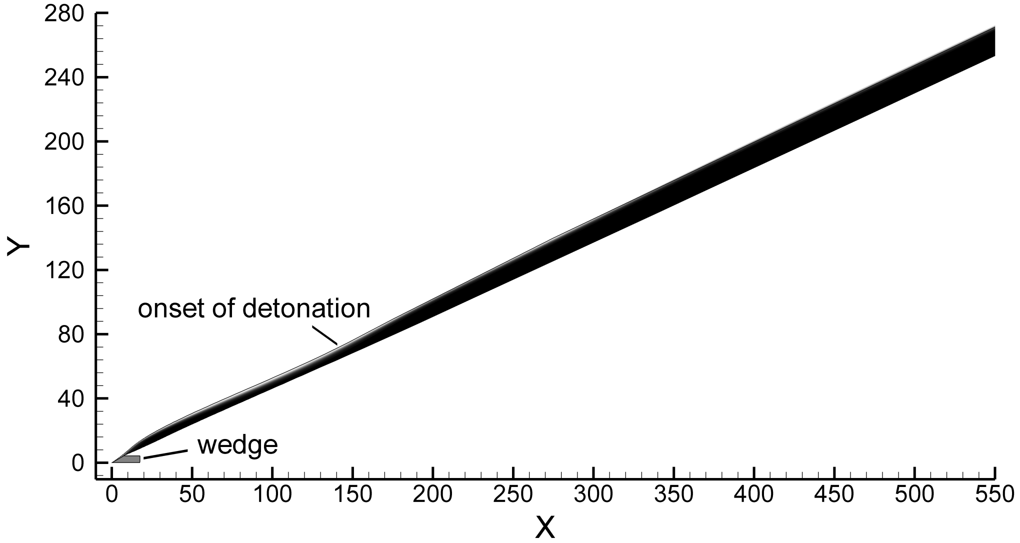

Figure 6–10: Contours of the reaction progress variable for a supercritical case

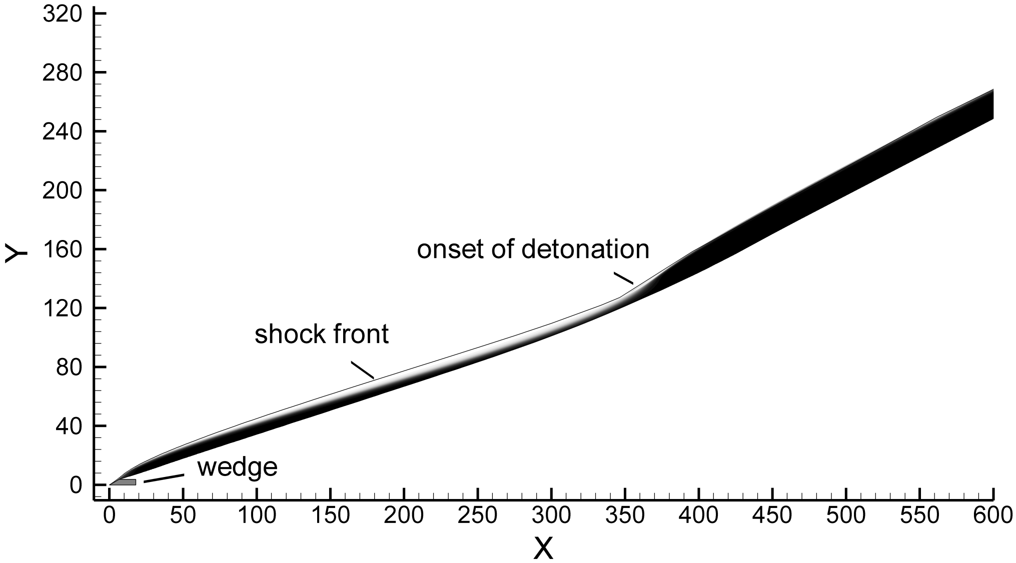

Figure 6–11: Contours of the reaction progress variable for a critical case

The evolution of the wave angle for the three initiation regimes is shown in Fig. 6–12. The corner of the wedge is located at approximately $X = 8$. For $0 < X < 8$, the wave angle increases due to the formation of an overdriven ODW in front of the wedge. The expansion waves interact with the ODW for $X > 8$. In the subcritical case, the shock angle monotonically decays. In the supercritical case, the wave angle decays to about 2° lower than the CJ ODW angle and increases back to this value. In the critical case, the shock decays to an angle 9° lower than the CJ value and sharply increases at the initiation location. These three cases are qualitatively similar to the three regimes observed in blast or piston initiation of a detonation (see Fig. 6–5). The initiation distance is defined as the distance from the source ($Y = 0$) to the location where the wave angle crosses the CJ value on the reacceleration process. In

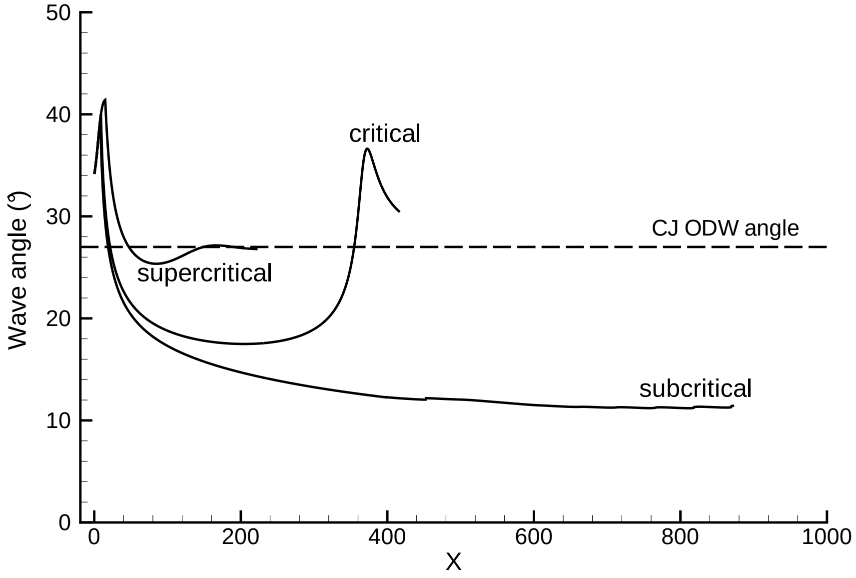

Figure 6–12: Evolution of the wave angle for subcritical, critical and supercritical regimes

the critical regime of Fig. 6–12, this process occurs at $X = 350$. This corresponds to a vertical location and initiation distance of $Y = \delta = 131$ (see Fig. 6–11).

The energy deposited by the source (a 2D wedge in this case) is the amount of work done to the gas. Since the planar configuration is considered, the energy per unit area is given by the pressure drag $E_s = D = 2p_sh$ where p_s is the pressure behind the inert oblique shock attached to the wedge. The factor 2 in this relation accounts for the fact that only half of the domain is simulated (see Fig. 6–8). The relation between the initiation and the source energy is shown in Fig. 6–13. In this figure, the wedge angle is $\phi = 25°$ and the energy is varied by changing the wedge height from 2.75 to 6 half-reaction lengths. It can be observed that, similar to the

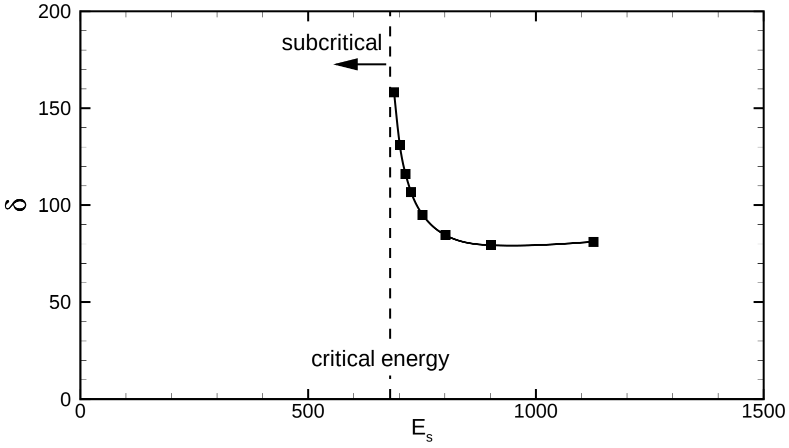

Figure 6–13: Relation between the initiation distance and the source energy for a 2D wedge, $\phi = 25°$

blast and piston initiation problems, the initiation distance increases exponentially as the critical energy is approached.

The critical energy was determined for wedge angles in the range $15° \leq \phi \leq 45°$. These results are displayed in Fig. 6–14 with the planar blast and planar piston results shown previously. For the 2D wedge results, the critical energy is related to the Mach number normal to the inert oblique shock attached to the wedge $M_{n,o} = M_o \sin\beta$ where β is the shock angle. For wedge angles between 15° and 25°, the critical energy for detonation initiation from a 2D wedge is very close to the results of the planar piston. This shows that the two problems are equivalent and the two requirements for the hypersonic equivalence principles are fulfilled (a freestream Mach number much larger than one and small deflection angles in the flowfield). For wedge angles larger than 30°, the deflection angles become important and the two trends start to deviate. The hypersonic equivalence principle thus breaks down for $\phi > 30°$.

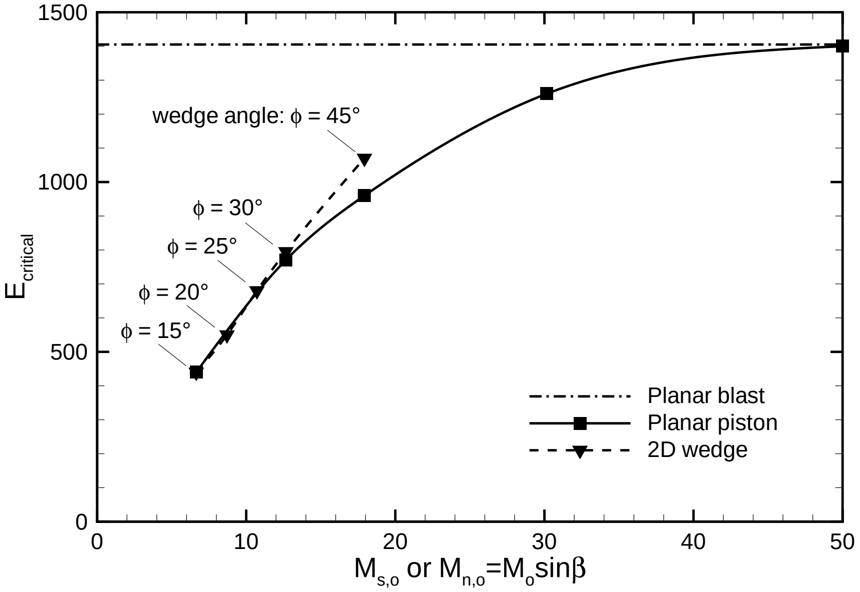

Figure 6–14: Critical energy for detonation initiation by a planar blast, a planar piston and a 2D wedge for different values of initial Mach number or Mach number normal to the oblique shock

Figure 6–14 indicates the conditions that are necessary in order for the 2D wedge to be equivalent to a planar blast initiation of a detonation. The wedge angle needs to be lower than 30° for the hypersonic equivalence principle to be valid and the Mach number normal to the oblique shock needs to be larger than 50 in order for the energy to be released effectively instantaneously. These two requirements are displayed in Fig. 6–15 relating the freestream Mach number to the wedge angle. This schematic shows the quantitative requirements in order for a detonation initiation event by a projectile to be equivalent to a blast initiation of a detonation event. These requirements result in very low projectile nose angles (smaller than 30°) and very large Mach numbers (greater than 100). These velocities are much larger than

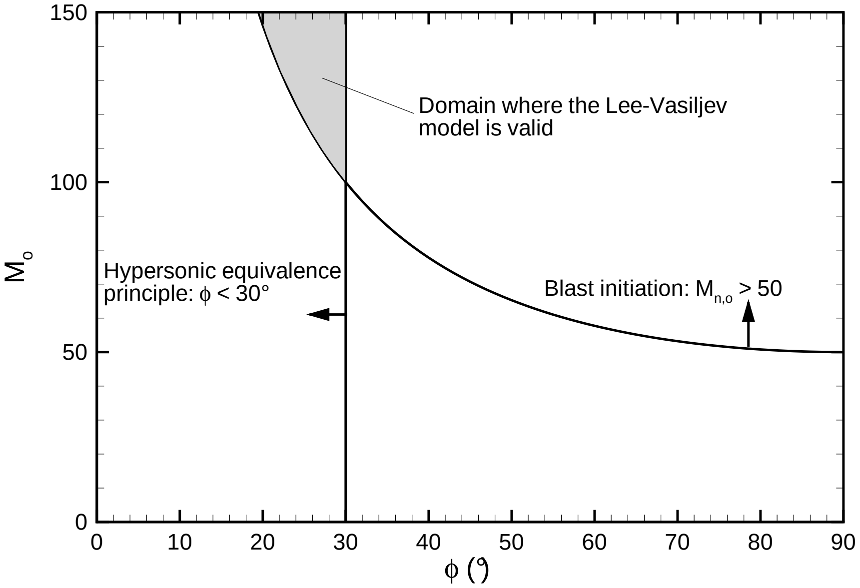

Figure 6–15: Domain of validity for the Lee-Vasiljev model

what is typically realized in experiments. Therefore, the good agreement obtained in Section 5.1.3 by equating the projectile drag to the critical energy of initiation in order to predict the experimental initiation of detonation by a projectile should be regarded as fortuitous and only qualitative in nature.

CHAPTER 7
Method of Characteristics — Supercritical Oblique and Conical Detonation Structure

In Chapters 5 and 6, theoretical models and simulations were presented in order to address the main objective of this thesis: to determine critical conditions for oblique detonation initiation from hypersonic projectiles. In this chapter, phenomena related to supercritical (or overdriven) ODWs initiated from semi-infinite wedges and cones are investigated. In Section 7.1, a ZND analysis is presented and adapted to model the planar structure of a normal and oblique detonation. Section 7.2 describes the computational tool used to validate the results of the MoC program. Section 7.3 is divided into three subsections concerning the validation of the MoC program, steady overdriven oblique and conical detonations, and the effect of high activation energy on the detonation structure.

7.1 One Dimensional (ZND) Analysis

The structure of a detonation wave is by nature a complex three-dimensional interaction between gasdynamics and chemical energy release. A simplified one-dimensional detonation structure consists of a shock front that compresses a gaseous mixture, followed by chemical energy release that drives the shock. This concept is known as the Zel'dovich-von Neumann-Doering (ZND) model. A planar or laminar detonation structure equivalently refers to this model. By assuming a shock velocity, the flow conditions behind it (at the von Neumann state) are given by the normal shock relations. The conservation laws (Euler equations) coupled to a chemical kinetics model are then used to simulate the chemical energy release and its effect on the flow conditions, until chemical equilibrium is reached. In a coordinate system fixed to the shock front, the Euler equations for a multi-species mixture are expressed as:

$$
\begin{aligned}
&\frac{d}{dx}\left(\rho u\right) = 0\\
&\frac{d}{dx}\left(p + \rho u^2\right) = 0\\
&\frac{d}{dx}\left(h + \frac{u^2}{2}\right) = 0\\
&\frac{d}{dx}\left(\rho u Z_i\right) = \sigma_i
\end{aligned}
\tag{7.1}
$$

where p is the pressure, ρ is the density, u is the velocity, h is the enthalpy, Z_i is the mass fraction of species i and σ_i is its net production rate. After several manipulations (provided in Appendix C), this set of equations can be transformed into a system of total differential equations in the following manner:

$$
\begin{aligned}
&\frac{dp}{dx} = \frac{u\psi}{1 - M^2}\\
&\frac{d\rho}{dx} = \frac{\psi}{u\left(1 - M^2\right)}\\
&\frac{du}{dx} = \frac{-\psi}{\rho\left(1 - M^2\right)}\\
&\frac{dZ_i}{dx} = \frac{\sigma_i}{\rho u}
\end{aligned}
\tag{7.2}
$$

where

$$\psi = \sum_i \sigma_i \left(\frac{h_i}{c_p T} - \frac{W}{W_i} \right) \tag{7.3}$$

In the above set of differential equations, M is the Mach number, ψ is the thermicity term and W is the molecular weight of the mixture. In some cases, it is advantageous to model the chemistry as a single Arrhenius reaction in a calorically perfect, constant molecular weight gas in order to considerably reduce computational costs. In such a case, the set of differential equations 7.2 is still valid, with $Z_i = Z$ being the reaction progress variable from the reactant ($Z = 1$) to the product ($Z = 0$). Also, the net production rate is given by:

$$\sigma = -k\rho Z \exp\left(\frac{-E_a \rho}{p} \right) \tag{7.4}$$

and the thermicity by:

$$\psi = \frac{Q\,(\gamma - 1)\,\sigma}{a^2} \tag{7.5}$$

7.1.1 Normal Detonation Wave

An example is given below for a CJ laminar detonation structure traveling in a $2H_2$+O_2+7Ar mixture initially at 298 K and 20 kPa. The detailed reaction mechanism from Li et al. [73] was employed. The CJ velocity can be obtained either from the control volume formulation of the conservation equations at the upstream and downstream states (thus ignoring the structure) and assuming sonic velocity at the downstream state, or by integrating the ODE's that govern the structure and

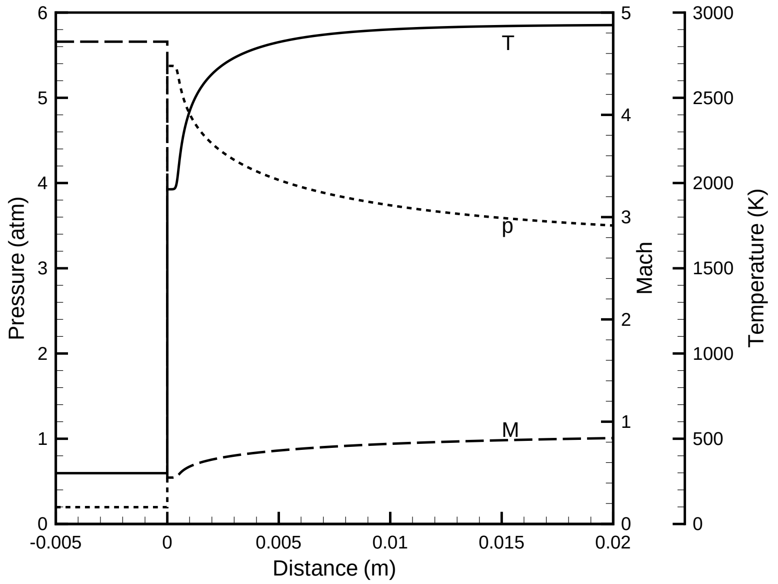

Figure 7–1: ZND detonation structure of a $2H_2$+O_2+7Ar mixture initially at 20 kPa and 298 K

decreasing the shock front velocity until the flow is equilibrium sonic at the downstream state. Figure 7–1 shows the temperature, pressure and Mach number profiles behind the shock front located at $x = 0$. In this calculation, the shock front velocity is 1647.9516 m/s and a slight decrease below this value (a decrease as small as 0.0001 m/s) produces a singularity (where the flow is sonic) in the detonation structure. The numerical result gives a post-detonation Mach number and velocity of 0.9167 and 924.29 m/s, respectively. The frozen sound speed at the same point is 1 008.6 m/s. The equilibrium sound speed can be obtained using, for example, the CEA code [82], giving 924.0 m/s. Therefore, the flow is equilibrium sonic at the end of the reaction zone and frozen subsonic throughout.

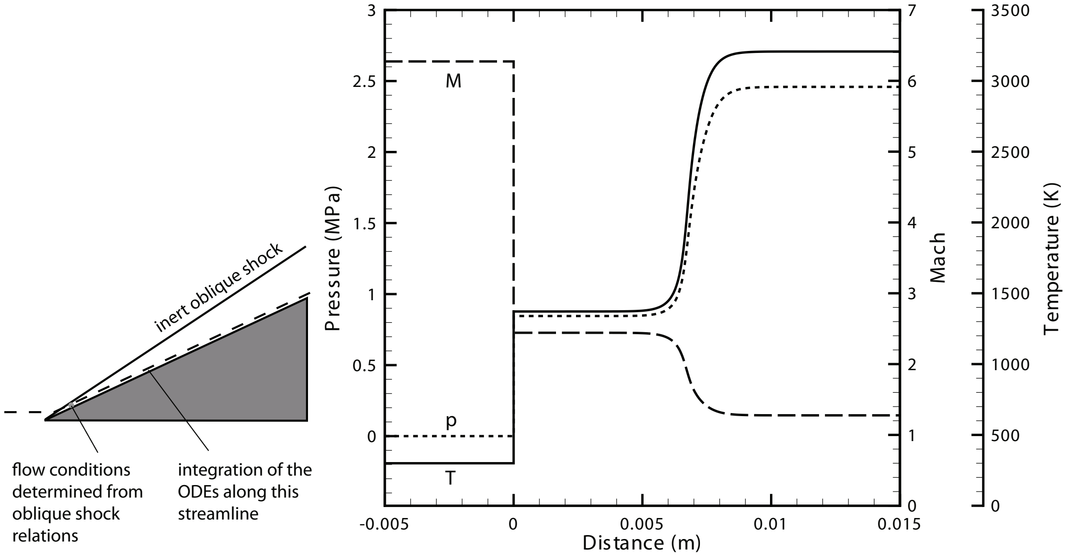

Figure 7–2: Profiles of the flow conditions where a fluid particle, from a $2H_2+O_2+7Ar$ mixture initially at 298 K, 50.7 kPa and 2 200 m/s, crosses a 33.6° oblique shock wave, corresponding to a wedge angle of 25°

7.1.2 Oblique Detonation Wave

A supersonic reactive flow that crosses an oblique shock wave generally remains supersonic behind it. The chemical energy release within such a flow causes it to decelerate in contrast to a normal detonation where the flow is accelerated behind the shock front. Figure 7–2 shows the pressure, temperature and Mach number of a fluid particle crossing an oblique shock. The streamline of this particle corresponds to the wall surface of the wedge (assuming an inviscid flow). The incoming $2H_2+O_2+7Ar$ mixture is at 298 K and 50.7 kPa. Its incoming velocity is 2 200 m/s and the mixture encounters a 25° wedge that produces a 33.6° oblique shock wave. The flow properties behind the shock are calculated from inert oblique shock relations, and the flow profiles are obtained from the integration of the set of ODEs, Eqs. 7.2, along

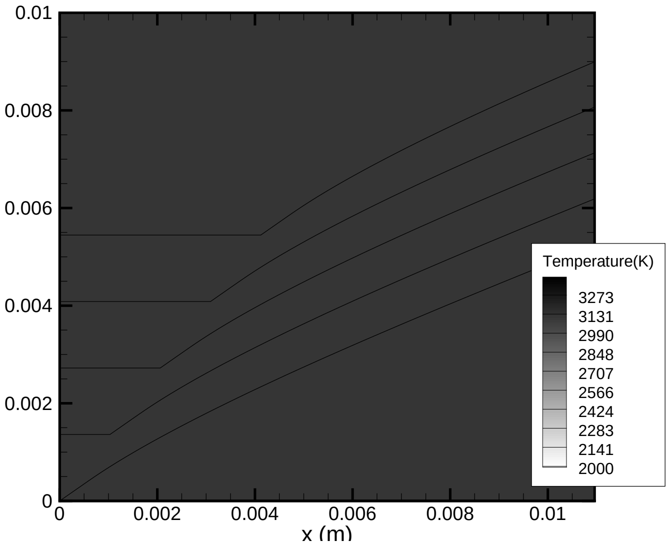

Figure 7–3: Laminar structure of an ODW. The mixture is $2H_2$+O_2+7Ar, the freestream conditions are 298 K, 50.7 kPa and 2 200 m/s and the detonation angle is 52.9° (corresponding to a wedge angle of 25°). The solid lines represent fluid particle streamlines.

the streamline. The Mach number profile shows that the flow downstream of the energy release zone is supersonic, with $M = 1.28$. The induction distance, defined as the distance between the shock and the location of maximum rate of heat release, is approximately 6.8 mm. This situation is referred to as oblique shock-induced combustion, as opposed to an oblique detonation wave, since the energy release is uncoupled from the oblique shock for this particular streamline (along the wedge surface). Far downstream of the wedge, the combustion front eventually couples with the oblique shock to form an ODW.

An example of an ODW inclined at 52.9° is shown in Fig. 7–3. The contours represent the temperature and the solid lines the streamlines. This figure was produced by calculating the ZND structure of a normal detonation (as shown in Fig. 7–1), rotating the reference frame such that the incoming velocity is perpendicular to the ODW and adding a constant tangential velocity. It is assumed that the chemical energy release only increases the velocity component normal to the ODW, which is valid if the ODW is straight. This hypothesis will be validated in Section 7.3.2 with two-dimensional simulations. At the chemical equilibrium state, the flow angle has decreased to 25°, which corresponds to the wedge angle. The induction distance behind the shock front (and perpendicular to it) is approximately 0.39 mm.

Note that the same freestream conditions and wedge angle were considered in Figs. 7–2 and 7–3. Therefore, one can observe the difference in the induction distance between the cases of oblique-shock-induced combustion at the tip of the wedge (6.8 mm) and an oblique detonation wave far from the tip of the wedge (0.39 mm). Hence, once the combustion front is coupled with the oblique shock, the induction distance is considerably decreased and the angle of the shock front is increased.

7.1.3 Polars

There is a range of wedge angles for which an ODW will attach to it. For a wedge angle larger than a certain value, a normal detonation is formed ahead of the wedge tip. There is also a minimum wedge angle that corresponds to a CJ ODW, i.e., for which the velocity component normal to the ODW is equal to the CJ velocity of the mixture. Detonation polars graphically represent the different ODW configurations by relating the wedge angle with the angle of the ODW. From the calculations that led to the contours and streamlines of Fig. 7–3, it is possible to obtain the ODW angle for different values of wedge angle, in order to produce detonation polars. Figure 7–4 presents ODW polars for a $2H_2+O_2+7Ar$ mixture initially at 298 K and 1 atm. The

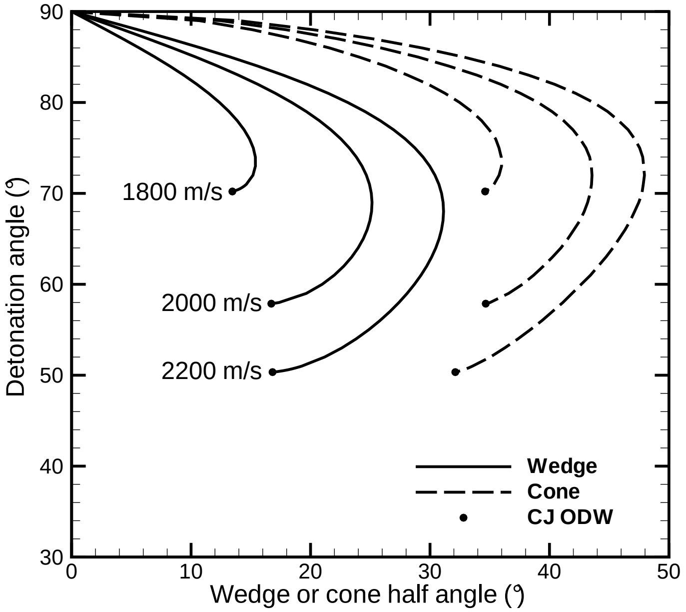

Figure 7–4: ODW polars for the $2H_2+O_2+7Ar$ mixture at 1 atm and 298 K

results are shown for different freestream velocities (1 800, 2 000 and 2 200 m/s) and for a wedge and a cone. For a freestream velocity of 2 200 m/s, the wedge angle that provides a CJ ODW is 16.8°, whereas the wedge angle at which the detonation wave becomes detached is 31.1°. There is also a solution for very steep ODWs (from ≈ 75° to 90°). These ODWs are equivalent to strong shock waves and are thus called strong ODWs. They are generally not observed experimentally. For slower velocities, the range of wedge angles that produces an attached ODW decreases. A wedge angle smaller than the CJ ODW wedge angle does not necessarily imply that it cannot initiate an ODW. As long as an expansion wave (called a Prandtl-Meyer wave) follows behind the end of the detonation reaction zone, the ODW will be stabilized at the CJ angle.

An ODW can also be attached to a cone. In principle, the structure of the ODW can be altered by its curvature around the axis of symmetry. This aspect will be considered in Section 7.3.2. In this simplified analysis, the ODW structure in a conical flow is assumed to be identical to that in a rectangular 2D flow. This assumption is valid far from the axis of symmetry where the curvature of the front is negligible. However, between the end of the ODW reaction zone and the cone surface, there is a third dimensional effect that permits the flow of detonation products to "expand", resulting in a steeper cone angle compared to a wedge for the same ODW angle. Figure 7–4 shows this difference with the dashed lines.

7.1.4 Comparison of the Detonation Angles with Experiments

In Section 4.2, the complete set of experimental results was presented and five combustion regimes were differentiated. For the cases where a prompt ODW is observed, the ODW angle in front of the cone can be measured experimentally and compared with the polar graph (Fig. 7–4). Referring to Fig. 4–7, Shots 140, 164 and 166 initiated a prompt ODW. For these three experiments, the cone half angle is smaller than the turning angle required for a CJ ODW (see the polar in Fig. 7–4). These flowfields are thus interpreted as a CJ ODW attached at the cone tip, followed by an expansion wave (a Prandtl-Meyer wave) between the end of the ODW reaction zone and the cone surface. An attached overdriven ODW is only observed for Shots 146 and 170. Table 7–1 presents a comparison between the ODW angle measured experimentally (taking the average angle of above and below the projectile) and obtained from the detonation polar. For Shot 146, the detonation polar gives an ODW angle 8° steeper than observed from the photograph. According to the flow conditions of Shot 170, the cone angle is theoretically steeper than the maximum cone angle at which an ODW can be attached, but an ODW angle of 67° was observed from the experiment. The discrepancy between the experimental and theoretical angles is possibly attributed to the front curvature of the detonation around the flight axis, which will be discussed in Section 7.3.2. For Shots 130 and 160, a bow-like (detached) detonation wave was observed from the photographs and is also predicted from the detonation polar.

Table 7–1: ODW angle from experiments and polars

Shot	Proj. vel.	Cone half angle	ODW angle (experiments)	ODW angle (polars)
146	2 180 m/s	40°	56°	64°
170	1 830 m/s	45°	67°	detached

7.2 CFD Method with Amrita

In order to validate the results from the MoC program presented in the next section, numerical simulations were conducted with the Amrita environment developed by Quirk [96]. This program solves the *unsteady* reactive Euler equations given by:

$$\frac{\partial}{\partial t}\begin{bmatrix}\rho\\ \rho u\\ \rho v\\ \rho e\\ \rho Z\end{bmatrix}+\frac{\partial}{\partial x}\begin{bmatrix}\rho u\\ \rho u^2+p\\ \rho uv\\ (\rho e+p)\,u\\ \rho Z u\end{bmatrix}+\frac{\partial}{\partial y}\begin{bmatrix}\rho v\\ \rho uv\\ \rho v^2+p\\ (\rho e+p)\,v\\ \rho Z v\end{bmatrix}=\begin{bmatrix}0\\ 0\\ 0\\ 0\\ \sigma\end{bmatrix} \tag{7.6}$$

Equations 6.2 and 6.3 are also used. Amrita employs a hierarchical system of mesh patches according to a mesh refinement scheme defined by the user. The coarsest mesh, which covers the entire numerical domain, is set such that there is one grid point per half-reaction length. Mesh refinement is automatically applied at the locations of steep gradients in the flow properties to correctly resolve the flowfield. The most refined grid level corresponds to 64 grid points per half-reaction length. The Lax-Friedrichs solver is used to evaluate the fluxes in the Euler equations. The complete numerical domain is initialized with the freestream values and the flow features evolve to their steady state by marching in time.

7.3 Method of Characteristics — Semi-Infinite Wedges and Cones

In this section, the MoC program, described in Section 6.1.2, was used to simulate reactive flows encountering semi-infinite wedges and cones. The purpose of these simulations is to validate the program, explore the formation process of an ODW, and determine the effect of the detonation front curvature (around the axis of symmetry) on its initiation and steady-state angle.

Figure 7–5 shows the boundary conditions for the semi-infinite wedge simulations. The horizontal wedge surface was employed. Figure 7–6 presents the problem setup for the simulations with semi-infinite cones.

The freestream conditions are set to:

$$p_o = 1, \qquad \rho_o = 1, \qquad u_o = 8\cos\phi, \qquad v_o = 8\sin\phi, \qquad Z_o = 1 \tag{7.7}$$

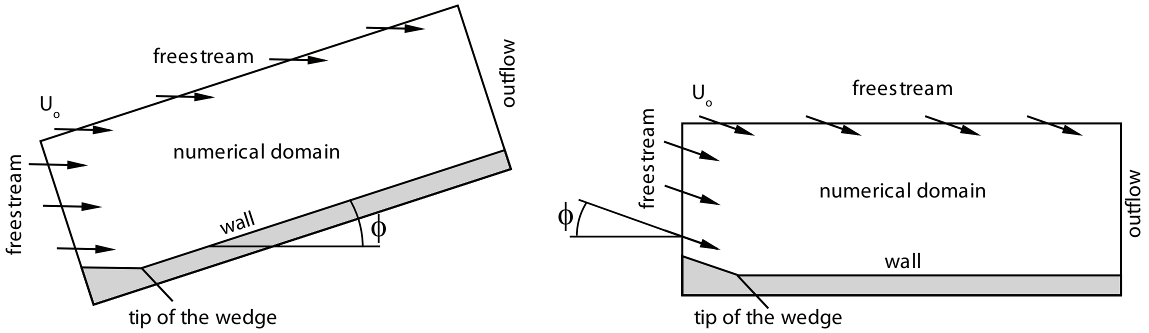

Figure 7–5: Numerical domain and boundary conditions for semi-infinite wedges (horizontal freestream direction on the left and horizontal wedge surface on the right)

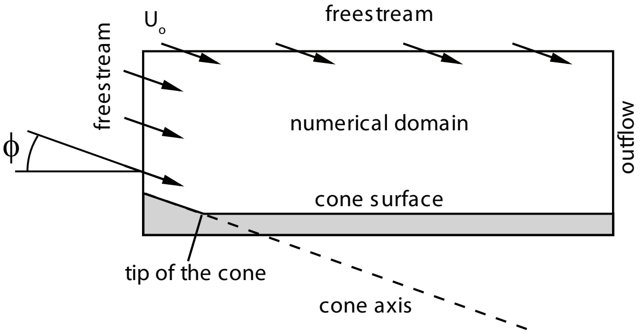

Figure 7–6: Numerical domain and boundary conditions for semi-infinite cones (horizontal cone surface)

The chemistry parameters for the next simulations are:

$$\gamma = 1.3, \qquad Q = 10, \qquad E_a = 10, 20, 25, 30 \tag{7.8}$$

The two varied parameters are the angle of the freestream (or equivalently the wedge or cone angle) and the activation energy. In Section 7.3.1, a baseline case is considered to validate the results from the MoC program with CFD simulations using Amrita. In Section 7.3.2, simulations with a low activation energy of $E_a = 10$ are presented. The effect of higher activation energies is addressed in Section 7.3.3.

7.3.1 Validation with Amrita

To present all the features of an ODW initiation from a wedge, a baseline case is presented where the parameters are given by Eqs. 7.7 and 7.8 with $\phi = 25°$ and $E_a = 20$. Figures 7–7 and 7–8 show the temperature contours obtained from the MoC and Amrita simulations, respectively, whereas Figs. 7–9 and 7–10 illustrate the pressure contours for the two programs. Qualitatively, the flowfields are in good agreement. A close view of the induction zone at the tip of the wedge is shown in Fig. 7–11 by the contours of the reaction progress variable. The coupling between the reaction front and the oblique shock can be observed as manifested by a progressive shortening of the post-shock induction length. Figure 7–12 shows the characteristics network at the tip of the wedge, where the streamlines and C^+ characteristics are traced. The adaptive refinement in the MoC program can be seen in Fig. 7–13.

In order to quantitatively compare the two simulations, Figs. 7–14 and 7–15 present the shock trajectory and the profile of the reaction progress variable along the wedge surface, respectively. The agreement is again very satisfactory. The angle

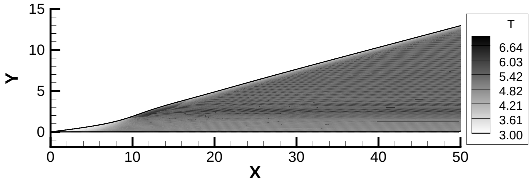

Figure 7–7: MoC — Temperature contours, $E_a = 20, \phi = 25°$

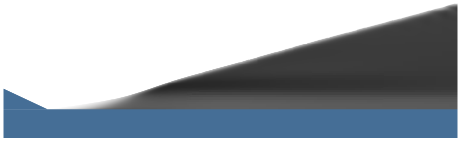

Figure 7–8: Amrita — Temperature contours, $E_a = 20, \phi = 25°$

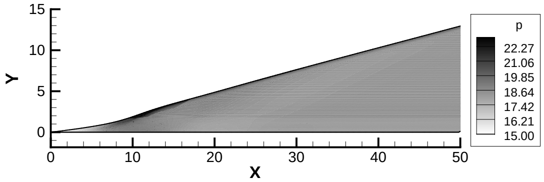

Figure 7–9: MoC — Pressure contours, $E_a = 20, \phi = 25°$

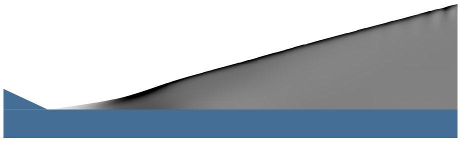

Figure 7–10: Amrita — Pressure contours, $E_a = 20, \phi = 25°$

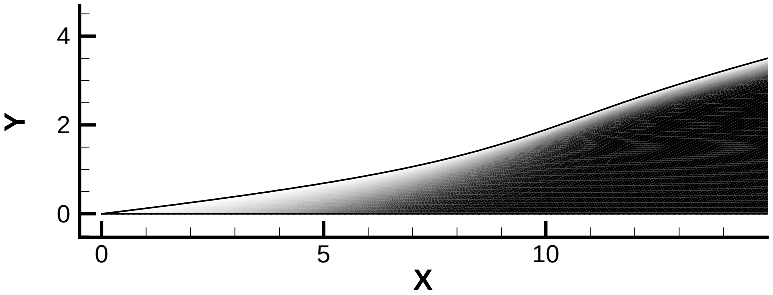

Figure 7–11: MoC — Z contours (white is $Z = 1$, black is $Z = 0$), $E_a = 20, \phi = 25°$

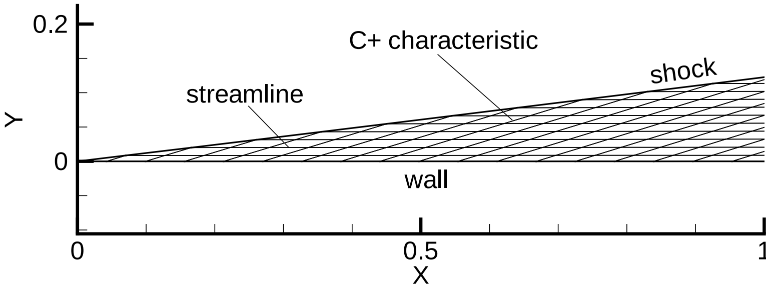

Figure 7–12: Typical characteristics network

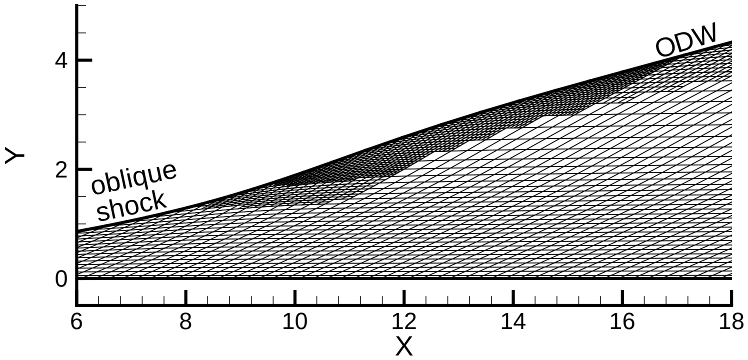

Figure 7–13: Example of network refinement

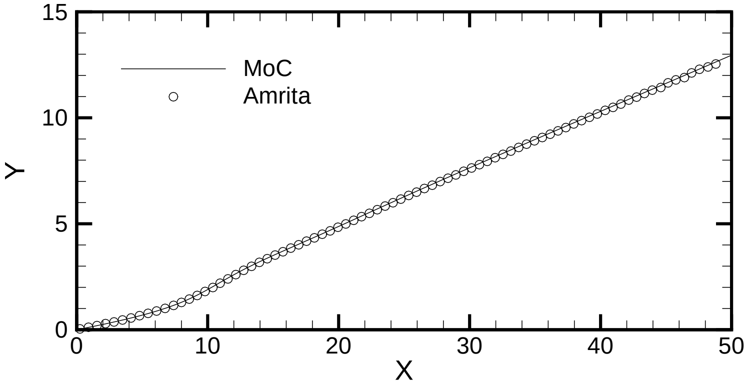

Figure 7–14: Shock trajectory, $E_a = 20, \phi = 25^\circ$

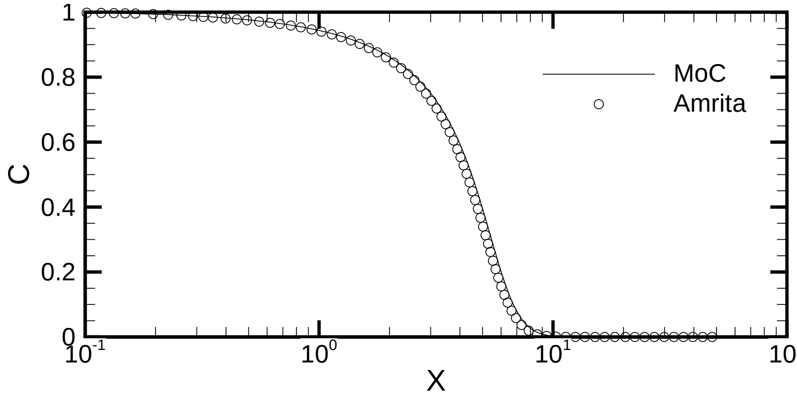

Figure 7–15: Z profile along the wall surface, $E_a = 20, \phi = 25^\circ$

of the shock obtained from the MoC program as a function of the distance from the tip of the wedge is shown in Fig. 7–16. At the tip of the wedge ($x = 0$), the shock angle is 31.9°, which corresponds to the value of an inert oblique shock. Downstream of the tip, the compression waves produced by the exothermic reactions interact with the shock and strengthen it. The maximum value of the shock angle is approximately 44.7°, where the reaction front couples with the shock. According to steady detonation polar analysis, this value is greater than the ODW angle (see next paragraph). Thereafter, the shock angle decreases and asymptotes to the ODW angle of 40.0°. Also shown in this figure is the effect of changing the number of characteristics per half-reaction length at the tip of the wedge from 10 to 80. The

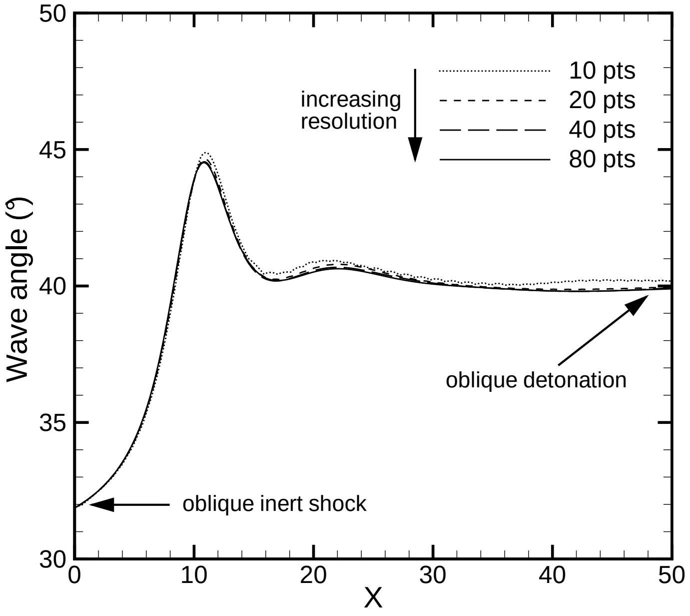

Figure 7–16: Oblique shock wave angle as a function of distance from wedge tip, showing transition from oblique inert shock to oblique detonation for four resolution levels, $E_a = 20, \phi = 25°$

curves of the two most refined simulations cannot be distinguished and therefore 40 points per half-reaction length at the tip of the wedge was considered sufficient to provide grid-independent results. It was verified that 10 characteristics (or points) per half-reaction length along any streamline behind the oblique shock is sufficient to provide a mesh-independent result.

7.3.2 Low Activation Energy

In this section, the activation energy is kept constant at $E_a = 10$. In addition to validating the results of the MoC program with CFD simulations, it is possible to compare the angle of a steady oblique or conical detonation with the predicted value calculated from conservation laws. Following the work of Pratt et al. [94], shock and detonation polars can be derived using the chemistry model employed in the present work.

Semi-Infinite Wedge. The polars corresponding to semi-infinite wedges are illustrated in Fig. 7–17. The open circles represent values from the MoC program. As shown in Fig. 7–16, the baseline case produces an oblique shock angle at the tip of the wedge of 31.9° and an ODW angle further downstream of 40.0°, corresponding to the two circles in Fig. 7–17 for $\phi = 25°$. The agreement between the polars and the MoC program is very good over the entire range of attached ODWs. The simulations show that CJ ODWs are initiated even for lower wedge angles than ϕ_{CJ} (obtained from the detonation polar).

The evolution of the wave angle for different wedge angles (between 4° and 25°) is shown in Fig. 7–18. Two overdriven ODWs are shown with $\phi = 20°$ and 25°. For $\phi \leq 11°$, the wave angle asymptotes to the CJ ODW value of 30.3° even for

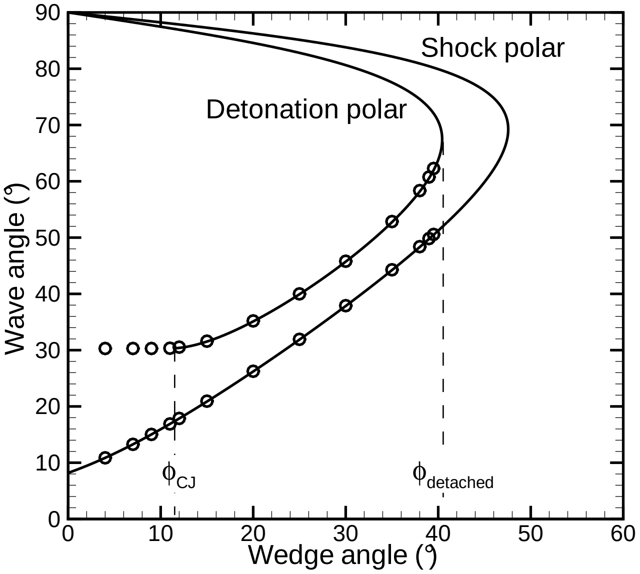

Figure 7–17: Shock and detonation polars. Circles are results from the MoC program

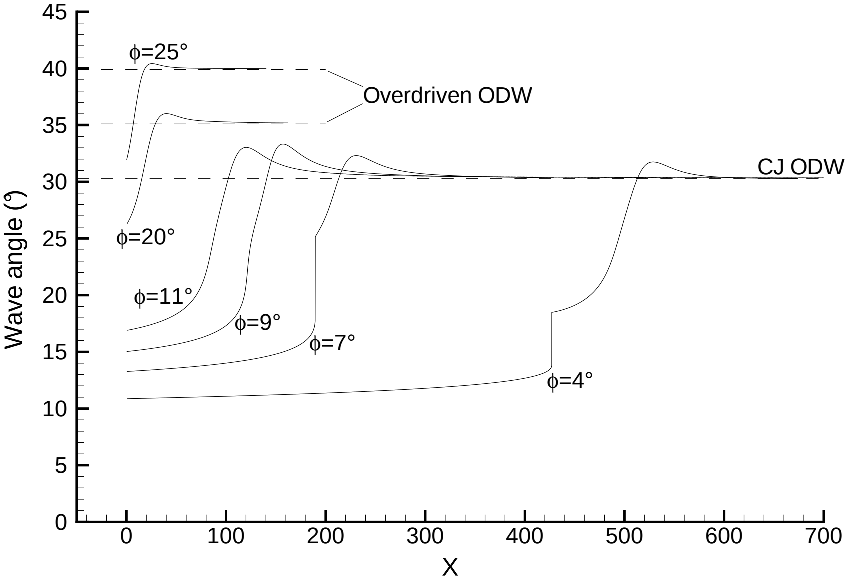

Figure 7–18: Evolution of the wave angle for different wedge angles

a wedge angle as low as $\phi = 4°$. This clearly shows that oblique shock-induced combustion where the reaction front remains uncoupled and at a fixed distance from the oblique shock is not an admissible solution. Instead, the reaction front couples with the oblique shock and forms a CJ ODW. For such low wedge angles ($\phi < \phi_{CJ}$), an expansion wave (or a Taylor wave) follows the end of the reaction zone. This type of flowfield is in accordance with the work of Ashford and Emanuel [3].

Semi-Infinite Cone. The MoC simulations of ODWs initiated from semi-infinite cones were also validated with shock and detonation polars. An example of the characteristic network in a conical flowfield is displayed in Fig. 7–19. As in a typical Taylor-Maccoll flowfield, the streamlines are curved and become parallel to the cone surface sufficiently downstream of the shock. In such a flowfield, the streamlines become closer to each other as x increases. A procedure is implemented in the MoC program to coarsen the network (or to skip a calculation point) where the distance between two streamlines is smaller than a value specified by the user.

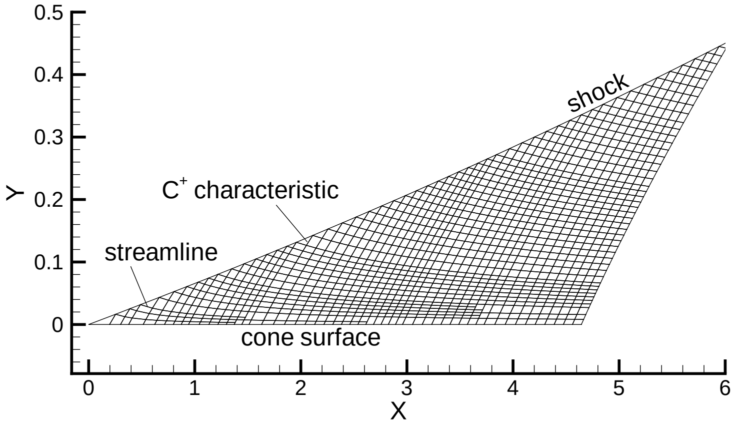

Figure 7–19: Typical characteristic network in a conical flowfield

Figure 7–20 presents the shock and detonation polars for semi-infinite cones. For the construction of these polars, the oblique shock and ODW structures are assumed to be identical to that of the semi-infinite wedge configuration, but a Taylor-Maccoll flowfield is imposed behind the oblique shock and ODW. The open circles refer to results from the MoC program, which are in very good agreement with the polars. CJ ODWs are also initiated for cone angles lower than ϕ_{CJ}. However, in this case, the ODW angle is slightly lower than that of the CJ ODW (calculated from the detonation polar). This is attributed to the front curvature, explained in more detail in the next paragraph.

Figure 7–21 presents the evolution of the wave angle for different values of cone angles between $\phi = 7°$ and 30°. The ODWs produced from cone angles of $\phi = 25°$ and 30° are overdriven ODWs, whereas cone angles for $\phi \leq \phi_{CJ}$ initiate CJ ODWs. In the conical configuration, the angle of the ODWs reaches a plateau where the reaction front couples with the oblique shock and continues to increase downstream of it towards the CJ value. Considering the cone angle of $\phi = 15°$, the plateau is at $140 < X < 180$ and in this range the ODW angle is 26.7°. For $X > 180$, the ODW angle increases to reach a value of 29.5° at $X = 900$. The 2.8° variation of the ODW angle is a result of the detonation front curvature. At $x = 160$, the curvature radius is smaller ($r_c = 61.4$) than at $x = 900$ ($r_c = 472$). It has been shown that the curvature of a detonation front can produce a velocity deficit [128, 43, 126]. In the case of an ODW, a velocity deficit translates into a reduction of the ODW angle, in order to reduce the normal velocity component with respect to the ODW to below the CJ value. Therefore, the ODW angle is expected to be the lowest at the location

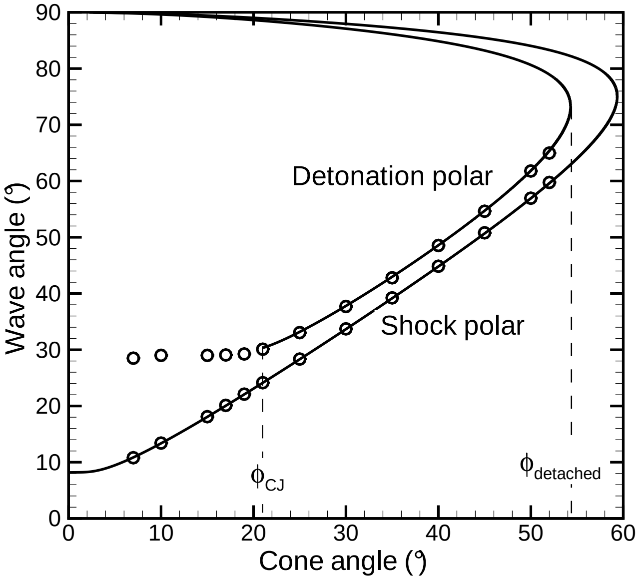

Figure 7–20: Shock and detonation polars for cones. Circles are results from the MoC program

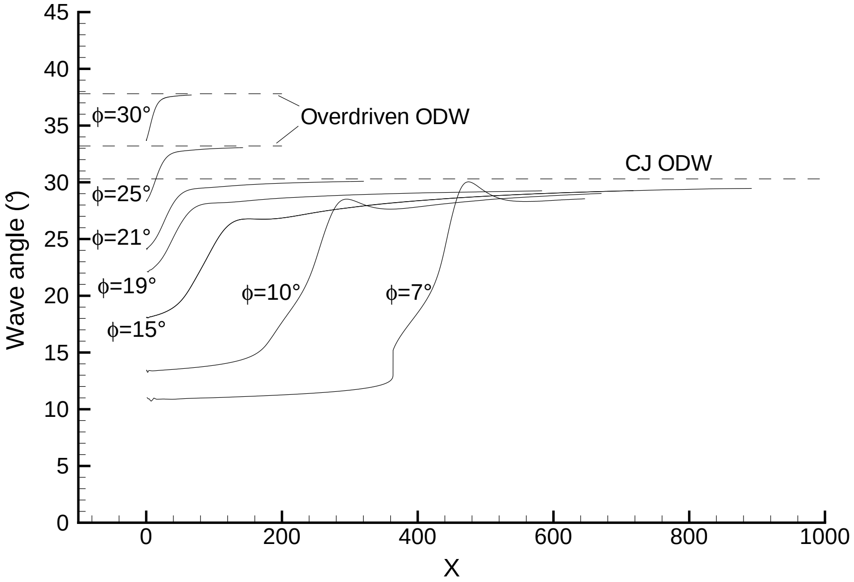

Figure 7–21: Evolution of the wave angle for different cone angles

of the smallest radius of curvature. In the farfield, the curvature effect decreases and the ODW angle asymptotes to the CJ ODW angle.

7.3.3 High Activation Energy

In this section, the effect of higher activation energies on the initiation of an ODW and its structure is investigated. Semi-infinite wedges and cones are also considered here.

In general, the activation energy of a mixture is associated with the ratio of the induction time over the reaction time. The effect of varying this parameter is shown in Fig. 7–22 where the profile of the reaction progress variable is plotted along the wedge surface for different values of E_a, with the flow conditions of the baseline case. In this figure, the induction and reaction lengths are illustrated for the case where $E_a = 10$. As the activation energy increases, the maximum rate of chemical energy release and the ratio $\Delta_{ind}/\Delta_{reac}$ increases as well.

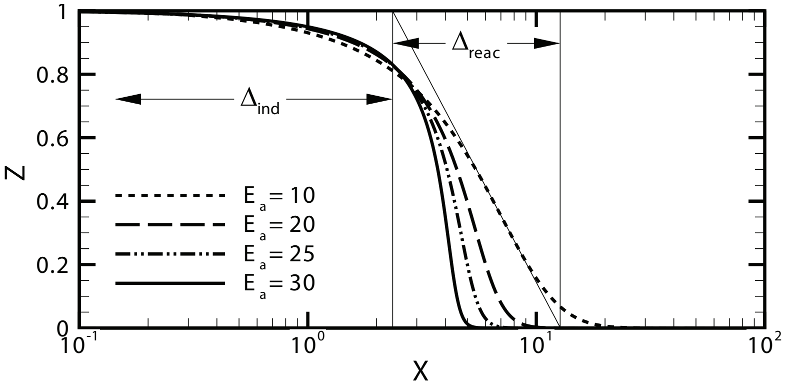

Figure 7–22: Z profile along the wall surface for different values of activation energy, $\phi = 25°$

Semi-Infinite Wedge. In the next simulations, the wedge angle ϕ and the activation energy E_a are the two varied parameters. Figure 7–23 presents the wave angle evolution for $25° \leq \phi \leq 39°$ and $10 \leq E_a \leq 30$. For $\phi = 25°$ and $E_a = 10$ (Fig. 7–23a), the reaction front smoothly couples with the oblique shock to form the ODW. Therefore, the wave angle increases gradually from the oblique shock angle of 31.9° to the ODW angle of 40.0°. For values of activation energy of 20 and 25, the wave angle overshoots at the location where the reaction front couples with the oblique shock ($x = 10.8$ and $x = 8.1$, respectively) and stabilizes downstream at the ODW angle of 40.0°. This overshoot corresponds to a location where the ODW is at a larger degree of overdrive compared to its steady-state angle, which is also an overdriven ODW (see Fig. 7–17). The case $E_a = 30$ exhibits the largest wave angle overshoot. The wave angle reaches 62.3° at $x = 6.3$, decreases to near the ODW angle and keeps oscillating between 37.0° and 45.6° downstream without converging to a constant ODW angle. From this figure, it can be observed that for moderate activation energies, the coupling between the reaction front and the oblique shock locally overdrives the ODW before reaching the steady-state angle. For large activation energies, the ODW is largely overdriven at its formation location and its angle oscillates about the value predicted by steady polar analysis. A discussion on the ODW overshoot and wave angle oscillation is provided below.

For a wedge angle of 30°, the shock and detonation polars give an oblique shock angle of 37.9° and an ODW angle of 45.8° (see Fig. 7–17). According to Fig. 7–23b, the results from the MoC program are in very good agreement; the oblique shock angle at the tip of the wedge is 37.9° and the steady-state ODW angle is 45.8° for

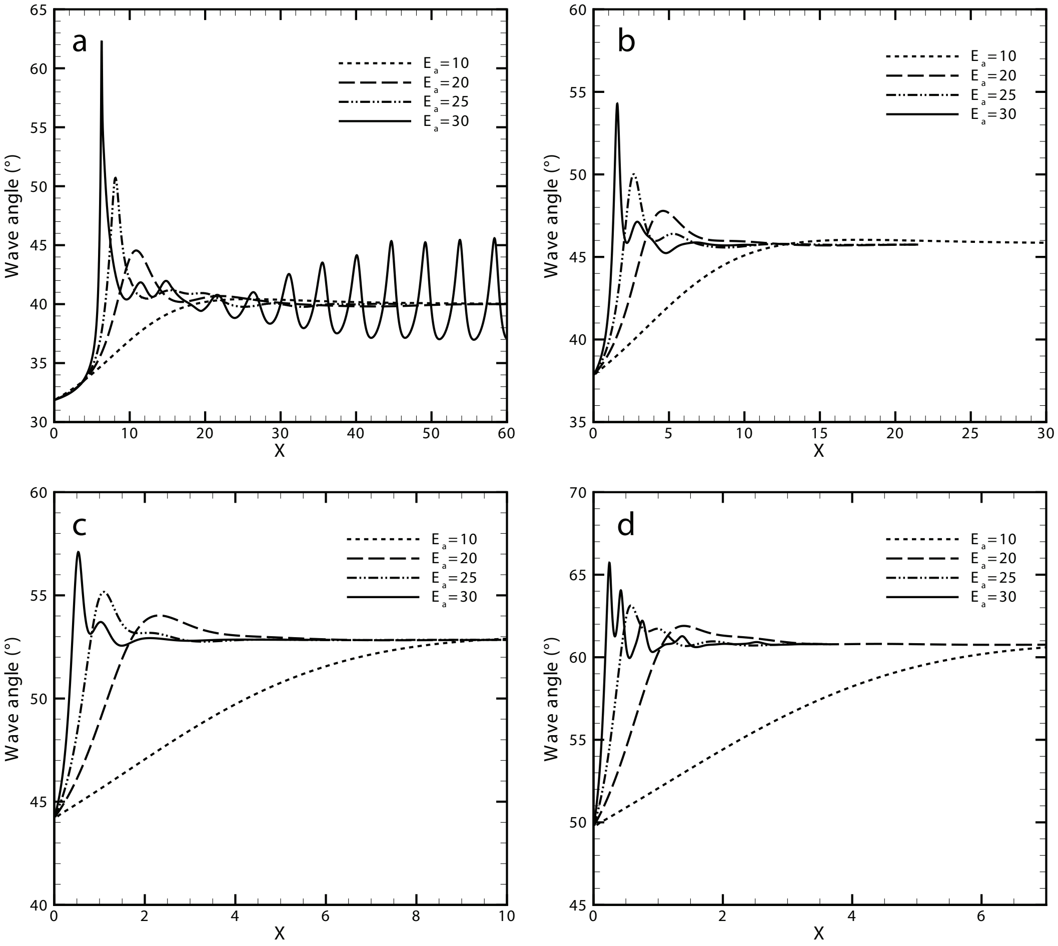

Figure 7–23: Wave angle as a function of the wedge angle and activation energy. a: $\phi = 25°$, b: $\phi = 30°$, c: $\phi = 35°$, d: $\phi = 39°$

all activation energies. Similar to Fig. 7–23a, an increase of the activation energy amplifies the degree of ODW overdrive where the reaction front couples with the oblique shock. However, for this value of wedge angle, the oscillation of the ODW angle is not observed. The results for $\phi = 35°$ (Fig. 7–23c) and $\phi = 39°$ (Fig. 7–23d) are qualitatively similar to the case $\phi = 30°$. The oblique shock and ODW angles also agree very well with the shock and detonation polars. One can study the effect of varying the wedge angle and keeping the activation energy constant. For instance, considering $E_a = 20$, the effect of increasing the wedge angle is to attenuate the overshoot phenomenon at the ODW formation location.

It is of interest to further explore the case $\phi = 25°$, $E_a = 30$ and to investigate the mechanism responsible for the ODW initiation process and oscillation of the ODW angle. Figure 7–24 presents the pressure contours in the numerical domain. The induction zone can be seen at the tip of the wedge (between $x = 0$ and approximately $x = 5$), as well as pressure fluctuations behind the shock due to the ODW angle oscillation. Figures 7–25 and 7–26 show an enlarged view of the induction zone with the contours of the reaction progress variable and a numerical Schlieren, respectively. In Fig. 7–25, the two arrows show the distance between the oblique shock and the

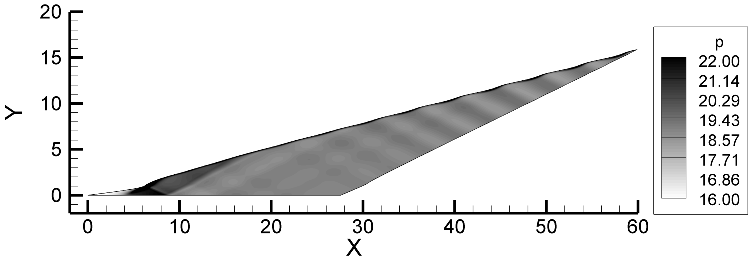

Figure 7–24: Pressure contours, $E_a = 30$, $\phi = 25°$

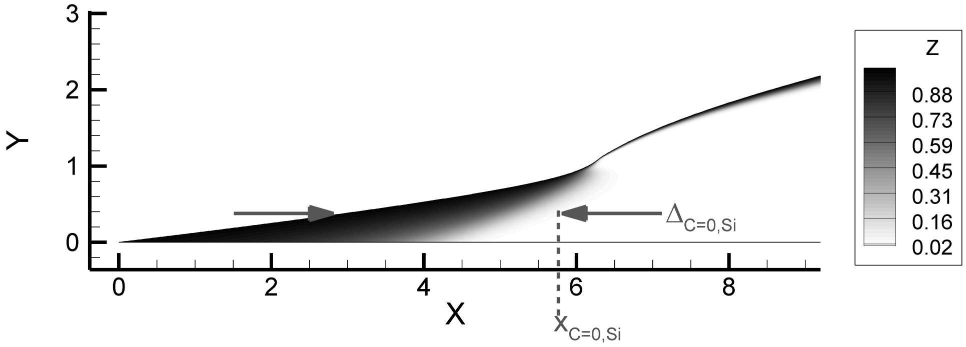

Figure 7–25: Z contours of the induction zone, $E_a = 30$, $\phi = 25°$

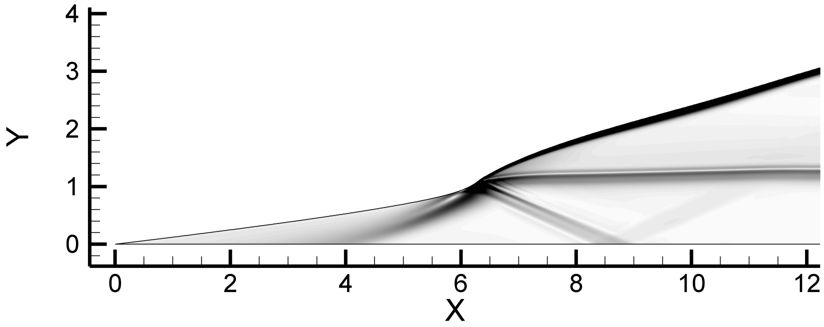

Figure 7–26: Numerical Schlieren of the induction zone, $E_a = 30$, $\phi = 25°$

location where $Z = 0$ for a streamline i, named S_i. Considering the streamline along the wedge surface, S_1, the reaction progress variable decreases to $Z = 0$ at approximately $x_{Z=0,S_1} = 4.5$, hence the distance between the shock and the location where $Z = 0$ is $\Delta_{Z=0,S_1} = 4.5$ for this streamline. Above the wall surface (for $0 < y < 1$), $\Delta_{Z=0}$ decreases and becomes very small at the coupling location ($y = 1.2$). One factor that can reduce $\Delta_{Z=0}$ (or equivalently the induction length) is the steepening of the oblique shock, due to the temperature increase. However, according to Fig. 7–23a, the oblique shock angle increases significantly only for $x > 4$ (or for $y > 0.56$). It can be observed (in Fig. 7–25) that for $0 < y < 0.56$, $\Delta_{Z=0}$ decreases for increasing y, even though the oblique shock angle is approximately constant at 33°. Therefore, a different mechanism is responsible for the induction length reduction. Recalling that along the streamline on the wedge surface S_1 $x_{Z=0,S_1} = 4.5$, there is a rapid energy release from the chemical reactions at this location, increasing the temperature and pressure of the flow. For the next streamline above S_1 (named S_2), $\Delta_{Z=0,S_2}$ is expected to be the same as $\Delta_{Z=0,S_1}$ since both streamlines cross an oblique shock of the same strength. However, since $x_{Z=0,S_1} < x_{Z=0,S_2}$, the energy along S_1 is released farther upstream than along S_2. The temperature and pressure increase associated to the energy release along S_1 is communicated to the fluid particles along S_2 via compression waves that travel along characteristics. Consequently, the induction length along S_2 is decreased and $\Delta_{Z=0,S_2} < \Delta_{Z=0,S_1}$ due to combustion along S_1. By following the same logic, $\Delta_{Z=0,S_3} < \Delta_{Z=0,S_2}$ due to combustion along S_2, etc. Therefore, the spatial gradient $\frac{dx_{Z=0}}{dy}$ causes the induction length reduction for $0 < y < 0.56$. For $y > 0.56$, the compression waves interact with the shock, steepen it, and contribute also to decrease the induction length behind the shock.

The phenomenon of reaction front acceleration by a spatial gradient of induction length was also observed in experimental and numerical investigations of direct initiation of gaseous detonations [66, 87, 70, 28]. Near the critical energy for detonation initiation, the blast velocity is observed to decay below the CJ velocity, forming a gradient of induction length behind the blast. At this stage, the reaction front is located significantly behind the blast, but starts to accelerate towards the blast wave. When the reaction front couples with the blast, the detonation is momentarily overdriven before again decelerating to the CJ velocity. Lee et al. [65] proposed the SWACER mechanism (shock wave amplification by coherent energy release) to describe this phenomenon of reaction front acceleration by a gradient of induction length.

The oscillation of the ODW angle is depicted in Fig. 7–27 with the contours of the reaction progress variable. According to this figure, the reaction zone is thinner as

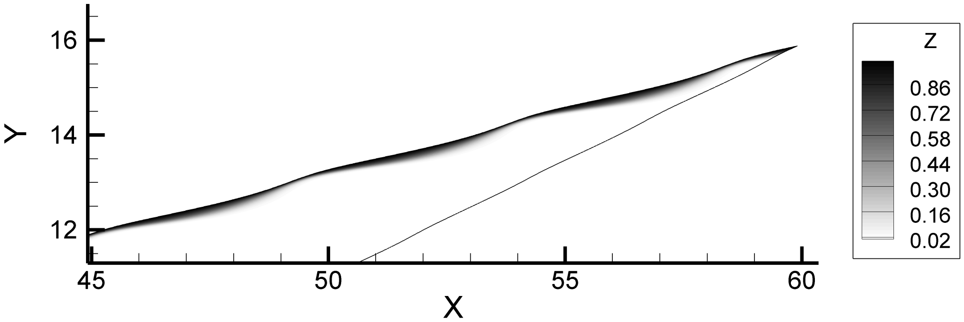

Figure 7–27: Z contours of an oscillating ODW, $E_a = 30$, $\phi = 25°$

the ODW angle steepens, and inversely is thicker as the ODW angle decreases. This situation is similar to the propagation of a one-dimensional, pulsating detonation [87], where the detonation velocity oscillates at a constant amplitude about the CJ value.

Semi-Infinite Cone. Figure 7–28 shows the evolution of the wave angle for the simulations with semi-infinite cones. The range of the cone angle is $25° \leq \phi \leq 50°$, while the range of the activation energy is still $10 \leq E_a \leq 30$. For the case $\phi = 25°$ and $E_a = 10$, the wave angle continuously increases from the oblique shock value of 28.3° to the ODW value of 33.0°. For $E_a = 20$, the wave angle reaches 35.4° where the reaction front couples with the oblique shock and keeps oscillating about the ODW steady-state angle. For $E_a = 25$, the amplitude of the oscillation is much larger than for the case $E_a = 20$. For the highest activation energy, the shock angle steepens to a point where the flow becomes subsonic behind it and forces the simulation to stop. In the case of a 30° cone half angle, Fig. 7–28b shows that the ODW angle converges to the steady-state value of 37.8° for $E_a = 10, 20$ and 25. For $E_a = 30$, an overshoot of the wave angle is observed at $x = 6$, followed by an oscillation of the ODW angle of increasing amplitude. For $\phi = 40°$ and 50°, the qualitative interpretation is similar; the wave angle increases from the oblique shock value to the ODW value with an overshoot for high activation energies.

In the conical configuration, oscillation of the ODW angle is observed for three cases: a) $\phi = 30°, E_a = 30$, b) $\phi = 25°, E_a = 20$ and c) $\phi = 25°, E_a = 25$. For case a), the amplitude of the oscillation increases with x. It is of interest to compare this case, where the steady-state ODW angle is 38°, with Fig. 7–23a ($E_a = 30$) in the wedge configuration, where the steady-state ODW angle is 40°. In the conical

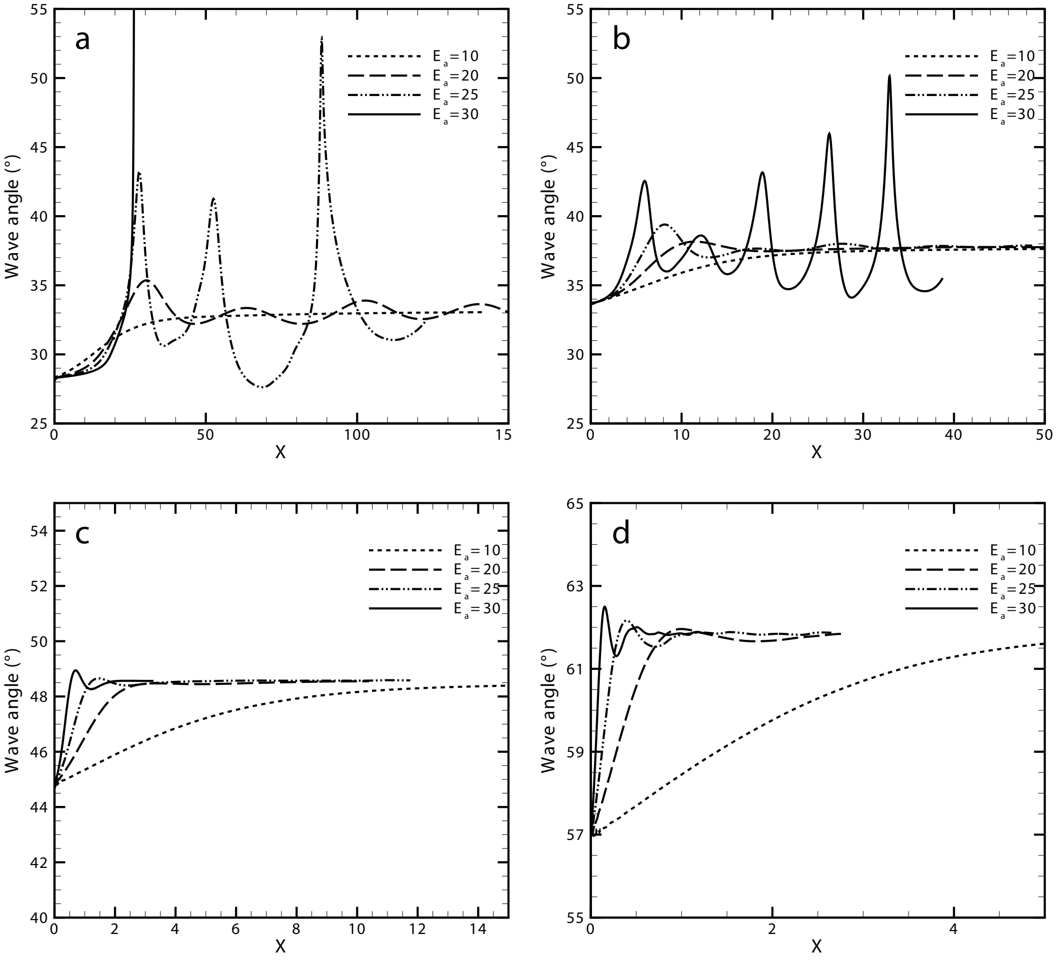

Figure 7–28: Wave angle as a function of the cone angle and the activation energy. a: $\phi = 25°$, b: $\phi = 30°$, c: $\phi = 40°$, d: $\phi = 50°$

configuration, the first overshoot does not exceed the steady-state value as much as in the wedge configuration. Further downstream, the oscillation amplitude increases in the conical configuration, whereas it stays constant in the wedge configuration.

Figure 7–29 depicts the contours of the reaction progress variable for case c), where the ODW angle oscillates with a large and irregular amplitude. The large variation of the induction length behind the shock can be observed in this figure, which can be associated with a coupling / decoupling phenomenon of the reaction front with the shock. The shock curvature around the cone axis possibly contributes to this phenomenon, but further investigations are required to verify this hypothesis.

In this chapter, theoretical considerations were presented to address different phenomena related to supercritical or overdriven ODWs. A one-dimensional ZND analysis was adapted to obtain the profile of the flow conditions across normal and oblique detonations, and behind an inert oblique shock attached to a wedge. A MoC program was validated with CFD calculations to simulate reactive flows over semi-infinite wedges and cones. For a low activation energy, the angle of steady ODWs

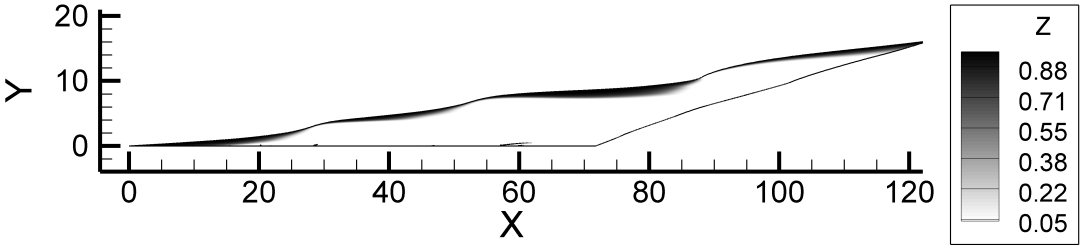

Figure 7–29: Z contours, $E_a = 25, \phi = 25°$

initiated from wedges and cones were in excellent agreement with the predicted values from a polar analysis. For a wedge or cone angle lower than ϕ_{CJ} (the wedge or cone angle for which a CJ ODW is attached), a CJ ODW was initiated, showing that shock-induced combustion with the reaction front remaining decoupled from the oblique shock was not an admissible solution. In the conical configuration, the curvature effect around the cone axis allowed a CJ ODW to be initiated at an angle lower than the CJ ODW angle calculated without the curvature effect. For higher activation energies, the initiation process of an ODW was explored. The acceleration of the reaction front at the end of the induction zone was caused by a spatial gradient of induction length. Also, the evolution of the ODW angle showed oscillations about the CJ ODW angle, similar to the oscillations of a pulsating detonation. The curvature effect seemed to amplify the oscillations.

CHAPTER 8
Cellular Structure of an ODW

The structure of a gaseous detonation wave is by nature three-dimensional and unsteady. It is composed of transverse shock waves propagating perpendicularly to the detonation propagation direction. By tracking the trajectory of these waves, a cellular pattern is obtained, as illustrated in Fig. 1–4. From the experimental results of the present investigation, a cellular structure can be observed along the front of the ODW for the cases of prompt and delayed ODW regimes (e.g., Figs 4–2 and 4–3). The theoretical analysis derived in Chapters 6 and 7 using the MoC program does not allow for the resolution of this cellular structure, since the governing equations are expressed in steady state. It rather simulates a laminar structure of an ODW, or a "two-dimensional ZND structure," with no time dependence. However, it is of interest to simulate the dynamics of an ODW and compare it to that of a normal detonation wave. More precisely, determining whether the dynamic detonation parameters, such as the characteristic cell size, are the same for both normal and oblique detonation waves is a relevant issue to address in this investigation.

In order to simulate the cellular structure of an ODW, the Amrita environment is employed, which was presented in Section 7.2. In this section, the same governing equations, chemistry model, refinement criteria, initialization procedure and boundary conditions are used.

The baseline case introduced in Section 7.3.1 (see Fig. 7–10) is reconsidered here with different values for the activation energy. The flow parameters for this case are repeated for completeness in Table 8–1.

Table 8–1: Conditions for the baseline case

Freestream	Chemistry	Wedge angle
$p = 1$ $\rho = 1$ $u = 8\cos\theta$ $v = -8\sin\theta$ $Z = 1$	$\gamma = 1.3$ $Q = 10$ $E_a = 10, 20, 25, 30$	$\phi = 25°$

Pressure contours of the flowfield for the different values of the activation energy are illustrated on the left-side of Fig. 8–1. In these flowfields, the contours are shown for a given time, once the ODW has stabilized to a steady-state value. To validate the obtained flowfields, the results from Amrita are compared with the results from the MoC program. The trajectory of the shock front given by the two methods is presented on the right-side of Fig. 8–1. For $E_a = 10$, there is a gradual transition from an oblique shock to an ODW and no instabilities can be observed. For $E_a = 20$, instabilities appear near the right boundary of the numerical domain. As the activation energy is increased, instabilities form closer to the wedge tip. As previously mentioned, such instabilities can not be captured by the MoC program since it provides steady solutions. From the temporal evolution of these flowfields, transverse shock waves move along the ODW front. It is therefore plausible that by tracking the motion of these transverse waves, a cellular pattern would be obtained, similar to the one observed for normal detonation waves. A method is thus needed to visualize the motion of the transverse waves.

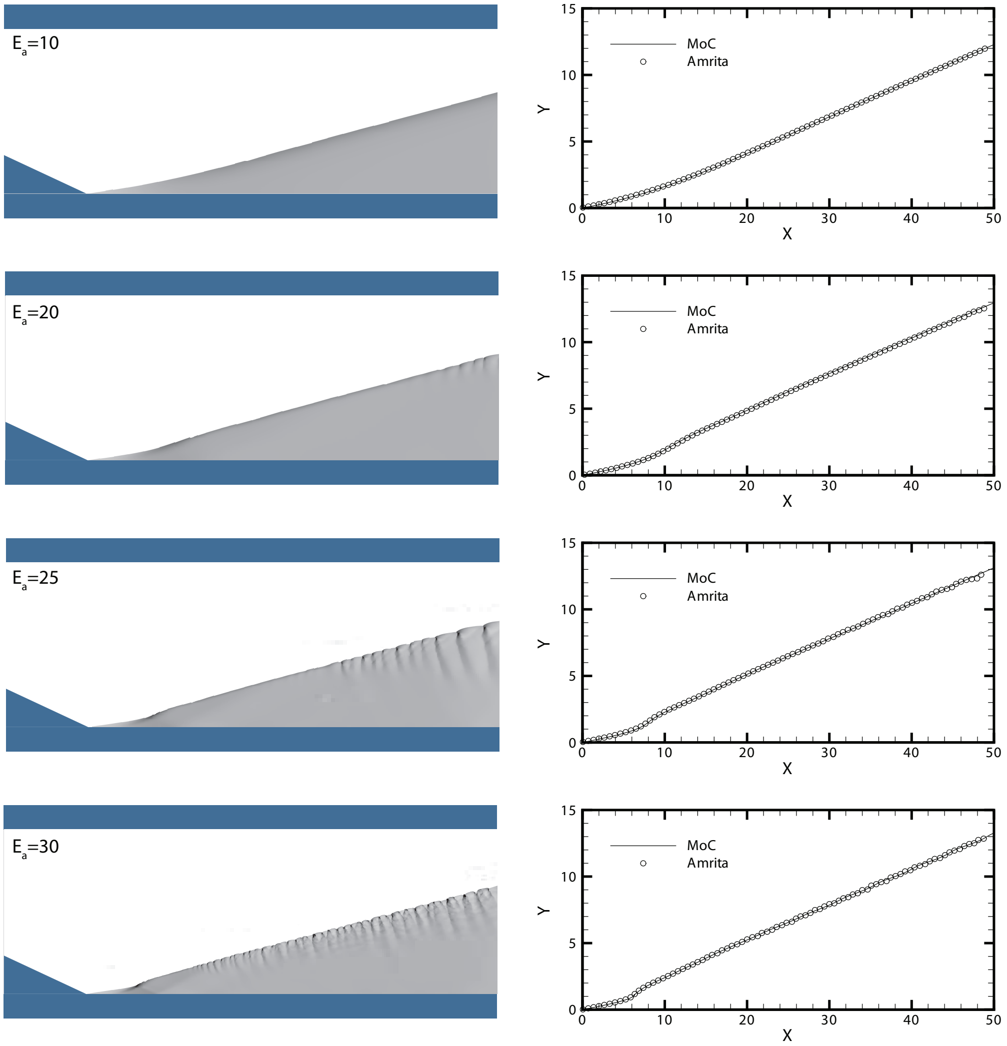

Figure 8–1: Pressure contours and shock front trajectory for the baseline case with different values of activation energy

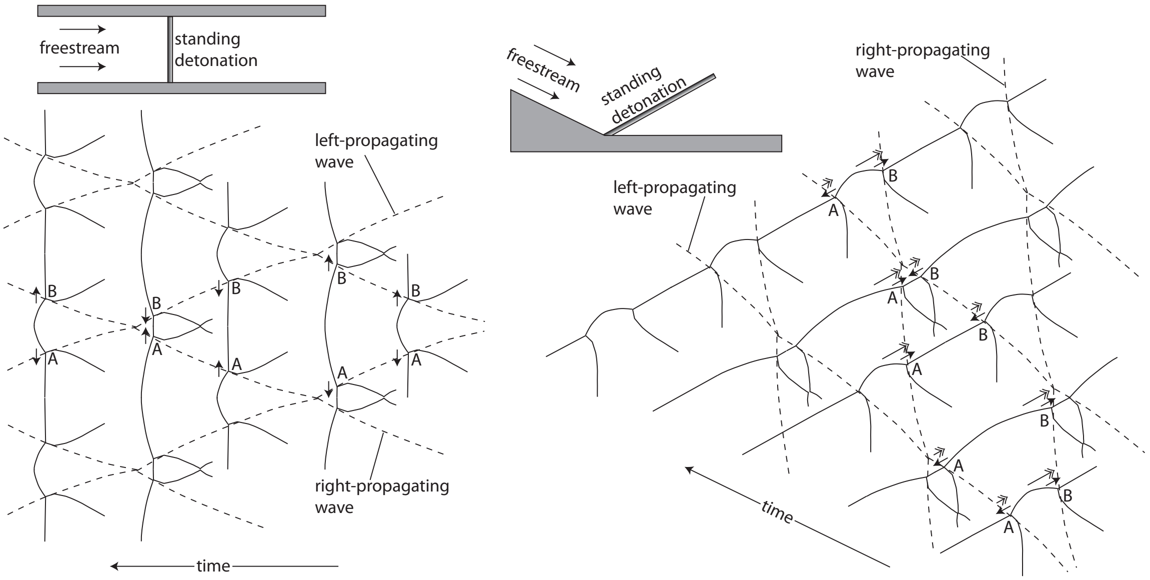

Figure 8–2: Schematic of the triple point trajectory in an ODW

To facilitate the interpretation of the cellular structure of an ODW, a comparison is first made with that of a normal detonation wave. The cellular structure of a normal detonation wave is presented as a schematic on the left-hand side of Fig. 8–2. In this illustration, the normal detonation is standing at a fixed location with respect to an observer. The freestream velocity corresponds to the CJ speed. To obtain the cellular structure of a standing detonation, one can imagine a smoke foil on the background sweeping in the same direction and at the same speed as the freestream. A pattern illustrated by the dashed lines would be obtained. The detonation is drawn at different locations on the pattern only for completeness. The arrows refer to the relative velocity direction of two triple points. Left- and right-propagating waves can be differentiated from such patterns. By applying the same concept to a standing oblique detonation wave, the cellular pattern shown by the dashed lines on the right-hand side of Fig. 8–2 would be obtained. In this case, the freestream velocity is larger than the CJ value. The single-headed arrows correspond to the velocity direction of two triple points relative to each other, while the two-headed arrows show their velocity direction relative to the non-moving wedge. According to this schematic, one can see that the left- and right-propagating waves are both swept away from the wedge tip by the tangential velocity component of the freestream.

To monitor the evolution of the instabilities in time from the numerical simulations, a series of pressure contours, corresponding to a known time sequence, can be superimposed and translated in a specific manner. The translation direction is opposite to that of the freestream, and the distance is given by the velocity of the freestream multiplied by the time interval between two figures. Figure 8–3 shows the ODW structure for the cases $\phi = 25^\circ$ and 29°. To construct these figures, 100 frames were used in each case. For the case $\phi = 25^\circ$, the flowfield displayed in Fig. 8–1 (with $E_a = 30$) was used as the first frame. After superimposing 100 frames, one can recognize two sets of pressure (or transverse) waves, thus forming a cellular structure. Near the induction zone, only the left-propagating waves are observed, while the right-propagating waves are initiated further downstream along the front. Both sets of transverse waves are swept away from the tip of the wedge. The size of the cells varies along the front and merging of transverse waves of the same family (mostly of the left-propagating waves) can be observed. Referring to the case $\phi = 29^\circ$, the induction zone is smaller and the transverse waves are initiated closer to the tip of the wedge. The size of the cell is more regular than for $\phi = 25^\circ$, and most of the transverse waves of the same family are parallel.

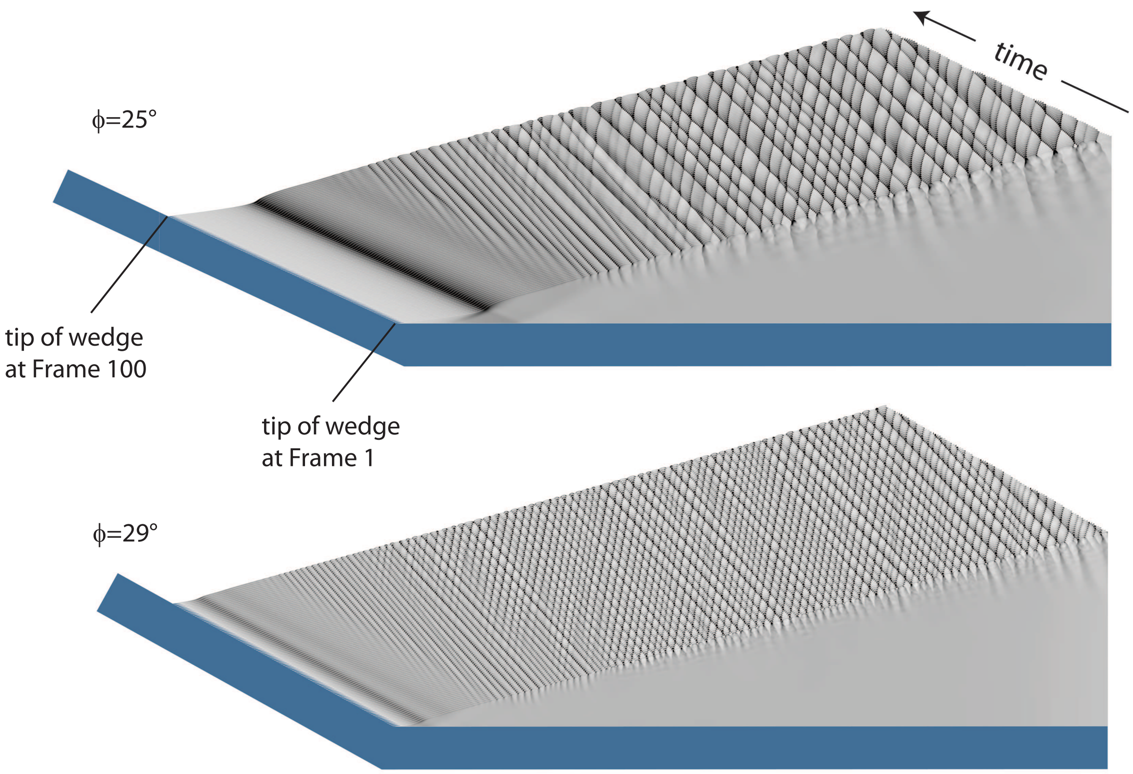

Figure 8–3: Cellular structure of an ODW for $\phi = 25^\circ$ and 29°

According to Fig. 8–3, it is shown that the structure of the simulated ODWs exhibits a cellular pattern similar to that observed in normal detonation waves. However, instabilities originating in ODWs are swept away along the detonation front. Therefore, new transverse waves are constantly generated at a certain distance from the wedge tip. The formation mechanisms of transverse waves in the structure of a detonation can thus be investigated though such simulations. This aspect differs from the simulations of a normal detonation since in this case, once the transverse waves are formed, they reflect off the top and bottom walls.

CHAPTER 9
Contributions and Recommendations

9.1 Contribution to Knowledge

Through an experimental investigation, initiation and stabilization of oblique detonation waves from conical projectiles launched at approximately 2 km/s into $2H_2+O_2+7Ar$ mixtures was demonstrated based on Schlieren photographs of the flowfield. The role of the projectile nose on the detonation initiation criterion was assessed by systematically varying the cone half angle (from 15° to 60°) and the initial pressure of the mixture (from 10 to 200 kPa). The range of these two parameters was wider than previously studied, providing unique flow features, especially at small cone angles and high pressures. From the experimental results, the conclusions and contributions are:

- At mixture pressures above 100 kPa, the transition from initiating a prompt ODW to initiation failure was observed by decreasing the cone angle. The critical flowfield (the delayed ODW) occurred at a cone half angle of 20° - 25°, where a visible induction zone preceded the onset of the ODW. This flowfield was obtained in the two-layer detonation experiments [122], but was monitored for the first time from conical projectiles.
- At cone half angles greater than 35°, the transition from initiating a prompt ODW to initiation failure was observed by decreasing the mixture pressure. The critical flowfield (the combustion instabilities) occurred at a pressure of

50 – 100 kPa. This flowfield has been previously studied numerically and theoretically when produced by spherical-nosed projectile, but no model has been developed for the conical configuration. Therefore, the flowfields presented in this study constitute a unique reference for the development of such a model.

- The cone angle of the projectile and the initial pressure of the mixture represent two parameters that control the requirement for detonation initiation. Chemical kinetics are primarily affected by the cone angle (via the shock strength) and the amount of energy deposited by the projectile is mainly influenced by the mixture pressure and cell size (via the projectile drag). It was shown that both parameters should be taken into account in the prediction of ODW initiation.

A theoretical investigation was conducted using the blast wave model and a critical Damköhler number to predict the conditions required to initiate an ODW. A 2D method of characteristics (MoC) program was developed to explore the critical conditions for detonation initiation, the initiation process of an ODW and the role of the detonation front curvature. Computational simulations were also performed to validate the MoC results, and to model the cellular structure of an ODW. The conclusions and contributions from this analysis are:

- The energetic limit (the Lee-Vasiljev model) agreed reasonably well with the experimental results for cone half angles greater than 35° and initial pressures below 100 kPa. At small cone angles and high initial pressures, this model underestimated the conditions required for detonation initiation. The trend of the critical Damköhler number followed more closely that of the experimental results at small cone angles and high pressures. The two types of transition from prompt ODW to initiation failure observed experimentally were therefore predicted qualitatively by these two requirements.

- Criticality to initiate ODWs from finite wedges was investigated using a MoC program with a simplified one-step Arrhenius chemical model. By comparing these simulations with the cases of planar blast and planar piston initiation of a detonation, the domain of validity of the Lee-Vasiljev model was rigorously determined. In order for the hypersonic equivalence principle to be valid, the wedge angle needs to be smaller than 30°. Furthermore, for the energy to be released effectively instantaneously, the Mach number normal to the oblique shock has to be larger than 50.
- Using a semi-infinite wedge geometry, the initiation process of an ODW was identified: chemical reactions induced behind an attached oblique shock, acceleration of the combustion front towards the oblique shock due to a spatial gradient of induction length and coupling of the combustion front with the oblique shock. With a semi-infinite conical geometry, it was observed that the curvature of the detonation front around the cone axis enhanced the coupling / decoupling phenomenon between the combustion front and the oblique shock and allowed self-supported ODWs at a smaller angle than at the CJ ODW angle.
- Unsteady 2D numerical simulations were conducted using a one-step Arrhenius chemical model to monitor the cellular structure of an ODW. A method was proposed to visualize the cellular pattern of standing ODWs by superimposing

a series of pressure contours. The patterns exhibited qualitative similarities with the cellular structure of a normal detonation wave.

9.2 Recommendations for Future Work

A number of variations and extensions to the experiments presented in this work are recommended to improve the understanding of the physics involved in the initiation of an ODW from a conical projectile.

The boundary between successful detonation initiation and initiation failure could be better defined using additional experimental data. A systematic study where the projectile velocity is the independent parameter would determine more precisely its effect on the detonation initiation criteria. Varying the projectile diameter would permit the validation of scaling relationships.

Further experiments in different mixtures could demonstrate whether the present analysis is universal. The mixture used in this study is considered regular, since its cellular structure exhibits very regular cell sizes. It would therefore be relevant to observe the flowfields and the transitions from prompt ODW to inert shock regimes using an irregular mixture, which exhibits an irregular cellular structure.

On a theoretical basis, an improved model for the prediction of the conditions required to initiate an ODW from conical projectiles could permit a quantitative agreement with the experimental results. The development of an unsteady 2D MoC program would be valuable to verify the steadiness of the global flowfield and to theoretically simulate the cellular structure of an ODW. Furthermore, the implementation of a realistic chemical reaction mechanism into the MoC program would produce flowfields that could be directly compared with the experimental photographs.

A thorough numerical investigation on the cellular structure of ODWs is required to address the following issues in relation to Fig. 8–3:

- Are the simulations sufficiently resolved? Is the numerical domain sufficiently long to allow the cellular structure to be fully developed?
- Is the characteristic cell size of an ODW structure the same as that of a normal detonation wave (for the same degree of overdrive)?
- Are the velocities of the left- and right-propagating waves the same? In other words, are the cells symmetric or altered by the freestream tangential velocity?
- What is the mechanism that produces the observed instabilities? What is the cause for the left-propagating waves to be initiated earlier than the right-propagating waves?
- Are there flow conditions for which the left-propagating waves propagate towards the tip of the wedge and alter the general structure of the ODW?

Bibliography

[1] J. K. Ahuja, A. Kumar, D. J. Singh, and S. N. Tiwari. Simulation of shock-induced combustion past blunt projectiles using shock-fitting technique. *Journal of Propulsion and Power*, 12(3):518–526, 1996.

[2] R. L. Alpert and T. Y. Toong. Periodicity in exothermic hypersonic flows about blunt projectiles. *Astronautica Acta*, 17:539–560, 1972.

[3] S. A. Ashford and G. Emanuel. Wave angle for oblique detonation waves. *Shock Waves*, 3(4):327–329, 1994.

[4] P. Batchelor. Development of a gaseous detonation driven hyper-velocity launcher. Master's thesis, McGill University, 2010.

[5] P. Bauer (ed). Fourth international workshop on ram accelerators. *Journal De Physique IV*, 10(Pr. 11), 2000.

[6] H. Behrens, H. F. Lehr, W. Struth, and F. Wecken. Shock-induced combustion by high-speed shots in explosive gas mixtures. Technical Report 4/67, Institute of Saint-Louis, 1967.

[7] H. Behrens, W. Struth, and F. Wecken. Studies of hypervelocity firings into mixtures of hydrogen with air or with oxygen. *Symposium (International) on Combustion*, 10(1):245–252, 1965.

[8] J.C. Bellet and G. Deshayes. Structure and propagation of detonation in gaseous mixtures in supersonic flow. *Astronautica Acta*, 15:465–472, 1970.

[9] W. B. Benedick, C. M. Guirao, R. Knystautas, and J. H. S. Lee. Critical charge for the direct initiation of detonation in gaseous fuel-air mixtures. *Progress in Astronautics and Aeronautics*, 106:181–202, 1986.

[10] F. S. Billig. Shock-wave shapes around spherical- and cylindrical-nosed bodies. *Journal of Spacecraft and Rockets*, 4(6):822–823, 1967.

[11] J. Buckmaster. The structural stability of oblique detonation waves. *Combustion Science and Technology*, 72:283–296, 1990.

[12] J. Buckmaster and C. J. Lee. Flow refraction by an uncoupled shock and reaction front. *AIAA Journal*, 28(7):1310–1312, 1990.

[13] J. L. Cambier, H. G. Adelman, and G. P. Menees. Numerical simulations of oblique detonations in supersonic combustion chambers. *Journal of Propulsion and Power*, 5(4):482–491, 1989.

[14] S. Yu Chernyavskii, N. N. Baulin, and A. S. Mkrtumov. High-speed flow of a mixture of hydrogen and oxygen over blunt bodies. *Combustion, Explosion and Shock Waves*, 9(6):687–690, 1973.

[15] G. G. Chernyi and S. Yu Chernyavskii. Motion of blunt bodies with high velocity in mixtures of hydrogen and oxygen. *Soviet Physics - Doklady*, 18(9):596–597, 1974.

[16] G. G. Chernyi, S. Yu Chernyavskii, and N. N. Baulin. High-velocity motion of bodies in a hydrogen-air mixture. *Soviet Physics - Doklady*, 31:706–707, 1986.

[17] J. Y. Choi, I. S. Jeung, and S. Lee. Dimensional analysis of the effect of flow conditions on shock-induced combustion. *Symposium (International) on Combustion*, 26(2):2925–2932, 1996.

[18] J. Y. Choi, I. S. Jeung, and Y. Yoon. Computational fluid dynamics algorithms for unsteady shock-induced combustion. part 1: Validation. *AIAA Journal*, 38(7):1179–1187, 2000.

[19] J. Y. Choi, D. W. Kim, I. S. Jeung, M. Fuhua, and V. Yang. Cell-like structure of unstable oblique detonation wave from high-resolution numerical simulation. *Proceedings of the Combustion Institute*, 31(2):2473–2480, 2007.

[20] J. Y. Choi, E. J. R. Shin, and I. S. Jeung. Unstable combustion induced by oblique shock waves at the non-attaching condition of the oblique detonation wave. *Proceedings of the Combustion Institute*, 32(2):2387–2396, 2009.

[21] E. K. Dabora, D. Desbordes, C. Guerraud, and H. G. Wagner. Oblique detonation at hypersonic velocities. *Progress in Astronautics and Aeronautics*, 131:187–201, 1989.

[22] E. K. Dabora, J. A. Nicholls, and R. B. Morrison. The influence of a compressible boundary on the propagation of gaseous detonations. *Symposium (International) on Combustion*, 10(1):817–830, 1965.

[23] Yu Daimon and A. Matsuo. Detailed features of one-dimensional detonations. *Physics of Fluids*, 15(1):112–122, 2003.

[24] Yu Daimon and A. Matsuo. Unsteady features on one-dimensional hydrogen-air detonations. *Physics of Fluids*, 19(11):116101–13, 2007.

[25] D. Desbordes, L. Hamada, and C. Guerraud. Supersonic H2-air combustions behind oblique shock waves. *Shock Waves*, 4(6):339–345, 1995.

[26] R. Dudebout, J. P. Sislian, and R. Oppitz. Numerical simulation of hypersonic shock-induced combustion ramjets. *Journal of Propulsion and Power*, 14(6):869–879, 1998.

[27] R. Dunlap, R. L. Brehm, and J. A. Nicholls. Preliminary study of application of steady-state detonative combustion to reaction engine. *Jet Propulsion*, 28(7):451–456, 1958.

[28] C. A. Eckett, J. J. Quirk, and J. E. Shepherd. The role of unsteadiness in direct initiation of gaseous detonations. *Journal of Fluid Mechanics*, 421:147–183, 2000.

[29] G. Emanuel and D. G. Tuckness. Steady, oblique, detonation waves. Technical Report UTA-MAE Research Report 2002-01, University of Texas at Arlington - Mechanical and Aerospace Engineering, 2002.

[30] G. Emanuel and D. G. Tuckness. Steady, oblique, detonation waves. *Shock Waves*, 13(6):445–451, 2004.

[31] T. Endo, J. Kasahara, A. Takeishi, and T. Fujiwara. Experiments on oblique detonation waves around hypersonic cone-nosed projectiles. In *16th International Colloquium on the Dynamics of Explosions and Reactive Systems*, pages 473–476, Cracow, Poland, 1997.

[32] B. C. Fan, M. Sichel, and C. W. Kauffman. Analysis of oblique shock-detonation wave interactions in the supersonic flow of a combustible medium. In *AIAA 26th Aerospace Sciences Meeting*, Reno, Nevada, 1988.

[33] W. Fickett and W. C. Davis. *Detonation*. University of California Press, 1979.

[34] T. Fujiwara, A. Matsuo, and H. Nomoto. A two-dimensional detonation supported by a blunt body or a wedge. In *AIAA 26th Aerospace Sciences Meeting*, Reno, Nevada, 1988.

[35] G. Fusina, J. P. Sislian, and B. Parent. Formation and stability of near Chapman-Jouguet standing oblique detonation waves. *AIAA Journal*, 43(7):1591–1604, 2005.

[36] K. Ghorbanian and J. D. Sterling. Influence of formation processes on oblique detonation wave stabilization. *Journal of Propulsion and Power*, 12(3):509–517, 1996.

[37] S. M. Gilinskii and G. G. Chernyi. Supersonic flow of combustible gas mixture past sphere with account for ignition delay time. *Fluid Dynamics*, 3(1):12–19, 1968.

[38] M. Grismer and J. Powers. Numerical predictions of oblique detonation stability boundaries. *Shock Waves*, 6(3):147–156, 1996.

[39] R. A. Gross. Oblique detonation waves. *AIAA Journal*, 1(5):1225–1227, 1963.

[40] R. A. Gross and W. Chinitz. Study of supersonic combustion. *Journal of Aerospace Science*, 27(7):517–524, 1960.

[41] R. K. Hanson, J. M. Seitzman, and P. H. Paul. Planar laser-fluorescence imaging of combustion gases. *Applied physics. B: Photophysics and laser chemistry*, 50(6):441–454, 1990.

[42] P. G. Harris, R. Farinaccio, R. A. Stowe, R. Link, D. Alexander, L. Donahue, J. P. Sislian, and B. Parent. Structure of conical oblique detonation waves. In *44th AIAA/ASME/SAE/ASEE Joint Propulsion Conference and Exhibit*, Hartford, CT, 2008.

[43] L. He and P. Clavin. On the direct initiation of gaseous detonations by an energy source. *Journal of Fluid Mechanics*, 277:227–248, 1994.

[44] A. Hertzberg, A. P. Bruckner, and D. W. Bogdanoff. Ram accelerator: A new chemical method for accelerating projectiles to ultrahigh velocities. *AIAA Journal*, 26(2):195–203, 1988.

[45] A. Hertzberg, A. P. Bruckner, and C. Knowlen. Experimental investigation of ram accelerator propulsion modes. *Shock Waves*, 1(1):17–25, 1991.

[46] A. J. Higgins. *Investigation of detonation initiation by supersonic blunt bodies.* PhD thesis, University of Washington, 1996.

[47] A. J. Higgins. Ram accelerators: Outstanding issues and new directions. *Journal of Propulsion and Power*, 22(6):1170–1187, 2006.

[48] A. J. Higgins and A. P. Bruckner. Experimental investigation of detonation initiation by hypervelocity blunt projectiles. In *34th AIAA Aerospace Sciences Meeting*, Reno, NV, 1996.

[49] A. J. Higgins, M. I. Radulescu, and J. H. S. Lee. Initiation of cylindrical detonation by rapid energy deposition along a line. *Symposium (International) on Combustion*, 27(2):2215–2223, 1998.

[50] H. G. Hornung. Gradients at a curved shock in reacting flow. *Shock Waves*, 8(1):11–21, 1998.

[51] A. Hosangadi, B. J. York, N. Sinha, and S. M. Dash. Progress in transient interior ballistic flowfield simulations using multi-dimensional upwind/implicit numerics. In *29th AIAA/SAE/ASME/ASEE Joint Propulsion Conference and Exhibit*, Monterey, CA, 1993.

[52] P. Hung. *Algorithms for reaction mechanism reduction and numerical simulation of detonations initiated by projectiles.* PhD thesis, California Institute of Technology, 2003.

[53] Y. Ju, G. Masuya, and A. Sasoh. Numerical and theoretical studies on detonation initiation by a supersonic projectile. *Symposium (International) on Combustion*, 27(2):2225–2231, 1998.

[54] M. Kamel, C. I. Morris, M. C. Thurber, S. D. Wehe, and R. K. Hanson. New expansion tube facility for the investigation of hypersonic reactive flow. In *33rd Aerospace Sciences Meeting and Exhibit*, Reno, NV, 1995.

[55] M. R. Kamel, C. I. Morris, I. G. Stouklov, and R. K. Hanson. PLIF imaging of hypersonic reactive flow around blunt bodies. *Symposium (International) on Combustion*, 26(2):2909–2915, 1996.

[56] M. J. Kaneshige. *Gaseous detonation initiation and stabilization by hypervelocity projectile.* PhD thesis, California Institute of Technology, 1999.

[57] M. J. Kaneshige and J. E. Shepherd. Oblique detonation stabilized on a hypervelocity projectile. *Symposium (International) on Combustion*, 26(2):3015–3022, 1996.

[58] J. Kasahara, T. Arai, S. Chiba, K. Takazawa, Yu Tanahashi, and A. Matsuo. Criticality for stabilized oblique detonation waves around spherical bodies in acetylene/oxygen/krypton mixtures. *Proceedings of the Combustion Institute*, 29(2):2817–2824, 2002.

[59] J. Kasahara, T. Fujiwara, T. Endo, and T. Arai. Chapman-Jouguet oblique detonation structure around hypersonic projectiles. *AIAA Journal*, 39(8):1553–1561, 2001.

[60] J. Kasahara, T. Horii, T. Endo, and T. Fujiwara. Experimental observation of unsteady H2-O2 combustion phenomena around hypersonic projectiles using a multiframe camera. *Symposium (International) on Combustion*, 26(2):2903–2908, 1996.

[61] R. Knystautas and J. H. Lee. On the effective energy for direct initiation of gaseous detonations. *Combustion and Flame*, 27:221–228, 1976.

[62] V. P. Korobeinikov. *Problems of Point-Blast Theory.* American Institute of Physics, 1991.

[63] P. V. Kryukov. Review of investigations under way on the large-scale tsniimash ballistic facility. *International Journal of Impact Engineering*, 23(1, Part 1):501–508, 1999.

[64] D. Glenn Lasseigne and M. Y. Hussaini. Interaction of disturbances with an oblique detonation wave attached to a wedge. *Physics of Fluids A, Fluid Dynamics*, 5(4):1047–1058, 1993.

[65] J. H. Lee, R. Knystautas, and N. Yoshikawa. Photochemical initiation of gaseous detonations. *Acta Astronautica*, 5(11-12):971–982, 1978.

[66] J. H. S. Lee. Initiation of gaseous detonation. *Annual Review of Physical Chemistry*, 28(1):75–104, 1977.

[67] J. H. S. Lee. Dynamic parameters of gaseous detonations. *Annual Review of Fluid Mechanics*, 16:311–336, 1984.

[68] J. H. S. Lee. Initiation of detonation by a hypervelocity projectile. *Progress in Astronautics and Aeronautics*, 173:293–310, 1997.

[69] J. H. S. Lee. *The Detonation Phenomenon.* Cambridge University Press, 2008.

[70] J. H. S. Lee and A. J. Higgins. Comments on criteria for direct initiation of detonation. *Philosophical Transactions of the Royal Society of London. Series A: Mathematical, Physical and Engineering Sciences*, 357(1764):3503–3521, 1999.

[71] H. F. Lehr. Experiments on shock-induced combustion. *Astronautica Acta*, 17:589–597, 1972.

[72] C. Li, K. Kailasanath, and E. S. Oran. Detonation structures behind oblique shocks. *Physics of Fluids*, 6(4):1600–1611, 1994.

[73] J. Li, Z. Zhao, A. Kazakov, and F. L. Dryer. An updated comprehensive kinetic model of hydrogen combustion. *International Journal of Chemical Kinetics*, 36(10):566–575, 2004.

[74] R. D. Linnell and J. Z. Bailey. Similarity-rule estimation. methods for cones and parabolic noses. *Journal of the Aeronautical Sciences*, 23(8):796–797, 1956.

[75] J. C. Liu, J. J. Liou, M. Sichel, C. W. Kauffman, and J. A. Nicholls. Diffraction and transmission of a detonation into a bounding explosive layer. *Symposium (International) on Combustion*, 21(1):1639–1647, 1988.

[76] A. Matsuo and K. Fujii. Computational study of large-disturbance oscillations in unsteady supersonic combustion around projectiles. *AIAA Journal*, 33(10):1828–1835, 1995.

[77] A. Matsuo and K. Fujii. Numerical investigation of the one-dimensional piston supported detonation waves. *Energy Conversion and Management*, 38(10-13):1283–1295, 1997.

[78] A. Matsuo and K. Fujii. Prediction method of unsteady combustion around hypersonic projectile in stoichiometric hydrogen-air. *AIAA Journal*, 36(10):1834–1841, 1998.

[79] A. Matsuo, K. Fujii, and T. Fujiwara. Flow features of shock-induced combustion around projectile traveling at hypervelocities. *AIAA Journal*, 33(6):1056–1063, 1995.

[80] A. Matsuo and T. Fujiwara. Numerical prediction of mechanism on oscillatory instabilities in shock-induced combustion. *Progress in Astronautics and Aeronautics*, 154:516–531, 1991.

[81] A. Matsuo and T. Fujiwara. Numerical investigation of oscillatory instability in shock-induced combustion around a blunt body. *AIAA Journal*, 31(10):1835–1841, 1993.

[82] B. J. McBride and S. Gordon. Computer program for calculation of complex chemical equilibrium compositions and applications. Technical Report NASA RP-1311, Lewis Research Center, 1996.

[83] W. W. McKenna. Interaction between detonation waves and flowfields. *AIAA Journal*, 5(5):868–873, 1967.

[84] J. B. McVey and T. Y. Toong. Mechanism of instabilities of exothermic hypersonic blunt-body flows. *Combustion Science and Technology*, 3:63–76, 1971.

[85] C. I. Morris, M. Kamel, M. C. Thurber, S. D. Wehe, and R. K. Hanson. Development of an expansion tube for investigation of combustion in supersonic projectile flowfields. In *31st AIAA/ASME/SAE/ASEE Joint Propulsion Conference*, San Diego, CA, 1995.

[86] C. I. Morris, M. R. Kamel, and R. K. Hanson. Shock-induced combustion in high-speed wedge flows. *Symposium (International) on Combustion*, 27(2):2157–2164, 1998.

[87] H. D. Ng and J. H. S. Lee. Direct initiation of detonation with a multi-step reaction scheme. *Journal of Fluid Mechanics*, 476:179–211, 2003.

[88] J. A. Nicholls. Standing detonation waves. *Symposium (International) on Combustion*, 9(1):488–498, 1963.

[89] J. A. Nicholls, E. Dabora, and R. Gealler. Studies in connection with stabilized gaseous detonation waves. *Symposium (International) on Combustion*, 7(1):766–772, 1958.

[90] M. V. Papalexandris. A numerical study of wedge-induced detonations. *Combustion and Flame*, 120:526–538, 2000.

[91] B. Parent and J. P. Sislian. Hypersonic mixing enhancement by compression at a high convective mach number. *AIAA Journal*, 42(4):787–795, 2004.

[92] J. M. Powers and K. A. Gonthier. Reaction zone structure for strong, weak overdriven, and weak underdriven oblique detonations. *Physics of Fluids A, Fluid Dynamics*, 4(9):2082–2089, 1992.

[93] J. M. Powers and D. Scott Stewart. Approximate solutions for oblique detonations in the hypersonic limit. *AIAA Journal*, 30(3):726–736, 1992.

[94] D. T. Pratt, J. W. Humphrey, and D. E. Glenn. Morphology of standing oblique detonation waves. *Journal of Propulsion and Power*, 7(5):837–845, 1991.

[95] H. N. Presles and P. Bauer. Detonation products gun. *Review of Scientific Instruments*, 54(11):1511–1512, 1983.

[96] J. J. Quirk. A parallel adaptive grid algorithm for computational shock hydrodynamics. *Applied Numerical Mathematics*, 20(4):427–453, 1996.

[97] M. I. Radulescu, A. J. Higgins, J. H. S. Lee, and S. B. Murray. On the explosion length invariance in direct initiation of detonation. *Proceedings of the Combustion Institute*, 28(1):637–644, 2000.

[98] M. I. Radulescu, A. J. Higgins, S. B. Murray, and J. H. S. Lee. An experimental investigation of the direct initiation of cylindrical detonations. *Journal of Fluid Mechanics*, 480:1–24, 2003.

[99] J. K. Richmond and R. P. Shreeve. Wind-tunnel measurements of ignition delay using shock-induced combustion. *AIAA Journal*, 5(10):1777–1784, 1967.

[100] P. M. Rubins and R. C. Bauer. Review of shock-induced supersonic combustion research and hypersonic applications. *Journal of Propulsion and Power*, 10(5):593–601, 1994.

[101] P. M. Rubins and T. H. M. Cunningham. Shock-induced supersonic combustion in constant-area duct. *Journal of Spacecraft and Rockets*, 2(2):199–205, 1965.

[102] P. M. Rubins and R. P. Rhodes Jr. Shock-induced combustion with oblique shocks – comparison of experiment and kinetic calculations. *AIAA Journal*, 1(12):2778–2784, 1963.

[103] F. W. Ruegg and W. W. Dorsey. A missile technique for the study of detonation waves. *Journal of Research of the National Bureau of Standards - C. Engineering and Instrumentation*, 66C(1):51–58, 1962.

[104] T. E. Schwartzentruber, J. P. Sislian, and B. Parent. Suppression of premature ignition in the premixed inlet flow of a shcramjet. *Journal of Propulsion and Power*, 21(1):87–94, 2005.

[105] L. I. Sedov. *Similarity and Dimensional Methods in Mechanics.* New York: Academic Press, 4th edn. academic edition, 1959.

[106] F. Seiler, G. Patz, G. Smeets, and J. Srulijes. Progress of ram acceleration with ISL's ramac 30. *Journal De Physique. IV France*, 10:Pr11–31 – Pr11–40, 2000.

[107] J. P. Sislian, R. P. Martens, T. E. Schwartzentruber, and B. Parent. Numerical simulation of a real shcramjet flowfield. *Journal of Propulsion and Power*, 22(5):1039–1048, 2006.

[108] J. P. Sislian and F. Y. Zhang. Simulation of conical detonation waves. In *Symposium on Interdisciplinary Shock Wave Research*, pages 449–461, Sendai, Japan, 2004.

[109] W. P. Sommers. Gaseous detonation wave interactions with nonrigid boundaries. *ARS Journal*, 31:1780–1782, 1961.

[110] W. P. Sommers and R. B. Morrison. Simulation of condensed-explosive detonation phenomena with gases. *Physics of Fluids*, 5(2):241–248, 1962.

[111] R. A. Strehlow. *Combustion Fundamentals.* McGraw-Hill, 1984.

[112] R. A. Strehlow, R. Liangminas, R. H. Watson, and J. R. Eyman. Transverse wave structure in detonations. *Symposium (International) on Combustion*, 11(1):683–692, 1967.

[113] W. Struth. Kurzzeitaufnahmen von schssen mit hyperschallgeschwindigkeit in reagierende gase. In *Proceedings of the Sixth International Congress on High-Speed Photography*, The Hague/Scheveningen (Netherlands), 1962.

[114] M. O. Sturtzer, K. Togami, S. Yamashita, and K. Takayama. Detonation wave generated by a hypervelocity projectile. *Heat Transfer Research*, 38(4):291–297, 2007.

[115] M. A. Sussman. A computational study of unsteady shock induced combustion of hydrogen-air mixtures. In *30th AIAA/ASME/SAE/ASEE Joint Propulsion Conference*, Indianapolis, IN, 1994.

[116] G. Taylor. The formation of a blast wave by a very intense explosion. i. theoretical discussion. *Proceedings of the Royal Society of London. Series A. Mathematical and Physical Sciences*, 201:159–174, 1950.

[117] A. A. Thaker and H. K. Chelliah. Numerical prediction of oblique detonation wave structures using detailed and reduced reaction mechanisms. *Combustion Theory and Modelling*, 1(4):347–376, 1997.

[118] N. A. Tonello, M. Sichei, and C. W. Kauffman. Mechanisms of detonation transmission in layered H2-O2 mixtures. *Shock Waves*, 5(4):225–238, 1995.

[119] R. L. Trimpi. A preliminary theoretical study of the expansion tube, a new device for producing high-enthalpy short-duration hypersonic gas flows. Technical Report NASA-TR-R-133, Langley Research Center, 1962.

[120] A. A. Vasiljev. Initiation of gaseous detonation by a high speed body. *Shock Waves*, 3(4):321–326, 1994.

[121] J. Verreault, P. Batchelor, and A. J. Higgins. Development of a detonation-driven gas gun capable of 3 km/s projectile velocity. In *27th International Symposium on Shock Waves*, St-Petersburg, Russia, 2009.

[122] C. Viguier, L. F. Figueira da Silva, D. Desbordes, and B. Deshaies. Onset of oblique detonation waves: comparison between experimental and numerical results for hydrogen-air mixtures. *Symposium (International) on Combustion*, 26(2):3023–3031, 1996.

[123] C. Viguier, A. Gourara, and D. Desbordes. Three-dimensional structure of stabilization of oblique detonation wave in hypersonic flow. *Symposium (International) on Combustion*, 27(2):2207–2214, 1998.

[124] C. Viguier, C. Guerraud, and D. Desbordes. H2-air and CH4-air detonations and combustions behind oblique shock waves. *Symposium (International) on Combustion*, 25(1):53–59, 1994.

[125] M. A. T. Walter and L. F. Figueira da Silva. Numerical study of detonation stabilization by finite length wedges. *AIAA Journal*, 44(2):353–361, 2006.

[126] S. D. Watt and G. J. Sharpe. Linear and nonlinear dynamics of cylindrically and spherically expanding detonation waves. *Journal of Fluid Mechanics*, 522:329–356, 2005.

[127] G. J. Wilson and M. A. Sussman. Computation of unsteady shock-induced combustion using logarithmic species conservation equations. *AIAA Journal*, 31(2):294–301, 1993.

[128] J. Yao and D. S. Stewart. On the normal detonation shock velocity-curvature relationship for materials with large activation energy. *Combustion and Flame*, 100(4):519–528, 1995.

[129] S. Yungster and K. Radhakrishnan. A fully implicit time accurate method for hypersonic combustion: application to shock-induced combustion instability. *Shock Waves*, 5(5):293–303, 1996.

[130] Ya. B. Zeldovich and O. Leipunskii. A study of chemical reactions in shock waves. *Acta Physicochimica U.R.S.S.*, 18(2-3):167–171, 1943.

[131] Ya. B. Zeldovich and I. Ia Shliapintoch. Initiation of explosive gaseous mixtures in shock waves. *Doklady Akademii Nauk SSSR*, 65(6):871–874, 1949.

[132] M. J. Zucrow and J. D. Hoffman. *Gas Dynamics, Vol. 2: Multidimensional Flow.* John Wiley & Sons Inc, 1977.

APPENDIX A
Facility Photographs

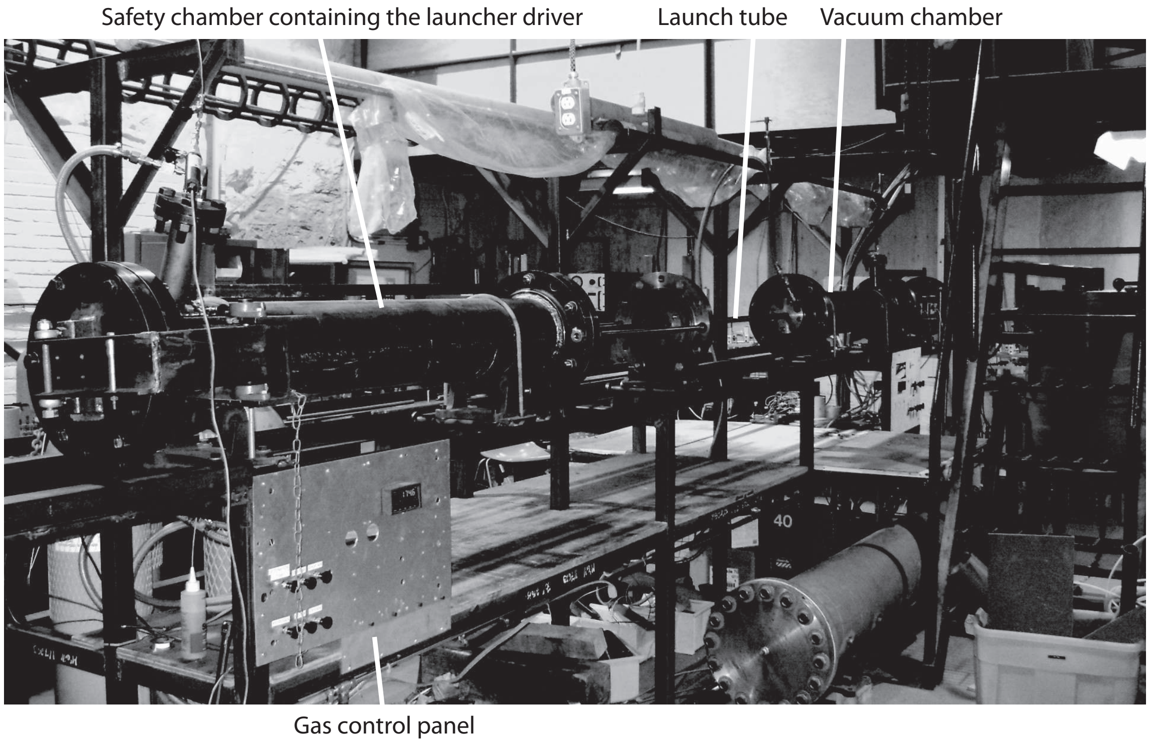

Figure A–1: Detonation-driven gas launcher

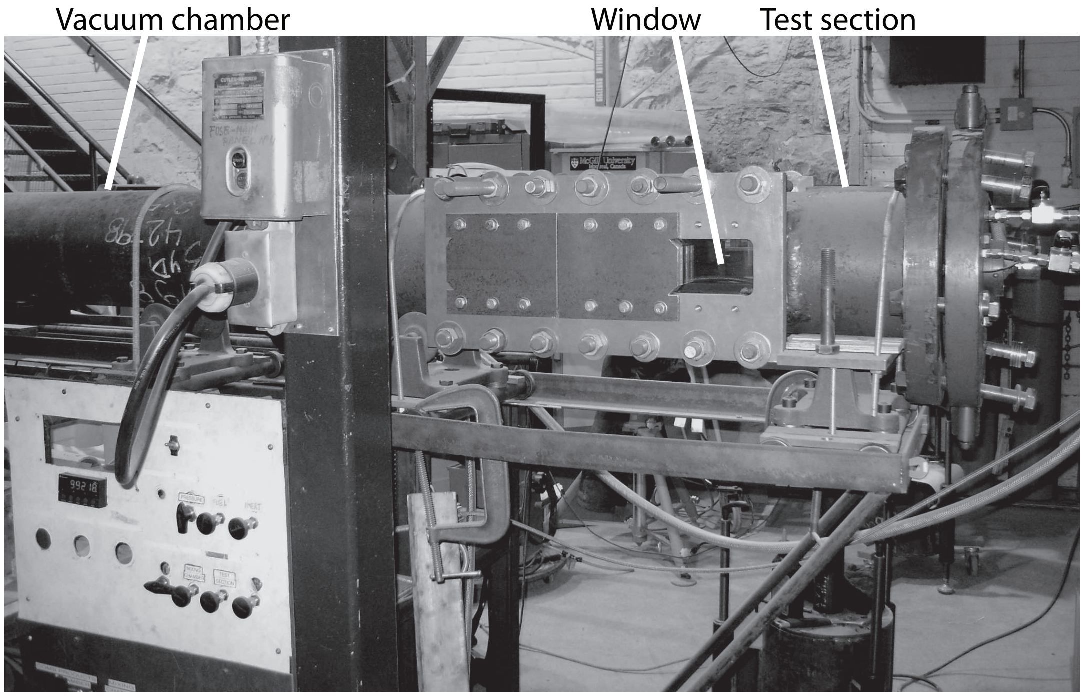

Figure A–2: Test section

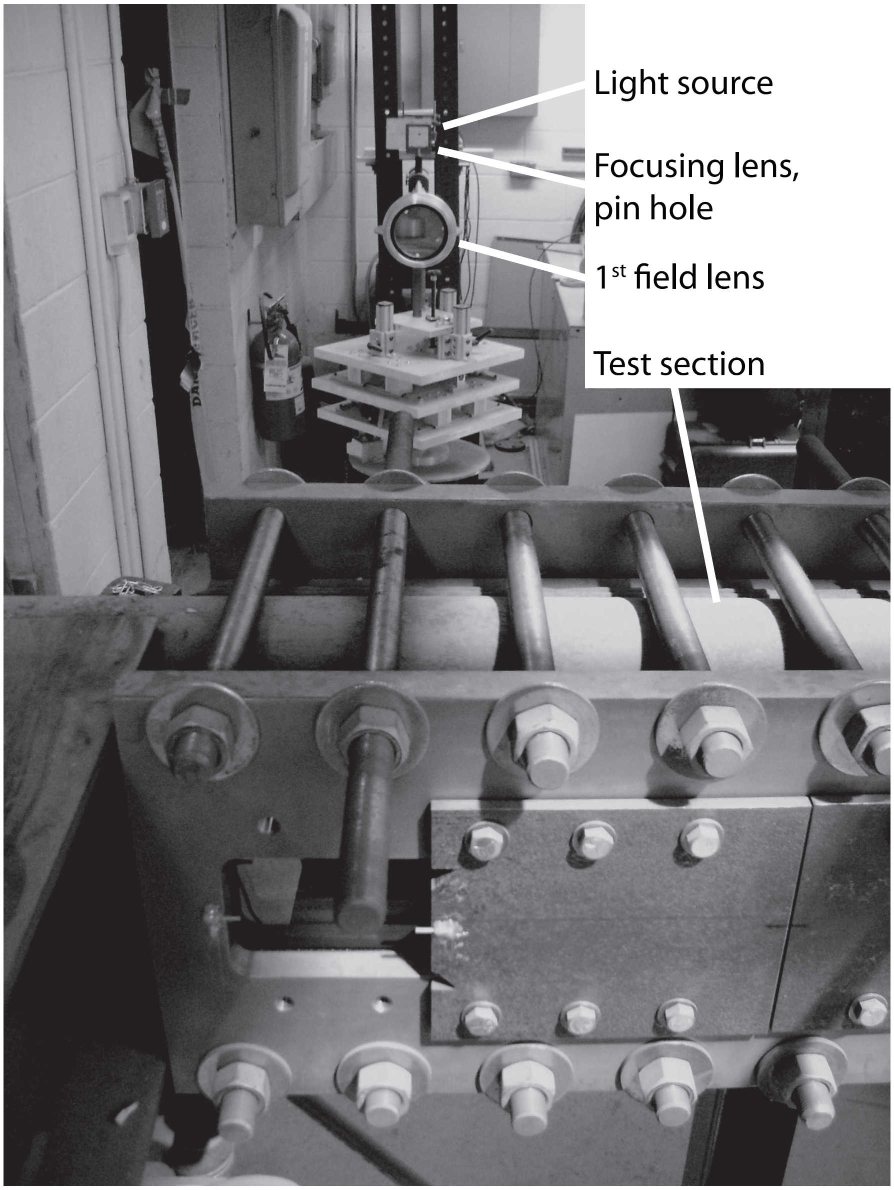

Figure A–3: Schlieren setup (light source side)

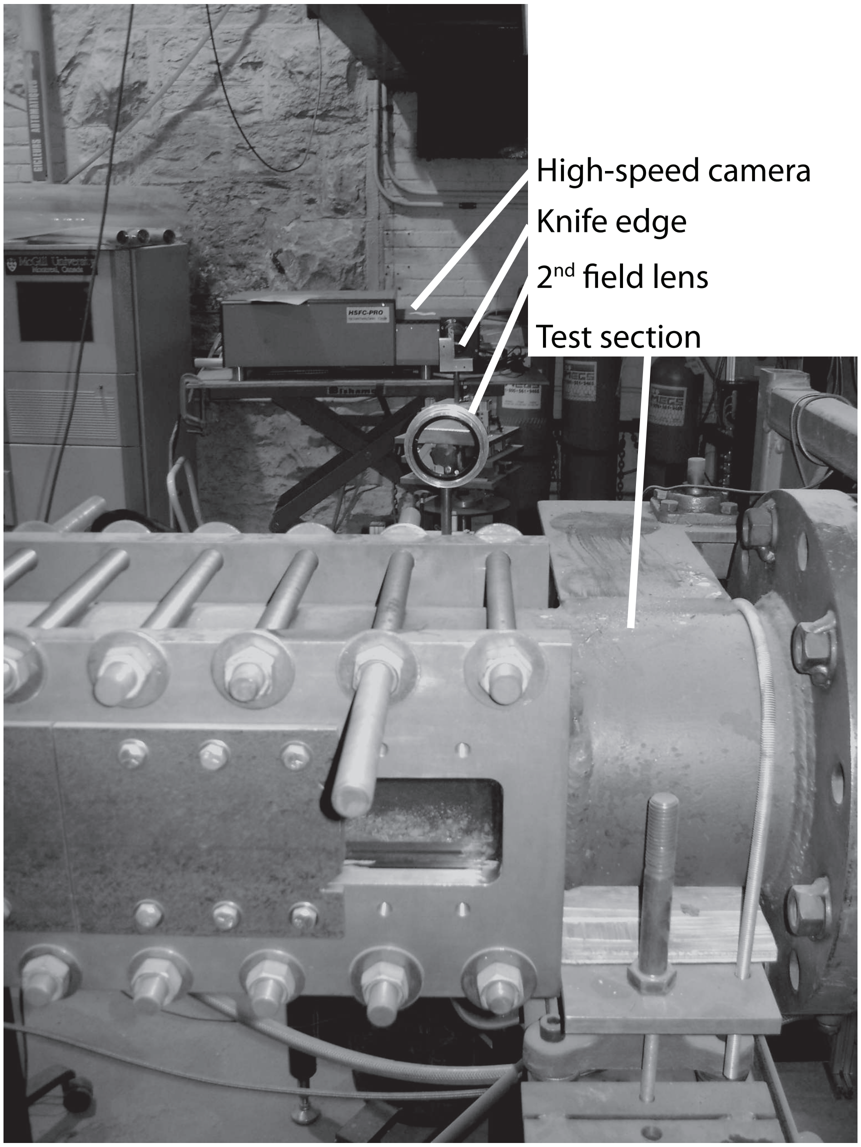

Figure A–4: Schlieren setup (camera side)

APPENDIX B
Discussion on the Experiments and Schlieren Photographs

A discussion on each experiment, classified by their combustion regime, is given below. The experimental conditions for all the experiments are provided in Table B–1 and the Schlieren photographs can be found at the end of this Appendix.

B.1 Discussion on the Prompt ODW Experiments

Shot 140; Fig. B–8. In this experiment, an ODW is attached at the tip of the cone and the angle of the ODW is constant in the three frames. However, the projectile velocity (1 690 m/s) is slightly lower than the CJ velocity (1 709 m/s). The detonation is thus expected to outrun the projectile. This observation was further addressed in Section 4.3. From Fig. B–8, the shape of the projectile seems to be smeared; the body diameter being smaller at the back and the cone surface being curved. The projectile material was probably eroded during its acceleration in the launch tube, and the cone can be rotated in such a way that the tip of the cone points towards or away from the observer, which explains the apparently curved surface.

Shots 164 and 166; Figs. B–23 and B–24. The flowfield of these two experiments is very similar. An ODW is attached a the tip of the cone. It can be observed that in each frame, the angle of the ODW is slightly smaller near the cone than in the farfield. The complete coupling between the reaction front and the oblique shock therefore occurs a certain distance away from the cone tip. However, the induction zone is not as clear as it is for Shot 154 (Fig. 4–3) and for this reason, Shots 164 and 166 were interpreted as cases of prompt ODW. Some luminosity is observed on the projectile surface, which is probably caused by ablation and reaction of the solid material with the gases of the test mixture.

Shots 146 and 170; Figs. B–11, B–28 and B–29. Shot 146 was discussed previously with Fig. 4–2. Shot 170 presents similar features since the ODW angle in front of the cone is larger than in the farfield, showing an overdriven ODW on a cone decaying to a self-sustained CJ ODW in the farfield. It is difficult to conclude whether the detonation is detached (and normal) in front of the cone. However, the standoff distance being nearly negligible, the ODW is assumed to be attached. The expected ODW angle based on a polar analysis was given in Section 5.2.2.

Shots 130 and 160; Figs. B–2 and B–19. For these two experiments, a normal overdriven detonation in front of the projectile nose switches to a self-sustained ODW in the farfield. In Shot 130, the projectile is significantly canted, but the ODW is symmetrical above and below the flight axis. Therefore, the shape of the projectile nose and its angle of attack are assumed to play a minor role in this case for the initiation of an ODW. The bluntness of the cone and the high mixture pressure contribute to this outcome. In Shot 160, the flow pattern behind the projectile is similar to the combustion instabilities shown in Fig. 4–4. However, in the third frame of Fig. B–19, the ODW is almost straight in the farfield and no decoupling between the reaction front and the oblique shock can be seen, which leads to the identification of the prompt ODW regime.

B.2 Discussion on the Delayed ODW Experiments

Shot 154; Fig. B–14. The third frame of this shot was described earlier with Fig. 4–3. According to the frames shown in Fig. B–14, the location of the triple point fluctuates back and forth along the cone surface. Despite this oscillation, it is interesting to observe the symmetry, above and below the flight axis, of the flowfield.

Shot 155; Fig. B–15. In this experiment, the features of the flowfield seem to be constant in the first three frames. At the tip of the cone, an inert oblique shock is observed. Steepening of the shock occurs at approximately one third of the cone length, where an oblique shock pattern can be seen between the cone surface and the external oblique shock (see the third frame). Near the projectile shoulder, the external oblique shock again steepens, corresponding to the onset of the ODW. The origin of the transition region between the inert shock and the onset of the ODW is undetermined. One can stipulate that a competing effect takes place between the coupling of the reaction front with the oblique shock and the large curvature of the shock around the cone which tends to quench the chemical reactions. This curvature effect was considered in Section 7.3.2.

Shot 153; Fig. B–13. Shot 153 shows the interesting case where the nose of the projectile (made of polycarbonate plastic) detaches from its titanium shell which trails far behind. Surprisingly, the angle of attack of the nose is almost null and it provides a successful data point. A short induction zone is seen at the tip of the cone and the triple point is located at approximately one fourth of the cone length. A straight ODW takes place in the farfield.

Shot 162; Fig. B–21. This shot is probably the most intriguing of the whole campaign. An oblique shock is attached at the tip of the cone. At one third of the cone length, a different combustion regime occurs, similar to the combustion instabilities regime. In this region, the oblique shock is only slightly steeper than at the cone tip. Downstream of the projectile shoulder, the combustion instabilities regime becomes a self-sustained ODW that propagates in the farfield. The original features of this flowfield are not well understood. Undoubtedly, combustion initiation and quenching phenomena occur in the transition region between the inert shock and the ODW. The combustion oscillations probably increase the turbulence level, which is required to trigger the ODW.

B.3 Discussion on the Combustion Instabilities Experiments

Shots 134, 159 and 171; Figs. B–3, B–18, B–30 and B–31. Shot 171 was described earlier with Fig. 4–4. Shot 134 reveals very similar features since significant density variations are observed, as well as the decoupling of the combustion instabilities from the shock above and below the projectile. This type of flowfield also characterizes Shot 159 with a higher instabilities frequency.

Shots 136 and 151; Figs. B–5 and B–12. The combustion instabilities regime was also obtained for Shots 136 and 151 with large density oscillations and decoupling of the pulsations from the oblique shock. However, the projectile was flying at a slight angle of attack. Due to the fact that no noticeable difference can be seen between the top half and the bottom half of the flowfield (in other words, the flowfield seems symmetrical around the flight axis), it was concluded that a projectile flying straight at the same flow conditions would produce the same combustion regime.

Shot 129; Fig. B–1. In this experiment, combustion instabilities are observed behind the oblique shock, but the decoupling between the oscillations and the shock is not observed. This flowfield resembles that of Shot 160 (Fig. B–19) defined as a prompt ODW. However, in Shot 129, a kink can be observed along the front at the top half of the figure, and the front is continuously curved at the bottom half. These two features are an indication that the reaction front fails to completely couple with the shock and thus fails to initiate an ODW.

Shot 135; Fig. B–4. In the second frame of Shot 135, a smooth reaction front decouples from the oblique shock near the shoulder of the projectile. Near the back of the projectile, two striations can be seen at the boundary of the reacted gas envelope, in the form of the regular regime of McVey and Toong [84]. In the third frame, the combustion instabilities around the projectile are extinguished and only the decoupling smooth reaction front remains. This flowfield seems to be at the boundary between the combustion instabilities regime and the wave splitting regime.

B.4 Discussion on the Wave Splitting Experiments

Shots 137 and 156; Figs. B–6 and B–16. Shot 156 was described earlier with Fig. 4–5. In Shot 137, wave splitting can be seen, along with instabilities near the tip of the cone in both the second and third frames. This flowfield seems to be at the boundary between the combustion instabilities regime and the wave splitting regime. Since no combustion oscillations in the form of the large-disturbance or the regular regimes are observed behind the projectile, this experiment was referred to as the wave splitting regime.

B.5 Discussion on the Inert Shock Experiments

Shots 141, 157, 161 and 163; Figs. B–9, B–17, B–20 and B–22. Shot 163 was described earlier with Fig. 4–6. These 4 shots show very clean flowfields where the projectile flies straight and an inert conical shock is attached at the tip of the cone without any visible combustion activity around and behind the projectile.

Shots 139 and 142; Figs. B–7 and B–10. In both Shots 139 and 142, the projectile flies at an angle of attack of approximately 9°. The flowfield is significantly asymmetrical with respect to the flight axis. However, downstream of the strongest shock wave (above the projectile in Shot 139 and below the projectile in Shot 142), no combustion is initiated. Therefore, it was assumed that the inert shock regime would be obtained, had the projectile flown straight.

Shot 167; Fig. B–25. Shot 167 shows a case where the front part of the projectile (made of polycarbonate plastic) detached from the titanium shell during the acceleration in the launched tube. Interestingly, the front part flew straight and the inert shock regime is observed.

Shots 168 and 169; Figs. B–26 and B–27. For both Shots 168 and 169, some luminosity can be observed in the early frames, which seems to vanish in the last frames of both experiments. Furthermore, in Shot 169, some wrinkles can be seen in front of the cone nose. This indicates that combustion phenomena occur locally at the cone nose. However, neither combustion instabilities nor a decoupling smooth reaction front can be observed around and behind the projectile. Therefore, the local combustion activity occurring in the early frames is assumed to be a transitional phenomenon and the last frames of both shots reveal the inert shock regime.

Table B–1: Experimental conditions for all experiments

Shot #	Cone half angle (°)	Mixture pressure (kPa)	Projectile velocity (m/s)	Combustion regime
129	45	80	2 150	comb. inst.
130	60	159	1 750	prompt ODW
134	45	97	1 720	comb. inst.
135	60	46	1 790	comb. inst.
136	45	61	1 850	comb. inst.
137	30	68	1 930	wave splitting
139	20	200	1 810	inert shock
140	30	200	1 690	prompt ODW
141	20	202	1 600	inert shock
142	20	183	1 530	inert shock
146	40	101	2 180	prompt ODW
151	60	65	1 980	comb. inst.
153	25	126	2 200	delayed ODW
154	25	120	1 740	delayed ODW
155	20	130	1 900	delayed ODW
156	25	80	1 900	wave splitting
157	15	124	1 920	inert shock
159	60	76	1 870	comb. inst.
160	60	95	1 850	prompt ODW
161	45	10	1 880	inert shock
162	20	150	1 970	delayed ODW
163	20	63	2 060	inert shock
164	30	151	1 830	prompt ODW
166	25	190	2 100	prompt ODW
167	15	151	1 950	inert shock
168	45	33	1 930	inert shock
169	60	20	1 850	inert shock
170	45	102	1 830	prompt ODW
171	35	81	1 790	comb. inst.

Shot 129

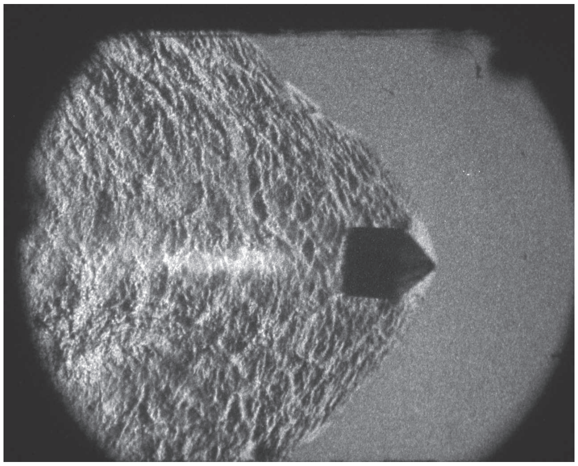

Figure B–1: Shot 129

Shot 130

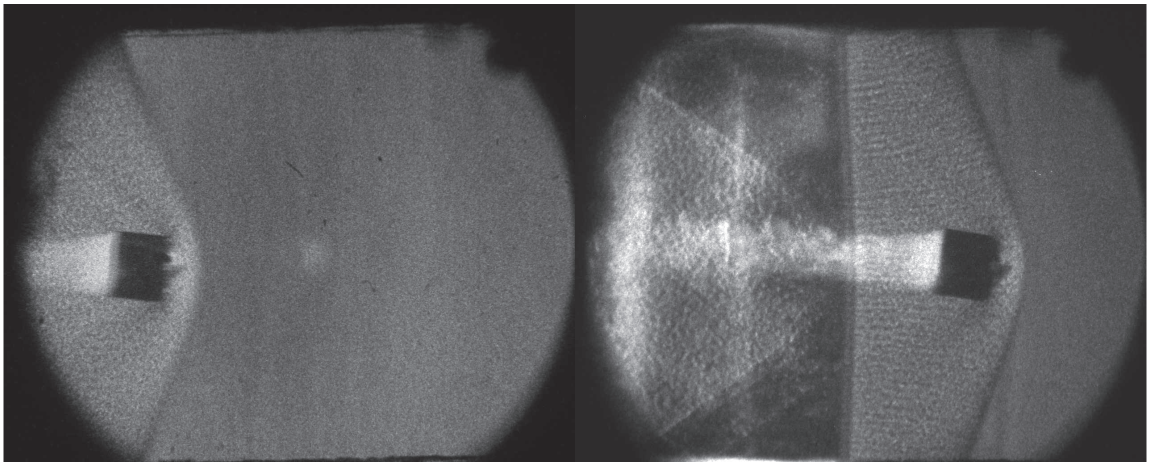

Figure B–2: Shot 130

Shot 134

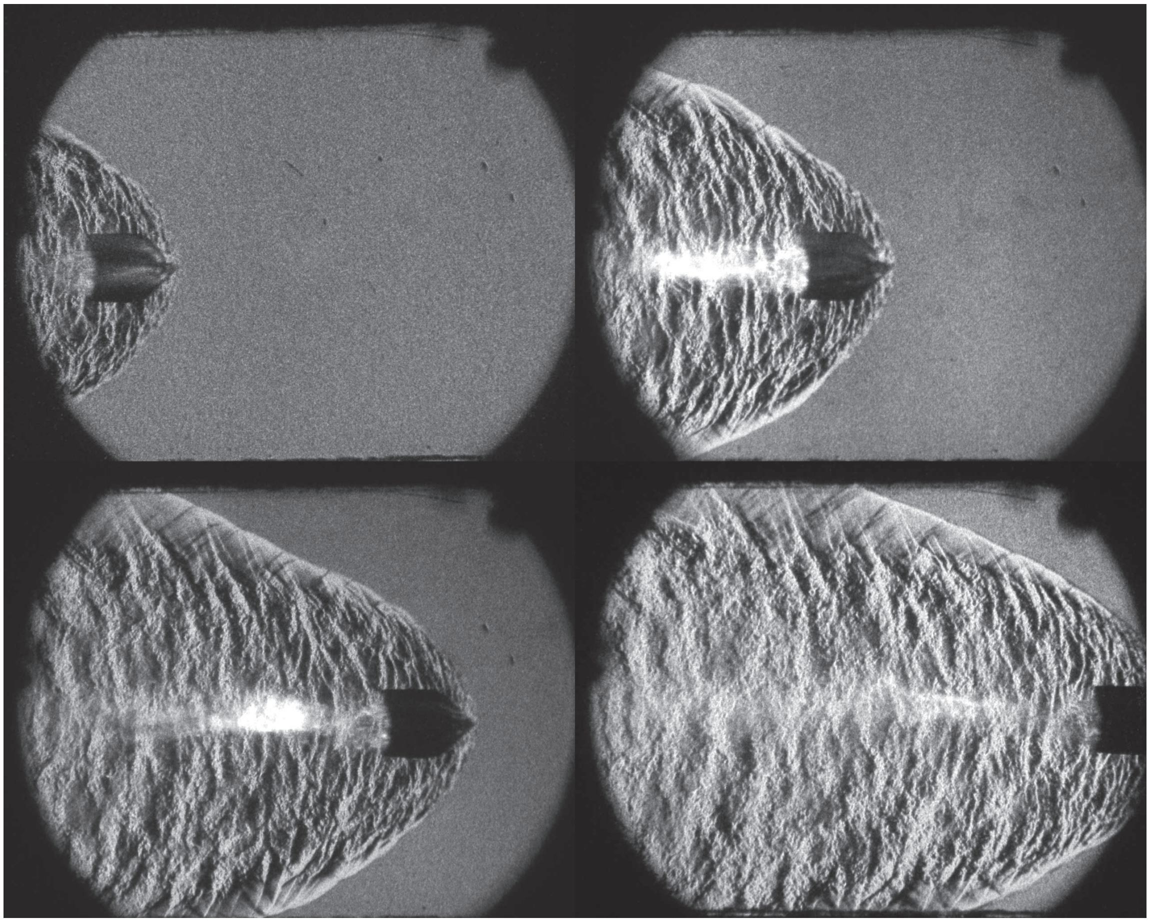

Figure B–3: Shot 134

Shot 135

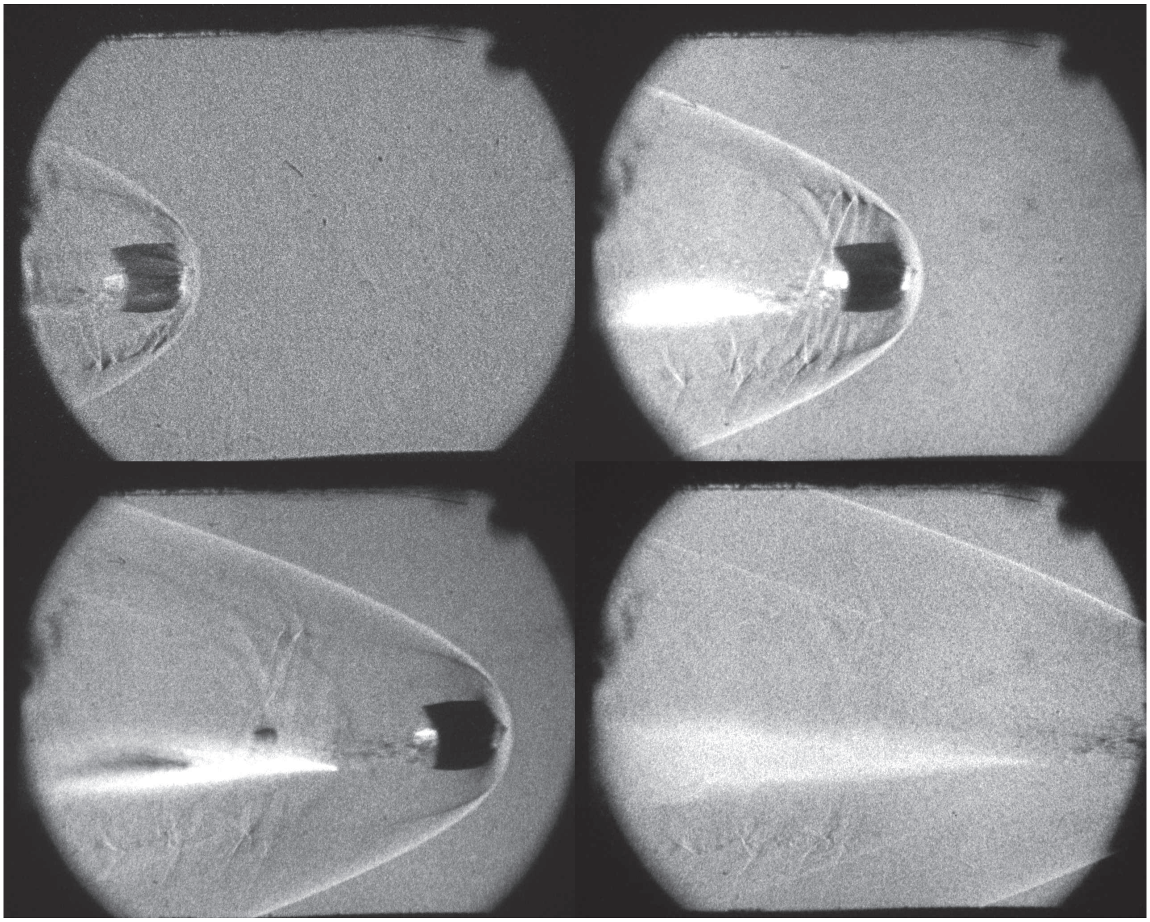

Figure B–4: Shot 135

Shot 136

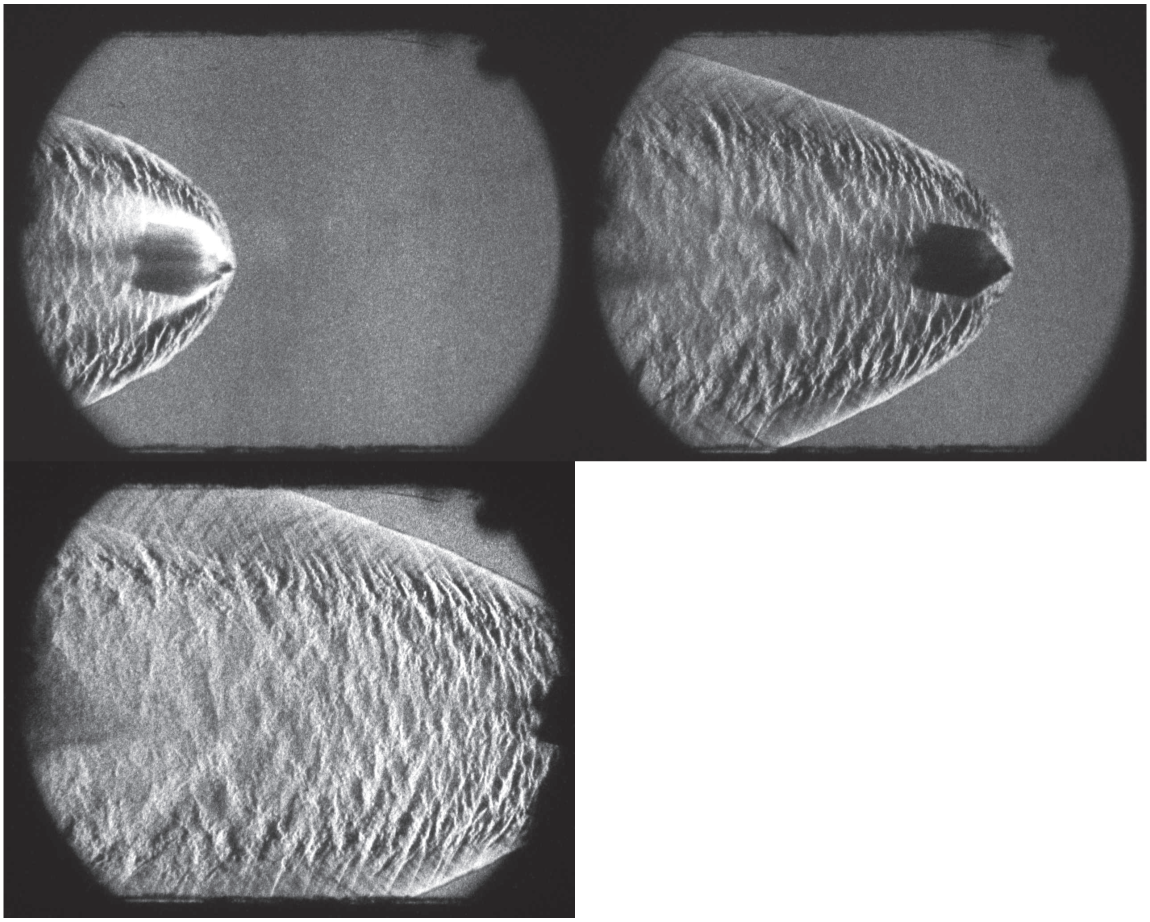

Figure B–5: Shot 136

Shot 137

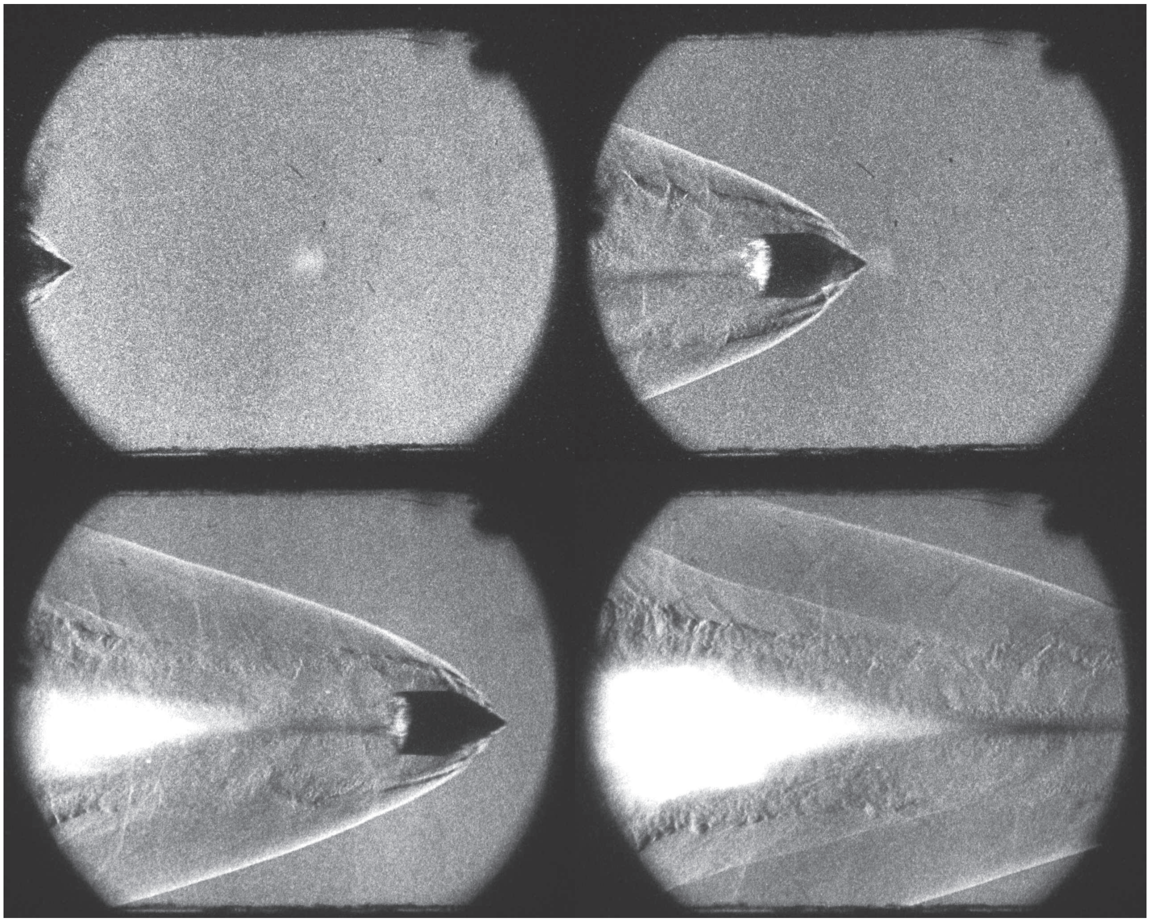

Figure B–6: Shot 137

Shot 139

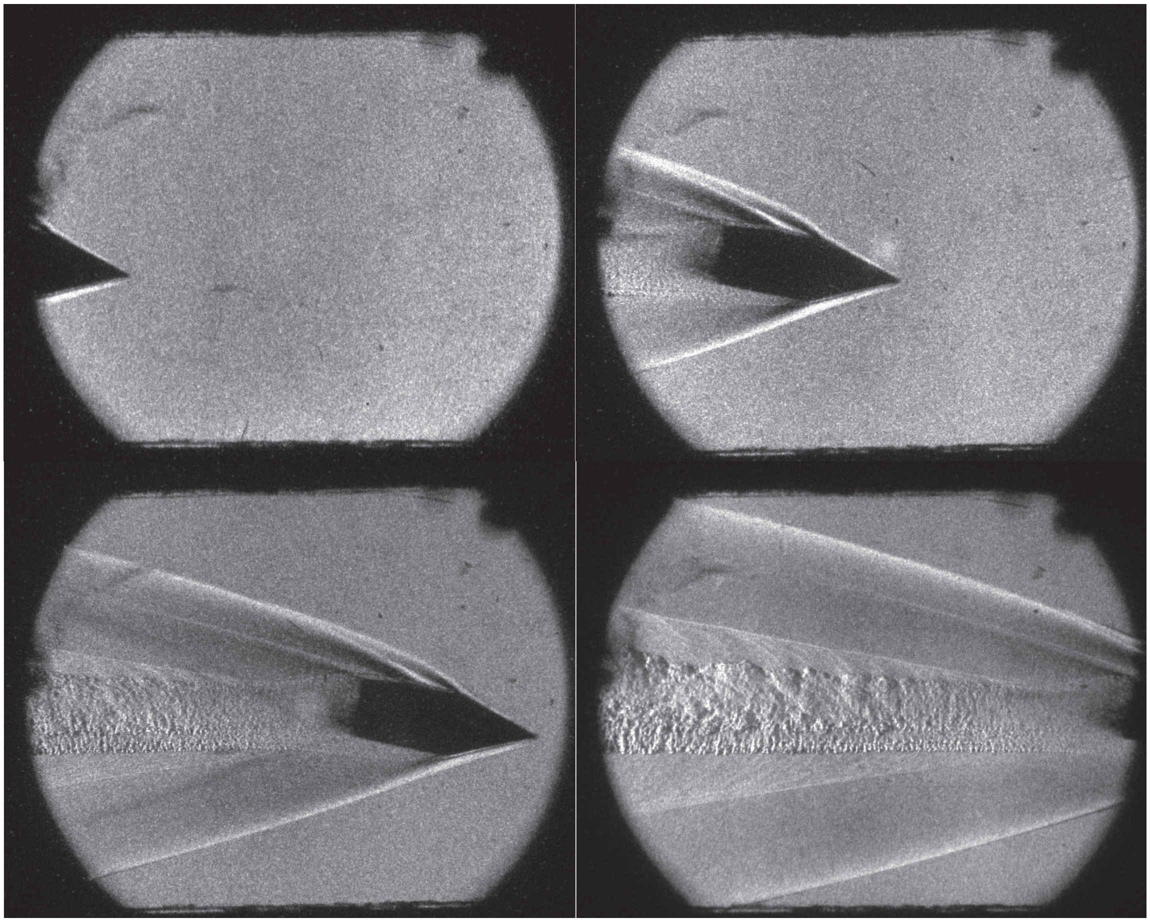

Figure B–7: Shot 139

Shot 140

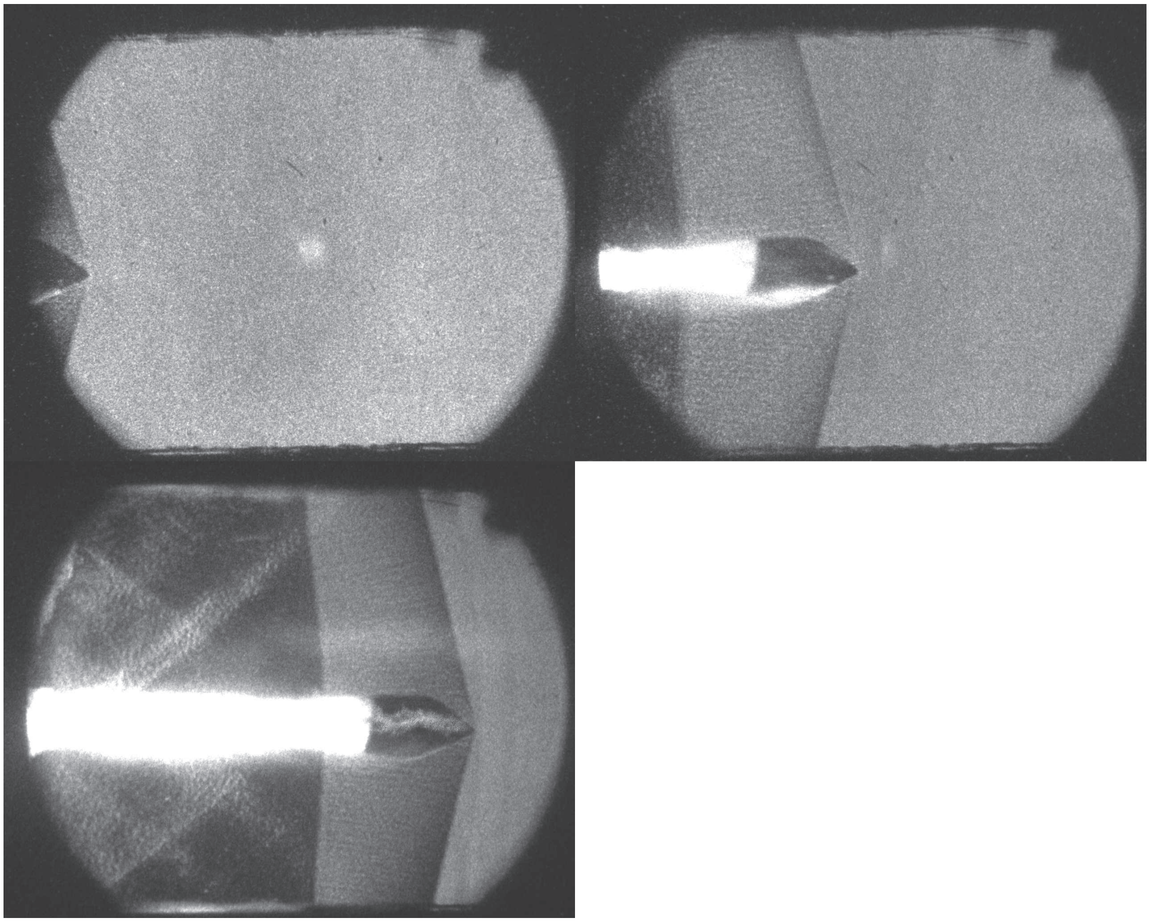

Figure B–8: Shot 140

Shot 141

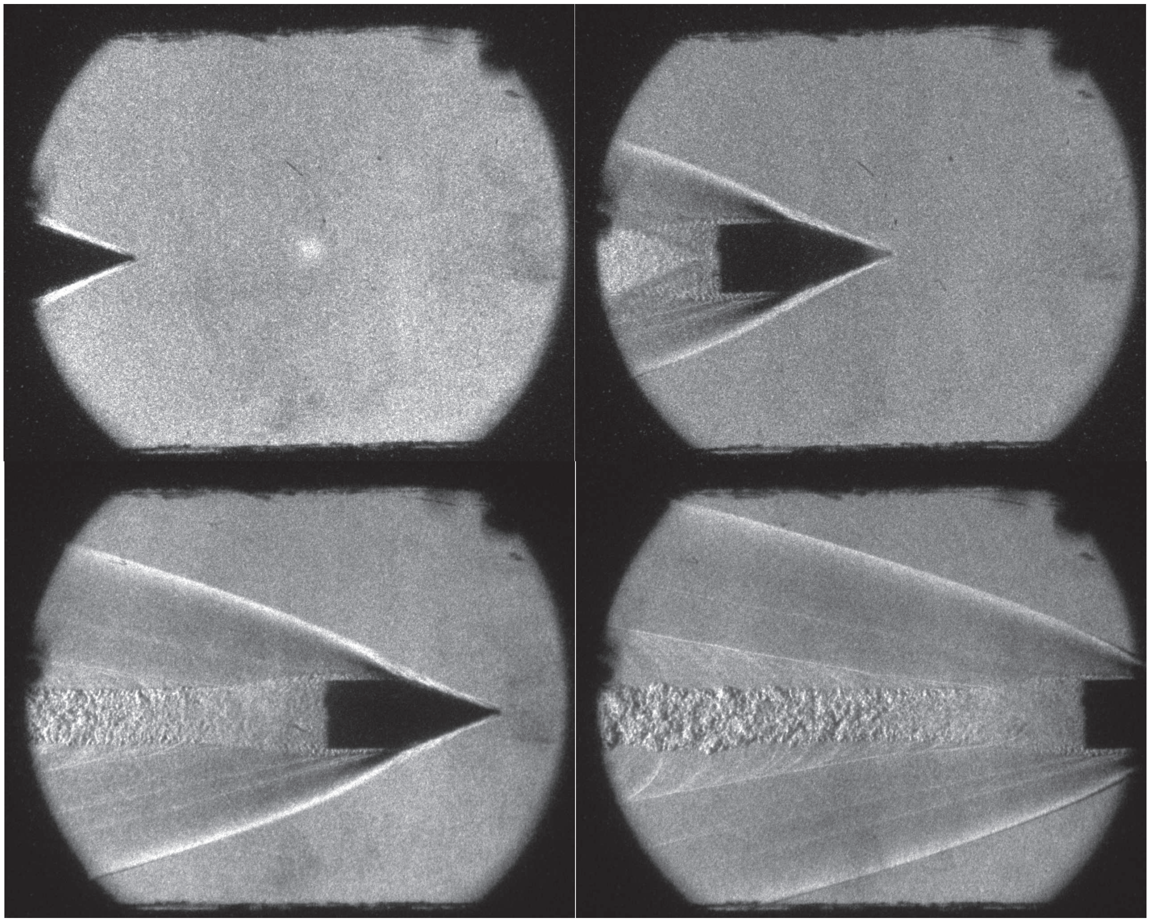

Figure B–9: Shot 141

Shot 142

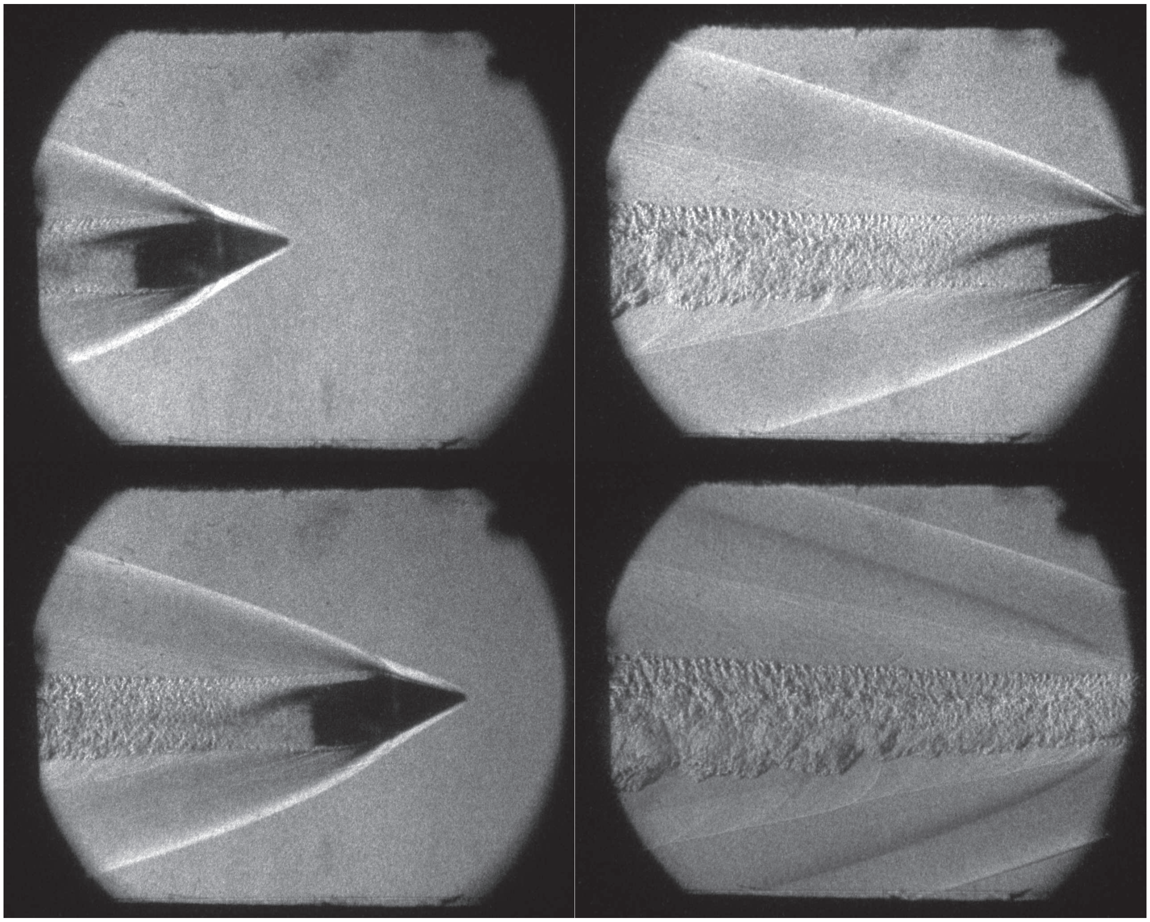

Figure B–10: Shot 142

Shot 146

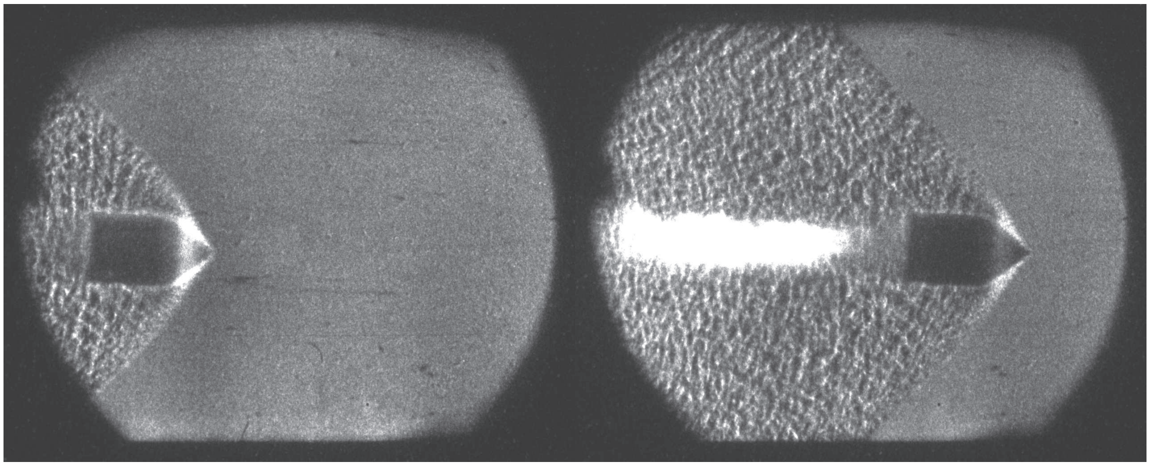

Figure B–11: Shot 146

Shot 151

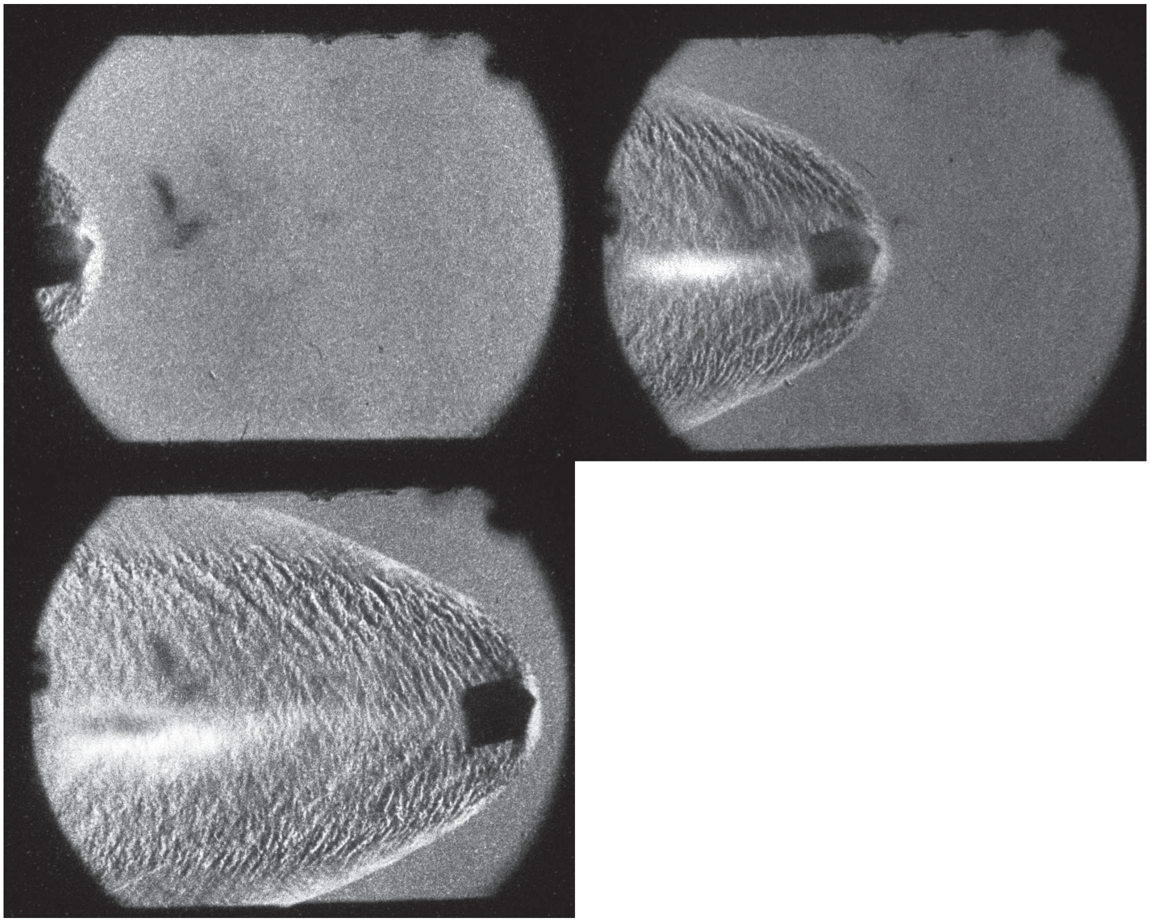

Figure B–12: Shot 151

Shot 153

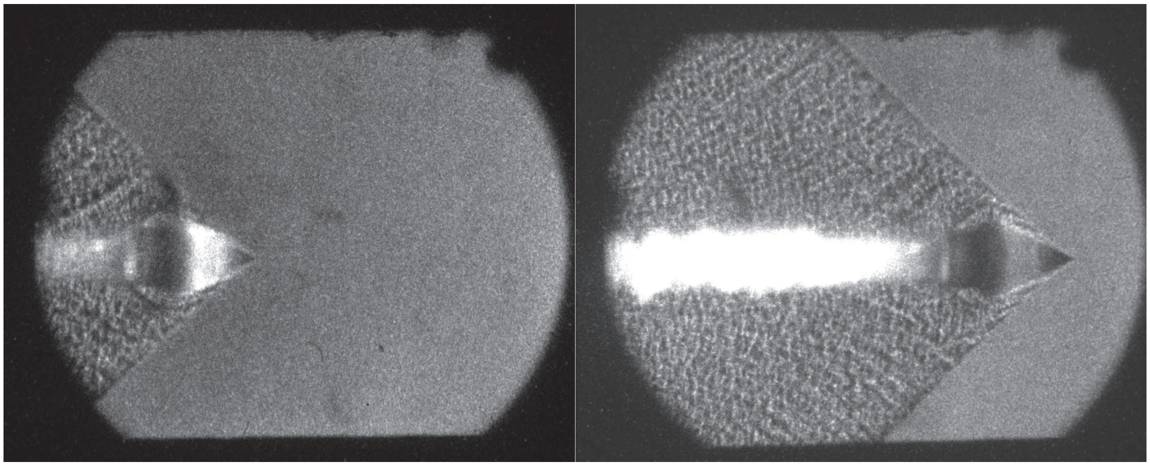

Figure B–13: Shot 153

Shot 154

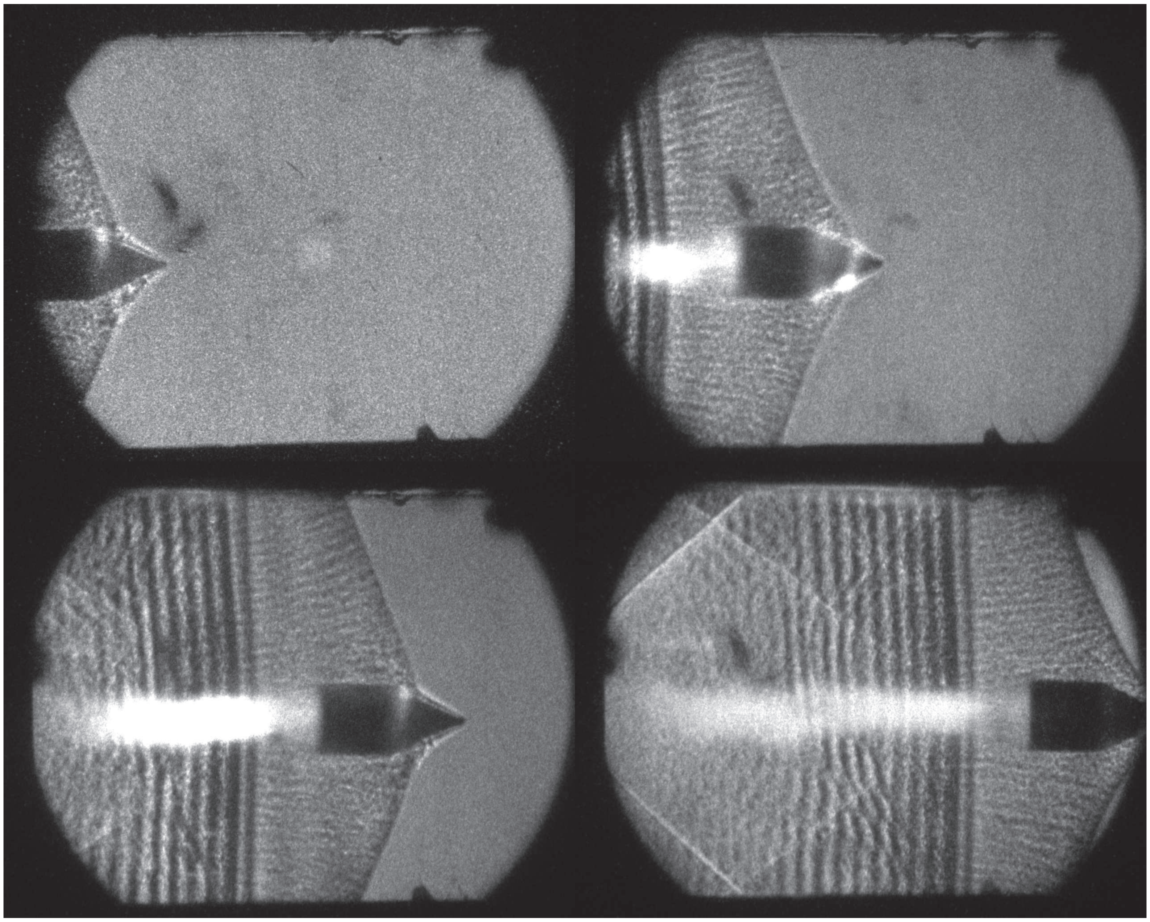

Figure B–14: Shot 154

Shot 155

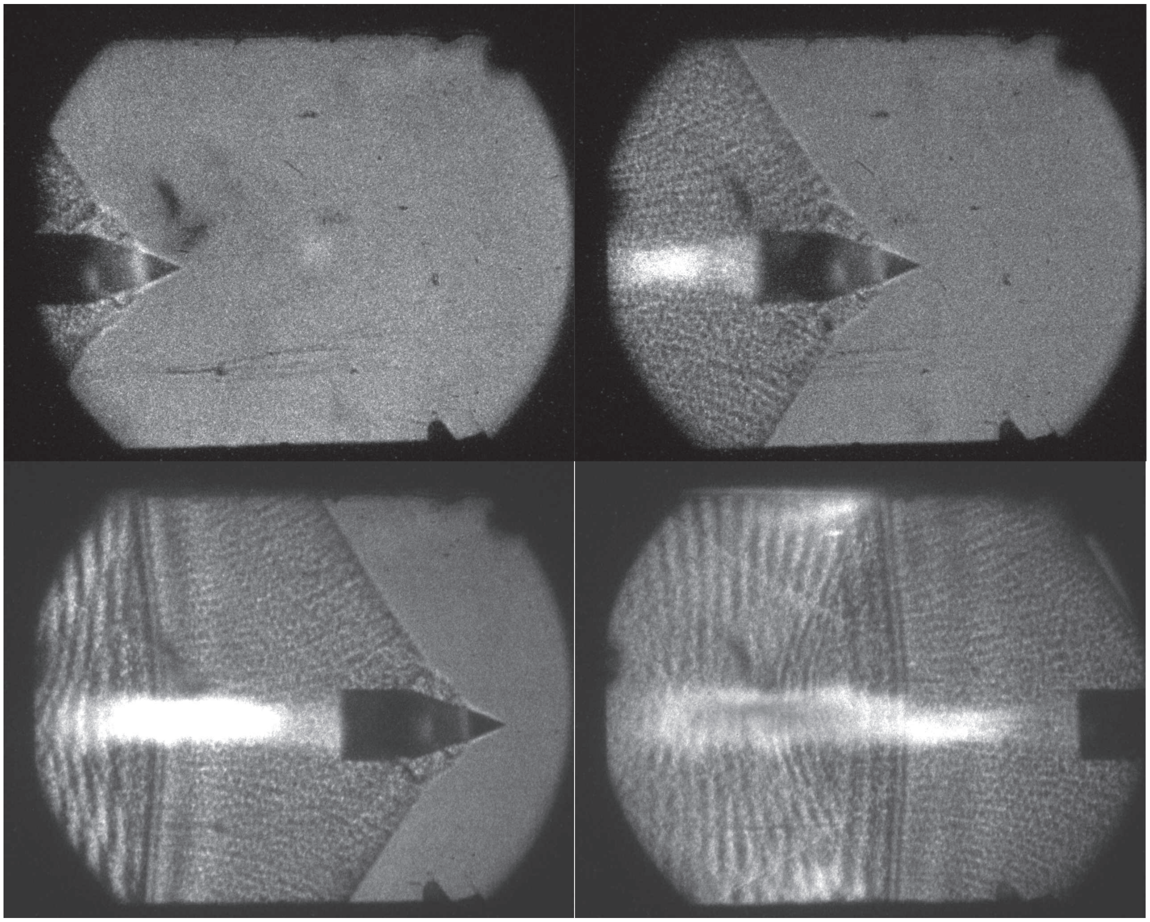

Figure B–15: Shot 155

Shot 156

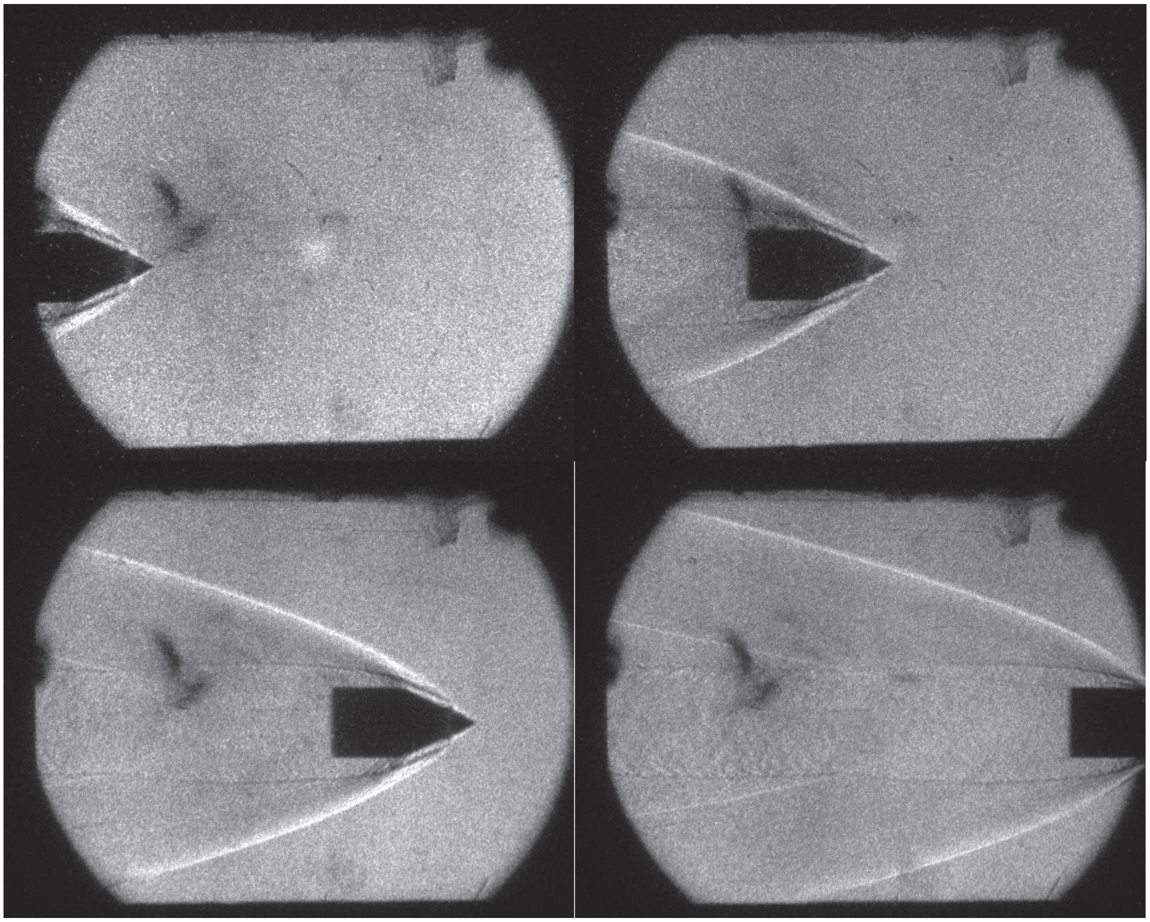

Figure B–16: Shot 156

Shot 157

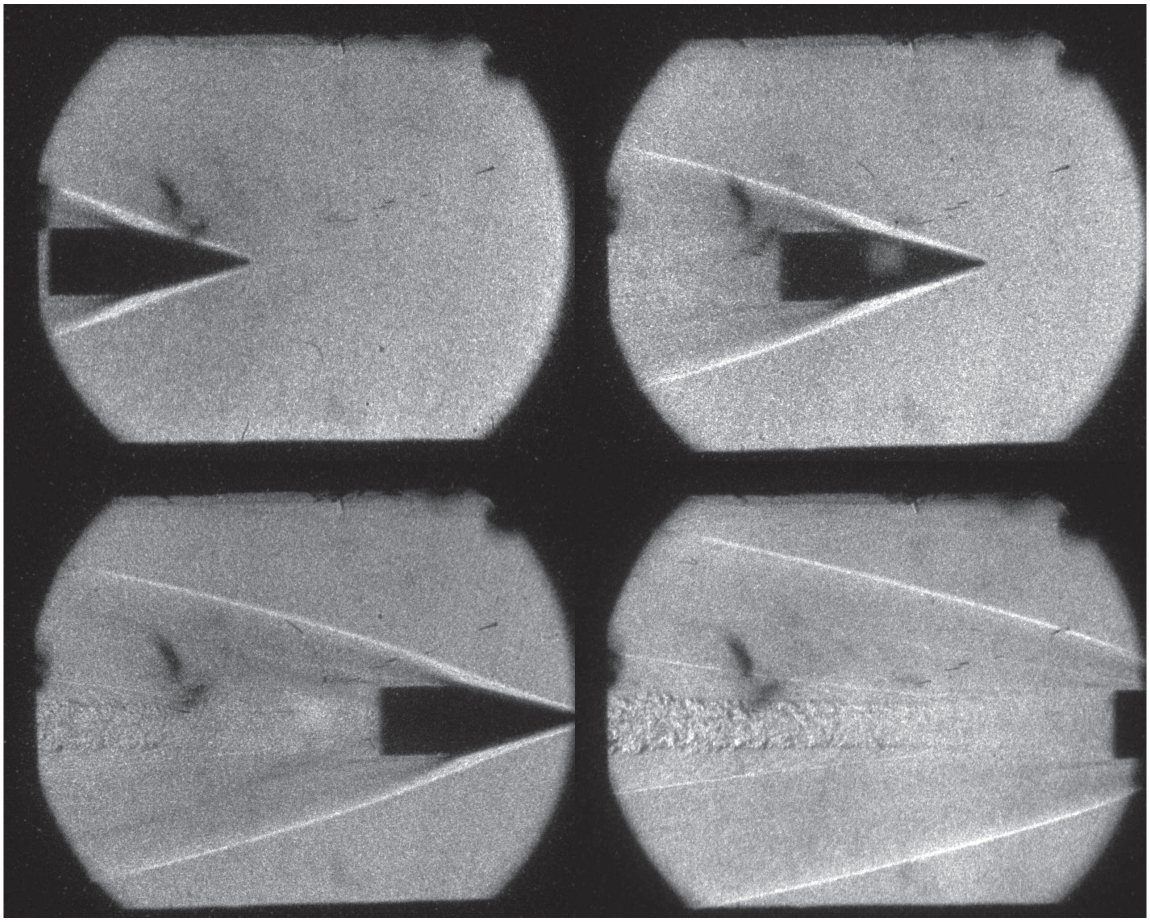

Figure B–17: Shot 157

Shot 159

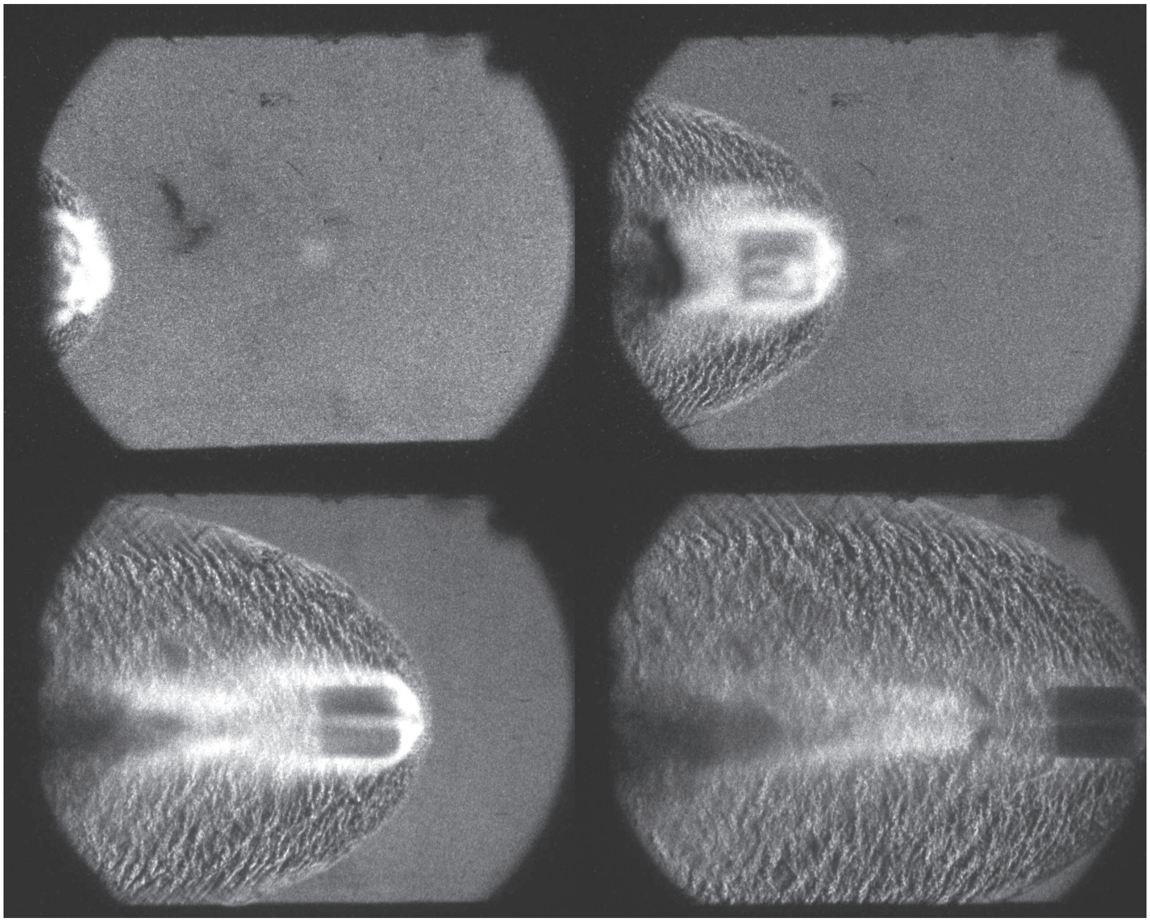

Figure B–18: Shot 159

Shot 160

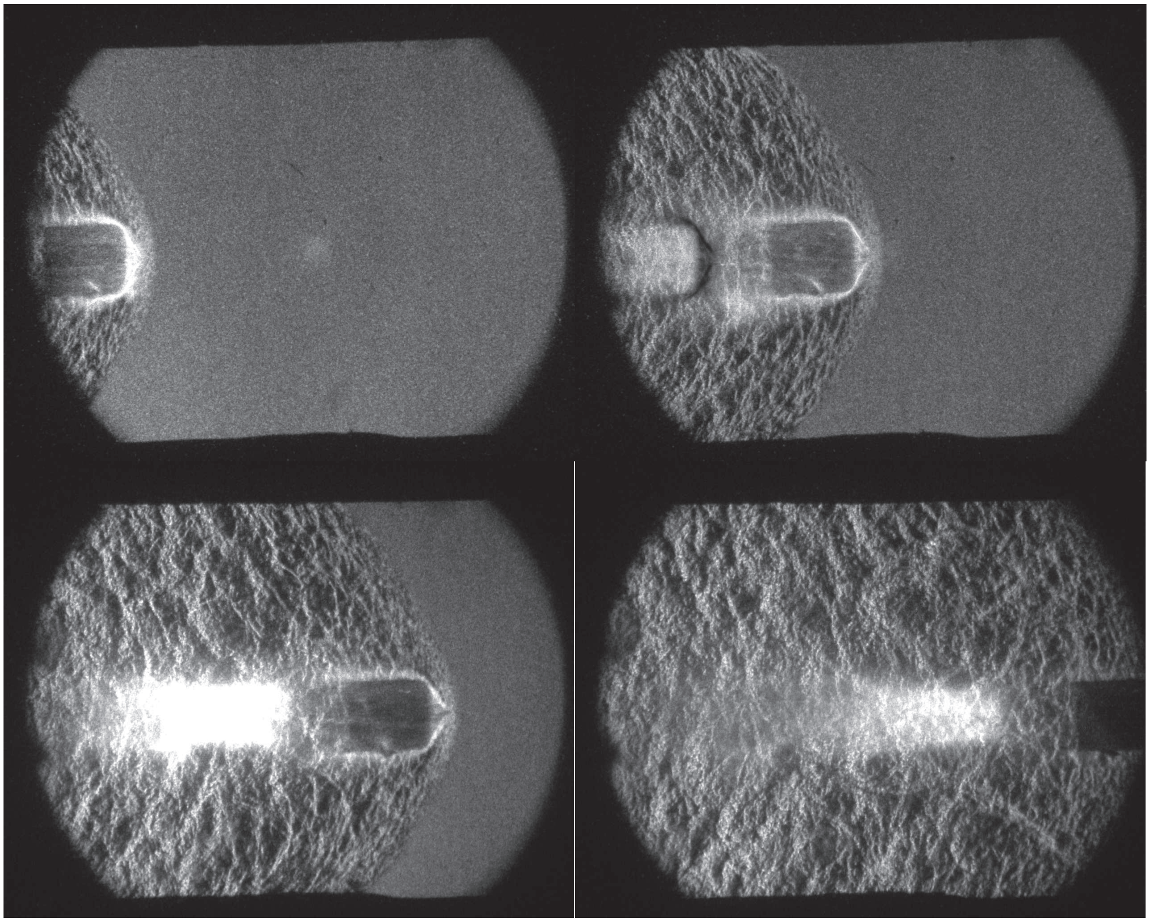

Figure B–19: Shot 160

Shot 161

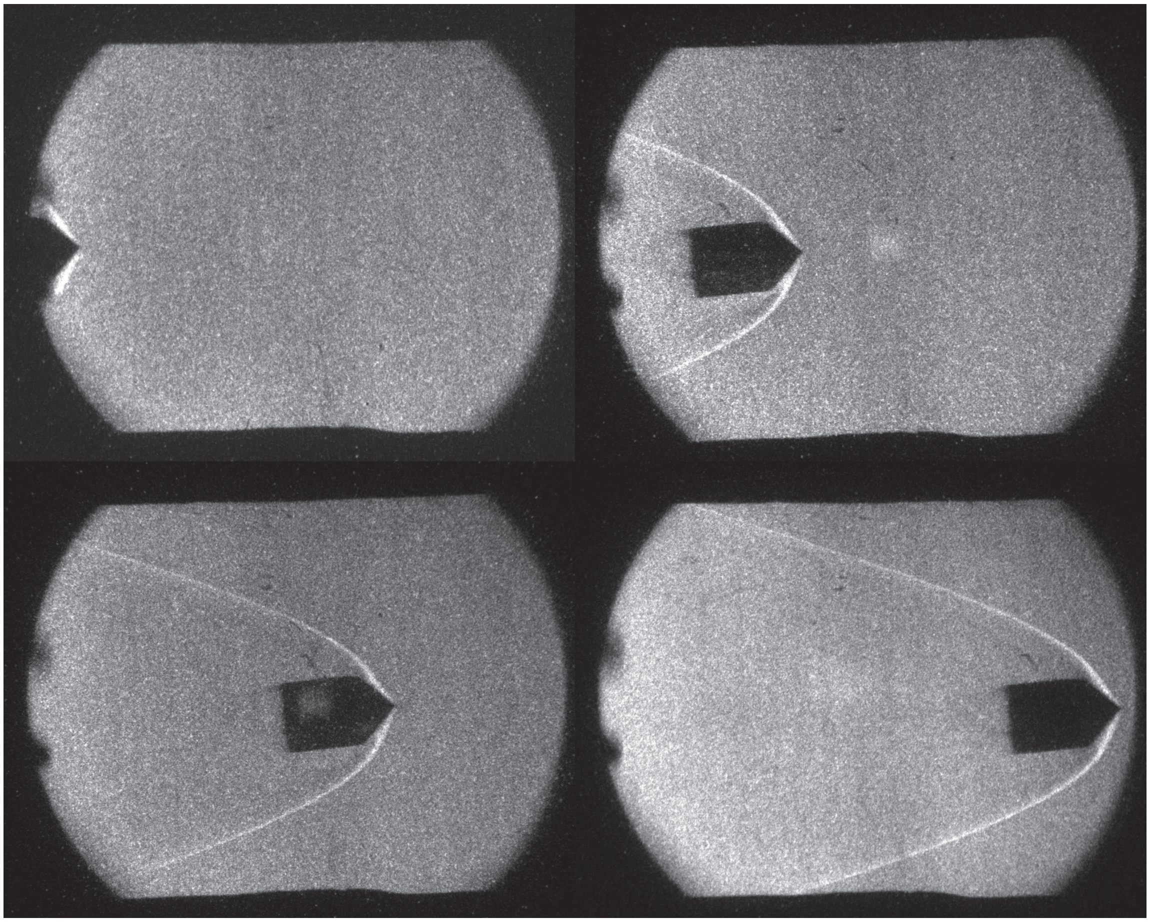

Figure B–20: Shot 161

Shot 162

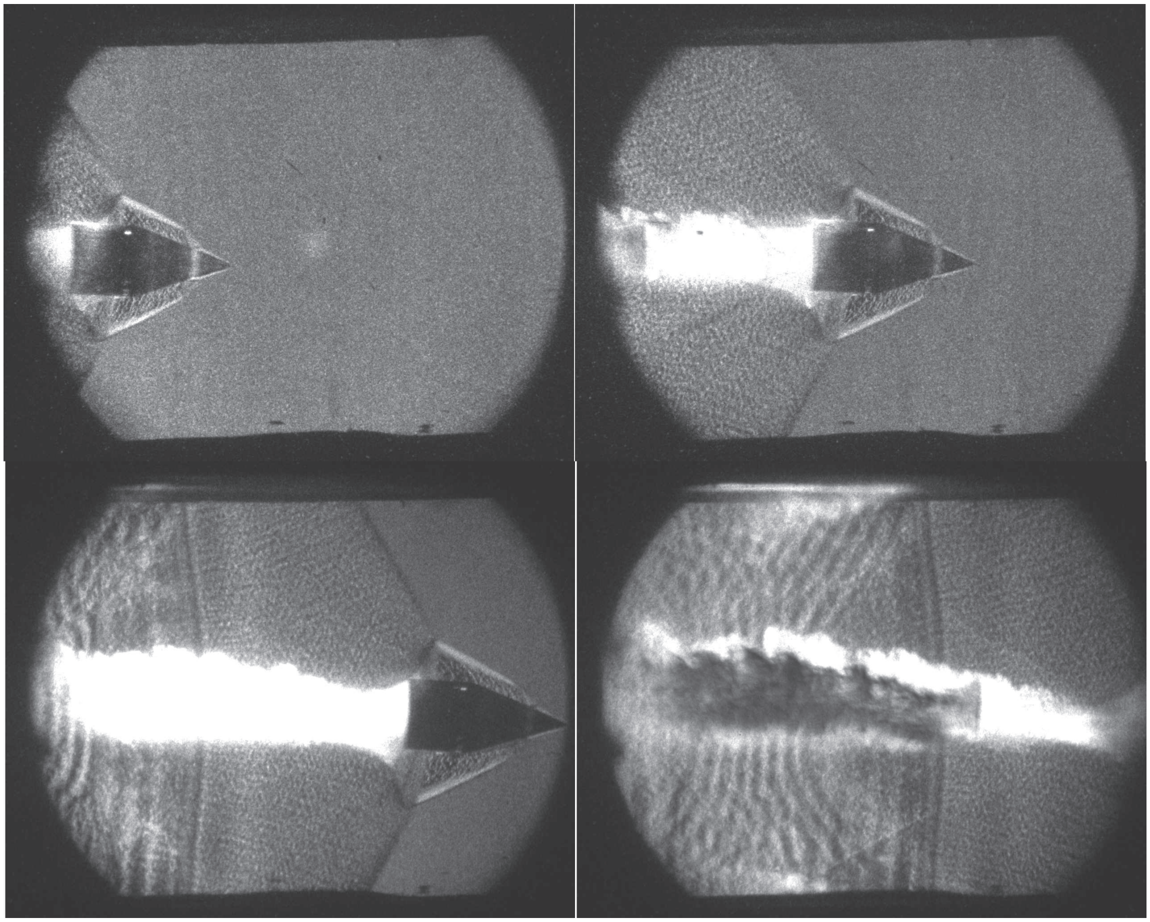

Figure B–21: Shot 162

Shot 163

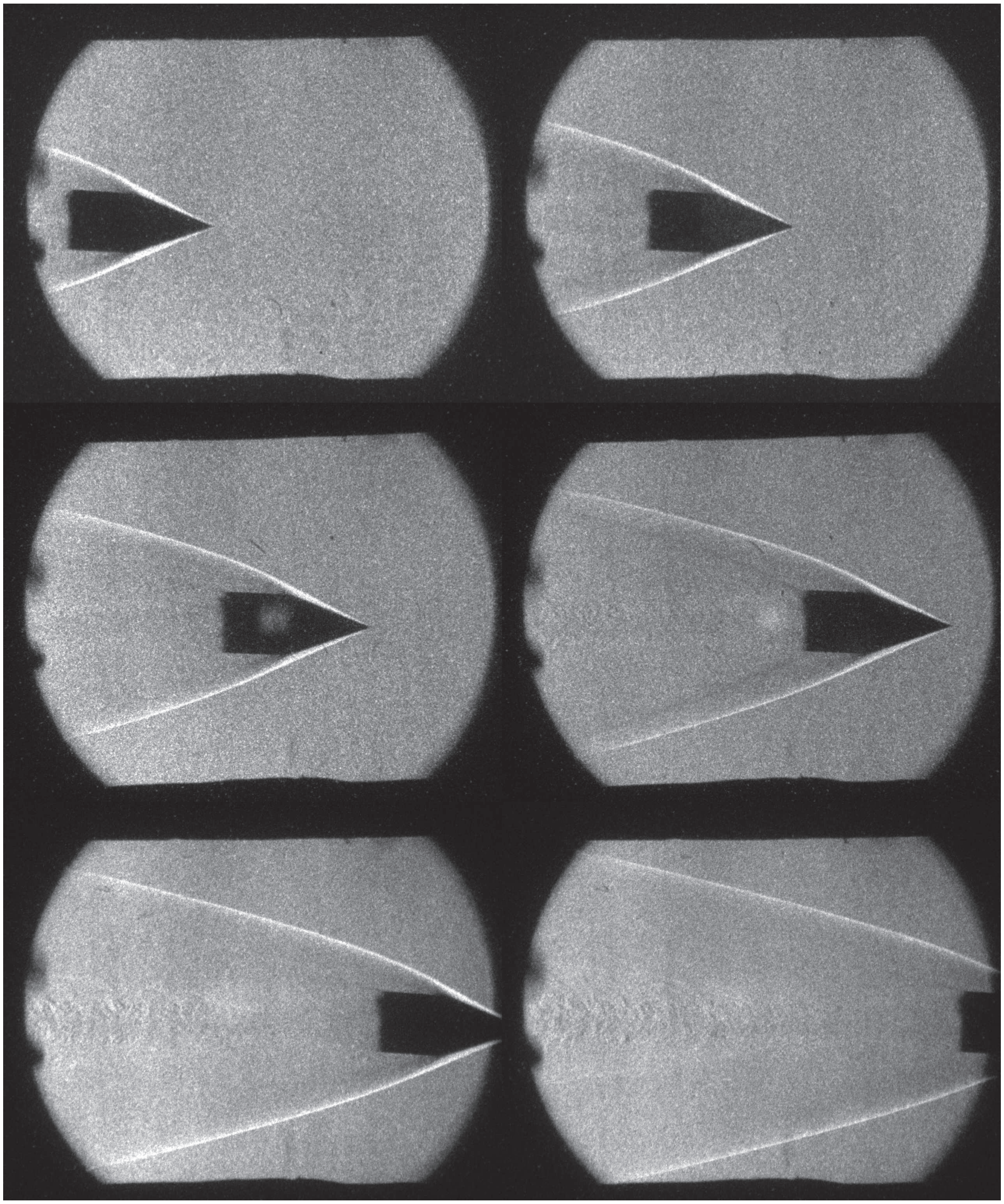

Figure B–22: Shot 163

Shot 164

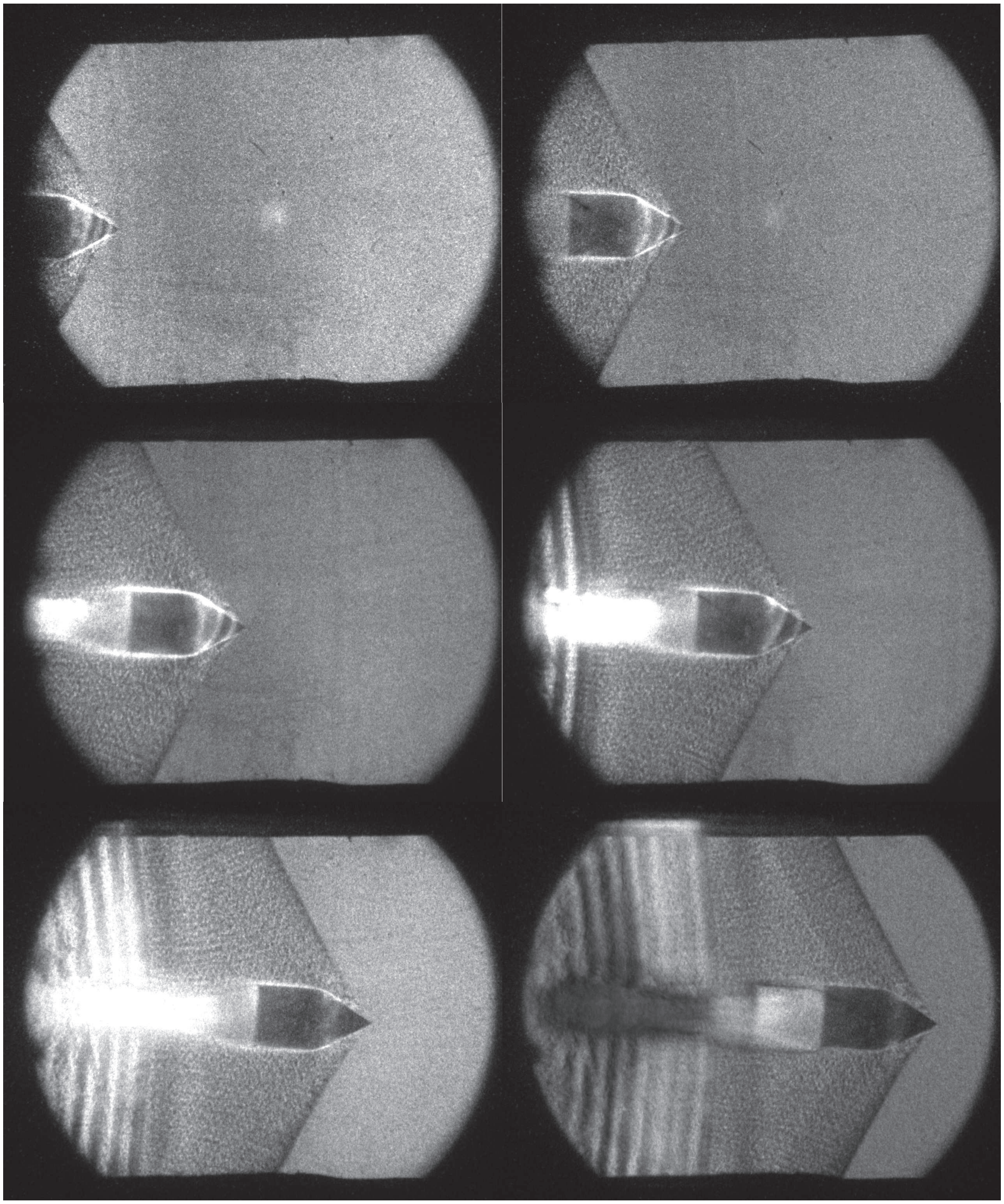

Figure B–23: Shot 164

Shot 166

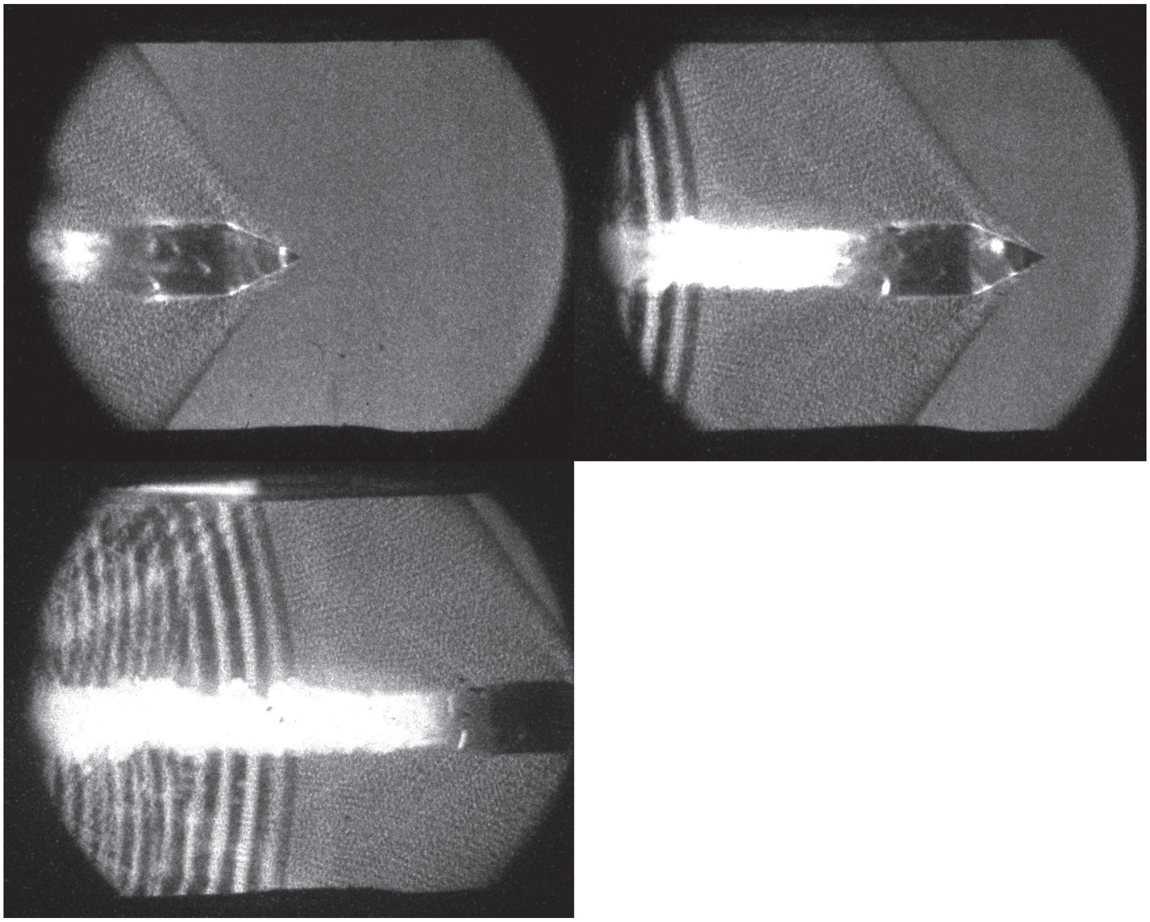

Figure B–24: Shot 166

Shot 167

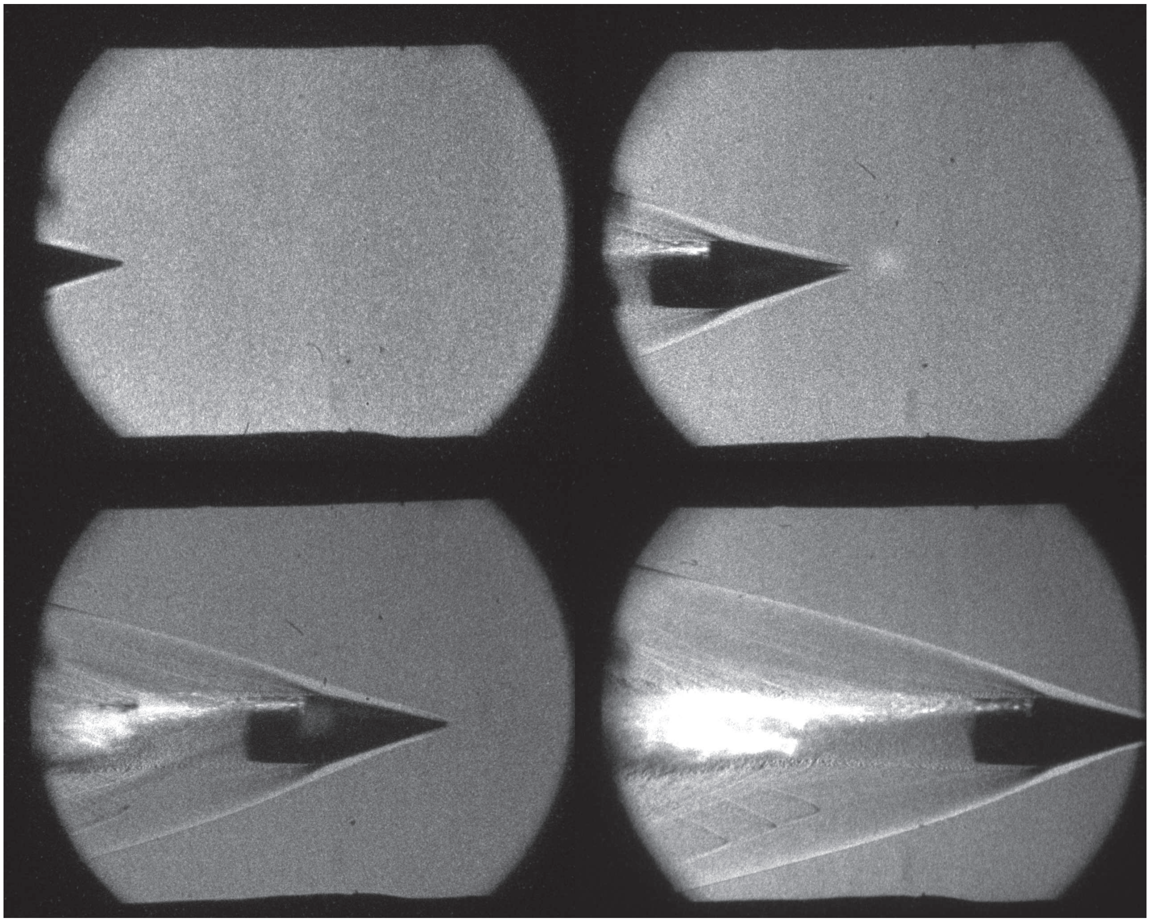

Figure B–25: Shot 167

Shot 168

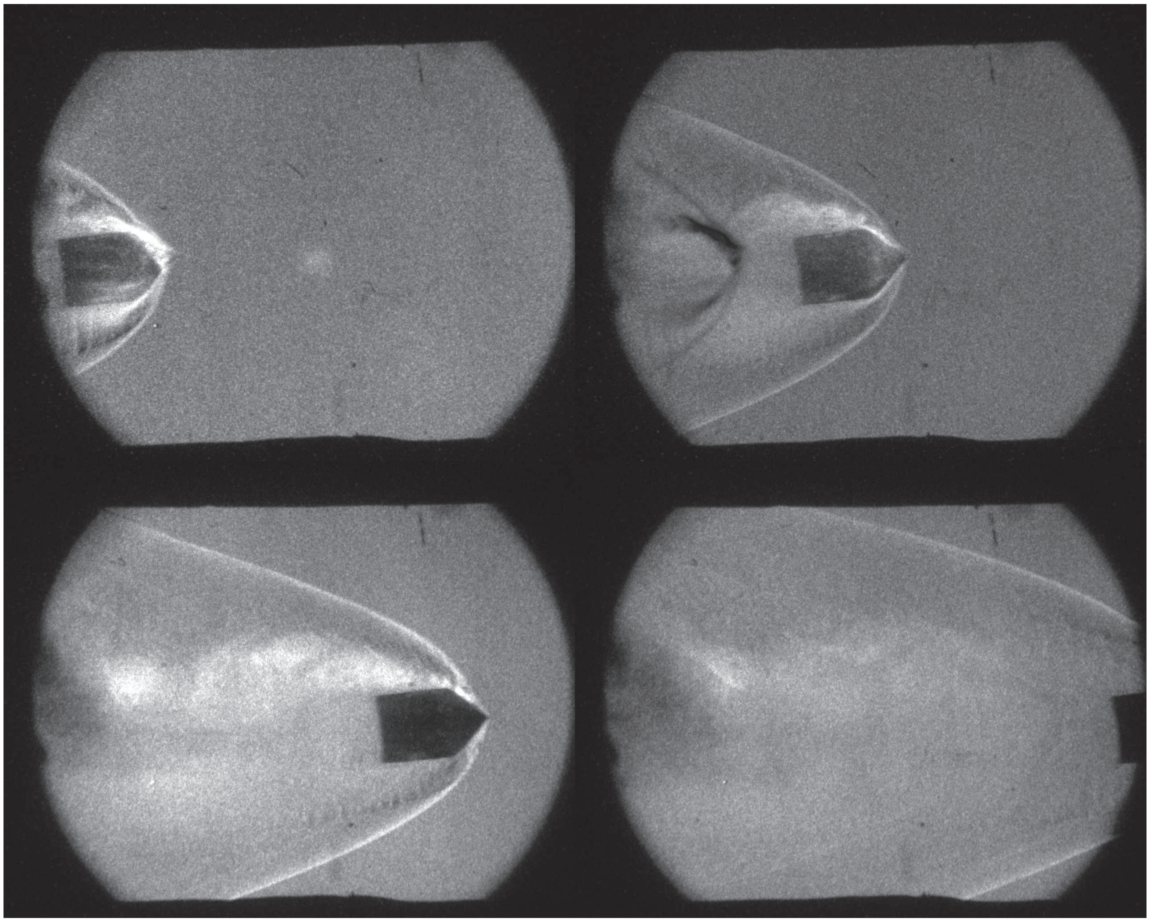

Figure B–26: Shot 168

Shot 169

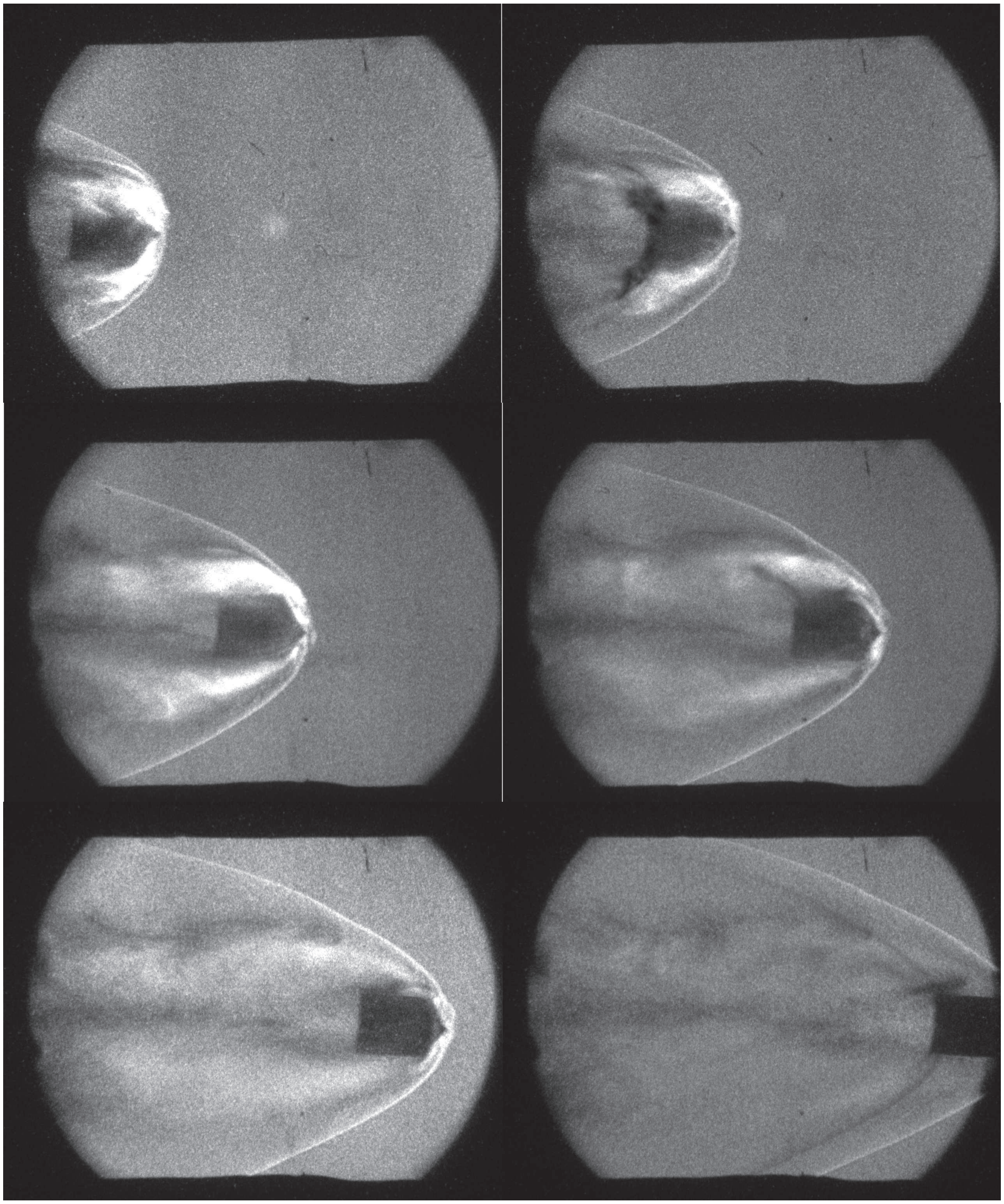

Figure B–27: Shot 169

Shot 170 (Frames 1 to 4)

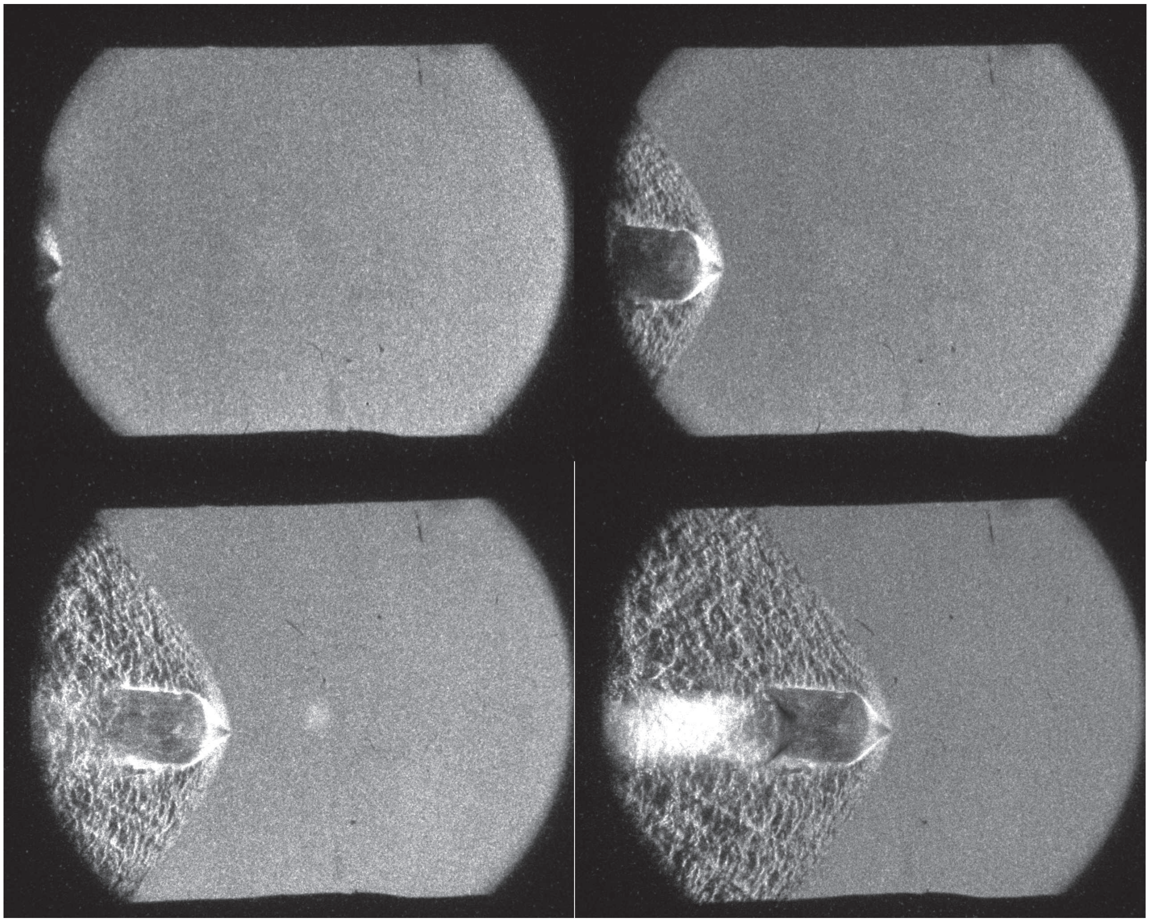

Figure B–28: Shot 170 (Frames 1 to 4)

Shot 170 (Frames 5 to 8)

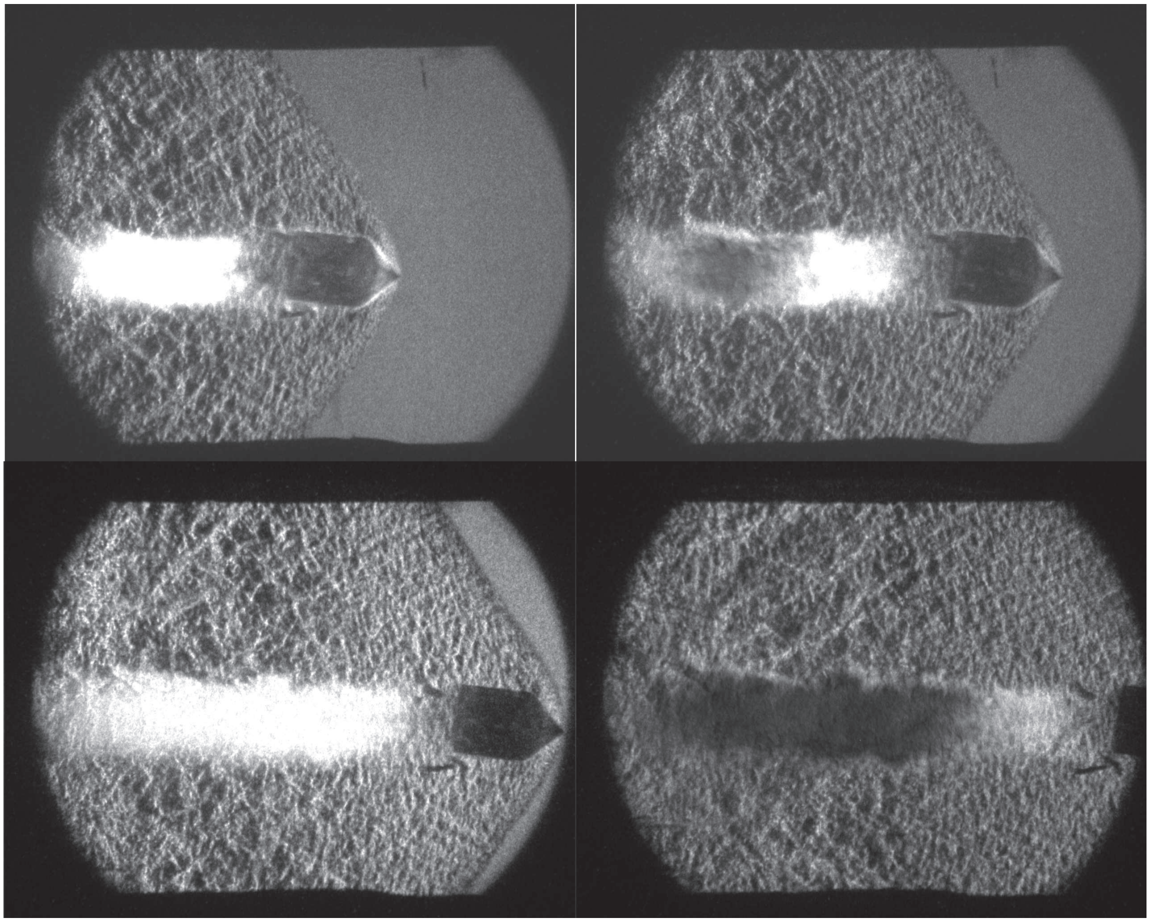

Figure B–29: Shot 170 (Frames 5 to 8)

Shot 171 (Frames 1 to 4)

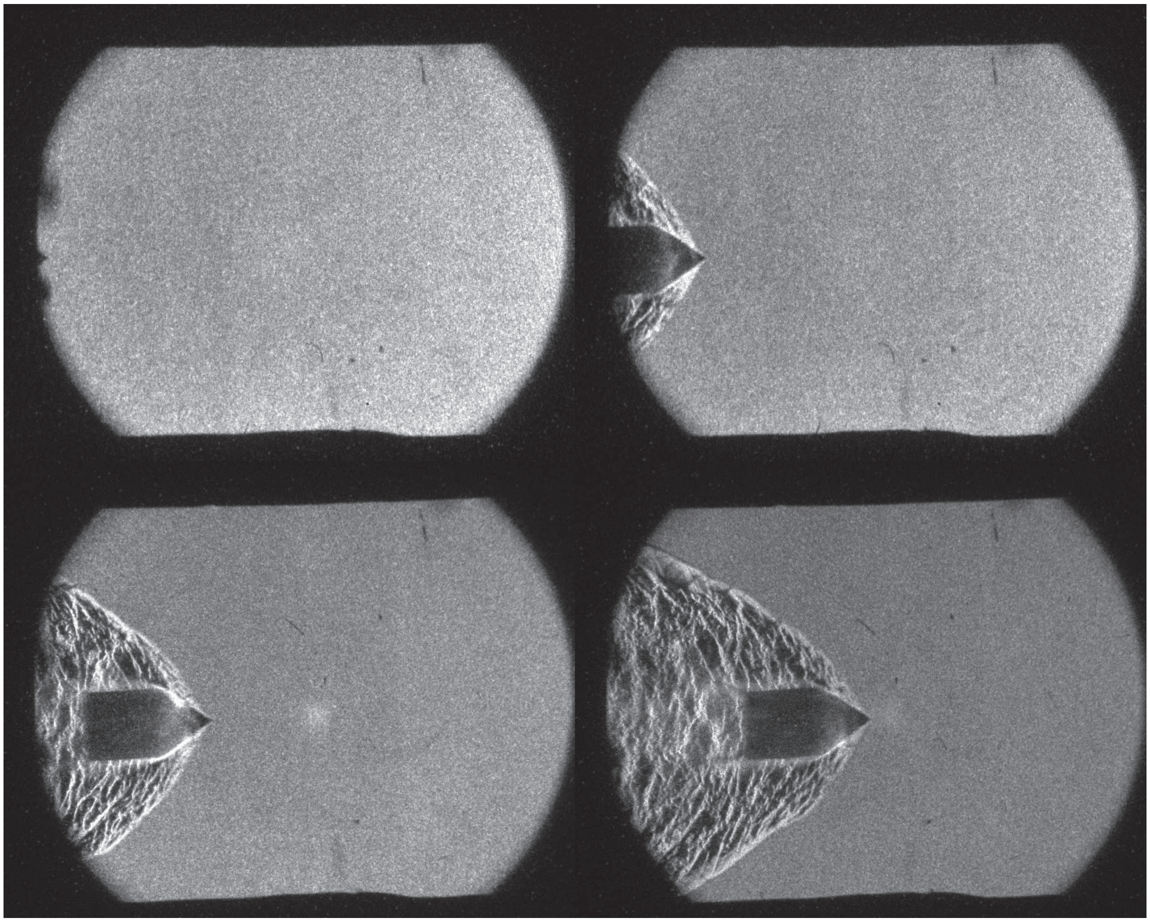

Figure B–30: Shot 171 (Frames 1 to 4)

Shot 171 (Frames 5 to 8)

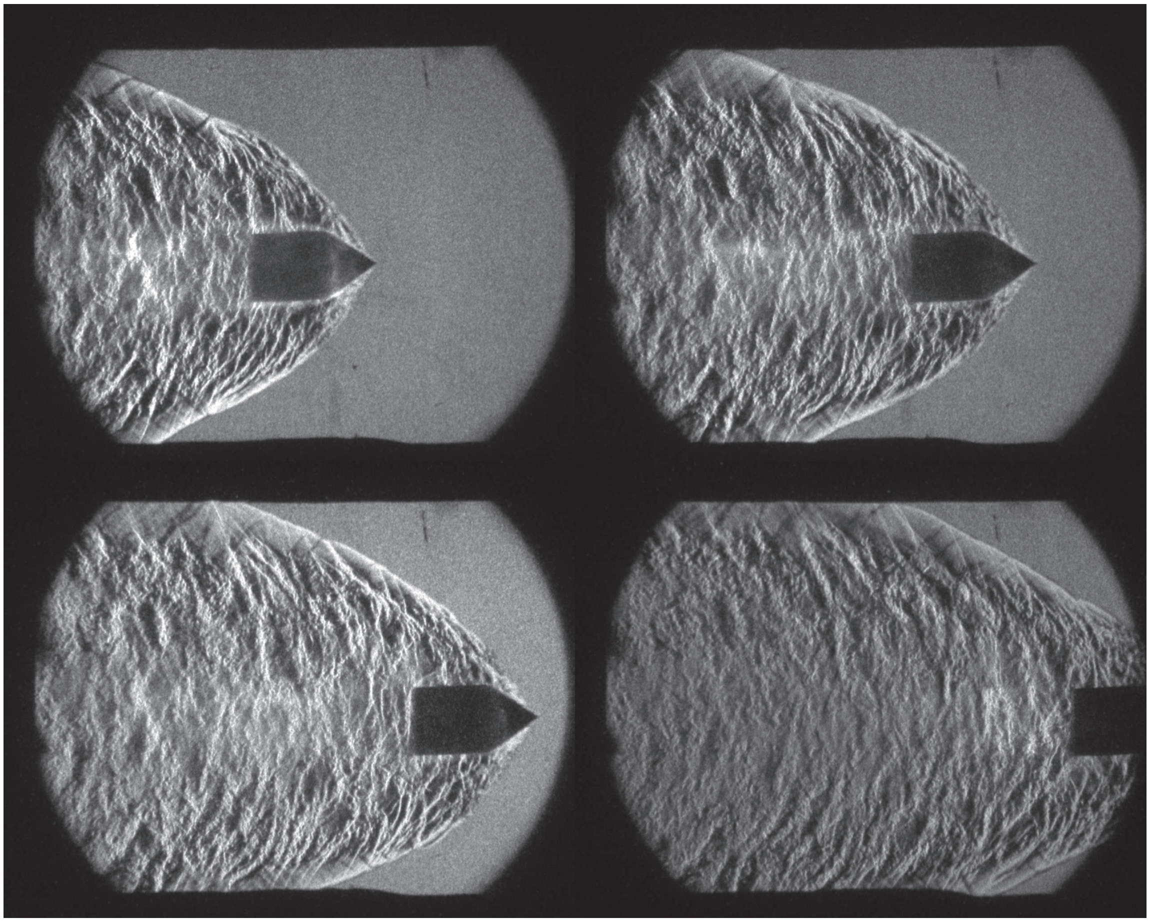

Figure B–31: Shot 171 (Frames 5 to 8)

APPENDIX C
ZND Formulation

This Appendix describes in details the implementation of the governing equations for compressible reacting flows using a full chemistry model. The flow is assumed to be inviscid, one dimensional and steady. Furthermore, any diffusive transport processes are ignored, as well as real gas effects, such as molecular dissociation and vibrational relaxation. The governing equations for such a system with N species and R reactions are given by the reactive Euler equations:

$$\frac{d}{dx}\left(\rho u\right) = 0 \tag{C.1}$$

$$\frac{d}{dx}\left(C_i \rho u\right) = \sigma_i \qquad i = 1, \dots, N \tag{C.2}$$

$$\frac{d}{dx}\left(\rho u^2 + p\right) = 0 \tag{C.3}$$

$$\frac{d}{dx}\left(\rho u\left(h + \frac{u^2}{2}\right)\right) = 0 \tag{C.4}$$

In this set of equations, there are six dependent variables: density ρ, velocity u, mass fraction C_i of component i, mass production rate σ_i of component i, pressure p and enthalpy h. In addition to the above governing equations, the following equations are required:

$$h = \sum_{i=1}^{N} C_i h_i^o = \sum_{i=1}^{N} C_i \left(h_{f,i}^o + \int_{T^{ref}}^{T} c_{p_i} \left(\bar{T}\right) d\bar{T} \right) \tag{C.5}$$

$$p = \rho \frac{\bar{R}}{W} T \tag{C.6}$$

$$\frac{1}{W} = \sum_{i=1}^{N} \frac{C_i}{W_i} \tag{C.7}$$

$$\sigma_i = W_i \sum_{r=1}^{R} \Gamma_r \left(\nu''_{i,r} - \nu'_{i,r}\right) \left(k_{f,r} \prod_{j=1}^{N} \chi_{j,r}^{\nu'_{j,r}} - k_{b,r} \prod_{j=1}^{N} \chi_{j,r}^{\nu''_{j,r}} \right) \qquad i = 1, \ldots, N \tag{C.8}$$

$$k_{f,r} = A_r T^{b_r} \exp\left(\frac{-E_{a,r}}{\bar{R}T} \right) \qquad r = 1, \ldots, R \tag{C.9}$$

$$k_{b,r} = \frac{k_{f,r}}{K_{c,r}} \qquad r = 1, \ldots, R \tag{C.10}$$

$$K_{c,r} = \exp\left(\sum_{j=1}^{N} \left(\nu''_{j,r} - \nu'_{j,r}\right) \left(\frac{s_j^o}{\bar{R}} - \frac{h_j^o}{\bar{R}T} \right) \right) \left(\frac{p^{ref}}{\bar{R}T} \right)^{\sum_{j=1}^{N} \left(\nu''_{j,r} - \nu'_{j,r}\right)} \qquad r = 1, \ldots, R \tag{C.11}$$

In Equations C.5 to C.11, $\bar{T}$ is a dummy variable of integration, $\bar{R}$ is the universal gas constant, $\nu'_{i,r}$ and $\nu''_{i,r}$ are the stoichiometric coefficients of species i in reaction r as a reactant and as a product, respectively, χ_j is the molar concentration of species j, Γ_r, A_r, b_r and $E_{a,r}$ are parameters provided by the detailed chemistry, s_i^o and h_i^o are the entropy and enthalpy, respectively, of species i at the reference pressure.

The reaction mechanism used for the present study is a revised model of hydrogen combustion including 9 species and 19 reactions [73]. Equations C.1 to C.6 consist of $5 + N$ equations for the $5 + N$ dependent variables ρ, u, p, h, T, C_1, $\ldots$, C_N. At each numerical integration point, the flow conditions are solved and the frozen properties at that location can be calculated using the following relations:

$$c_p = \sum_{i=1}^{N} C_i c_{p,i} \tag{C.12}$$

$$c_v = \sum_{i=1}^{N} C_i c_{v,i} \tag{C.13}$$

$$\frac{\bar{R}}{W} = c_p - c_v \tag{C.14}$$

$$\gamma = \frac{c_p}{c_v} \tag{C.15}$$

$$a = \sqrt{\gamma \frac{p}{\rho}} \tag{C.16}$$

$$M = \frac{u}{a} \tag{C.17}$$

The purpose is to obtain explicit relations for the pressure, density, velocity and mass fractions variations in the spatial domain. In order to do that, several manipulations of the above equations are required and they are given below. The explicit relation for the mass fractions variation can be obtained by rewriting Equation C.2:

$$\rho u \frac{dC_i}{dx} + C_i \frac{d(\rho u)}{dx} = \sigma_i \qquad i = 1, \ldots, N \tag{C.18}$$

From the conservation of mass for the mixture (Equation C.1), the second term on the left-hand side of Equation C.18 vanishes:

$$\frac{dC_i}{dx} = \frac{\sigma_i}{\rho u} \qquad i = 1, \ldots, N \tag{C.19}$$

In Equation C.19, the mass production rate σ_i is expressed in kg/(m^3·s) and is defined as the mass change per volume of species i due to chemical reactions. This parameter is calculated by the reaction mechanism in Equation C.8. One can see that the mass fraction change of species i is only affected by the mass change rate of that species, since the term ρu is constant via the conservation of mass equation.

The purpose of the next manipulations is to get an explicit expression for the pressure variation. Equation C.4 requires that:

$$\frac{d}{dx}\left(h + \frac{u^2}{2}\right) = 0 \tag{C.20}$$

or

$$-\frac{d\left(\frac{u^2}{2}\right)}{dx} = -u\frac{du}{dx} = \frac{dh}{dx} \tag{C.21}$$

Using Equation C.5, the right-hand side of Equation C.21 becomes:

$$\frac{dh}{dx} = \sum_{i=1}^{N} \left[\frac{dC_i}{dx} \left(h_{f,i}^o + \int_{T^{ref}}^{T} c_p \left(\bar{T}\right) d\bar{T} \right) + C_i \left(\frac{dh_{f,i}^o}{dx} + \frac{d}{dx} \int_{T^{ref}}^{T} c_{p_i} \left(\bar{T}\right) d\bar{T} \right) \right] \tag{C.22}$$

which reduces to:

$$\frac{dh}{dx} = \sum_{i=1}^{N} \left[\frac{dC_i}{dx} h_i + C_i \frac{d}{dx} \int_{T^{ref}}^{T} c_{p_i} \left(\bar{T}\right) d\bar{T} \right] \tag{C.23}$$

The second term on the right-hand side of Equation C.23 represents a differentiation of an integral. However, the integral accounts for the change of the specific heat c_p for species between the temperatures T^{ref} and T. The variable used for the integration between these two temperatures is arbitrary and in this case is $\bar{T}$, which has nothing to do with the spatial variation of the temperature. Therefore, Equation C.23 becomes:

$$\frac{dh}{dx} = \sum_{i=1}^{N} \left[\frac{dC_i}{dx} h_i \right] + \sum_{i=1}^{N} \left[C_i c_{p_i} \frac{dT}{dx} \right] = \sum_{i=1}^{N} \left[\frac{dC_i}{dx} h_i \right] + c_p \frac{dT}{dx} \tag{C.24}$$

Substituting Equation C.24 into Equation C.21:

$$-u \frac{du}{dx} = \sum_{i=1}^{N} \left[\frac{dC_i}{dx} h_i \right] + c_p \frac{dT}{dx} \tag{C.25}$$

We now develop the conservation of momentum equation (Equation C.3):

$$\frac{d\rho u^2}{dx} + \frac{dp}{dx} = u \frac{d\rho u}{dx} + \rho u \frac{du}{dx} + \frac{dp}{dx} = \rho u \frac{du}{dx} + \frac{dp}{dx} = 0 \tag{C.26}$$

In Equation C.26, the conservation of mass for the mixture Equation C.1 was used to eliminate the term $\frac{d\rho u}{dx}$. An explicit expression for the pressure variation can be obtained and Equation C.25 can be used to get:

$$\frac{dp}{dx} = -\rho u \frac{du}{dx} = \rho \left\{ \sum_{i=1}^{N} \left[\frac{dC_i}{dx} h_i \right] + c_p \frac{dT}{dx} \right\} \tag{C.27}$$

We now need an expression for the temperature variation, which can be obtained by differentiating the equation of state, Equation C.6:

$$T = \frac{pW}{\rho \bar{R}} \tag{C.28}$$

$$\frac{dT}{dx} = \frac{W}{\rho \bar{R}} \frac{dp}{dx} + \frac{p}{\rho \bar{R}} \frac{dW}{dx} - \frac{pW}{\rho^2 \bar{R}} \frac{d\rho}{dx} \tag{C.29}$$

Dividing by T:

$$\frac{1}{T} \frac{dT}{dx} = \frac{W}{T \rho \bar{R}} \frac{dp}{dx} + \frac{p}{T \rho \bar{R}} \frac{dW}{dx} - \frac{pW}{T \rho^2 \bar{R}} \frac{d\rho}{dx} \tag{C.30}$$

$$\frac{1}{T} \frac{dT}{dx} = \frac{1}{p} \frac{dp}{dx} + \frac{1}{W} \frac{dW}{dx} - \frac{1}{\rho} \frac{d\rho}{dx} \tag{C.31}$$

The variation of the mixture molecular mass can be expressed in terms of the mass production rate by differentiating Equation C.7 and by using Equation C.19:

$$\frac{-1}{W^2} \frac{dW}{dx} = \sum_{i=1}^{N} \frac{1}{W_i} \frac{dC_i}{dx} \tag{C.32}$$

$$\frac{1}{W}\frac{dW}{dx} = -W\sum_{i=1}^{N}\frac{1}{W_i}\frac{\sigma_i}{\rho u} \tag{C.33}$$

$$\frac{1}{W}\frac{dW}{dx} = \frac{-W}{\rho u}\sum_{i=1}^{N}\frac{\sigma_i}{W_i} \tag{C.34}$$

Substituting Equation C.34 into Equation C.31 gives:

$$\frac{1}{T}\frac{dT}{dx} = \frac{1}{p}\frac{dp}{dx} - \frac{W}{\rho u}\sum_{i=1}^{N}\frac{\sigma_i}{W_i} - \frac{1}{\rho}\frac{d\rho}{dx} \tag{C.35}$$

Substituting Equatino C.35 into Equation C.27 gives:

$$\frac{dp}{dx} = \rho\left\{\sum_{i=1}^{N}\left[\frac{dC_i}{dx}h_i\right] + c_pT\left[\frac{1}{p}\frac{dp}{dx} - \frac{W}{\rho u}\sum_{i=1}^{N}\frac{\sigma_i}{W_i} - \frac{1}{\rho}\frac{d\rho}{dx}\right]\right\} \tag{C.36}$$

Using Equation C.19 in Equation C.36:

$$\frac{dp}{dx} = \frac{1}{u}\sum_{i=1}^{N}(\sigma_i h_i) + \frac{\rho c_p T}{p}\frac{dp}{dx} - \frac{W c_p T}{u}\sum_{i=1}^{N}\left(\frac{\sigma_i}{W_i}\right) - c_pT\frac{d\rho}{dx} \tag{C.37}$$

The density variation in Equation C.37 can be expressed as a pressure variation, which is obtained by using the conservation of mass, Equation C.1:

$$u\frac{d\rho}{dx} + \rho\frac{du}{dx} = 0 \tag{C.38}$$

$$\frac{d\rho}{dx} = -\frac{\rho}{u}\frac{du}{dx} \tag{C.39}$$

and the conservation of momentum, Equation C.3 or C.27:

$$\frac{du}{dx} = -\frac{1}{\rho u}\frac{dp}{dx} \tag{C.40}$$

The density variation in terms of the pressure variation is therefore:

$$\frac{d\rho}{dx} = \frac{1}{u^2}\frac{dp}{dx} \tag{C.41}$$

Substituting Equation C.41 in Equation C.37 gives:

$$\frac{dp}{dx} = \frac{\rho c_p T}{p}\frac{dp}{dx} - \frac{c_p T}{u^2}\frac{dp}{dx} + \frac{1}{u}\sum_{i=1}^{N}(\sigma_i h_i) - \frac{W c_p T}{u}\sum_{i=1}^{N}\left(\frac{\sigma_i}{W_i}\right) \tag{C.42}$$

Rearranging the above equation:

$$\frac{dp}{dx}\left(1 - \frac{\rho c_p T}{p} + \frac{c_p T}{u^2}\right) = \frac{1}{u}\sum_{i=1}^{N}(\sigma_i h_i) - \frac{W c_p T}{u}\sum_{i=1}^{N}\left(\frac{\sigma_i}{W_i}\right) \tag{C.43}$$

Multiplying by $\frac{u^2}{c_p T}$:

$$\frac{dp}{dx}\left(\frac{u^2}{c_p T} - \frac{\rho u^2}{p} + 1\right) = u\sum_{i=1}^{N}\left(\frac{\sigma_i h_i}{c_p T} - \frac{W\sigma_i}{W_i}\right) \tag{C.44}$$

The terms in the left brackets of Equation C.44 can be arranged as follows

$$1 + u^2\left(\frac{1}{c_p T} - \frac{\rho}{p}\right) = 1 + u^2\left(\frac{p - \rho c_p T}{p c_p T}\right) = 1 + u^2\left(\frac{p - \rho c_p \frac{p}{\rho R}}{p c_p \frac{p}{\rho R}}\right) = 1 + u^2\left(\frac{R - c_p}{\frac{p}{\rho} c_p}\right) \tag{C.45}$$

Using Equations C.12 to C.17, Equation C.45 becomes:

$$1 + u^2 \left(\frac{-c_v}{\frac{p}{\rho} c_p} \right) = 1 - u^2 \left(\frac{1}{\frac{p}{\rho} \frac{c_p}{c_v}} \right) = 1 - \frac{u^2}{\frac{p}{\rho} \gamma} = 1 - \frac{u^2}{a^2} = 1 - M^2 \tag{C.46}$$

Substituting Equation C.46 into Equation C.44 gives the final expression for the pressure variation:

$$\frac{dp}{dx} = \frac{u \sum_{i=1}^{N} \left(\frac{\sigma_i h_i}{c_p T} - \frac{W \sigma_i}{W_i} \right)}{1 - M^2} \tag{C.47}$$

The density variation can be obtained by substituting Equation C.47 in Equation C.41:

$$\frac{d\rho}{dx} = \frac{\sum_{i=1}^{N} \left(\frac{\sigma_i h_i}{c_p T} - \frac{W \sigma_i}{W_i} \right)}{u \left(1 - M^2 \right)} \tag{C.48}$$

The velocity variation can be obtained by substituting Equation C.47 in Equation C.40:

$$\frac{du}{dx} = \frac{\sum_{i=1}^{N} \left(\frac{W \sigma_i}{W_i} - \frac{\sigma_i h_i}{c_p T} \right)}{\rho \left(1 - M^2 \right)} \tag{C.49}$$

Recalling the mass fractions variation, Equation C.19:

$$\frac{dC_i}{dx} = \frac{\sigma_i}{\rho u} \qquad i = 1, \ldots, N \tag{C.50}$$

The system of $3 + N$ ODEs are given by Equations C.47 to C.50 and T, c_p, h_i, σ_i, W and M are calculated, respectively, by the algebraic equations C.6, C.12, C.5, C.8, C.7 and C.17 at each integration point.